CONTROL TECHNIQUES FOR IMPROVED PERFORMANCE OF MICROGRID INTEGRATED WITH RES

A Thesis

Submitted in Partial Fulfillment of the Requirements for the Award of Degree of

DOCTOR OF PHILOSOPHY

by

Shruti Prajapati

(Roll No. 2K21/PHDEE/03)

Under the Supervision of
Prof. Rachana Garg and Prof. Priya Mahajan
Department of Electrical Engineering
Delhi Technological University, Delhi-110042



Department of Electrical Engineering DELHI TECHNOLOGICAL UNIVERSITY

(Formerly Delhi College of Engineering)
Shahbad Daulatpur, Main Bawana Road, Delhi-110042, India

September, 2025

©Delhi Technological University – 2025 All rights reserved

Acknowledgement

It is a great pleasure to express my gratitude to all those who have contributed towards the successful completion of my Ph.D. work. First of all, I am thankful to God, who has blessed me with the continuous enthusiasm and strength to acquire knowledge and learning.

I would like to take this opportunity to show my gratitude toward various people who had helped in the cause. I would like to extend my sincere gratitude to my supervisors, **Prof. Rachana Garg** and **Prof. Priya Mahajan**, for their invaluable guidance and firm support during the course of my research work. Their support and vision, evolved me as a better person, not only in the professional field but also in the personal life. It has been a privilege to work under their supervision and an experience to cherish forever.

I extend my gratitude to **Prof. Prateek Sharma** (Vice-Chancellor) and **Prof. Rinku Sharma** (Dean - Academic PG) for their cooperation and support for providing a supportive environment to complete my research at Delhi Technological University. I would also like to thank **Prof. Rachana Garg** in capacity of the Head of the Department, and the Chairperson, DRC Electrical Engineering Department, Delhi Technological University, New Delhi for being visionary about the required research environment in the department. I am also very thankful to all the **faculty members and staff** of the department for sharing their knowledge, to aid in the concern.

I would also like to thank all of them who have been helpful and were associated with me directly and indirectly throughout the work. I would like to thank my colleagues Ms. Manvi Mishra, Ms. Shefali Painuli, Mrs. Priya Rai, Mr. Atul Awasthi and Souvik Bera, for stimulating discussions and technical support at various stages of the research work.

I want to express my deepest appreciation to my parents Mrs. Kamini Devi and Mr. Devendra Prajapati for their unconditional love, support, patience, and encouragement. I also want to extend my gratitude to my sisters Mrs. Sristi and Ms. Swati, brother Mr. Aditya Prajapati and brother-in-law Mr. Gaurav Upadhayay for their support and motivation. I also want to appreciate the constant support of my friend Mr. Kishan Jaiswal for supporting me in this adventurous journey.

(Shruti Prajapati)



DELHI TECHNOLOGICAL UNIVERSITY

(Formerly Delhi College of Engineering)

Shahbad Daulatpur, Main Bawana Road, Delhi-42

Candidate's Declaration

I Shruti Prajapati hereby certify that the work which is being presented in the thesis entitled "Control Techniques for Improved Performance of Microgrid Integrated with RES" in partial fulfilment of the requirements for the award of the Degree of Doctor of Philosophy, submitted in the Department of Electrical Engineering, Delhi Technological University is an authentic record of my own work carried out during the period from 2021 to 2025 under the supervision of Dr. (Prof.) Rachana Garg and Dr. (Prof.) Priya Mahajan.

The matter presented in the thesis has not been submitted by me for the award of any other degree of this or any other Institute.

This is to certify that the candidate has incorporated all the corrections suggested by the examiner in the thesis and the statement made by the candidate is correct to the best of our knowledge.

Candidates' Signature

Signature of Supervisor(s)



DELHI TECHNOLOGICAL UNIVERSITY

(Formerly Delhi College of Engineering)

Shahbad Daulatpur, Main Bawana Road, Delhi-42

Certificate by the Supervisors

Certified that **Shruti Prajapati** (enrolment no: 2K21/Ph. DEE/03) has carried out her research work presented in this thesis entitled "Control Techniques for Improved Performance of Microgrid Integrated with RES" for the award of **Doctor of Philosophy** from the Department of Electrical Engineering, Delhi Technological University, Delhi, under our supervision. The thesis embodies results of original work, and studies are carried out by the student herself and the contents of the thesis do not form the basis for the award of any other degree to the candidate or to anybody else from this or any other University/Institution.

Dr. (Prof.) Rachana Garg

_ _

Dr. (Prof.) Priya Mahajan

Professor

Professor

Department of Electrical Engineering, Delhi Technological University, Shahbad Daulatpur, Main Bawana Road, Delhi-110042, India Department of Electrical Engineering, Delhi Technological University, Shahbad Daulatpur, Main Bawana Road, Delhi-110042, India

Date:

29-09-2025

CONTROL TECHNIQUES FOR IMPROVED PERFORMANCE OF MICROGRID INTEGRATED WITH RES

Abstract

Environmental, economic, and technological concerns have prompted the development of electrical systems based on the distributed generation (DG) model, which is associated with small-scale power generation and is primarily comprised of renewable energy sources (RES). These RES have significantly contributed to the advancement of microgrids, making them a viable alternative to conventional grids. Among all RES, solar photovoltaic (PV) is one of the most widely utilized due to its accessibility, ease of installation, and low maintenance requirements. Solar energy plays a significant role in environmental conservation and fostering a cleaner society. Additionally, advancements in technology have made PV modules increasingly cost-effective and efficient.

However, due to their dependence on meteorological conditions for energy generation, solar photovoltaic systems (SPS) exhibit uncertainty in power output. Solar cells display nonlinear I-V and P-V characteristics that are influenced by external variables such as solar irradiation, humidity, temperature, geographical location, and various dynamic conditions. Consequently, the development of sophisticated control strategies is critical to ensure the efficient operation of solar PV systems.

To address these challenges, a novel MPPT algorithm is developed by integrating the Incremental Conductance (INC) method with a double closed-loop voltage control strategy. This hybrid approach enables accurate MPP tracking while simultaneously regulating the DC bus voltage, thus enhancing the reliability of standalone hybrid microgrids. The proposed strategy is supported by a bidirectional DC-DC converter that facilitates intelligent charge/discharge control of the BESS, maintaining DC voltage stability within state-of-charge (SOC) limits.

In the subsequent phase, the research advances to the development of intelligent, data-driven MPPT algorithms for grid-connected PV systems. An Artificial Neural Network (ANN)-based MPPT controller is designed and trained using a diverse dataset that captures the spatiotemporal variations in solar irradiance and temperature. To enhance the adaptability and generalization capabilities of the ANN model, the Horned Lizard Optimization (HLO) algorithm—a recent bio-inspired metaheuristic technique—is employed to optimally tune the ANN's internal parameters. The resulting ANN-HLO MPPT controller demonstrates superior tracking accuracy, faster convergence, and robust performance under rapidly changing irradiance conditions.

Performance robustness is validated using a three-month real-time solar irradiance dataset obtained from NASA and NREL for two geographically distinct locations: Shahabad Daulatpur (Delhi) in northern India and Chikkaballapur (Karnataka) in southern India. These datasets enable realistic and comprehensive testing of the MPPT controller under dynamic conditions, including irradiance fluctuations, temperature changes, voltage sag/swell events, and nonlinear load disturbances. Compliance with the EN50530 MPPT efficiency standard is also established for both fast and slow-

changing irradiance scenarios. Performance benchmarking confirms higher tracking accuracy, reduced settling time, and enhanced energy yield in comparison to existing techniques. Additionally, sensitivity analysis substantiates the algorithm's robustness across a wide range of operating conditions.

Recognizing the crucial role of inverter control in grid-tied systems, the thesis proceeds with an exhaustive study of DC link voltage regulation techniques. While conventional PI controllers are widely used, they often struggle to maintain voltage stability under fluctuating irradiance and nonlinear load conditions. To overcome this limitation, metaheuristic optimization techniques such as Cuckoo Search Optimization (CSO) and Honey Badger Algorithm (HBA) are introduced to optimally tune the PI controller gains (Kp and Ki). These techniques minimize integral error criteria and improve dynamic system response. The proposed control scheme maintains unity power factor operation and ensures harmonic distortion remains within IEEE-519 limits, even under complex nonlinear loading scenarios.

The thesis also includes performance evaluation using statistical metrics such as Mean Absolute Error (MAE), Root Mean Square Error (RMSE), and Mean Square Error (MSE), offering quantitative validation of the proposed control strategies. Comparative analysis of conventional PI, ANN-PI, CSO-PI, and HBA-PI controllers is carried out through MATLAB/Simulink simulations under varying scenarios, including sudden load changes and irradiance dips, demonstrating the superiority of the optimization-enhanced approaches.

In addition to advanced control methodologies, the thesis addresses one of the most critical protection challenges in grid-connected PV systems: islanding detection. A voltage ripple-based islanding detection method is studied, which accurately identifies grid disconnection events by analysing characteristic disturbances in the DC link voltage waveform. This method ensures minimal non-detection zones (NDZ), rapid response time, and compliance with IEEE 1547 and IEC 62116 standards.

Overall, this thesis contributes significantly to the domain of solar PV-based power systems by integrating classical control theories with cutting-edge artificial intelligence and optimization methods. The proposed control strategies deliver improved energy efficiency, enhanced system reliability, and resilient performance under diverse environmental and operational scenarios. The outcomes of this work have direct applications in the design and deployment of next-generation smart microgrids, aligning with the global pursuit of clean, sustainable energy solutions.

.

List of Publications

Journal Publication

- 1. Prajapati, Shruti, Rachana Garg, and Priya Mahajan. "Novel adaptive MPPT technique for enhanced performance of grid integrated solar photovoltaic system." *Computers and Electrical Engineering* 120 (2024): 109648. https://doi.org/10.1016/j.compeleceng.2024.109648. (SCIE Journal, Impact factor-4.9, Elsevier.)
- Prajapati, Shruti, Rachana Garg, and Priya Mahajan. "Modified control approach for MPP tracking and DC bus voltage regulation in a hybrid standalone microgrid." *Electric Power Systems Research* 236 (2024): 110935. https://doi.org/10.1016/j.epsr.2024.110935. (SCIE Journal, Impact factor-4.2, Elsevier.)
- 3. Prajapati, Shruti, Rachana Garg, and Priya Mahajan. "Honey badger algorithm-based PI controller for DC link voltage control of solar photovoltaic system connected to grid for enhanced power quality." *Electric Power Components and Systems* (2024): 1-20. https://doi.org/10.1080/15325008.2024.2304147 (SCIE Journal, Impact factor-1.5, Taylor and Francis.)
- 4. Prajapati, S., Garg, R. and Mahajan, P Performance Enhancement of grid tied SPV system using Evolutionary Optimization Technique. 2025 https://doi.org/10.1007/s12046-025-02872-1. (SCIE Journal, Impact factor-1.4, Springer.)

International Conference Publications

- 1. S. Prajapati, R. Garg and P. Mahajan, "Evolutionary Algorithm for Enhanced Performance of Grid Connected SPV System," 2022 5th International Conference on Contemporary Computing and Informatics (IC3I), Uttar Pradesh, India, 2022, pp. 814-820, doi: 10.1109/IC3I56241.2022.10072539
- 2. S. Prajapati, R. Garg and P. Mahajan, "Passive Islanding Detection Approach for Grid Integrated SPV System," 2024 IEEE Region 10 Symposium (TENSYMP), New Delhi, India, 2024, pp. 1-5, doi: 10.1109/TENSYMP61132.2024.10752124.
- 3. S. Prajapati, R. Garg and P. Mahajan, "Model Predictive Control for Hybrid Standalone PV Microgrid" Gridcon 2025 (Presented)
- 4. Prajapati, R. Garg and P. Mahajan, "Intelligent ANN control technique for grid integrated SPV System" (Communicated)

Table of Content

Title	Pag	ge No.
Acknow	wledgement	i
Candid	date's Declaration	ii
Certifi	cate by the Supervisors	iii
Abstra	nct	iv
List of	Publications	vi
Table o	of Content	vii
List of	Tables	xiv
List of	Figures	xvi
List of	Abbreviations and Nomenclature	XX
CHAP	TER 1: INTRODUCTION	1
1.1	Introduction	1
1.2	Overview of RES based microgrid	3
1.3	Solar PV based microgrid	4
	1.3.1 Standalone solar PV based microgrid	4
	1.3.2 Grid connected solar PV based microgrid	5
1.4	MPPT techniques for standalone and grid connected RES based micro	_
1.5	Inverter control and DC bus voltage regulation of standalone and grid connected RES based microgrid	6
1.6	Islanding detection of solar PV based microgrid	7
1.7	Motivation and research objectives	7
1.8	Problem Identification	8
1.9	Organization of thesis	9
1.10	Concluding remarks	11
CHAP	TER 2: LITERATURE REVIEW	12
2.1 Iı	ntroduction	12
	MPPT control techniques for hybrid standalone and grid connected solar system	
	2.2.1 Classical MPPT Techniques	13
	2.2.2 Intelligent MPPT Techniques	13

2.2.3 Optimization MPPT Techniques	15
2.2.4 Hybrid MPPT Techniques	16
2.3 Inverter control techniques and DC bus voltage regulation of standalor grid integrated RES system	
2.3.1 Linear Controller	17
2.3.2 Non-Linear Controller	18
2.3.3 Robust Controller	19
2.3.4 Adaptive Controller	19
2.3.5 Predictive Controller	19
2.3.6 Intelligent Controller	20
2.4 Islanding detection techniques for grid integrated solar PV system	22
2.4.1 Classical Islanding detection techniques	23
2.4.2 Modern Islanding detection techniques	24
2.5 Identified research gaps	24
2.6 Concluding remarks	25
CHAPTER 3: PERFORMANCE ENHANCEMENT OF HYBRID	
STANDALONE RES BASED MICROGRID	
3.1 Introduction	
3.2 Modelling and design of Hybrid microgrid system	
3.2.1 Solar PV modelling	
3.2.2 Modelling of wind turbine	
3.2.3 Modelling of PMSG	
3.2.4 DC-DC Boost converter modelling	
3.2.5 DC-DC Buck- Boost converter modelling	
3.2.6 Battery energy storage system modelling	
3.2.7 LC Filter Modelling	33
3.3 MPPT control techniques for standalone RES based microgrid	34
3.3.1 Perturb and Observe (P&O) technique	34
3.3.2 Incremental Conductance (INC) technique	34
3.3.3 Particle Swarm Optimization technique	35
3.3.4 Cuckoo Search Optimization technique	37
3.3.5 Proposed Modified MPPT (INC with Double close loop controller) technique	38
3.3.6 Control Technique for bidirectional converter.	39

3.3.7 Working of battery energy storage system40
3.4 Control techniques for standalone inverter
3.4.1 Droop Control strategy41
3.4.2 Model Predictive control
3.5 Result and Discussion
3.5.1 Performance evaluation of PV-BESS hybrid microgrid using proposed modified MPPT and inverter droop control
3.5.1.1 System response under different irradiation condition47
3.5.1.2 System response under load varying condition
3.5.1.3 System response under variable nonlinear load condition49
3.5.1.4 System response under unbalanced load condition49
3.5.1.5 Comparison of PV power output at different irradiance using proposed novel MPPT technique and existing control techniques
3.5.1.6 Comparison of transient response of DC bus voltage on different irradiation using proposed novel MPPT techniques and existing control techniques
3.5.1.7 Comparison of MPPT Efficiency test EN50530 using developed and existing control techniques
3.5.2 Performance evaluation of PV-Wind-BESS hybrid microgrid using proposed modified MPPT and inverter droop control
3.5.2.1 System response under battery charging condition55
3.5.2.2 System response under battery discharging condition 57
3.5.2.3 System response under non-linear variable load condition 57
3.5.2.4 System response under variable irradiation condition 58
3.5.2.5 System response under variable wind speed condition 58
3.5.2.6 Comparative analysis of transient response of DC bus voltage under variable wind speed using proposed and existing control techniques
3.5.3 Performance evaluation and result discussion using proposed modified MPPT technique and Model Predictive Control technique for inverter
3.5.3.1 System response under variable linear load demand61
3.5.3.2 System response under variable non-linear load demand 61
3.5.3.3 System response under unbalanced non- linear load demand
3.5.3.4 Comparative analysis of Droop controller and Model

	nique with the proposed modified63
3.6 Scalability and cost implication of double conductance	*
3.7 Concluding remarks	65
CHAPTER 4: MPPT CONTROL TECHNIC SOLAR PV BASED MICROGRID	
4.1 Introduction	66
4.2 MPPT techniques for grid integrated so	lar PV system66
4.2.1 Artificial Neural Network (ANN	I) based MPPT control technique .67
4.2.2 Optimized ANN based MPPT co	ontrol techniques68
	zation (PSO)-ANN MPPT control
	BC)-ANN MPPT control techniques70
4.2.2.3 Harmony Search (HS) A	NN MPPT control techniques71
	Optimization (TLBO)-ANN MPPT 72
	mizer (DMO)-ANN MPPT control
	Optimization (HLO)-ANN MPPT
4.3 Result evaluation and discussion using control technique	
	the system under variable load Conditions (STC)83
4.3.2 Performance evaluation of tradiation condition	the system under variable load and
conditions (Sag, Swell and u	the System under abnormal grid unbalanced grid voltage) and load
4.3.4 Sensitivity analysis of HLO-A	ANN MPPT technique86
4.4 Comparative analysis of proposed HLO	-ANN algorithm87
4.4.1 Comparative analysis of propose other techniques in terms of grid	ed HLO-ANN MPPT techniques with current harmonics87
4.4.2 Comparative analysis of propose other techniques for dynamic irr	ed HLO-ANN MPPT techniques with adiation variation89
4.4.3 Comparative analysis of propose	ed HLO-ANN MPPT techniques with

	other techniques for dynamic temperature variation92
	4.4.4 MPPT Efficiency test EN5053094
	4.4.5 Transient analysis of DC bus voltage at different irradiation95
	4.4.6 Comparison of convergence rate and error parameters of different algorithm
	4.4.7 Validation of the proposed algorithm considering test data set 97
	4.4.8 Benchmark analysis
	4.4.9 Computational complexity analysis
	4.4.10 Scalability and cost implication of HLO-ANN MPPT controlle102
4.5	Concluding remarks
	APTER 5: INVERTER CONTROL TECHNIQUES FOR GRID- EGRATED SOLAR PV BASED MICROGRID104
5.1	Introduction
5.2	Inverter control techniques for grid integrated solar PV system 105
	5.2.1 Synchronous Reference Frame Theory
5.3	Synchronous Reference Frame Theory with advanced PI-Controller 107
	5.3.1 SRFT with ANN-PI Controller for Inverter
	5.3.2 SRFT with Optimization based -PI Controller for Inverter 109
	5.3.2.1 Cuckoo Search optimization
	5.3.2.2 An overview of HBA optimization algorithm
5.4	Performance evaluation and result discussion
	5.4.1 Performance evaluation and result discussion using ANN-PI Controller
	5.4.1.1 System performance under variable linear load and variable insolation condition
	5.4.1.2 System performance under variable and unbalanced non-linear load condition
	5.4.1.3 System performance under grid voltage disturbance, sag and swell condition
	5.4.1.4 Comparative Analysis of ANN-PI controller with PI controller
	5.4.2 Performance evaluation and result discussion using CSO-PI Controller
	5.4.2.1 System performance under variable linear load and varying insolation
	5.4.2.2 System performance under variable nonlinear load and

	varying insolation
5.4.2.3	System performance under nonlinear unbalanced load condition
5.4.2.4	System performance under nonlinear load with unbalanced grid voltage condition
5.4.2.5	System performance under nonlinear load for grid voltage sag and swell condition
5.4.2.6	Comparison analysis of proposed CSO-PI technique with PSO-PI and PI controller in term of total harmonic distortion
5.4.2.7	Comparison analysis of proposed CSO-PI technique with PSO-PI and PI controller in term of performances indices
5.4.2.8	Comparison of proposed CSO-PI technique with PSO-PI and PI controller in term of maximum power point tracking and DC bus voltage regulation
	ance evaluation and result discussion using HBA-PI er
5.4.3.1	System response under linear load and irradiation variation
5.4.3.2	System response under non-linear load and irradiation variation
5.4.3.3	System response under non-linear unbalanced load condition
5.4.3.4	System response under unbalanced grid condition 134
5.4.3.5	System response under grid voltage sag and voltage swell condition
5.4.3.6	Comparison of the proposed HBA-PI controller with PSO-PI and PI controller in term of grid current harmonics 135
5.4.3.7	Transient analysis of PV output at different irradiation for non-linear load with HBA- PI, PSO-PI and PI controllers
5.4.3.8	Transient analysis of DC link voltage for non-linear load with HBA -PI, PSO-PI and PI controller
5.4.3.9	Comparison of PI controller with PSO-PI and HBA-PI controller based on performance indices and time complexity
5.4.3.1	0 Stability analysis
	ANN-PI, CSO-PI and HBA-PI controller141

5.5

5.6		parison of HLO-ANN MPPT with HBA-PI controller, CSO- N-PI	
5.7	Conc	luding remarks	143
		: ISLANDING DETECTION TECHNIQUE FOR GRIDED PV BASED MICROGRID	
6.1	Introd	duction	144
6.2	Syste	m description	144
6.3	Volta	ge ripple-based islanding detection technique	145
6.4	Perfo	rmance analysis of islanding detection technique	147
	6.4.1	Islanding of grid integrated SPV system with 0 % of active mismatch condition	
	6.4.2	Islanding of grid integrated SPV system with 30 % of active mismatch condition	-
	6.4.3	Sudden load variation at point of common coupling	150
	6.4.4	Grid side distortion	150
6.5	Comp	parative analysis of islanding detection techniques	151
6.6	Conc	luding remarks	152
		: CONCLUSION, SOCIAL IMPACT OF RESEARCH A OPE OF WORK	
7.1	Introd	luction	153
7.2	Conc	lusion of the study	153
7.3	Socia	l Impact of Research	154
7.4	Futur	e Scope	155
REFE	RENCI	ES	156
APPE	NDIX		168
Currio	ահատ Ն	Jitae	170

List of Tables

Table 3.1 Comparison of proposed modified MPPT technique at different irradiation using P&O, INC, PSO and CSO based MPPT techniques51
Table 3.2 Transient assessment of DC voltage for nonlinear loads with P&O, INC, PSO, CSO and proposed modified controller on different irradiation52
Table 3.3 Maximum power obtained using MPPT at various time intervals54
Table 3.4 Comparison of THD of output voltage using droop controller and MPC with proposed MPPT technique
Table 4.1 Colour palette designed for skin lightening or darkening78
Table 4.2 Power sharing among inverter, grid, and load for variable loads condition
Table 4.3 Power sharing among inverter, grid, and load for variable load and irradiation conditions
Table 4.4 Sensitivity analysis for different search agents of proposed HLO-ANN MPPT technique
Table 4.5 Comparison of FFT spectrum of Proposed HLO-ANN MPPT technique with PSO-ANN, ABC-ANN, HS-ANN, TLBO-ANN, DMO-ANN MPPT techniques for THD in grid current
Table 4.6 Comparison of Proposed HLO-ANN MPPT technique with PSO-ANN, ABC-ANN, HS-ANN, TLBO-ANN, DMO-ANN, PSO, INC and P&O MPPT techniques for maximum power tracking under different irradiation condition (Shahabad Daulatpur village data)
Table 4.7 Comparison of Proposed HLO-ANN MPPT technique with INC, P&O, PSO, PSO-ANN, ABC-ANN, HS-ANN, TLBO-ANN and DMO-ANN MPPT techniques for maximum power tracking under different irradiation condition (Chikkaballapur Karnataka data92
Table. 4.8 Comparison of Proposed HLO-ANN MPPT technique with INC, P&O, PSO, PSO-ANN, ABC-ANN, HS-ANN, TLBO-ANN, DMO-ANN MPPT techniques for maximum power tracking under different temperature (Temp.)
Table 4.9 Comparison of Proposed HLO-ANN MPPT technique with INC, P&O, PSO, PSO-ANN, ABC-ANN, HS-ANN, TLBO-ANN, DMO-ANN, PSO, INC and P&O MPPT techniques for ENE530 Test
Table.4.10 Transient analysis of DC bus voltage using proposed HLO-ANN and DMO-ANN, TLBO-ANN, HS-ANN, ABC-ANN, and PSO-ANN for non-linear load
Table 4.11 Error parameters analysis for different MPPT algorithms
Table 4.12 Benchmarking performance of proposed HLO-ANN MPPT techniques with other MPPT techniques
Table 4.13 Computational Complexity Analysis of HLO Algorithm Procedures 101

Table 5.1 Comparison of PV power Output of ANN-PI with PI and PSO-PI controller
Table 5.2 Comparison of grid current harmonics with PI and PSO-PI and ANN-PI controller
Table 5.3 Comparison of ANN-PI with PI and PSO-PI controller in term of performance dynamic
Table 5.4 Comparison of CSO- PI controller with PSO- PI controller and PI controller for grid current harmonics
Table 5.5 Comparison of different technique based on performance indices 129
Table 5.6 Comparison analysis of maximum power obtained using different control algorithm
Table 5.7 Comparison analysis of DC bus voltage obtained using different control algorithm
Table 5.8 Comparison of HBA - PI controller with PSO - PI controller & PI controller for THD in current
Table 5.9 Comparison of INC MPPT technique at different irradiation using PI controller, PSO-PI controller and HBA-PI controller
Table 5.10 Transient analysis of DC link voltage for nonlinear load with PI, PSO -PI and HBA-PI controller on different irradiation
Table 5.11 Comparison of PI controller with PSO- PI and HBA-PI controller based on performance indices
Table 5.12 Gain value and Time complexity of PI , PSO-PI and HBA –PI controller
Table 5.13 Controller Parameters and performance characteristics of proposed HBA controller
Table 5.14 Comparison of ANN-PI, CSO-PI and HBA-PI controller in term of PV power output
Table 5.15 Comparison of ANN-PI, CSO-PI and HBA-PI controller in term of grid current harmonics
Table 5.16 Comparison of HLO-ANN MPPT with ANN-PI, CSO-PI and HBA-PI controller in term of grid current harmonics
Table 5.17 Comparison of HLO-ANN MPPT with ANN-PI, CSO-PI and HBA-PI controller in term of maximum power point tracking
Table 6.1 Comparison of proposed islanding detection technique with existing techniques

List of Figures

Fig. 1.1 Global Renewable Energy Growth Trends (2000-2030) – IEA	1
Fig. 1.2 Fig.1.2 India's Installed Renewable Energy Capacities (MW) as of 31st March 2025 – MNRE	2
Fig. 1.3 Installed Renewable Energy Capacity Achieved in FY 2024–25 (April 1, 2024 – March 31, 2025) in MW MNRE	2
Fig. 1.4 Renewable Energy-Based Microgrid System	3
Fig. 1.5 Standalone solar PV Based Microgrid	4
Fig.1.6 Grid connected solar PV based microgrid	5
Fig. 1.7 I-V and P-V characteristic of SPV	6
Fig. 2.1 Classification of MPPT algorithm	. 12
Fig. 2.2 Classification of Inverter control techniques	. 17
Fig. 2.3 Classifications of Islanding detection techniques	. 22
Fig. 3.1 Hierarchal configuration of solar PV array	. 28
Fig. 3.2 Equivalent circuit of a solar PV Ideal and practical equivalent circuit	. 28
Fig. 3.3 P-V & I-V characteristics graph of proposed solar PV	. 29
Fig. 3.4 Turbine Power characteristics	. 30
Fig. 3.5 Equivalent circuit of Boost Converter	. 31
Fig. 3.6 Equivalent circuit of buck-boost converter	. 32
Fig. 3.7 Equivalent circuit diagram of battery	. 33
Fig. 3.8 Flow chart of Perturb and Observe algorithm	. 35
Fig. 3.9 Flow chart of Incremental Conductance algorithm	. 35
Fig. 3.10 Flow chart of Particle swarm optimization algorithm	. 36
Fig. 3.11 Flow chart of Cuckoo search optimization algorithm	. 38
Fig. 3.12 Proposed improved control technique for solar MPPT	. 39
Fig. 3.13 Control technique for bidirectional Buck-Boost converter	. 40
Fig. 3.14 Flow chart of energy management of hybrid standalone microgrid	. 41
Fig. 3.15 Power control loop	. 42
Fig. 3.16 Voltage and current control loop	. 43
Fig. 3.17 PWM sinusoidal switching reference generation for inverter	. 43
Fig. 3.18 Eight possible voltage vector created by the inverter	. 44
Fig. 3.19 Filter model	. 44
Fig. 3.20 PV-BESS hybrid standalone microgrid	. 46
Fig. 3.21 Waveform under linear load and irradiation variation	. 48
Fig. 3.22 Waveform under load variation	. 49

Fig. 3.23 Waveform under nonlinear load condition	50
Fig. 3.24 Waveform under nonlinear unbalance load condition	50
Fig. 3.25 Transient response of PV power output for nonlinear load under various irradiation conditions	
Fig. 3.26 Transient analysis of DC bus voltage for nonlinear load	53
Fig. 3.27 PV power output waveform of different MPPT algorithms for MPPT EN50530 efficiency test	54
Fig. 3.28 Schematic diagram of hybrid standalone PV microgrid with MPC control	
Fig. 3.29 Waveform under battery charging conditions	56
Fig. 3.30 Waveform under battery discharging condition	56
Fig. 3.31 Waveform under non-linear variable load condition	57
Fig. 3.32 Waveform under variable irradiation condition	58
Fig. 3.33 Waveform under variable wind speed condition	59
Fig. 3.34 Variable wind speed	59
Fig. 3.35 Transient response of DC bus voltage under variable wind speed	59
Fig. 3.36 Schematic diagram of hybrid standalone PV microgrid with MPC control.	
Fig. 3.37 System response under variable linear load demand	
Fig. 3.38 System performance under variable non-linear load demand	62
Fig. 3.39 System performance under unbalance non-linear load demand	62
Fig. 3.40 Harmonic Spectrum of output voltage using droop controller for non-lin load (using MPC and droop controller	
Fig. 3.41 DC bus voltage response of nonlinear load using droop controller and N	
Fig. 4.1 Block diagram of internal structure of ANN based MPPT algorithm	68
Fig. 4.2Block diagram of HLO-ANN MPPT Technique	75
Fig. 4.3 Representation of colour space for CIE, $L \alpha^* \beta^*$ and $L c^* h$	77
Fig. 4.4 Crypsis behavior of Horned Lizard.	77
Fig. 4.5 Horned lizard shooting blood.	79
Fig. 4.6 Horned lizard escaping from predators	80
Fig. 4.7 Schematic diagram of proposed grid integrated solar PV system	82
Fig. 4.8 Block diagram of scenarios considered during comparative analysis	83
Fig. 4.9 Performance of the System under Steady State	84
Fig. 4.10 Performance of the System under dynamic State	85
Fig. 4.11 Performance of the System under abnormal grid and load unbalance	86
Fig. 4.12 Sensitivity analysis for different search agents of proposed HLO-ANN	

MPPT technique87
Fig. 4.13 FFT spectra of grid current and non-linear load for different scenarios 88
Fig. 4.14 P-V and I-V characteristics for different irradiation of solar array 90
Fig. 4.15 Maximum power tracked under dynamic irradiation variation (Shahabad Daulatpur village data)
Fig. 4.16 Maximum power tracked under dynamic irradiation variation (Shahabad Chikkaballapur Karnataka data)
Fig. 4.17 Proposed HLO-ANN MPPT technique with other MPPT technique for different temperature condition
Fig. 4.18 Dynamic variation in irradiation level for the standard MPPT efficiency test of EN 50530
Fig. 4.19 Power versus time graphs for different MPPT algorithms
Fig. 4.20 Transient analysis of DC bus voltage proposed HLO-ANN and DMO-ANN TLBO-ANN, HS-ANN, ABC-ANN, and PSO-ANN for non-linear load 97
Fig. 4.21 Convergence curve of all the algorithms
Fig. 4.22 Validation of trained neural network
Fig. 5.1 Schematic diagram of grid integrated PV system
Fig. 5.2 Schematic diagram of synchronous reference frame theory
Fig. 5.3 Block diagram of ANN based PI controller
1.8. 0.6 2.6 0.1 0.1 0.1 1.1 0.1 0.1 0.1 0.1 0.1 0.1
Fig. 5.4 Lévy flight distribution
Fig. 5.4 Lévy flight distribution
 Fig. 5.4 Lévy flight distribution
Fig. 5.4 Lévy flight distribution
 Fig. 5.4 Lévy flight distribution
Fig. 5.4 Lévy flight distribution

Fig. 5.18 Waveform of non-linear load under unbalanced load condition
Fig. 5.19 THD of load current and grid current for non –linear unbalanced load 126
Fig. 5.20 Waveforms of non-linear load under unbalanced grid voltage condition 127
Fig. 5.21 THD of load current and grid current for non –linear load under unbalanced grid voltage
Fig. 5.22 Waveform of non-linear load under grid voltage sag and swell condition
Fig. 5.23 Comparison of maximum power obtained using different control algorithm
Fig. 5.24 Comparison of DC bus voltage regulation using different control algorithm130
Fig. 5.25 Waveform under linear load and irradiation variation
Fig. 5.26 Waveform under nonlinear load variation and irradiation variation 132
Fig. 5.27 THD of I_{load} and I_{grid} for non-linear load
Fig. 5.28 Waveform under nonlinear unbalance load variation
Fig. 5.29 THD of I_{load} and I_{grid} under non - linear unbalanced load condition 134
Fig. 5.30 Waveform under unbalance grid condition
Fig. 5.31 Waveform under grid voltage sag and swell condition
Fig. 5.32 THD of I_{load} and I_{grid} for non-linear load (using PI, PSO-PI and HBA-PI)
Fig. 5.33 Transient response of INC MPPT technique at different irradiation using PI controller, PSO-PI controller and HBA-PI controller
Fig. 5.34 Response of DC bus voltage for non-linear load with HBA based PI, PSO based PI & PI controller
Fig. 5.35 Convergence curve of proposed HBA algorithm
Fig. 5.36 Block diagram of Linearized proposed controller
Fig. 5.37 Stability analysis of controller through Bode plot
Fig. 6.1 Schematic diagram of proposed model
Fig. 6.2 Proposed Islanding technique
Fig. 6.3 Islanding detection of grid integrated SPV system with zero active power mismatch
Fig. 6.4 Islanding detection of grid integrated SPV system with 30 % active power mismatch
mismatch 149

List of Abbreviations and Nomenclature

AC Alternate Current
ACO Ant Colony Optimization
ABC Artificial Bee Colony

AI Artificial Intelligence

ANFIS Adaptive Neuro-Fuzzy Inference System

ANN Artificial Neural Network
AFD Active Frequency Drift

BESS Battery Energy Storage System

BP Backpropagation

CWT Continuous Wavelets Transforms

CCS-MPC Continuous Control Set Model Predictive Control

DWT Discrete Wavelets Transforms

DC Direct Current

DMO Dwarf Mongoose Optimizer

FCS-MPC Finite Control Set Model Predictive Control

FSSO Flying Squirrel Search Optimization FFNN Feed Forward Neural Network

FL-MPPT Fuzzy Logic Maximum Power Point Tracking

FLS Fuzzy Logic System FY Financial year

FOA Firefly Optimization Algorithm

GA Genetic Algorithm

GDO Gradient Descent Optimization
GCCs Grid Connected Converters
GMPP Global Maximum Power Point

GW Giga Watt

GWO Grey Wolf Optimization
GSS Golden Section Search

HC Hill climbing

HBA Honey Badger Algorithm

IGBT Insulated Gate Bipolar Transistor IMDT Improved Mixed Droop Technique

INC Incremental Conductance

IT-2 FLC Interval Type-2 fuzzy logic control IDT Islanding Detection Techniques

LM Levenberg-Marquardt

LMPP Local Maximum Power Point

MG Microgrid

MAE Mean Absolute Error
MATLAB Matrix Laboratory
ML Machine Learning
MOPs Multi-Objective Problems

MPP Maximum Power Point

MPPT Maximum Power Point Tracking

MSE Mean Square Error MPC Model Predictive Control

NASA National Aeronautics and Space Administration

NDZ Non Detection Zone
PLL Phase-Locked Loop

PCC Point of Common Coupling

P&O Perturb & Observe
PR Proportional Resonant
PI Proportional Integral

PCI Proportional Complex Integral PSO Particle Swarm Optimization

PV Photo Voltaic

PWM Pulse Width Modulation
ROCOF Rate of Change of Frequency
ROCOP Rate of Change of Power
RMSE Root Mean Square Error
RCC Ripple Correlation Control
SMC Sliding Mode Control
SFS Sandia Frequency Shift

TLBO Teacher Learning Based Optimization

TI Tilt-Integral

THD Total Harmonic Distortion
WPT Wavelet Packet Transform

CHAPTER-1

INTRODUCTION

1.1 INTRODUCTION

The global energy crisis has raised concern about energy resources and climate impact worldwide. Fuel-based electricity generation significantly increases greenhouse gas (GHG) emissions, exacerbating the situation. As electricity demand rises, the need for sustainable alternatives increases. The global electrical industry is undergoing a significant transformation as it transitions from fossil fuels to renewable energy sources (RESs) to meet the growing demand for electricity. This transformation, driven by the demand for sustainability, poses a huge challenge to the sector, which formerly relied on fossil fuels. The development and integration of renewable energy solutions have become a key priority for ensuring a more reliable and sustainable power supply. This shift is essential for mitigating climate change and lowering the carbon footprint of energy production by replacing high-emission fuels with renewable resources. These sources are naturally decentralized, plentiful, and locally accessible. In the face of shifting global energy markets, they are essential in reducing reliance on imported fossil fuels and offering stability [1].

Global renewable electricity generation is expected to exceed 17,000 terawatt-hours (TWh) by 2030, an increase of about 90% over 2023[2] as can be seen in Fig.1.1. This would be sufficient to supply China and the United States' combined electricity needs by 2030.

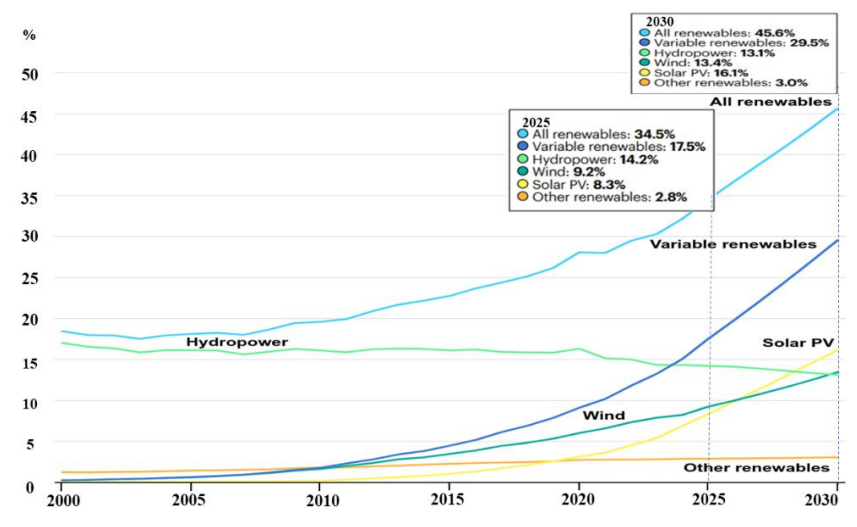


Fig.1.1 Global Renewable Energy Growth Trends (2000-2030) – IEA [2]

Renewable energy is expected to surpass coal-fired generation by 2025. In 2026, wind and solar power generation are both expected to outperform nuclear power generation. In 2029, solar PV energy generation will overtake hydropower, making it the world's greatest renewable power source, with wind-based generation predicted to surpass hydropower in 2030.[2]

Solar PV and wind energy have become more cost-effective than most fossil fuel and

non-fossil fuel alternatives in the majority of countries. Supported by favorable government policies, the deployment of these renewable technologies is expected to continue increasing over the next five years, with solar PV and wind projected to account for a record 96% of total new power capacity additions.

India is strategically harnessing the output of electrical energy from renewable energy resources by utilizing its advantageous geographic location. India offers numerous opportunities to develop robust renewable energy infrastructure due to its diverse climate and topography. India is moving quickly to fulfil the higher benchmark for generating electricity from renewable resources, according to the Ministry of New and Renewable Energy (MNRE). India's Total Renewable Energy Installed Capacity (MW) as on 31st March 2025 is 172.36GW(Fig.1.2). Total Capacity Installed (in FY 2024–25) is 28,723.65 MW (or 28.72 GW) (Fig.1.3) [3].

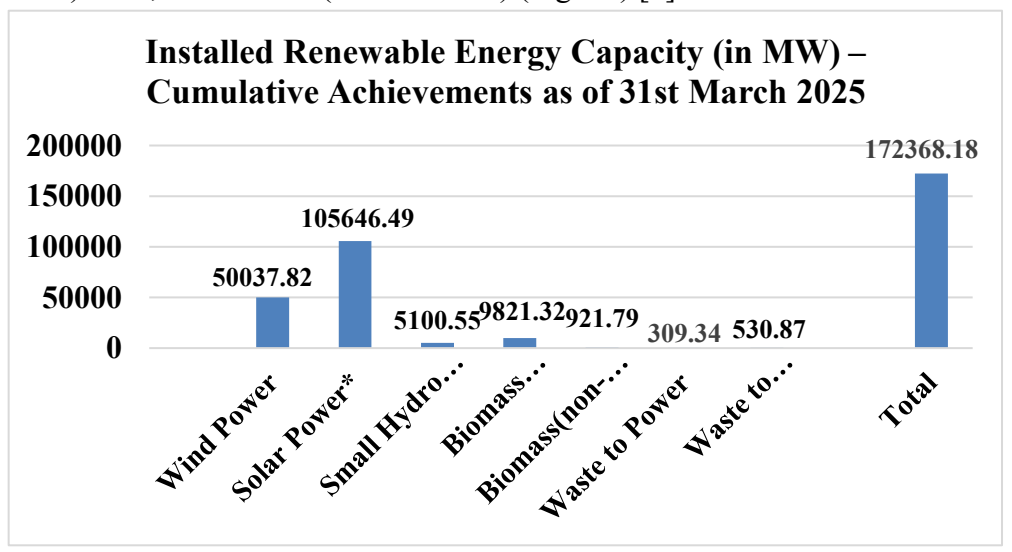


Fig.1.2 India's Installed Renewable Energy Capacities (MW) as of 31st March 2025 – MNRE [3]

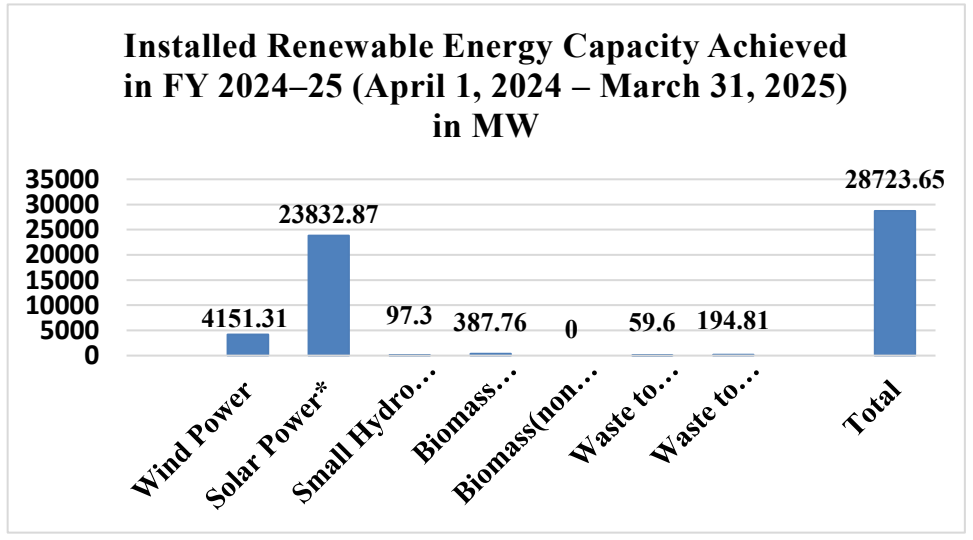


Fig.1.3 Installed Renewable Energy Capacity Achieved in FY 2024–25 (April 1, 2024 – March 31, 2025) in MW MNRE [3]

1.2 OVERVIEW OF RES BASED MICROGRID

Conventional fossil fuel-based power plants have a number of drawbacks, including power losses, higher prices, decreased system efficiency, and environmental contamination. A number of distributed generators, including photovoltaic cells, wind turbines, and micro-hydro units, are employed in the distribution network in place of a single major power source. Although these micro-sources utilize renewable energy sources such as solar and wind, which are environmentally friendly, they are inherently intermittent in nature. These micro-sources and loads are grouped together because they may be controlled to supply electricity to the surrounding area, giving rise to the idea of a microgrid as shown in Fig.1.4. A microgrid is a group of interconnected loads and distributed energy resources within clearly defined electrical boundaries that acts as a single controllable entity with respect to the grid and can operate in both gridconnected and islanded modes. Typically, a microgrid integrates renewable energy sources such as solar PV, along with energy storage systems, to enhance local reliability, sustainability, and resilience. An effective, affordable, and robust local power system made up of distributed energy resources (DERs), a microgrid provides power to nearby loads with fewer losses than a conventional system with lengthy transmission lines. An independent section of the electrical network, a microgrid can be deployed with local loads without the need for a transmission system, according to utilities. For the customer, it is a carefully designed system that uses a power optimizer, local controller, and protective system to deliver effective, dependable, and steady electricity.

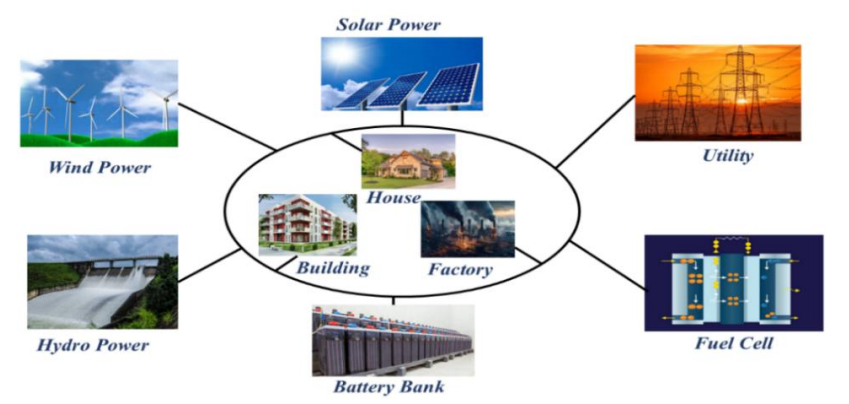


Fig.1.4 Renewable energy-based microgrid system

In general, microgrids can operate in two different modes: grid-connected mode and islanded mode. In grid-connected mode, the microgrid draws power from both the utility grid and distributed energy resources (DERs), with DERs serving as the main source of power. The utility grid supplements any additional power requirements and helps maintain voltage and frequency stability, ensuring the reliable operation of the microgrid. In islanded mode, DERs become the sole source of power, as the microgrid operates independently from the main grid. Effective energy management is especially important in this mode to match power generation with varying load demands [4].

1.3 SOLAR PV BASED MICROGRID

The popularity of solar energy sources has grown exponentially in recent years among the different kinds of renewable energy sources. This is brought about by factors including higher solar cell efficiency, significant improvements in power electronic device interface, modular solar energy systems, lower maintenance requirements, noiseless operation, and a decline in solar energy costs. By 2050, solar energy is predicted to rank among the world's main sources of electricity. A solar photovoltaic (PV)-based microgrid is a decentralized energy system that generates electricity using solar panels, stores excess energy in battery storage systems, and distributes power to connected loads. Such microgrids can operate independently in standalone mode or remain connected to the main grid, thereby enhancing the flexibility, reliability, and resilience of the power supply. [5]

1.3.1 STANDALONE SOLAR PV BASED MICROGRID

Standalone solar PV based microgrid function autonomously of the central power utility grid, delivering power to remote areas where utility grid expansion is not viable. The amount of electricity delivered to the load in a standalone photovoltaic system is determined by the amount of solar energy that is available. Solar PV is an intermittent energy source which poses significant technological and financial hurdles for controlling loads. An energy storage system must be included in addition to a PV system in order to solve this problem. The most widely utilized storage device is the battery, which is essential to ensuring that the load constantly has power.

The standalone system is being studied extensively as a standard standalone microgrid since energy storage has been integrated into the system. In addition to critical installations, this stand-alone power system can be utilized in remote rural locations with limited access to the grid and solar energy.[6] A standalone SPV-based microgrid can be constructed as single or three phase. Fig.1.5 is a block diagram for a stand-alone PV system with battery energy storage system (BESS). The system consists of a PV array, a battery energy storage system, a DC-DC converter, an inverter, and a load.

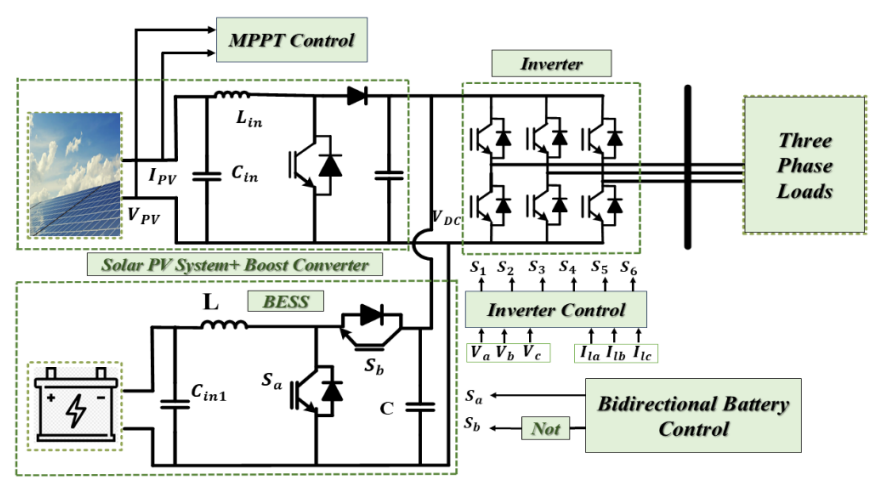


Fig.1.5 Standalone solar PV based microgrid

1.3.2 GRID CONNECTED SOLAR PV BASED MICROGRID

Grid-connected SPV-based microgrid is a system that allows for bidirectional power transfer. It consists of solar panels, a dc-dc converter, a power source inverter, interface inductors, and loads. The power flow through a grid-connected microgrid is bidirectional. If the load demand is less than the output of the SPV power generation, the excess power from the SPV is transmitted to the grid; if the load demand exceeds the SPV power generation, the grid supplies the remaining load power. The inverter is one of the most critical components in the SPV-based microgrid. A PV inverter is employed to convert the generated dc voltage to ac voltage. A grid-tied SPV-based microgrid can be structured as single, two, or three phases. Single-stage and two-stage systems can be employed as single or three-phase. Three phase grid-tied SPV-based microgrids can be configured as three phase three wire or three phase four wire systems. Fig.1.6 depicts a two-stage grid-tied PV-based microgrid with the PV array integrated into a three-phase grid.[7].

The fundamental unit of a PV array is the PV cell, which is an active transducer that transforms energy from sunlight (photons) into electricity (current). PV cells are connected in series or parallel to form PV modules. These modules can then be connected in series or parallel to build a PV array with specified output voltage and current. The system comprises of two stages of conversion: first, variable dc from the solar PV array is converted into fixed dc of the required magnitude by a boost converter, and then a grid-connected PV inverter is utilized to convert this dc voltage into ac voltage of the desired magnitude and frequency for supplying an ac load.[8]

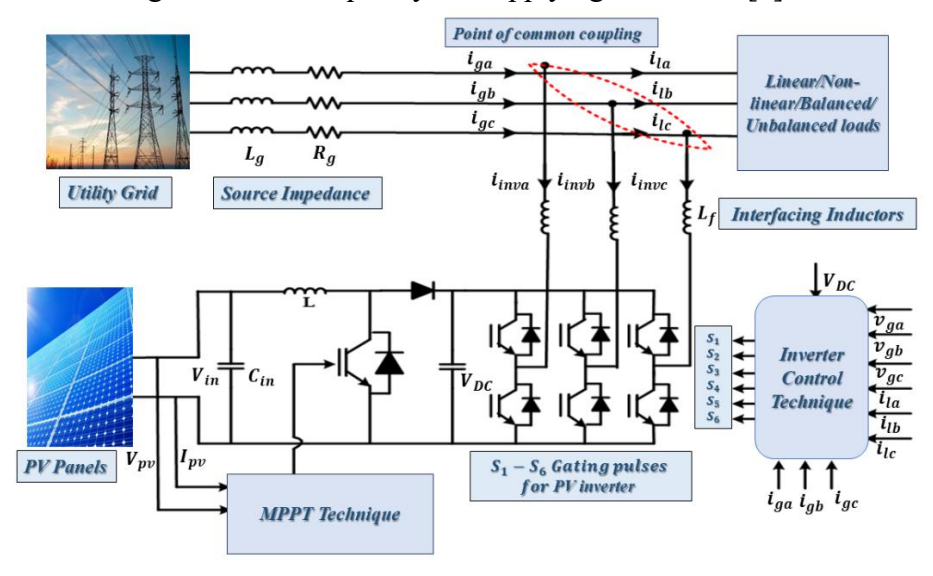


Fig. 1.6 Grid connected solar PV based microgrid

1.4 MPPT TECHNIQUE FOR STANDALONE AND GRID CONNECTED RES BASED MICROGRIDS

The increased PV installation capacity has also resulted in the advancement of the PV power conversion stage. PV power converters have become more efficient, compact,

and reliable, allowing for maximum power from the sun in residential, commercial, and industrial application. This advancement is due to the PV converter market's stringent requirements, which include maximum power point tracker (MPPT) [2].

The Maximum Power Point Tracker (MPPT) is a critical component of a photovoltaic (PV) system, enabling optimal power extraction at the Maximum Power Point (MPP). Given the nonlinear I-V and P-V characteristics influenced by solar irradiance and cell temperature, implementing a real-time control strategy is essential for effective MPP tracking.

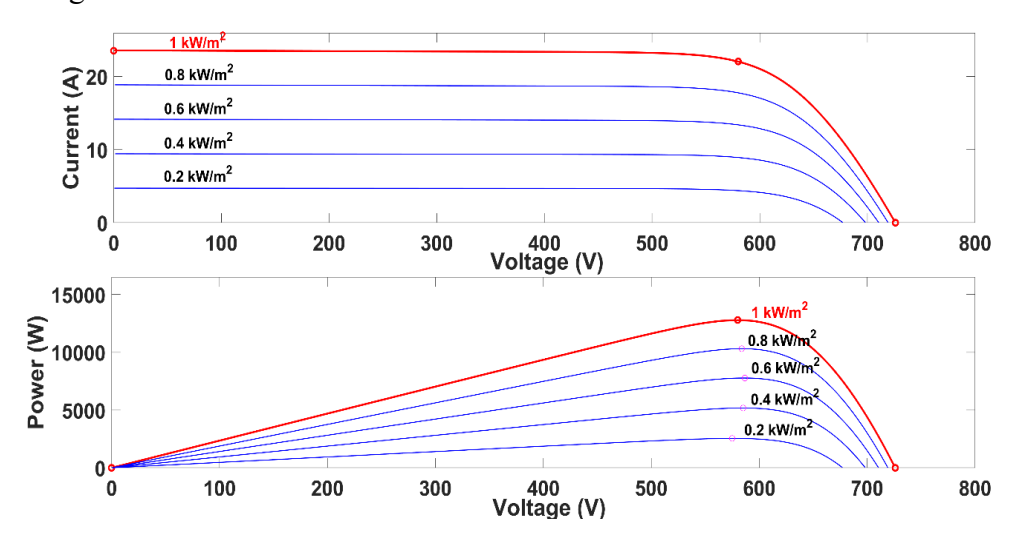


Fig.1.7 I-V and P-V characteristic of SPV

The Maximum Power Point Tracking (MPPT) technique focuses the peak of the solar panel's I-V and P-V characteristic curves, as shown in Fig.1.7, to ensure operation at maximum efficiency. This peak, known as the Maximum Power Point (MPP), is achieved by a DC-DC power converter that dynamically adjusts the operating voltage of the photovoltaic (PV) system to extract the maximum available power.[9]-[10]

1.5. INVERTER CONTROL AND DC BUS VOLTAGE REGULATION OF STANDALONE AND GRID CONNECTED RES BASED MICROGRID

Power converters are integral to modern industrial systems, enabling reliable and efficient energy transfer between electrical sources, loads, and the utility grid. Typical power converter topologies include a dc-link as an intermediate step, a grid-connected converter, and a passive filter. Examples include renewable energy sources, active power filters, and back-up (such as battery energy storage) systems. Efficient dc-link voltage control is crucial for reducing voltage variations produced by random changes in the power drawn by the grid-connected converter [11].

PV arrays with maximum power point tracking are integrated with the primary voltage source inverter (VSI) and auxiliary VSI dc links. The primary VSI functions in a grid-interfaced mode with current control. Voltage control, on the other hand, is used in an autonomous mode as a grid forming inverter during grid interruption, maintaining frequency and voltage across the point of common coupling (PCC) to provide loads with continuous power. To ensure steady MG performance under dynamic settings,

the voltage source inverter (VSI) control algorithm must be proficient.

Inverters are essential components of microgrids, as they can be controlled to maintain optimal network performance by synchronizing frequency and voltage, as well as by sharing active and reactive power among multiple inverters. Inverter-based microgrids are controlled at three levels: primary, secondary, and tertiary. Each level's control design considers both frequency and voltage control. A droop controller manages active/reactive power sharing and inverter frequency/voltage synchronization at the primary level. The secondary level, often an integral-type controller, compensates for frequency/voltage steady-state error while maintaining active/reactive power distribution. When the microgrid is connected to the main grid, the tertiary control level manages power flows among the solar PV, battery, load, and the grid. Recent research on inverter-based microgrids has focused on developing control models to address key challenges such as frequency and voltage regulation, synchronization, active and reactive power sharing, inverter power limitations, and overall system stability. [12]-[14]

1.6. ISLANDING DETECTION OF SOLAR PV BASED MICROGRID

Three-phase power converters connect distributed energy resources, such as renewable sources and energy storage systems, to the AC grid or microgrid. The technical challenges of distributed or local control of these converters include achieving stable steady-state operations, seamless power transitions between grid-connected and islanded modes, and ensuring compliance with IEEE standards and grid codes.[15]

Despite the advantages of renewable energy sources (RES), they also present certain risks, such as unintended islanding, safety issues, and reverse power flow. As a result, integrating distributed generators (DGs) into the grid requires addressing protection and safety concerns within the distribution network. Islanding occurs when a portion of the utility system, which includes both load and distributed resources, continues to operate while disconnected from the main utility grid. In this situation, distributed generators (DGs) remain energized and supply power solely to local loads, without being connected to the larger power grid.[16]

1.7. MOTIVATION AND RESEARCH OBJECTIVES

Developing SPV-based solar microgrids can provide solutions that overcome energy challenges with their sustainability, accessibility, and resilience. SPV microgrids rely on clean and renewable energy from the sun and contribute significantly in reducing fossil fuel utilization, greenhouse gas emissions and slowing down the adverse impacts of climate change. Furthermore, SPV based microgrids aid in conserving the environment and building a future with lesser impulses through discontinuation of traditional power generating systems. These microgrids, in particular, facilitate the electrification of rural, mountainous and remote areas that lack traditional infrastructure and have a grid extension that is spreads vertically which is expensive. These microgrids eliminate energy poverty by improving life for the millions of people that do not have

uninterrupted SPV electricity through a decentralized and self-sustained energy provision. There is accessibility to modern healthcare, education and jobs, along with boosted community empowerment by energy autonomy, which all contribute to socioeconomic progress. The relatively new technologies that consist of solar panels, energy storage devices and additional infrastructure have witnessed a considerable drop in their cost. As a result, solar photovoltaic based micros grids become economically viable for both the developed and developing regions. Combined with the advent of lithium-ion batteries as energy storage devices, these microgrids provide power even during nonsunny hours, and therefore, ensure the availability of electricity. This reinforces energy security by minimizing reliance on centralized networks that are inherently susceptible to outages or damage during extreme weather conditions. Therefore, solar photovoltaic based microgrids are instrumental in the development of resilient energy systems especially in the disaster afflicted regions where the demand for self-sufficient power systems is inevitable.

The support extended for developing microgrids by governments, international agencies and private enterprises is on the rise as a result of fiscal and policy changes, research funding and taxation incentives. Due to their scalability varying from small rural settlements to sprawling industrial plants, these SPV based micro grids are a cost effective and efficient answer to the global energy requirements. The research being undertaken right now will have a long-lasting effect and will also serve the purpose of offering contemporary clean energy solutions, supporting the cause of sustainable development in the process. By focusing on solar photovoltaic (SPV)-based microgrids, some of the most challenging global energy issues can be addressed, paving the way for universal access to renewable energy. This approach supports the development of robust and sustainable communities powered by clean energy sources.

As discussed above, the benefits of PV-based microgrids inspired and led to the following research objectives:

- 1) Development of novel MPPT technique for grid connected solar photovoltaic system for enhanced performance.
- 2) Development of novel control algorithms for grid connected photovoltaic inverter system.
- 3) Design and development of hybrid micro-grid and efficient control technique to improve the performance of the system.
- 4) Islanding detection and development of control technique of microgrid under islanding condition.

1.8. PROBLEM IDENTIFICATION

Based on the above objectives, following problems are identified:

1. Solar PV output is inherently intermittent and unpredictable due to climatic variations. While traditional MPPT methods are widely used, they often suffer from slow convergence, oscillations, and the risk of locking into local maxima under rapidly changing irradiance or partial shading. These limitations reduce energy yield and

compromise system stability in both standalone and grid-connected settings. Although intelligent methods—such as ANN, fuzzy logic, ANFIS, and various metaheuristics—have been explored, they tend to be complex, computationally demanding, and costly. Hybrid approaches offer promise by enhancing tracking speed and accuracy while reducing oscillations.

- 2. Existing inverter control strategies perform adequately under steady-state conditions but often fail to maintain optimal power output during grid disturbances and transients, such as voltage sags, frequency shifts, and harmonics. As a result, power quality degrades and grid stability and reliability are undermined. There's a pressing need for advanced control algorithms that dynamically adapt to grid fluctuations, ensuring consistent, high performance under both normal and abnormal conditions.
- 3. Hybrid solar/battery microgrids face challenges in maintaining grid stability amid fluctuating supply and demand, especially when powering linear, nonlinear, or unbalanced loads. Poorly designed control systems can lead to voltage and frequency deviations, inefficient resource dispatch, and power-quality issues. While several control strategies exist, comprehensive solutions that integrate effective stability control with DC-bus voltage regulation remain lacking.
- 4. Unintentional islanding—when a microgrid continues to power local loads after grid disconnection—is a major safety and reliability concern. Passive and active detection methods frequently exhibit large non-detection zones (NDZ), slow detection times, and negative impacts on power quality. Delays in islanding detection can endanger maintenance personnel and damage equipment. Faster, more reliable detection methods with minimal NDZ and enhanced control during islanding are urgently required to preserve microgrid stability in all operating modes.

1.9 ORGANISATION OF THESIS

Chapter-1 contains the introduction of the research work, its motivation, research objectives, and the problem statements. This chapter also describes the organization of the thesis.

Chapter-2 presents a comprehensive review of standalone and grid-connected solar photovoltaic (SPV) microgrids and their control technologies. It begins with the operational strategies, design aspects, and efficiency challenges of standalone SPV systems integrated with battery energy storage. The focus then shifts to grid-connected systems, emphasizing grid integration, inverter control, synchronization, and compliance with grid codes. The chapter reviews various MPPT techniques—classical, intelligent, optimization-based, and hybrid—evaluating their performance under changing atmospheric conditions. It also examines inverter control methods, including linear, non-linear, robust, adaptive, predictive, and intelligent controllers. Unintentional islanding and its detection methods, both classical and modern, are discussed to ensure grid stability and safety. The chapter concludes by identifying key research gaps for future investigation.

Chapter-3 This chapter focuses on a hybrid standalone solar PV microgrid system with integrated battery energy storage, with a particular emphasis on effective DC link voltage control. This chapter introduces a novel MPPT strategy that combines the strengths of the Incremental Conductance (INC) method with a double closed-loop controller. The proposed technique is intended to achieve two key goals: maximising power extraction from the PV system and ensuring a steady DC bus voltage during dynamic operation. Furthermore, the control method adds to harmonic mitigation, which improves overall power quality and system performance. Furthermore, this chapter describes control for a hybrid standalone inverter that provides quick and precise dynamic responses to varying load needs. The given control mechanism has been thoroughly evaluated for efficacy and robustness. The system's performance is analysed using MATLAB/Simulink, providing insights into its operation under various operating conditions.

Chapter-4 This chapter describes the design and implementation of a novel Horned Lizard Optimized Artificial Neural Network (HLO-ANN) MPPT technique for grid-connected solar PV systems. The proposed HLO-ANN technique combines the fast-learning capability of ANN with the global optimization strength of the Horned Lizard Optimization technique, allowing for precise and adaptive tracking of the maximum power point under dynamic environmental and load conditions. This methodology outperforms traditional and standard ANN-based MPPT methods, making it ideal for modern grid-connected PV systems.

Chapter-5 This chapter focuses on the design and implementation of a novel Honey Badger Algorithm-based PI (HBA-PI) controller for inverter control in grid-integrated solar PV systems. Inverter control plays a vital role in ensuring efficient DC-AC conversion, grid synchronization, and stable system performance under fluctuating environmental and load conditions. The proposed HBA-PI controller is specifically developed to achieve precise regulation of the DC link voltage, ensuring reliable power delivery from the PV array to the grid. In addition to the HBA-PI approach, this chapter also explores other optimization-based control techniques, including Cuckoo Search Optimized PI (CSO-PI) and Artificial Neural Network-based PI (ANN-PI) controllers. However, the primary focus remains on the HBA-PI controller due to its superior convergence speed, robustness, and dynamic response in maintaining voltage stability and enhancing overall system efficacy.

Chapter-6 This chapter presents a passive islanding detection technique for gridintegrated solar PV systems based on voltage ripple analysis at the point of common coupling (PCC). The proposed method uses time-domain spectral analysis to detect abnormal ripple content in the VSI output voltage. Islanding is confirmed when the ripple exceeds a defined threshold for a specific duration. Unlike conventional passive techniques, this method effectively detects islanding even under minimal power mismatch without false detections. It demonstrates high accuracy and rapid detection within 3ms across various operating conditions, with no non-detection zones observed.

Chapter-7 This chapter summarizes the key findings and conclusions of the proposed work, highlighting the contributions made toward improving solar PV-based microgrid systems. It also outlines potential directions for future research and discusses the broader social impact of the work in promoting clean energy access, especially in remote and underserved areas. The thesis concludes with a comprehensive list of references and relevant appendices

1.10 CONCLUDING REMARKS

This chapter provides a summary of the research work conducted and included in this dissertation. This chapter discusses the need for solar PV-based microgrids, including hybrid stand-alone systems, grid-connected systems, and grid-tied systems with islanding detection. The motivation and objectives of the research work are laid out, and the research issues are outlined. The research objectives highlight the need for unique approaches for tracking maximum power points, controlling DC link voltages regulation, and detecting islanding. Additionally, the structure and organization of the thesis have been outlined to support a coherent presentation of the proposed methodologies and findings.

CHAPTER-2 LITERATURE REVIEW

2.1 INTRODUCTION

A literature survey in the relevant fields of the research activity has been conducted in order to obtain the proper perspective of the research challenges. The following topics are briefly reviewed in this chapter: (i) the maximum power point tracking algorithm for solar PV systems, both standalone and grid-connected; and (ii) the regulation of DC link voltage for standalone PV systems with battery energy storage systems. (iii)PV inverter control algorithm for grid-connected solar photovoltaic systems ((iv) Grid-tied photovoltaic system islanding detection.

2.2 MPPT CONTROL TECHNIQUES FOR HYBRID STANDALONE AND GRID CONNECTED SOLAR PV SYSTEM

Solar photovoltaic (PV) is a promising power generating alternative for sustainable energy development among the other RE resources. However, solar power generation varies greatly because of seasonal weather patterns and the non-linear nature of solar irradiation, necessitating backup systems or hybrid applications. Solar irradiation is not highly correlated across close locations on a small-time scale, contributing to fluctuations in PV power output and losses. The maximum power point tracking (MPPT) technology is crucial for improving the efficiency of PV systems. To optimize the output power of a solar power system, it is necessary to develop effective maximum power point tracking due to the non-linear nature of PV arrays [17]-[18].

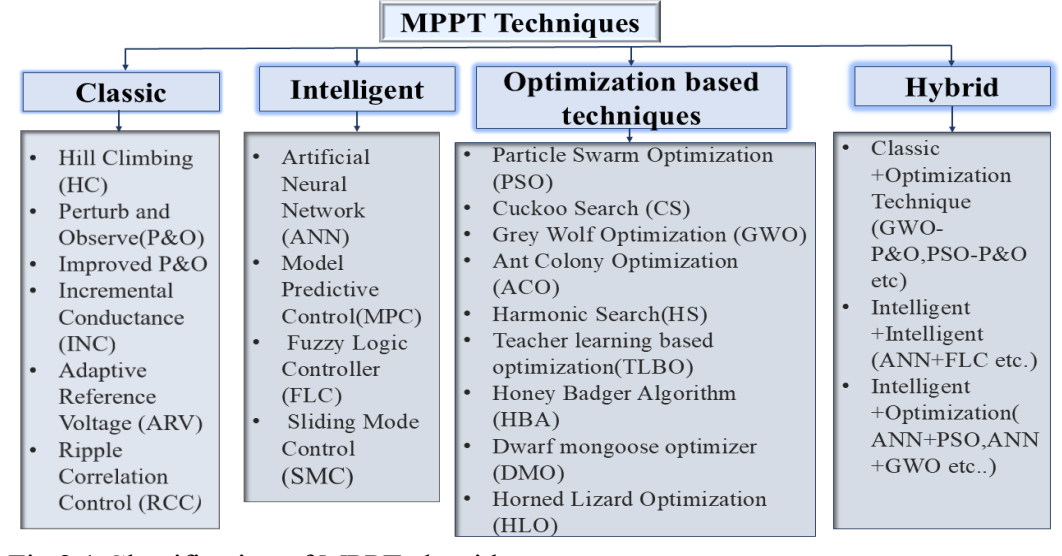


Fig.2.1 Classification of MPPT algorithm

A reliable technique for tracking maximum power points (MPPs) is crucial. This chapter provides a comprehensive overview of MPPT approaches used in PV systems, including recent articles on design methodologies. MPP is classified into four categories: classical, intelligent, optimum, and hybrid, based on the tracking algorithm used under different circumstances as shown in Fig.2.1 [19].

2.2.1 Classical MPPT Techniques:

Traditional MPPT methods can be classified as online or offline approaches. It is essentially the simplest and easiest MPPT algorithm. The maximal conventional MPPT algorithm proceeds through the fundamental phases to reach the MPP point. They calculate power and compare it to prior levels at each stage. The algorithm's direction and movement were determined by the power change value. Many standard MPPT algorithms have previously been released. The hill climbing technique, perturb and observe (P&O), and incremental conductance (INC) are most commonly employed in real-world PV systems because to their ease of implementation. The P&O MPPT approach compares recent power output samples to previous ones. For example, $P_{current} - P_{previous} = \Delta P$. If $\Delta P > 0$, the algorithm continues to change the voltage in the same direction as the last adjustment; if $\Delta P < 0$, it reverses the direction. When $\Delta P = 0$, it maintains the current voltage. The P&O MPPT algorithm modifies the perturbation size at predefined intervals [20]-[21]. The Hill climbing (HC) and P&O approaches differ only in one aspect: the perturbation parameter. To track the MPP, the P&O senses and perturb voltage or current, while the HC perturb the duty cycle. Both techniques face the challenge of balancing performance between steady-state and dynamic response error. The HC technique, which uses voltage control, faces a greater challenge.[22] The incremental conductance technique compares the PV module's incremental and instantaneous conductance to calculate its terminal voltage. The maximum power point is achieved when the incremental conductance matches the instantaneous conductance. The power curve shows a positive slope, with output power increasing as the PV module's terminal voltage reaches operational limits. As the terminal voltage of PV modules exceeds MPP, the output power decreases and the power curve slopes negatively [23]-[24]. Ripple Correlation Control (RCC) is an MPPT approach that uses ripple in PV voltage and current. To achieve the maximum power point and reduce the power gradient, RCC correlates the time derivative of the PV array's time-varying power with the time derivative of its current or voltage. RCC can be created using simple and inexpensive analogue circuitry [25]. Adaptive reference voltage. MPPT dynamically adjusts the PV system's reference voltage in response to real-time factors such as irradiance and temperature, allowing it to more efficiently monitor the Maximum Power Point but Adaptive reference voltage. MPPT necessitates complicated algorithms and real-time data processing, which raises computational demands and implementation costs [26].

2.2.2 Intelligent MPPT Techniques:

Enhancing the MPPT method is crucial in maximizing efficiency, specifically during dynamic changes in climatic conditions. Controllers have been developed for conventional PV systems with the aid of mathematical modeling, but this approach is quite complex and unmanageable for a large class of systems. Nevertheless, other approaches such as Artificial Neural Networks (ANN), Fuzzy Logic, Model Predictive Control (MPC), and Sliding Mode Control (SMC) are coming into the spotlight

because they do not need an accurate mathematical description of the system to find the MPP. These methods increase the performance of tracking and provide more degrees of freedom to the system using learning from data, prediction algorithms, or robust control techniques. This FLC has two benefits over other strategies: 1) it does not require a perfect mathematical model of the system, and 2) controller design is solely in the hands of humans. Fuzzy techniques typically involve three stages: fuzzification, fuzzy rules, and defuzzification. Fuzzification is transforming PV parameters into language variables using if-then rules. Human knowledge is used to design for specific application needs. Defuzzification is an inversion of fuzzification that uses mathematical interactions to extract linguistic or crisp inputs. This procedure uses the maximum membership function, centroid method, and weighted average approaches for computation. The defuzzification technique converts the FLC output from a linguistic variable to a numerical variable, which is then sent as an analogue signal to the converter. One significant disadvantage is that they rely on expert knowledge to define membership functions and rule sets, which may not necessarily translate well across different PV systems.[27]-[28]. The procedure of convergence is the most crucial feature for any controller. This process may take longer if there are abrupt changes or unforeseen interruptions. A powerful intelligence-based SMC tracks the MPP swiftly and efficiently. The sliding mode process can be represented in three modes: travers ability, reachability, and equivalent control. First, select the appropriate sliding surface for the application. This technique manages the system's nonlinear characteristics. This technique's key advantage is its independence from PV arrays and configuration size. This non-linear approach effectively tracks the MPP and reduces converter ripple when integrated into the grid Although it is fast, the switching frequency in the converter used is unstable. [29]-[30]. Model Predictive Control (MPC) for MPPT is an advanced method that use a mathematical model of the solar PV system to predict network behaviour and optimize power output. In this method, the controller predicts future power generation utilizing current conditions (such as irradiance and temperature) and adjusts the operating point to match the MPP. The MPC approach determines the optimal control actions by solving an optimization problem at each sample interval, taking into account future states and restrictions. However, MPC necessitates accurate system simulation and extensive computational resources, which can be difficult in real-time applications.[31]-[32]. This intelligence-based ANN is the most effective solution for complicated problems. These ANN applications do not require detailed system or mathematical modelling knowledge. By properly mapping the system's input-output, they may effectively manage complicated challenges. ANN is an intelligence-based improved MPPT technology that relies on the learning process and biological properties of neurons. The ANN consists of three layers: input, hidden, and output, and is part of a multi-layer feed-forward system. This technique can use PV module data like V_{oc} and I_{sc} , ambient information like irradiance and temperature, or a combination of both. The result will be either V_{MPP} , V_{ref} , or GMPP. The hidden layer modifies weights and biases to

estimate the best-targeted value (GMPP) based on available inputs. The duty signal directs the converter to follow the MPP based on the calculations performed in that layer but selection of PV panels is crucial for optimal application of the ANN approach in predicting real-time difficulties [33]-[34].

2.2.3 Optimization based MPPT Techniques:

Optimization-based MPPT controllers can iteratively reach maximum power points utilizing mathematical formulae. The literature has numerous metaheuristic optimization techniques that investigate the successful performance of solar PV systems. This PSO uses a bio-inspired algorithm modelled after bird flocking. Obtaining the best answer requires a few or fewer assumptions. This bio-process considers each PV array or module as a molecule, with MPP as the target objective to track. The PSO technique focuses on the search method, allowing for easy tracking of the GMPP [35]. Research suggests that improving the PSO approach can reduce steady-state oscillations and fluctuations by following the MPP point. The particles can be effectively instated around the MPP to avoid both unneeded and excessive seeking, and a situation in which the swarm efficiently looks the zone turns out to be too small, returning the genuine MPP in less time [36]. CS-based MPP, also known as cuckoo-oriented brood parasitism, is another optimization strategy. The cuckoo's nature serves as a metaphor for selecting the optimum option during MPP tracking. The analogy is shown in [37] will demonstrate a clear tracking mechanism. The cuckoo's egg is the current best solution, while the eggs already in the nest are the solutions. Using suitable fitness functions, the inferior solution (old egg) is removed and replaced with the best solution (cuckoo's egg). Although these techniques are inexpensive, they require more time to reach MPP. In [38] author has proposed a new strategy to improve this technique by combining with the golden section search (GSS) technique. The first CS approach tracks the area closest to the MPP, followed by an iterative search for the exact GMPP using GSS. This hybrid methodology accelerates GMPP while maintaining tracking speed. GWO, a nature-inspired algorithm, is an effective way to monitor MPP when the problem is unformatted or incomplete. S. Mirjalili et al. [39] suggested a GWO calculation-based MPPT approach to illustrate the leadership hierarchy and chase mechanism of grey wolves. The GWO-MPPT technique is comparatively simple to use, operates smoothly, and has less oscillation compare to conventional and improved conventional MPPT technique making it ideal for hybrid PV systems with multiple MPP. Additionally, the literature recommends several optimizations algorithm-based MPPT controllers for improved performance, including Ant Colony Optimization (ACO) [40], Harmonic Search [41], Teacher Learning Based Optimization (TLBO) [42], Honey Badger Algorithm (HBA) [43], and Dwarf Mongoose Optimizer (DMO) [44].

2.2.4 Hybrid MPPT Techniques:

Hybrid MPPT controllers aim to overcome the limitations of independent algorithms, representing current advancements in the field. MPPT controllers can combine traditional and advanced algorithms for optimization, among others. In [45] a hybrid technique (PSO+INC and PSO+P&O) for a single-stage grid-connected PV system. This approach optimizes a single objective function with restrictions to maximize PV system output power while penalizing step size. The hybrid technique enhances system efficiency by reducing settling time and ripple output power, resulting in faster tracking and less oscillation in steady state. For the precise distribution of active power in a system, an improved mixed droop technique (IMDT) with a sliding mode (SM) controller was used in [46]. The improvement in the quality of power delivered to the customers in terms of lower settling time, voltage undershoot/overshoot, and THD demonstrated the potential of the proposed hybrid approach. To achieve the best efficiency for solar PV systems, a new hybrid Maximum Power Point Tracking (MPPT) technique utilizing Flying Squirrel Search Optimization (PSO ML FSSO) and machine learning trained on particle swarm optimization (PSO ML) was suggested in [47]. This hybrid approach decreased the settling time and increased efficiency. Several other hybrid MPPT technique such as ANN-PSO [48], adaptive neuro-fuzzy inference system (ANFIS).[49], HC-ANFIS [50], GWO-P&O [51] etc. has been studied in the literature.

2.3 INVERTER CONTROL TECHNIQUE AND DC BUS VOLTAGE REGULATION OF STANDALONE AND GRID INTEGRATED RES SYSTEM

Environmental, economic, and technological concerns have prompted the development of electrical systems based on the distributed generation (DG) model, which is associated with small-scale power generation and mostly comprised of renewable energy sources (RES). These renewable energy sources have significantly aided in the development of microgrids, enabling them to become a viable substitute for traditional grids. Due to the rising penetration of RES and its inconsistent availability, ancillary services like the BESS are required to make sure continuous power supply especially when utility grid is not available. Among all the RES, solar photovoltaic is one of the most widely used renewable energy sources due to its accessibility, ease of installation. Also, as power electronics technology advances, renewable energy sources are increasingly being used as primary energy sources in standalone power systems. This lowers generation costs, reduces environmental pollution, and improves power supply in remote areas. Droop control is a popular grid-forming control approach that allows inverters to regulate frequency and voltage using active and reactive power control, respectively.[52].

Stand-alone systems are the most cost-effective option for remote PV installations. Examples include distant stations, emergency power units, and manufacturing plants with delicate electronics. Standalone systems have disadvantages such as low capacity, high battery costs, and limited storage capacity, resulting in wasted energy and

increased costs. Adoption of Grid Connected or Standalone systems depends on economic feasibility and load considerations, in addition to accessibility and climate change benefits. In grid-connected systems, surplus electricity can be utilized back into the grid. Grid-connected systems are not affected by low load factors, which are common in rural electricity scenarios. The grid acts as an infinite storage unit, allowing for continuous operation and eliminating the need for additional storage batteries for wind and solar PV [53]

Control techniques for inverter and DC bus voltage regulation vary significantly between standalone and grid integrated system due to their different operational challenges and requirements. In stand-alone systems, inverters must operate in grid-forming mode to provide voltage and frequency stability in the absence of a grid reference, as well as to deal with load variations and fluctuations in renewable energy. These systems rely largely on control loops and effective voltage regulation techniques, especially during nonlinear or severe loading conditions.

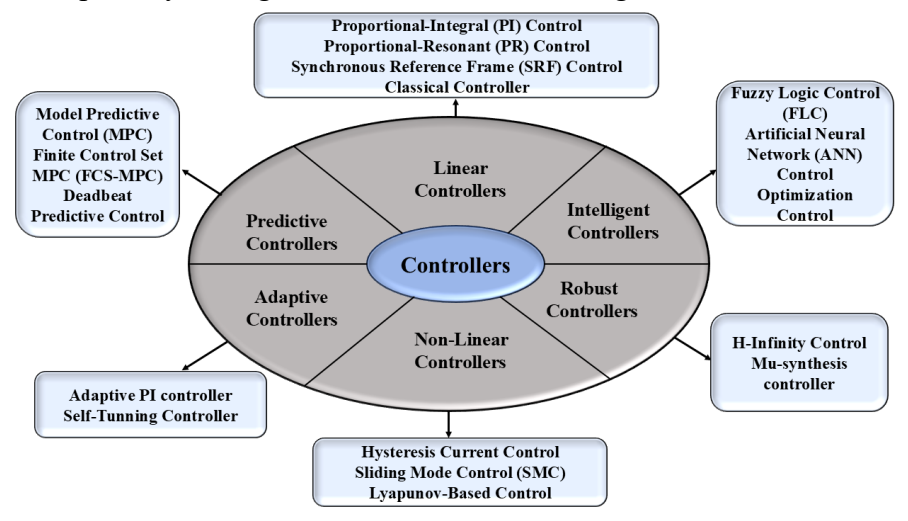


Fig.2.2 Classification of Inverter control techniques [54]

In contrast, grid-connected systems run in grid-following mode, which requires inverters to synchronize with grid parameters and handle power injection, harmonics, and grid code compliance.

To address these issues, several kinds of advanced control technique have been developed. These techniques are generally classed as linear, nonlinear, robust, adaptive, predictive, and intelligent control systems, with each having its own set of advantages and disadvantages as shown in Fig.2.2[54]. In both standalone and grid-integrated systems, the control strategy chosen is crucial for assuring system stability, enhancing power quality, and effective energy management.

2.3.1 Linear Controller:

Linear control techniques, such as proportional-integral (PI), proportional-resonant (PR), and tilt-integral (TI) controllers, constitute the backbone of inverter control techniques in both standalone and grid integrated solar PV systems because of their simplicity and ease of implementation. In standalone systems, TI controllers have

showed promise in regulating DC bus voltage and maximizing energy extraction under a variety of environmental conditions. However, the practical application of such systems faces obstacles such as sensor reliance, tuning complexity, and poor robustness under major shocks.

In grid-tied systems, however, linear controllers like as PI (in synchronous reference frame) and PR (in stationary frame) are extensively used for current regulation and harmonic attenuation using LCL-filtered inverters. While these controllers meet power quality standards and support dynamic performance, they also require extensive tuning and may have limitations in disturbance rejection or multi-harmonic correction. The PR controller's harmonic compensators can only handle a limited number of low-order harmonics due to system instability when the compensated frequency exceeds the system bandwidth. [55-59].

2.3.2Non-linear Controller:

Nonlinear controllers provide considerable advantages over classical and linear controllers for dealing with system uncertainties, external disturbances, and nonlinear dynamics. Nonlinear control approaches, as opposed to classic controllers such as PID or PR, which rely on linear assumptions, provide increased robustness, faster transient response, and more stability under variable operating conditions. As stated in [60] a feedback linearization control approach takes into account system nonlinearity to obtain reduced THD under nonlinear loads. However, as this approach lacks memory, any system performance issues can be observed in subsequent cycles.

The Sliding Mode Control (SMC) approach is used to regulate output voltage in PWM inverters. This approach has the main advantage of being insensitive to load disruptions and parameter fluctuations. In an ideal scenario, invariant steady-state response is possible. However, finding an appropriate sliding surface can be difficult. SMC performance suffers at low sampling rates. One disadvantage of using SMC for tracking variables is chattering [61]-[63] A hysteresis controller is a type of nonlinear controller. To create a hysteresis controller, an adaptive band must be designed to maintain a fixed switching frequency. Isolated neutral considerations are crucial as the controller's output determines the status of switches [64-65]. A Lyapunov-based controller is a nonlinear control method that provides system stability by establishing a control law based on a Lyapunov function, which is a mathematical function that reduces with time, guaranteeing convergence to a desired state [66]. In [67] author proposed control technique which is based on Direct Lyapunov technique to control the DC link voltage of a standalone system. The Direct Lyapunov technique ensures control system stability, is robust against un certainties, and is well-suited for nonlinear systems. However, it can be difficult to construct a suitable Lyapunov function and to demonstrate its features. The Direct Lyapunov technique can be computationally challenging for analysis and design, particularly for large-scale systems

2.3.3 Robust Controller:

Robust control is a control theory that designs controllers to handle uncertainty. These strategies aim to achieve robust performance and stability with minimum modelling errors. Robust control requires clearly defined criteria, explanations, and boundaries. This controller ensures stable and high-performing closed loop systems, even in multivariable systems [68]. H-infinity approaches involve representing a control problem as an optimization problem, which is subsequently solved. H-infinity approaches are suitable for multivariable system challenges. However, it is computationally difficult and requires a good model of the system being regulated. Additionally, nonlinear constraints are often not effectively managed [69]-[70]. The Mu-synthesis approach takes into account both structured and unstructured uncertainties when analysing system performance. This approach uses structured singular values to create the controller [71]. In [72] a robust μ value control approach that employs hybrid sensitivity theory is proposed. This technique not only achieves effective maximum power point tracking (MPPT), but it also improves DC bus voltage regulation and grid-connected current quality by including parameter perturbations into the DC/DC converter's average-state model.

2.3.4Adaptive Controller:

Adaptive control methods can automatically alter the control action in response to the system's operating conditions. Accurate system parameters are not necessary for optimal performance.

Standard PI controllers with constant gains are commonly employed for dc-link voltage management in single-phase grid-connected converters (GCCs), however they face a trade-off between eliminating voltage swings and decreasing grid current harmonics. An adaptive PI controller overcomes this constraint by dynamically modifying its parameters, resulting in improved performance, stability, and power quality under varying operating situations [73]-[74]. The study in [75] proposes a selftuning adaptive control method with a robust system identification approach for a single-phase full-bridge inverter with an LC filter, ensuring stability and improved performance in dynamic situations. The adaptive self-tuning controller with recursive least squares identification and pole shifting control outperformed the standard PI controller in all test conditions. It performed reliably and consistently under various system conditions, giving it a suitable solution for dynamic micro-grid applications. One of the primary benefits of this method is its ability to improve transient response and robustness to shocks, making it ideal for modern grid-connected inverters. However, the complexity of implementation and increasing computational requirements are possible downsides. [76]

2.3.5 Predictive Controller:

Predictive controllers utilize a system model to forecast future behaviour of regulated parameters. The controller optimizes actuation based on stated criteria. This

controller's fast dynamic response, ability to accommodate nonlinearities and limitations, and ease of construction make it suitable for a variety of systems, including multivariable cases. Predictive controllers demand more calculations compared to conventional controllers. Model predictive control (MPC) incorporates a flexible criterion that minimizes a cost function to determine the optimal actions. This approach uses a system model to anticipate the behaviour of variables till a specified time. MPC can simply include nonlinearities and system restrictions into controller design [77]- [79]. In [80] a model predictive current control technique for multilevel converters and its application to a three-phase cascaded H-bridge inverter. This control approach uses a discrete-time system model to anticipate future current values for all voltage vectors and select the vector with the lowest cost function. Finite control set model predictive control (FCS-MPC) is frequently used in nonlinear power converters, including multilevel converters, due to its intuitive handling of multivariable optimization, constraints, and nonlinearities. FCS-MPC provides greater dynamic performance than standard proportional-integral control techniques [81]. Unlike FCS-MPC, PWM modulators have a set switching frequency, resulting in harmonic spectra focused around the carrier frequency and multiples. To improve converter predictive control, several writers suggest using continuous control set MPC (CCS-MPC) with a PWM modulator [82]. In [83], an improved Deadbeat Controller (DBC) for a grid-tied Flying Capacitors Inverter is investigated. DBC balances capacitor voltages and injects current into the grid with minimal Total Harmonic Distortion (THD) [84]-[85]. This approach provides the following advantages, using a weighted state space model improves current tracking quality at zero crossing instants and provides superior steady-state performance (reduced current THD) compared to other prediction-based control systems like Finite-Control-Set Model Predictive Control.

2.3.6 Intelligent Controller

Although traditional control techniques are simple and dependable, they are always unable to deal with the complex coupling and interaction issues in PV inverter systems. AI-based control system optimization improves PV inverter efficiency by addressing complex control concerns such nonlinear dynamic interaction and multiple time-scale coupling.

Fuzzy control is a popular method for controlling PV inverter systems, including fuzzy PID, repetitive-fuzzy, and fuzzy PCI (proportional complex integral with PR control). The most significant advantage of fuzzy control is its ability to achieve self-tuning of parameters, allowing for real-time controller adjustment based on system operation state [86].

Intelligent control methods, including fuzzy logic control (FLC), expert system control (ES), artificial neural networks (ANN), and adaptive neuro-fuzzy inference system (ANFIS), provide considerable benefits for dealing with complex and uncertain models. These solutions improve the stability and reliability of PV systems. As PV plants expand and power grids become more complicated, it becomes challenging to

effectively predict and regulate the nonlinear and multi-coupled PV inverter system [87]-[89]. Fuzzy logic control (FLC) is one of the more established intelligent control techniques that works well with objects whose dynamic properties are difficult to obtain. FLC does not necessitate a mathematical model to accurately explain the system or insight into its intricate parameters and structure. In terms of response time, stability time, and robustness, FLC performs better than traditional controllers and is less sensitive to changes in parameters and load [90]-[91]. In contrast to fuzzy control ANN control can accurately mimic any non-linear continuous function and is extremely adaptable to complex settings. It also has self-learning capabilities and can handle multiple objectives. Furthermore, ANN distributes and stores information in the neurons of the neural network, making it very robust and fault-tolerant. ANN's self-learning, self-organizing, and self-adaptive qualities can assist in dealing with uncertain or unfamiliar systems [92]-[93]. The use of ANNs in a PV inverter system can alleviate the challenges of defining controller parameters for complicated coupled nonlinear systems. However, training an artificial neural network requires a significant quantity of data and effort. Designing a neural network involves maximizing desired parameters after selecting the number of layers and neurons in each layer. The gradient descent optimization (GDO) method can be used to train the MLP controller (MLPC). ANN can be more efficient and reliable than sliding mode controllers [94]-[96]. The neuro-fuzzy controller combines fuzzy control concepts with FLC and ANN, offering benefits such as neural network learning, parallel knowledge/data processing, and human-like fuzzy logic reasoning. The ANFIS fuzzy inference system uses the Takagi-Sugeno model. Neural networks implement the essential fuzzy control processes (fuzzification, fuzzy inference, and defuzzification). Neural networks may extract rules from input and output data, resulting in an adaptive neuro-fuzzy controller. The system can self-adapt, organize, and learn by altering fuzzy inference control rules through offline training and online learning algorithms [97]-[98]

Several strategies have been proposed in the literature to accomplish effective PQ control while maintaining power quality. All of the experiments listed above aimed to obtain a quick dynamic response with the least static error. The controllers in the mentioned studies achieve the desired power sharing ratio with appropriate dynamic response. However, the lack of automatic parameter tuning leads to significant overshoot and settling time during abrupt load changes. To improve the system's performance and stability, an optimization approach is needed to determine optimal values for controlling parameters [99]-[100]. Some of the optimization approaches utilized in microgrid application are explained here, as it is difficult to cover them all. One of the most popular metaheuristic optimization methods for improving power quality and controlling the voltage-frequency of AC MGs is the PSO. PSO has several advantages over genetic algorithms (GA), such as being easier to construct with fewer tuning factors, having a more effective memory capacity, and being more effective at preserving the swarm's variety. Additionally, in contrast to GA, PSO lacks sophisticated evolution operators like crossover and mutation and does not place a

heavy computing load on the microcontroller [101]-[102]. The Firefly optimization algorithm (FOA) was created and simulated in another investigation [103] in order to optimize the tuning of PI controllers in a grid-tied hybrid wind/photovoltaic system. The study's goal was to control the system frequency and voltage at the PCC during fault and load-changing scenarios. In [104], the PI parameters for controlling active and reactive power in an AC MG were adjusted using the Artificial Bee Colony (ABC) method. In both islanded and grid-connected modes of operation, droop control was used to regulate voltage and frequency variations. Additionally, the ABC optimization technique was used to improve the power and current controller settings in order to provide the best dynamic response of the MG system under study. Choosing the right optimization method for a specific problem is crucial for achieving minimization or maximizing of a fitness function. This literature review examines popular and recent algorithms.

2.4 ISLANDING DETECTION TECHNIQUES FOR GRID INTEGRATED SOLAR PV SYSTEM

Integrating microgrids with distributed energy resources (DERs) offers numerous benefits to the power grid, including improved power quality, increased energy efficiency, and lower carbon emissions. Microgrids function in either grid-connected or island modes, using distinct methodologies. Unintentional islanding is a critical technical concern in microgrids. Failure to trip the system can have substantial consequences for protection, security, voltage and frequency stability, and safety. Fast and efficient islanding detection is crucial for reliable microgrid operations. There are two types of islanding detection techniques (IDT): classic and modern as depicted in Fig.2.3. A number of methods are examined, such as remote and local IDTs. Once more, the local IDTs are categorized into three groups: active, passive, and hybrid. Additionally, a quick illustration of intelligently based IDTs and signal processing has been discussed. [105]

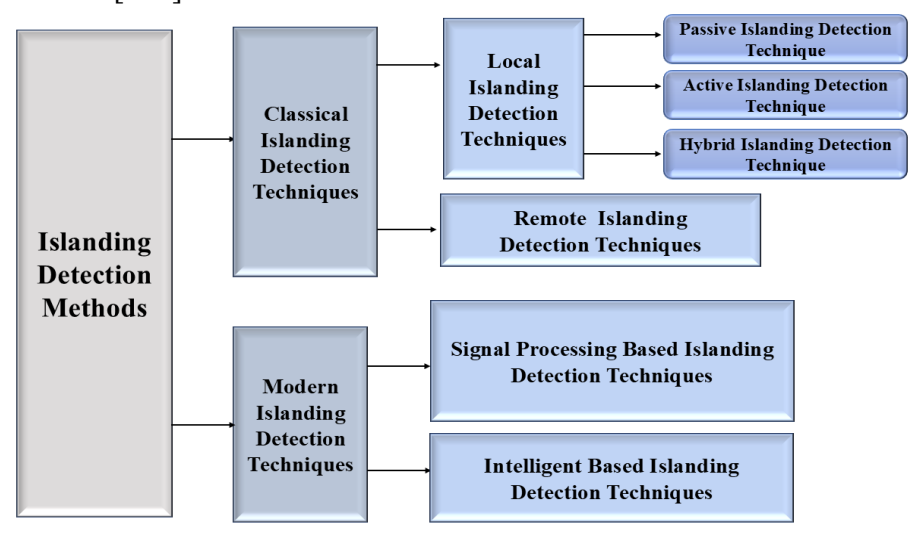


Fig.2.3 Classifications of Islanding detection techniques

2.4.1 Classical Islanding Detection Techniques:

Classical islanding detection methods are classified as local or remote, as illustrated in Fig. Local approaches, such as passive, active, and hybrid, measure certain parameters or variables on the microgrid side. Remote approaches use communication between microgrids and the main grid to monitor breakers quickly. Passive islanding strategies are based on parameter thresholds. Their benefits include simple implementation (no controller needed), no decrease of PV inverter power quality, and low cost. Their main shortcomings are a huge NDZ and in effectiveness in multi-inverter systems. Passive islanding detection techniques include over/under voltage and frequency (OV/UV/UF), phase jump detection (PJD), voltage harmonic monitoring, current harmonic monitoring, rate of change of power output (ROCOP), and rate of change of frequency (ROCOF). The OVP/UVP and OFP/UFP techniques include defining a threshold value for voltage and frequency at the point of common coupling (PCC).

Disconnection occurs when voltage or frequency values exceed specified limitations in the circuit. Most standards have specific typical voltage/frequency ranges. Phase jump detection disables an inverter when there is a phase discrepancy between the output voltage and current, such as during islanding. Its primary benefit is its efficiency, even with many inverters [106]-[107]. Active approaches detect islanding by injecting minor disturbances at the PV inverter output. Their key advantage is a lower NDZ than passive approaches. The main disadvantages include worsening output power quality, which can cause instability in the PV inverter, and the requirement for additional controllers, which adds complexity [108]. A few examples of active islanding detection techniques are impedance measurement (IM), sliding mode frequency shift (SMFS), active phase shift (APS), Sandia frequency shift (SFS), or active frequency drift with positive feedback. The Impedance Measurement (IM) approach detects islanding by monitoring variations in inverter output impedance caused by a loss of the main power supply. When the grid connection fails, differences in impedance indicate an islanding condition. In the Sliding Mode Frequency Shift (SMS) or Active Phase Shift (APS) approach, the current-voltage phase angle is designed to be proportional to the frequency of the Point of Common Coupling (PCC) voltage. This technique is commonly done by connecting an input filter to the Phase-Locked Loop (PLL), which tracks frequency deviations to identify islanding effectively. Sandia Frequency Shift (SFS) or Active Frequency Drift (AFD) with Positive Feedback method is an improved version of AFD) that uses positive feedback to expedite the islanding detection process. SFS effectively prevents islanding by introducing controlled frequency perturbations that cause the system frequency to wander away from normal operating circumstances, resulting in disconnection when an islanding event occurs. [109]-[112].

Hybrid strategies use both active and passive detection methods. Passive techniques detect islanding before using active procedures. These solutions reduce NDZ and have no substantial impact on grid power quality. Positive Feedback (PF) and Voltage

Unbalance (VU) This approach detects islanding by utilizing both active and passive (VU). Combining the two strategies overcomes their weaknesses. The system continuously monitors the three phase output voltages of the DG to determine the VU as specified. Disturbances to DGs cause a surge in VU. An island is detected when the spike exceeds the set value. [113]-[114]. The Voltage and Reactive Power Shift approach monitors voltage change over time to calculate covariance. The adaptive reactive power shift algorithm (ARPS) is then used for identification. When an island is suspected, the reactive power shift increases the phase shift action, resulting in a rapid frequency change during islanding [115].

Remote islanding detection methods rely on communication between the utility and PV inverter units. This approach does not have NDZ and does not affect the power quality of PV inverters. While effective in multi-inverter systems, it is costly to implement (particularly in small systems) and requires a complex communication strategy. The following section outlines common communication tactics [116].

2.4.2 Modern Islanding Detection Techniques:

Modern methods rely on signal processing and classifiers, but traditional IDMs, which are essentially passive, remain the foundation. These strategies increase the performance of traditional IDMs. Signal processing approaches first appeared in the literature in 2005, as they gained traction in power systems. These methods use signal processing technologies to extract features from signals for identification. Some useful tools include the Wavelet transform (WT), Stockwell transform (ST), Hilbert Huyang transform (HHT), time-time transform (TT), and mathematical morphology (MM). Over the past two decades, WT has been widely used in signal processing. Its key advantage is its capacity to expand a signal in the frequency domain while maintaining time information. For applications that require both time and frequency, use WT. There are various variations of WT available. Depending on the application, several methods are preferable over others. There are three types of wavelets transforms: continuous (CWT), discrete (DWT), and wavelet packet transform (WPT).[117]-[118]. Soft computing and intelligent-based IDMs are similar to signal processing and communication technologies, but do not need thresholds. We suggest intelligent ways to limit the NDZ and its impact on power quality, and have created high-precision classification models. Various intelligent classifiers, data mining techniques, and soft computing algorithms based on human, bird, fish, or animal intelligence are commonly employed to detect islanding. These strategies can solve multi-objective problems (MOPs) that standard approaches cannot [119]-[120].

2.5 IDENTIFIED RESEARCH GAPS

The production of power from renewable sources has become necessary to preserve the ecological balance due to the ongoing depletion of fossil fuels and their adverse impacts on the environment. One of the most promising choices among the many renewable resources is the solar photovoltaic system, and early characterization studies are necessary to choose the ideal operating conditions for maximum utilization.

- Current control methods concentrate on keeping the DC bus voltage constant, but more research is needed to develop real-time adaptive control solutions in extremely dynamic environments. Predictive control powered by AI can improve response time and voltage stability. While voltage regulation and harmonic abatement are addressed by existing hybrid standalone inverter control techniques, more work is required to incorporate sophisticated nonlinear control algorithms for improved performance under dynamically varying load situations.
- When irradiation changes quickly, traditional MPPT systems have trouble in tracking. Although ANN-based optimization has been investigated, hybrid AI-optimization methods (such evolutionary computing and deep reinforcement learning) may improve accuracy and response time even further.
- The adaptability of current ANN-optimized MPPT techniques to real-time environmental variations is limited by their reliance on offline training datasets. System flexibility may be increased by creating ANN MPPT algorithms based on online learning. It is still difficult to strike a balance between computational load and high-precision optimization. For real-world grid applications, more compact and effective AI models ought to be researched.
- Existing inverter control solutions have difficulties when dealing with an unbalanced and distorted grid. Advanced control approaches, such as model predictive control (MPC) and sliding mode control (SMC), need to be improved to provide steady synchronization.
- DC-Link Voltage Stability with High Renewable Penetration: With increased PV integration into the grid, maintaining DC bus voltage stability in the face of high temperature and load demand fluctuations remains a concern. AI-powered predictive controllers may provide more accurate and adaptable voltage management. Traditional inverter controllers focus on harmonic abatement, while deep learning-based control strategies could improve real-time harmonic compensation and power quality.
- Existing passive and active islanding detection systems have issues with detection speed and non-detection zones (NDZ). AI-powered classification methods, such as machine learning-based pattern recognition, may boost detection accuracy. Modern grids necessitate islanding detection solutions that are smoothly integrated with smart grid communication protocols. The role of IoT and cloud-based monitoring in real-time island detection has yet to be investigated. Conventional islanding detection methods may produce false positives, resulting in wasteful disconnections. Hybrid AI techniques that combine deep learning with real-time voltage and frequency analysis may improve reliability.

2.6 CONCLUDING REMARKS

This chapter presents a comprehensive review of the literature on MPPT control techniques for both standalone and grid-connected solar PV-based microgrids. It highlights key research contributions in the design and development of grid integrated

solar PV systems, focusing on voltage source inverter (VSI) control strategies and DC-link voltage regulation. Furthermore, various islanding detection techniques for grid-connected PV systems are examined. The chapter also reviews the work of numerous researchers in the field of control and optimization of grid-connected solar PV microgrids. Based on the surveyed literature, the research gaps have been identified, which form the foundation for the subsequent work presented in this thesis.

CHAPTER-3

PERFORMANCE ENHANCEMENT OF HYBRID STANDALONE RES BASED MICROGRID

3.1 INTRODUCTION

Standalone PV based microgrid has emerged as potential solutions to electricity challenges in the region where grid is not available. The battery energy storage system (BESS) is integrated into the system to facilitate synchronized load control and power flow. Variation in solar irradiation, load demand and fluctuation in battery SOC results in DC voltage fluctuation and maximum power point tracking challenges. Hybrid PV-Battery systems therefore must require control algorithms that can both flexibly adjust power flows as well as stabilize bus voltages.

This chapter focuses on the design and development of a hybrid standalone solar PV-based microgrid. The system is modeled and simulated using the MATLAB/Simulink environment to evaluate its performance under various operating conditions. Detailed mathematical modeling and parameter design of the proposed microgrid are presented in the subsequent sections.

A modified MPPT technique is proposed, which integrates the Incremental Conductance (INC) algorithm with a double closed-loop controller to effectively track the maximum power point and regulate the DC bus voltage under various dynamic and atmospheric conditions. To demonstrate the superiority of the proposed algorithm, its performance is compared with existing MPPT algorithms.

3.2 MODELLING AND DESIGN OF HYBRID MICROGRID SYSTEM

A hybrid standalone microgrid system consists of multiple renewable energy sources, such as a solar photovoltaic (SPV) system and a wind energy conversion system, integrated with a battery energy storage unit. These sources work together to ensure a continuous and reliable power supply without dependence on the main grid. Maximum power point tracking (MPPT) techniques and bidirectional battery control are employed for efficient energy extraction, storage, and management. Inverters with dedicated control strategies maintain voltage and frequency stability while supplying both linear and nonlinear loads. The detailed modeling of each subsystem—Solar PV, wind turbine with permanent magnet synchronous generator (PMSG), power converters, and battery storage—is presented in the following section.

3.2.1 Solar PV modelling

The term 'solar photovoltaic (PV) modelling' refers to the mathematical representation of a PV system's performance under various operating conditions and environmental factors. Hierarchal configuration of PV array is depicted in Fig.3.1. Using variables like solar irradiation, temperature, and load conditions, it simulates the PV module's electrical properties, such as current, voltage, power production, and efficiency.

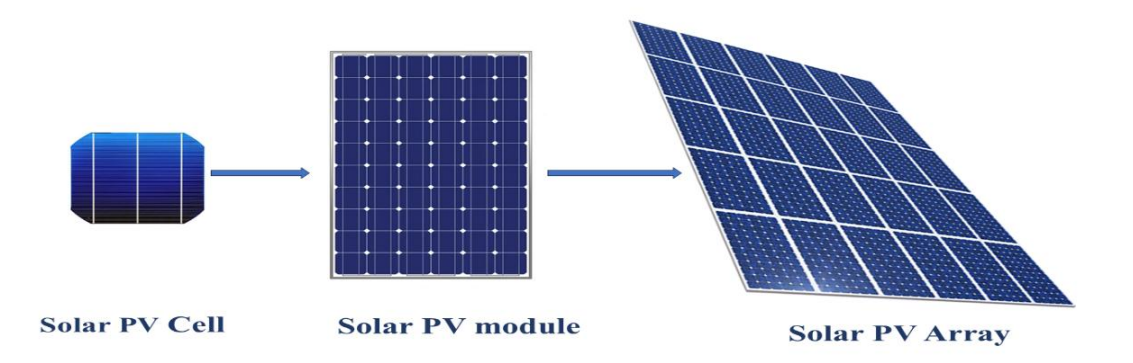


Fig.3.1 Hierarchal configuration of solar PV array

PV arrays consist of multiple modules connected in series and parallel to attain the required voltage and current. Fig. 3.2 (a) and 3.2 (b) show equivalent circuit diagrams of ideal and practical solar cells. By using Kirchhoff's law (KCL), the mathematical equations of a photovoltaic cell can be determined from Fig. 3.2 (a) and 3.2 (b) equation (1) can be used to represent the ideal photovoltaic cell output current for Fig. 3.2 (a). [121]

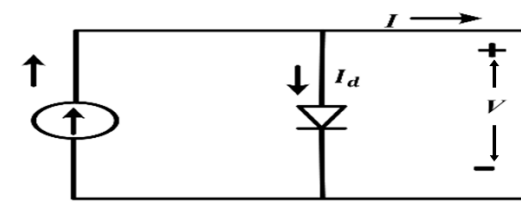


Fig. 3.2 (a) Equivalent circuit of a solar PV with ideal single diode model

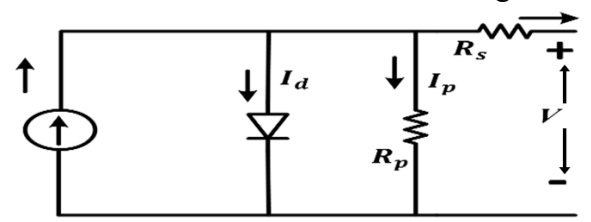


Fig. 3.2 (b) Equivalent circuit of a solar PV with practical model with R_s and R_p

$$I = I_{pht} - I_d \tag{3.1}$$

$$I_d = I_0 \left[exp\left(\frac{V}{YV_T}\right) - 1 \right] \tag{3.2}$$

$$Iph = \frac{1}{\mathcal{R}_{pht-STC}} \left(I_{pht_{STC}} + K_t (T - T_{STC}) \right) \times \mathcal{R}$$
(3.3)

$$V_T = \frac{k \cdot T}{q} \tag{3.4}$$

where, I_{pht} , I_d and I_0 are photo, diode and leakage currents in Amp , V is the voltage given to the diode, q is charge $1.602*10^{-19}\mathrm{C}$, I_{pht_STC} and \mathcal{R}_{pht_STC} are photovoltaic current and irradiance value at STC , K_t is temperature coefficient , \mathcal{R} is irradiance, V_T is thermal voltage in volt , k is Boltzmann constant $1.381*10^{23}$ J/K and Y is ideality factor . The series and parallel resistances of the network are represented by $R_s\&R_p$ in Fig.3.2(b). Now, using KCL in Fig.3.2 (b). Equation (3.5) is used to express output current.

$$I = I_{pht} - I_{d} - I_{p} \tag{3.5}$$

$$I = I_{pht} - I_0 \left[exp\left(\frac{V}{YV_T}\right) - 1 \right] - I_p \tag{3.6}$$

$$I = I_{pht} - I_0 \left[exp\left(\frac{V + IR_S}{YV_T}\right) - 1 \right] - \left(\frac{V + IR_S}{R_p}\right)$$
(3.7)

Following the series and parallel connection of cells, the output current (I_{op}) of the photovoltaic array is represented by equation 3.8.

$$I_{op} = I_{pht} N_p - N_p I_0 \left[exp\left(\frac{V + IR_S}{N_S Y V_T}\right) - 1 \right] - \left(\frac{V + IR_S}{R_p}\right)$$
(3.8)

where $N_S \& N_p$ is number of cells tied in series & parallel.

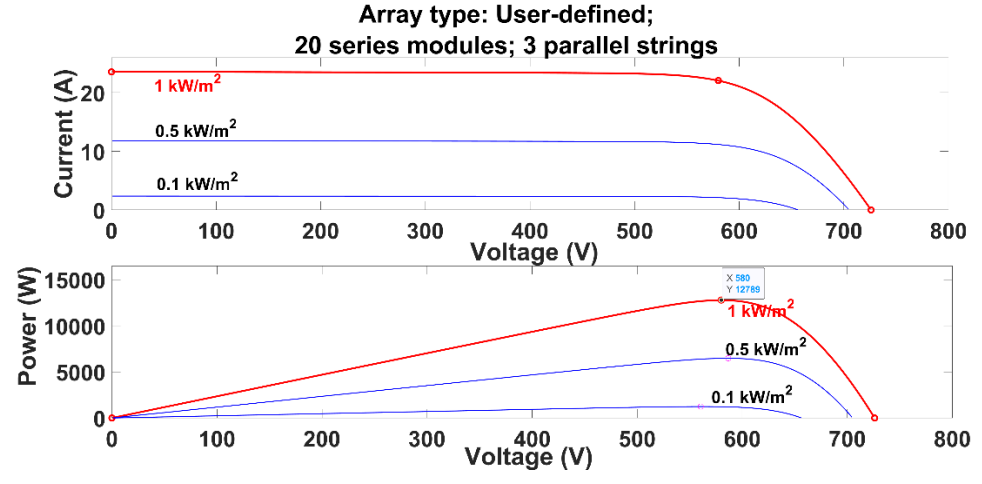


Fig. 3.3 P-V & I-V characteristics graph of proposed solar PV

PV arrays are created by connecting PV modules in series or parallel to achieve the necessary rating. PV array I-V and P-V characteristics vary with solar irradiation intensity and temperature. Additional information was obtained through the use of power and voltage (P-V) and current and voltage (I-V) curves. This study focuses on a 12.78 kW solar PV installation. Fig.3.3 displays the P-V curve and I-V curve for various solar irradiation levels.

3.2.2 Modeling of Wind Turbine

A wind turbine equipped with a Permanent Magnet Synchronous Generator (PMSG) efficiently converts the mechanical energy from wind into electrical power. The generated AC power from the PMSG is converted into DC power using a rectifier. The DC power is further processed using a boost converter and then fed to the grid or connected load. A wind turbine generates mechanical power from wind is expressed as equation (3.9):

$$P_{\text{mec}} = \frac{1}{2} \rho A_{\text{r}} C_{\text{p}}(\lambda, \beta) v_{\text{w}}^{3}$$
(3.9)

The turbine power coefficient (Cp) represents overall turbine efficiency and can be described using equations (3.10) and (3.11)

$$C_{p}(\lambda, \beta) = C_{1}\left(\left(\frac{C_{2}}{\lambda_{i}}\right) - C_{3}\beta - C_{4}\right)e^{\left(\frac{-C_{6}}{\lambda_{i}}\right)} + C_{5}\lambda$$
(3.10)

$$\frac{1}{\lambda_{i}} = \frac{1}{\lambda_{i} + 0.08\beta} - \frac{0.035}{\beta^{3} + 1} \tag{3.11}$$

where, P_{mec} mechanical power, C_p power coefficient, ρ air density kg/m³, A_r area swept by the blades, λ function of blade, β pitch angle, ω_r rotational speed, C_1 , C_2 , C_3 , C_4 , C_5 and C_6 (0.5176, 116, 0.4, 5, 21, and 0.0068).

3.2.3 Modelling of PMSG

The dynamic mathematical equations for a three-phase PMSG can be expressed in a synchronously rotating dq reference frame as equations (3.12) and (3.13).

$$\frac{d\psi_{q}}{dt} = v_{sq} - R_{s}i_{sq} - w_{e}\psi_{d}$$
(3.12)

$$\frac{d\psi_d}{dt} = v_{sd} - R_s i_{sd} - w_e \psi_q \tag{3.13}$$

Flux linkages of the PMSG $(\psi_d,\,\psi_q)$ are determined by

$$\psi_{d} = L_{d}i_{sd} + \psi_{m} \tag{3.14}$$

$$\psi_{\mathbf{q}} = \mathbf{L}_{\mathbf{q}} \mathbf{i}_{\mathbf{s}\mathbf{q}} \tag{3.15}$$

The electromagnetic torque (T_e) can be calculated as

$$T_{e} = \frac{3}{4} \frac{p}{L_{d}} \frac{|\psi_{s}|}{L_{q}} \left[2|\psi_{m}|L_{q}\sin\delta + |\psi_{s}| \left(L_{d} - L_{q}\right)\sin2\delta \right]$$
 (3.16)

$$T_{e} = \frac{3}{4} \frac{p}{L_{s}} |\psi_{s}| |\psi_{m}| \sin \delta \tag{3.17}$$

where, v_{sq} and v_{sd} q- and d-axis stator terminal voltages, i_{sq} and i_{sd} q- and d-axis stator currents, R_s stator resistance, w_e electrical angular velocity, ψ_d and ψ_q q- and d-axis flux linkage, L_q and L_d are q- and d-axis inductance and T_e electromagnetic torque.

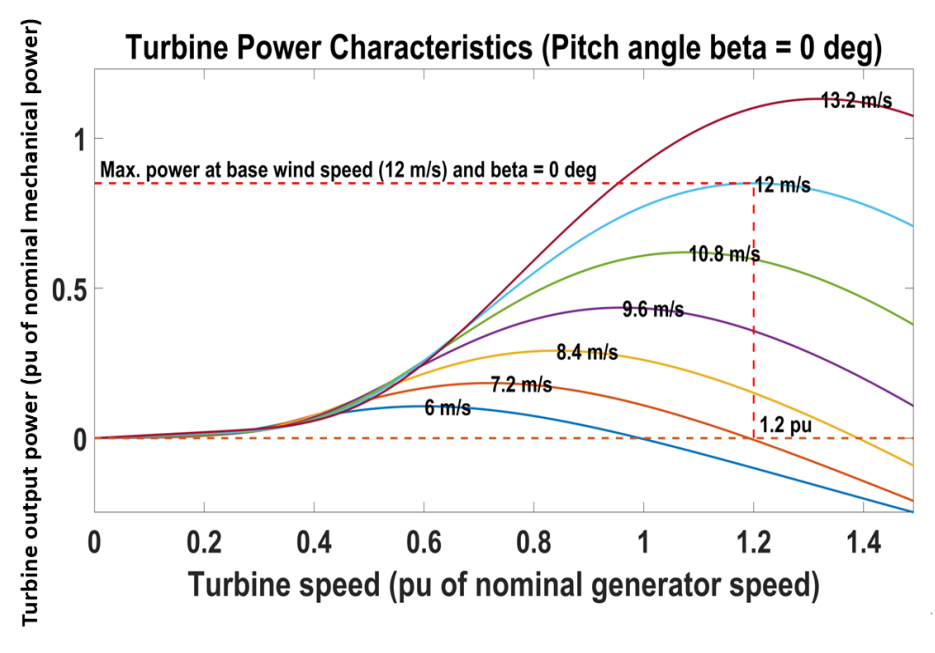


Fig. 3.4 Turbine Power characteristics

The wind turbine system under consideration has a rated mechanical power of 12.3 kW, and the base wind speed is defined as 12 m/s as can be seen from Fig.3.4. At this base wind speed, the maximum mechanical power output of the turbine is 0.85 per unit

(pu) of its rated capacity, which equates to an actual mechanical power of 10.455 kW (calculated as 0.85×12.3 kW). Considering a generator efficiency of 90%, the corresponding electrical output power is calculated to be 9.41 kW (0.9×10.455 kW). These numerical details are consistent with the turbine power characteristic curve provided for a pitch angle $\beta = 0^{\circ}$. The graph illustrates how the turbine output power, expressed in pu of nominal mechanical power, varies with turbine speed at different wind speeds. For a wind speed of 12 m/s, the turbine output reaches its maximum at around 1.2 pu turbine speed, and the output power plateaus at 0.85 pu, aligning with the values given in the table. This curve highlights the optimal operating point for maximum power extraction and supports the calculated output values.

3.2.4 DC-DC Boost converter modelling

A DC-DC boost converter is needed to obtain a fixed DC voltage and to increase the input voltage of the inverter because the output obtained from a solar array is susceptible to voltage fluctuation. As depicted in fig.3.5 the boost converter diagram includes an IGBT switch, an inductor, a diode, and a shunt capacitor. Value of inductance, capacitance and duty cycle can be computed using equations (3.18), (3.19) and (3.20). [122]-[123].

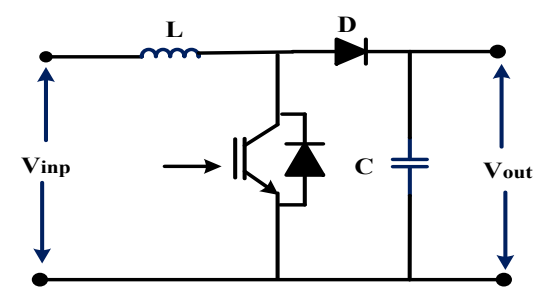


Fig.3.5 Equivalent circuit of Boost Converter

$$L = \frac{V_{inp}*(V_{out} - V_{inp})}{(\triangle If_{sf}V_{out})}$$
(3.18)

$$\alpha = 1 - \left(\frac{V_{inp}}{V_{out}}\right) \tag{3.19}$$

$$C = \frac{I*(V_{out} - V_{inp})}{(\triangle V f_{sf} V_{out})} \tag{3.20}$$

Where, input and output voltage of a boost converter are denoted by $V_{\rm inp}$ & V_{out} whereas α represents the duty cycle. f_{sf} is the switching frequency, I is the average output current, and ΔI is the output ripple current equal to 10% of input current. The converter's reference duty ratio is calculated using the MPPT algorithm. The boost converter's IGBT switch generates a gating signal at a switching frequency of 10 kHz.

3.2.5 DC-DC Buck - Boost converter modelling

The buck-boost converter is crucial in a standalone solar PV system as it regulates the DC bus voltage, allowing for efficient power transfer between the solar PV array, battery storage, and load. As the output voltage of a solar PV system varies with

irradiance and temperature, the buck-boost converter adjusts the voltage by either stepping it up (boost mode) or stepping it down (buck mode) to maintain a stable and dependable DC bus voltage. This regulation is critical for appropriate battery charging, preventing overcharging or undercharging, which increases the battery's longevity [124].

In fig.3.6, the bidirectional buck -boost converter is depicted. The converter has two switches Sw_1 , Sw_2 , diodes D_1 , D_2 , inductor (L_1) and capacitor (C_1) The converter works in two modes i.e., buck and boost.

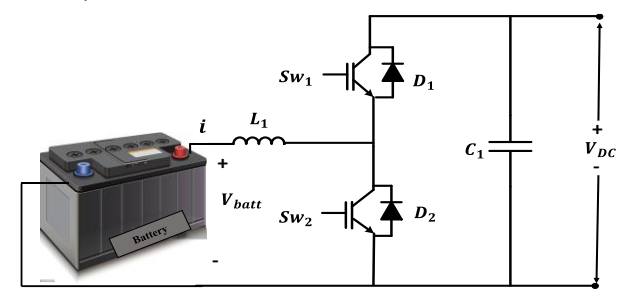


Fig.3.6 Equivalent circuit of Buck-Boost Converter

Boost Mode: In this mode, switch Sw_2 and D_1 diode conduct based on the duty cycle, whereas switch Sw_1 and, D_2 diode remain off continuously. This mode can be separated into two intervals based on the conduction of switch Sw_2 and diode D_1 .

Interval 1: (Sw_1 -OFF, D_1 -OFF; Sw_2 -ON, D_2 -OFF)- In this state, Sw_2 is active and considered short-circuited. The lower voltage battery charges the inductor, causing the current to increase until the gate pulse is withdrawn from Sw_2 . In this mode, the diode D_1 is reverse biased and the switch Sw_1 is turned off, resulting in no current flowing through Sw_1 .

Interval 2: (Sw_1 -OFF, D_1 -ON; Sw_2 -OFF, D_2 -OFF)- In this state, both Sw_1 and Sw_2 are turned off, indicating an open circuit. The inductor's current cannot change instantly, thus the voltage across it reverses and acts in series with the input voltage. As the diode D_1 is forward biased, the inductor current charges the output capacitor C1, resulting in a greater voltage. Consequently, the output voltage increases.

Buck Mode: The switch Sw_1 and diode D_2 conduct based on the duty cycle, whereas the switch Sw_2 and diode D_1 remain off at all times. This mode can be separated into two intervals based on the conduction of switch Sw_2 and diode D_1 .

Interval 1: (Sw_1 -ON, D_1 -OFF; Sw_2 -OFF, D_2 -OFF). In this phase, Sw_1 is active and can be termed short-circuited. The higher voltage battery will charge the inductor, which will then charge the output capacitor.

Interval 2: (Sw_1 - OFF, D1 OFF; Sw_2 - OFF, D2- ON). In this setting, Sw_2 and Sw_1 are both turned off. The freewheeling diode D_2 discharges the inductor current, which cannot alter instantly. The voltage across the load is stepped down compared to the input voltage.

3.2.6 Battery energy storage system modelling

Battery energy storage system is mainly employed with standalone photovoltaic system. The stored energy in the battery is utilized to feed the load in situations where the solar PV system is unable to provide power to it.

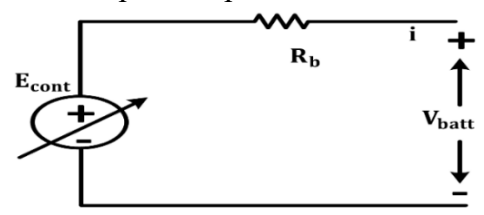


Fig.3.7 Equivalent circuit diagram of battery

Fig.3.7 illustrates an equivalent circuit diagram for a battery, where resistance and a voltage-controlled source are connected in series. From Fig.3.7 we can write-

$$V_{batt} = E_{cont} - R_b i (3.21)$$

Where, V_{batt} represent actual voltage, E_{cont} represents controlled voltage, R_b is the internal resistance and i is the battery current. Controlled voltage of battery is expressed by equation (3.22) and (3.23).

$$E_{cont} = E_0 - \rho \frac{Q}{Q - it} \cdot it - \rho \frac{Q}{Q - it} i * + Exp(t) [For discharging]$$
 (3.22)

$$E_{cont} = E_0 - \rho \frac{Q}{Q - it} \cdot it - \rho \frac{Q}{it - 0.1.Q} i * + Exp(t) [For charging]$$
 (3.23)

Where, E_0 represents constant open circuit voltage, ρ represents polarization constant, Q represents the battery capacity and battery's actual charge is represented by $it = \int idt$, and its reference current is denoted by i* and Exp(t) exponential zone voltage. In the system under consideration, a MATLAB/Simulink integrated Lithium-ion battery has been utilized. The battery's specifications are as follows:

Battery must offer the required 14kW of load for around an hour, considering 50% depth of discharge when solar power is zero.

Battery rating =
$$\frac{14kW*1h}{420V*0.5} = 66.66A$$
 (3.24)

To supply 14 kW, 35 batteries of 12V,67Ah are required.

3.2.7 LC Filter modelling

The LC values were used to provide sufficient bandwidth at the reference and cutoff frequencies. The capacitor's function is to reduce harmonics by serving as a low-impedance path to the ground. It is important to select a capacitor that provides a high-power factor at the reference frequency; equation (3.25) is used to determine the capacitance [125].

$$C_{f} = \frac{P * \varphi}{(2 * \pi * f * (V_{I-I})^{2})}$$
(3.25)

Reactive power factor is represented by φ . The rated power is P and the line frequency is f. The L value for the LC filter is determined using equation (3.26).

$$L_f = \frac{1}{4\pi^2 C_f f_r} \tag{3.26}$$

Where, f_r is resonance frequency.

3.3 MPPT CONTROL TECHNIQUES FOR STANDALONE RES BASED MICROGRID

In hybrid standalone RES based microgrid, MPPT, DC bus voltage, and inverter management strategies are necessary to guarantee effective energy use, steady power delivery, and system dependability. MPPT increases total efficiency by dynamically modifying the operating point under changing solar conditions, maximizing energy extraction from the PV array. A steady and controlled DC link voltage is maintained by DC bus voltage regulation, minimizing instability and guaranteeing smooth power delivery. This is essential for the seamless integration of batteries, inverters, and loads. In the meantime, inverter management makes sure that DC power is converted into a steady AC output with the right voltage, frequency, and phase regulation—all of which are necessary for powering delicate AC loads. By combining these strategies, hybrid standalone solar PV systems become more efficient for off-grid and backup power applications by improving their performance, stability, and dependability.

Due to unpredictable weather, the maximum power produced by a photovoltaic system can fluctuate. To determine the maximum power that can be extracted from a PV module, MPPT is utilized. The MPPT algorithm's objective is to control the DC-DC converter's duty cycle in order to increase output voltage and control the operating point at the point when the solar PV system generates the most power. The maximum power point, also known as the peak power voltage, is the voltage at which a photovoltaic module may generate its maximum power. Various MPPT controllers are examined in thesis work including:

- i. Perturb and Observe (P&O) technique
- ii. Incremental Conductance (INC)technique
- iii. Particle swarm optimization technique
- iv. Cuckoo search optimization technique
- v. Proposed modified MPPT (INC with Double close loop) technique

3.3.1. Perturb and Observe (P&O) Technique

Perturb and observe involves regularly changing the duty cycle and comparing the resulting PV output power to the preceding perturbation. The operating point movement is determined by measuring the power (ΔP) and voltage (ΔV) derivatives. If a perturbation affects array power, the next perturbation follows in the same (or opposite) direction, as shown in the Fig.3.8. [126].

3.3.2 Incremental Conductance (INC) Technique

Flowchart of INC technique are as shown in Fig.3.9. The incremental conductance (INC) algorithm is used as the primary MPPT technique. It continuously measures the power, voltage, and current of the solar panel and calculates the rate of change of

power with respect to voltage (dP/dV). By comparing dP/dV) with the rate of change of voltage (dV/dt), the algorithm determines if the system is operating at the maximum power point (MPP). If they are equal, the system is at the MPP, and no adjustments are required [127].

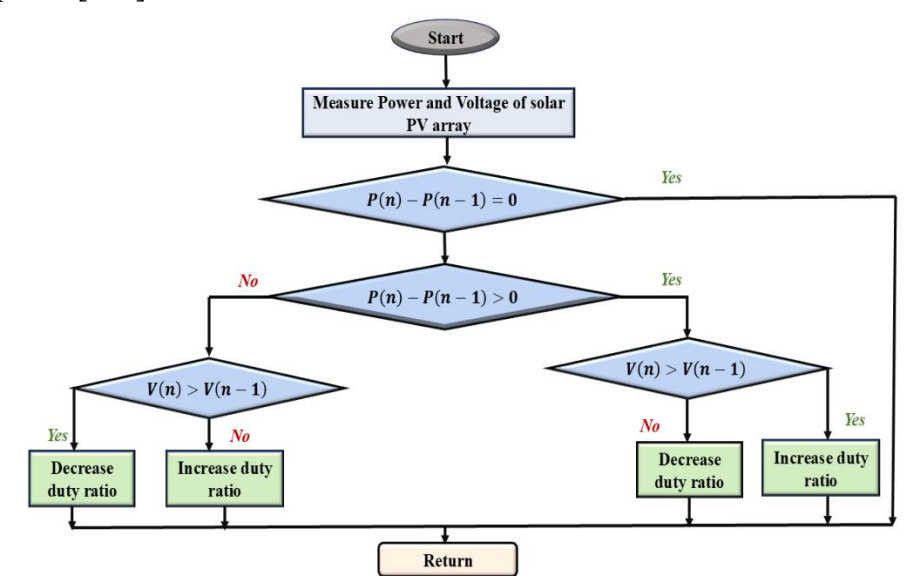


Fig.3.8. Flow chart of Perturb and Observe algorithm

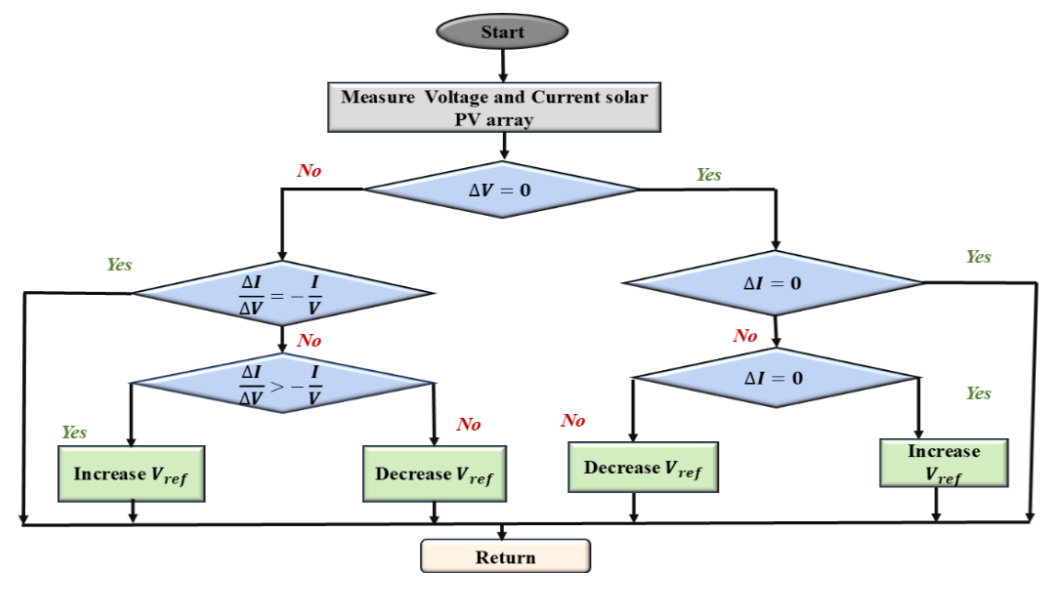


Fig.3.9 Flow chart of Incremental Conductance algorithm

3.3.3 Particle Swarm Optimization technique

Particle optimization technique (PSO) is a population-based evolutionary algorithm (EA) for search optimization. The principle was inspired by bird flock behavior to solve search and optimization problems. The PSO approach examines each particle's best position (P_{best}) and group's best position (G_{best}) in a D-dimensional search space. Each particle moves at a speed determined by these values. Each particle in a population exchanges information during its search process. During the search process,

each particle in the swarm interacts with its neighbors and quickly converges to the best position in the search space. Each particle's location is influenced by their best neighborhood particle (P_{best}) and the global best position (G_{best}) of the entire population [128].

The i^{th} position (x_i) for each particle is updated using equation (3.27):

$$x_i^{k+1} = x_i^k + \varphi_i^{k+1} \tag{3.27}$$

Where k indicates the iteration counter. The velocity component, φ_i , denotes the step size and is adjusted iteratively to allow particles to explore any region of the search space. The velocity is modified as equation (3.28):

$$\varphi_i^{k+1} = \omega \varphi_i^k + c_1 r_1 \{ P_{best} - x_i^k \} + c_2 r_2 \{ G_{best} - x_i^k \}$$
(3.28)

The inertia weight (w) determines how an antecedent particle's velocity affects its present velocity. Consider c_1 and c_2 as acceleration coefficients. The random variables r_1 and r_2 are evenly distributed within [0, 1]. P_{best} , i represents the personal best position of particle i, whereas G_{best} represents the best position of the entire swarm. If the particle position represents the real duty cycle and velocity represents the perturbation, the equation can be modified as shown below.

$$d_i^{k+1} = d_i^k + \varphi_i^{k+1} \tag{3.29}$$

According to equation (3.29), the perturbation on the duty cycle depends on G_{best} and G_{best} . Flow chart of PSO technique are as shown in Fig.3.10.

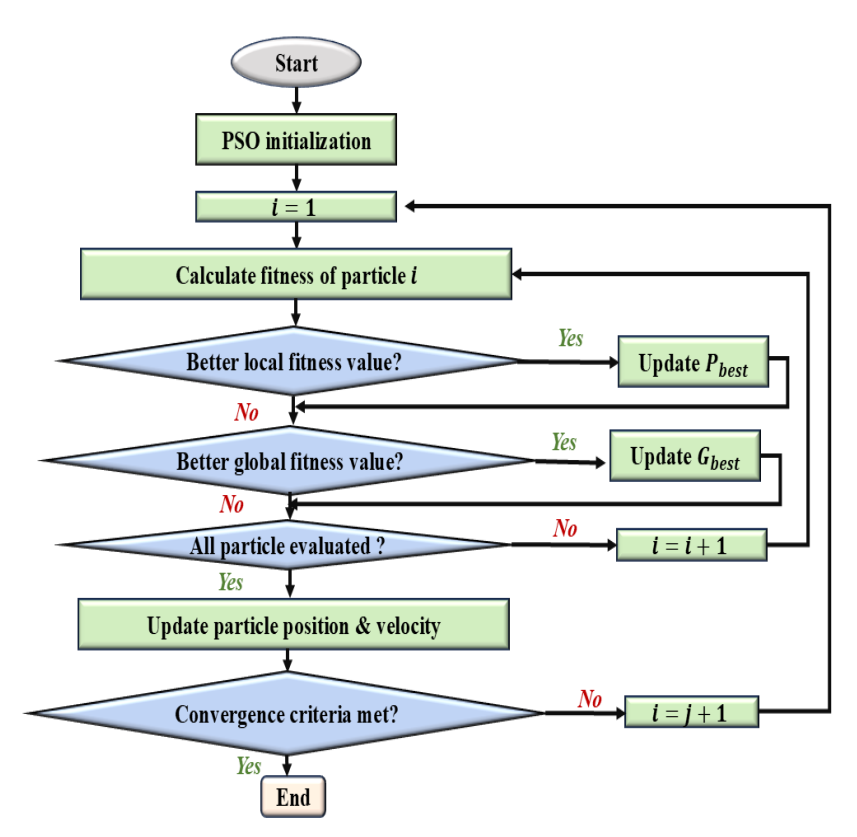


Fig.3.10 Flow chart of Particle swarm optimization algorithm

3.3.4 Cuckoo Search Optimization technique

In this algorithm, cuckoo birds select host birds with the same egg and nest features. So that cuckoos' birds can lay their egg in host bird nest. If host birds discover a cuckoo bird's egg, either host birds dump egg or destroy the nest and construct a new nest. Cuckoo Search mainly follows three basic rules [129].

- 1. Cuckoo birds lay one egg at a particular time and keep egg in a randomly selected nest. 2. Nest with better feature of eggs will carry forward the next generation.
- 3. The total no of available nests is set and egg-lay by cuckoo birds found by host birds with the probability of Pa \in [0, 1].

$$x_i^{t+1} = x_i^t + \alpha \oplus Le"vy \tag{3.30}$$

 x_i^t refers to sample/egg, i denote the number of samples, t is the iteration count, α is the step size, \bigoplus means entry-wise multiplication, $Le'vy(\lambda)$ is Le'vy distribution given by equation (3.31):

$$Le'vy \approx u = t^{-\lambda} \tag{3.31}$$

The Le'vy flight is used here for cuckoo bird to generate new solution. Le'vy flights are a kind of random trajectories walk where steps size is determined from Le'vy distribution. In this present work, CSA is implemented to optimize the duty cycle of boost converter. Fig. 3.11 depicts the flowchart of the CSO MPPT technique.

To start, n number of random duty cycles between 0 to 1 is created and given to the boost converter for initial objective function for each duty cycle as expressed as equation (3.32).

$$d_i = d_{min} + rand[0\ 1](d_{max} - d_{min})$$
(3.32)

The initial duty cycles are given to the converter to generate new solution and to form the current nest. The corresponding power for each duty cycle is determined by using current and voltage of the solar panel. Maximum power provided by its corresponding duty cycle is considered as the current best. Le'vy flight is performed to generate new optimal duty cycle using expression (3.33).

$$d_i^{(t+1)} = d_{best}^t + \alpha \oplus Le"vy(\lambda)$$
(3.33)

This process will repeat until the maximum power is obtained.

The modified MPPT technique, which combines the incremental conductance (IC) method with double closed-loop control, outperforms existing MPPT techniques such as Perturb and Observe (P&O), Particle Swarm Optimization (PSO), and Cuckoo Search by providing faster and more accurate tracking, better DC bus voltage regulation, and fewer power oscillations. Unlike P&O, which experiences steady-state oscillations, and IC, which issues with delayed convergence, the updated technique ensures stable and exact MPP tracking. It also outperforms PSO and Cuckoo MPPT, which can be computationally costly and slow in dynamic circumstances, by delivering faster transient reaction and stable performance even with varying irradiance.

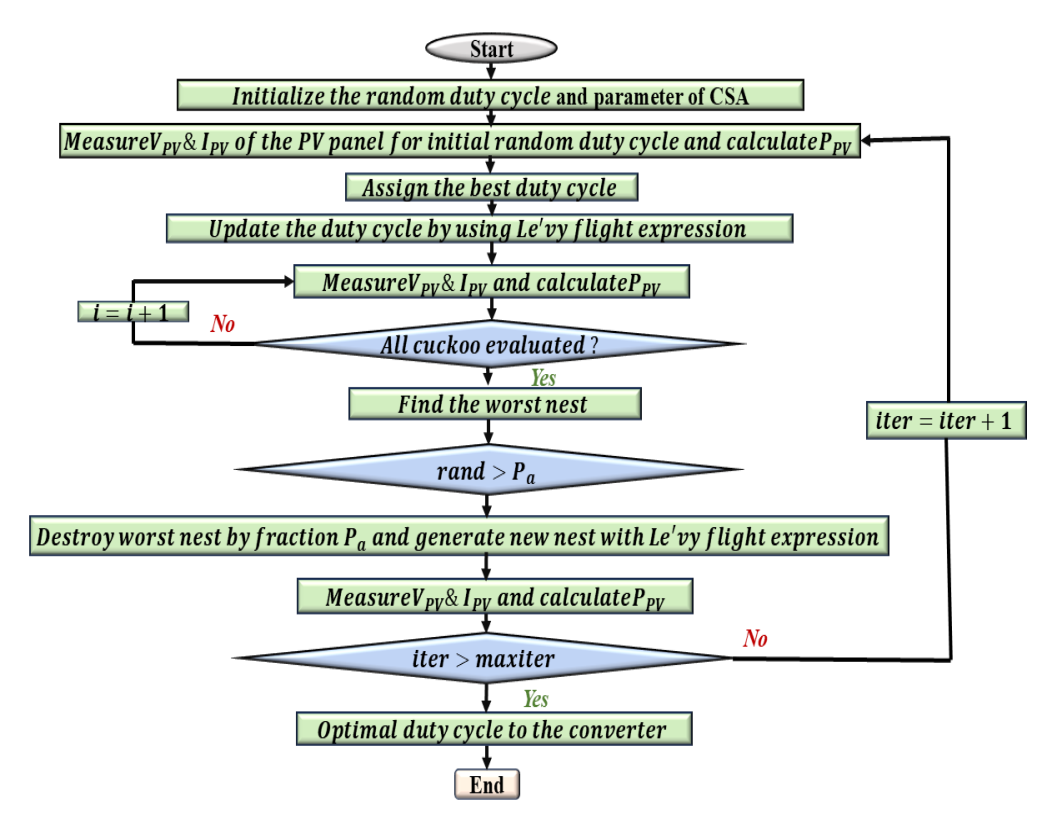


Fig.3.11 Flow chart of Cuckoo search optimization algorithm

3.3.5 Proposed Modified MPPT (INC with Double close loop) technique

The modified MPPT technique combines the advantages of the incremental conductance method and the double closed-loop MPPT technique. This modified approach aims to improve DC bus voltage regulation, MPPT tracking and accuracy in photovoltaic systems [130].

In this approach, the incremental conductance (INC) algorithm is used as the primary MPPT technique. It continuously measures the power, voltage, and current of the solar panel and calculates the rate of change of power with respect to voltage (dP/dV). By comparing (dP/dV) with the rate of change of voltage (dV/dt), the algorithm determines if the system is operating at the maximum power point (MPP). If they are equal, the system is at the MPP, and no adjustments are required.

However, DC bus voltage fluctuates due to rapid change in generation from the solar panels due to which INC method may not be able to accurately track the MPP alone. In such cases, the double closed-loop MPPT technique is combine with INC and employed as a new modified MPPT method to enhance the tracking performance by regulating DC bus voltage.

From Fig.3.12 It can be observed that V_{PV_ref} is obtained from incremental conductance MPPT technique. Obtained V_{PV_ref} is compared with input voltage of PV (V_{PV}) which generate V_{PV_err} which is given to the PI controller to obtain optimal duty cycle as expressed in equations (3.34) and (3.35).

$$V_{PV_err(t)} = V_{PV} - V_{PV_{ref(t)}}$$

$$(3.34)$$

$$d1 = kp1(V_{PV_{err(t)}}) + ki1 \int_0^t (V_{PV_{err(t)}})$$
(3.35)

In double closed loop controller, DC bus voltage (V_{DC}) is compared with reference DC bus voltage (V_{DC_ref}) which generates voltage error as expressed in equation (3.26). then given to the voltage controller outer loop using PI controller (PI2) to generate reference current as expressed in equation (3.37).

$$V_{DC_err(t)} = V_{DC_ref(t)} - V_{DC} \tag{3.36}$$

$$IL_{-ref} kp2(V_{DC_{err(t)}}) + ki2 \int_{0}^{t} (V_{DC_{err(t)}})$$
 (3.37)

Similarly for inner loop, output reference current (I_{L_ref}) is compared with output boost current and given to the inner loop using PI controller to generate duty cycle as expressed in equation (3.38) and (3.39).

$$I_{-err(t)} = IL_{-ref} - IL \tag{3.38}$$

$$d2 = kp3(I_{-err(t)}) + ki3 \int_0^t (I_{-err(t)})$$
(3.39)

After that, the obtained duty cycle from the INC MPPT technique and the double-closed-loop MPPT controller are added together to get the optimal duty cycle as expressed in equation (3.40) where both the maximum power point and the DC bus voltage are maintained, and then the generated pulse is fed to the boost converter.

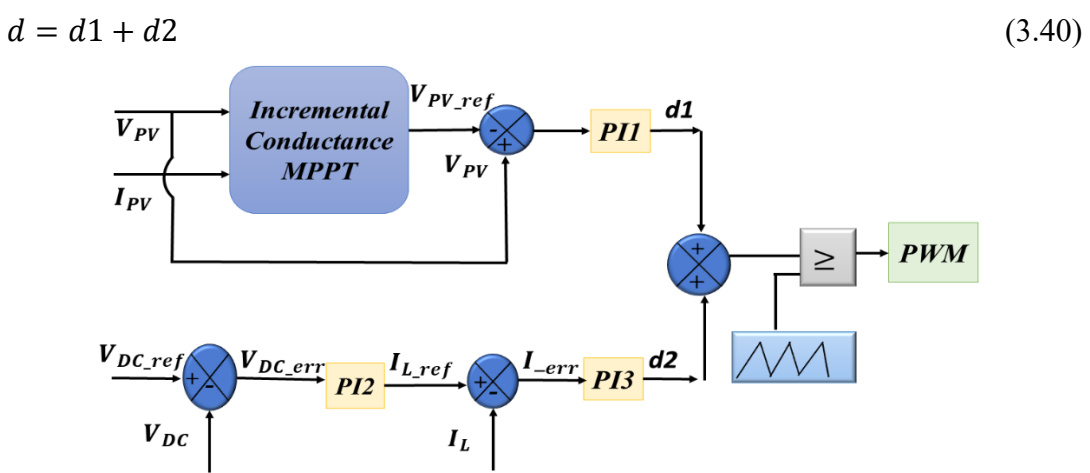


Fig.3.12 Proposed modified MPPT technique for solar PV

3.3.6 Control Technique for Bidirectional Converter

Fig.3.13 illustrates the bidirectional converter control in terms of managing both the sensing battery current and the DC bus voltage in both modes. Since switch S1 works in buck mode to charge the battery and switch S2 works in boost mode to discharge the battery, the converter has the potential to transfer power in both directions.

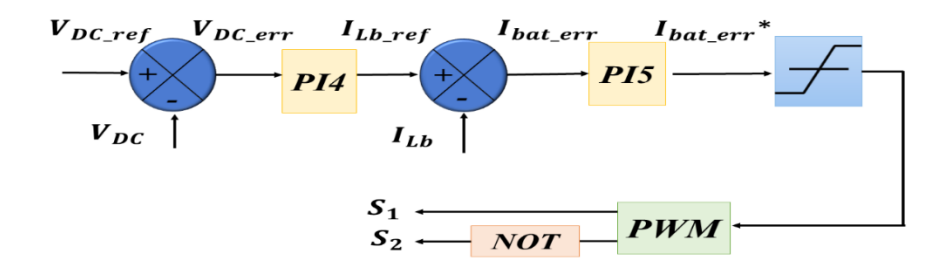


Fig.3.13 Control technique for bidirectional Buck-Boost converter

The comparison of DC bus voltage (V_{DC}) with the DC reference voltage (V_{PV_ref}) generates voltage error $(V_{PV\ err})$ which is sent to a PI4 controller.

Mathematically, It can be expressed as equation (3.41)

$$V_{DC_{err(t)}} = V_{DC_{ref(t)}} - V_{DC} (3.41)$$

Output of the PI controller is battery reference current which is expressed by equation (3.33)

$$ILb_{-ref_}kp4(V_{DC_{err(t)}}) + ki4\int_0^t (V_{DC_{err(t)}})$$
(3.42)

The comparison of output battery current (I_{Lb}) with reference current (I_{Lb_ref}) generates battery current error expressed as equation (3.43)

$$I_{batt\ err(t)} = ILb_{-ref} - ILb \tag{3.43}$$

 $I_{batt\ err(t)}$ is provided to PI controller for estimation of $I_{batterr^*}$.

$$I_{batt_{err}^*} = kp5(I_{batt_{err}(t)}) + ki5 \int_0^t (I_{batt_{err}(t)})$$
(3.44)

3.3.7 Working of battery energy storage system

By adjusting the voltage of the DC bus, the DC bus voltage control-based power management technique seeks to manage the power flow of the hybrid standalone microgrid.

Discharging mode: When the load demand exceeds the PV generation, there is a dip in the DC bus voltage. In this case, the converter operates in boost mode, allowing power to flow from the battery to the DC bus and meeting the load demands, which discharges the battery.

Charging mode: When the power produced from SPV is greater than the load demand, the converter operates in buck mode, allowing power to flow from the DC bus to the battery, thus charges the battery.

To prevent deep discharge of battery energy storage system (BESS) a lower threshold of 25% SOC has been consider while the upper threshold is 80% is considered. ε is a error threshold which is considered as $\pm 10V$. Flow chart of energy management of hybrid standalone microgrid ia as depicted in Fig.3.14.

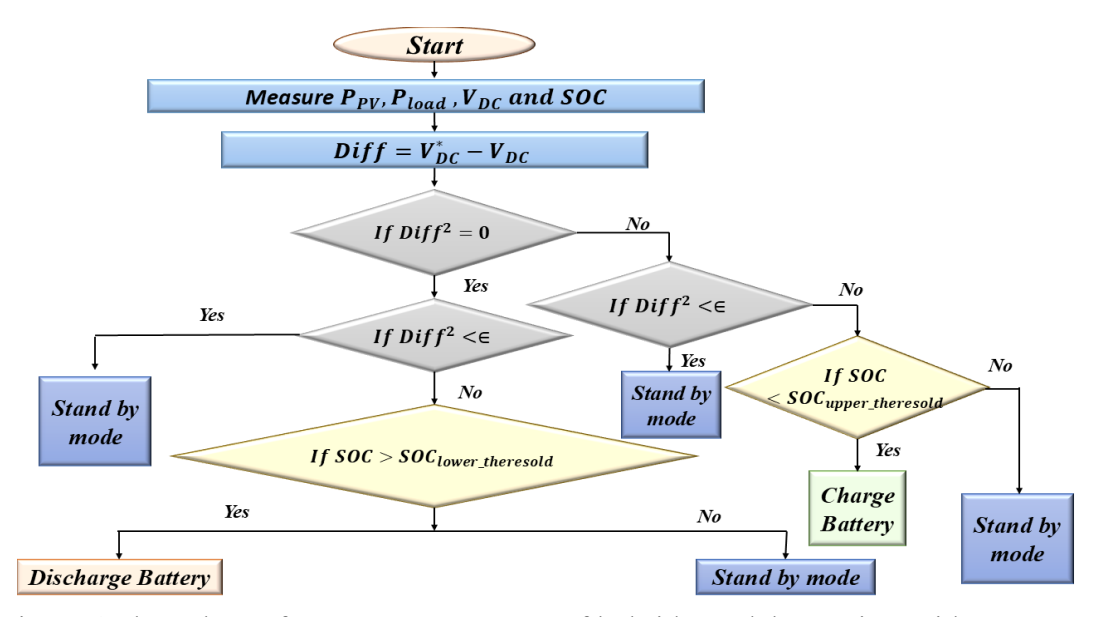


Fig.3.14 Flow chart of energy management of hybrid standalone microgrid

3.4 CONTROL TECHNIQUES FOR STANDALONE INVERTER

- i. Droop Control strategy
- ii. Model Predictive Control

3.4.1 Droop Control strategy

Control technique for inverter is presented in this section. Fig.3.15, 3.16 and 3.17. depict the entire control structure of the inverter control. A DG inverter's controller is comprised of three distinct parts. The first is an external power control loop that uses the droop characteristics set for the real and reactive powers to determine the magnitude, frequency, and, consequently, phase, of the fundamental component of the inverter output voltage. The voltage and current controllers, which make up the second and third sections of the control system, are made to reject high frequency disturbances and give the output filter sufficient damping [131].

Power Controller:

The first is an external power control loop that uses the droop characteristics established for the real and reactive powers to determine the phase, as well as the magnitude and frequency, of the fundamental component of the inverter output voltage.

$$\omega = \omega_n - m_p P \tag{3.45}$$

$$v_{odref}^* = V_n - m_q Q (3.46)$$

Where m_p , m_q are real and reactive power droop gain of inverter which can be calculated using equations (3.47) and (3.48).

$$m_p = \frac{\omega_{maximum} - \omega_{minimum}}{P_{maximum}} \tag{3.47}$$

$$m_q = \frac{v_{odmaximum} - v_{odminimum}}{o_{maximum}} \tag{3.48}$$

To determine the real and reactive powers P and Q the instantaneous power components are processed through low-pass filters to filter out noise present in the signals after transformation. As shown in Fig.3.13 The low-pass filter's cut-off frequency is represented by ω_c .

$$P = \frac{3}{2} \left(v_{od} i_{od} + v_{oq} i_{oq} \right) \tag{3.49}$$

$$Q = \frac{3}{2} \left(v_{oq} i_{od} - v_{od} i_{oq} \right) \tag{3.50}$$

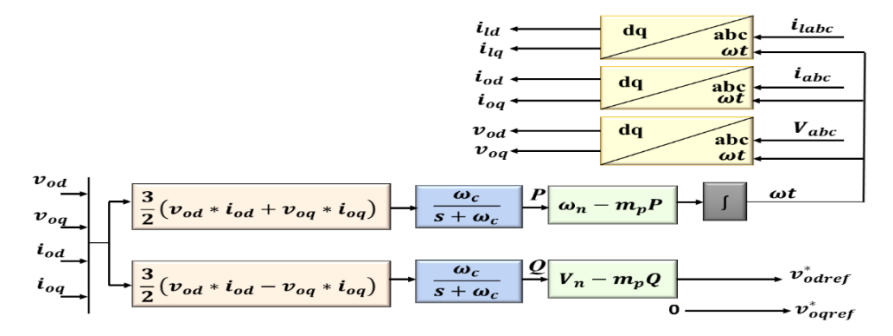


Fig.3.15 Power control loop

Voltage and Current loop:

Fig 3.15. and Fig.3.16. presents the voltage and current control loop and PWM sinusoidal switching reference generation for inverter. The voltage and current controllers are the second and third sections of the control system, and they are designed to reject high-frequency disturbances while also providing suitable damping for the output LC filter. Voltage and current loop are demonstrated in Fig 3.16 which consist of two blocks which are responsible for maintaining PCC voltage. The power controller block's Q-V droop equation provides the reference for the d-axis element, while the q-axis element reference is fixed to zero to synchronize the vector with the d-axis and decouple the d-q axis component of the transformed voltage. The expression utilized in creating the voltage block and current block is expressed in equations (3.51) -(3.54).

$$i_{ld}^* = Fi_{od} - \omega Cf v_{og} + K_{vv} (v_{odref}^* - v_{od}) + K_{vi} \int (v_{odref}^* - v_{od})$$
(3.51)

$$i_{lq}^* = Fi_{oq} - \omega C f v_{od} + K_{vp} (v_{oqref}^* - v_{oq}) + K_{vi} \int (v_{oqref}^* - v_{oq})$$
 (3.52)

$$v_{id}^* = -\omega L f i_{lq} + K_{cp} (i_{ld}^* - i_{ld}) + K_{ci} \int (i_{ld}^* - i_{ld})$$
(3.53)

$$v_{iq}^* = \omega L f i_{ld} + K_{cp} (i_{lq}^* - i_{lq}) + K_{ci} \int (i_{lq}^* - i_{lq})$$
(3.54)

Where i_{ld}^* , i_{lq}^* are the reference signal produce by the voltage control loop which are given to the current controller loop. K_{vp} , K_{vi} are the pi controller gain value. v_{id}^* , v_{iq}^* are the dc signal produced by the current loop for generating pulse, K_{cp} , K_{ci} are the gain value.

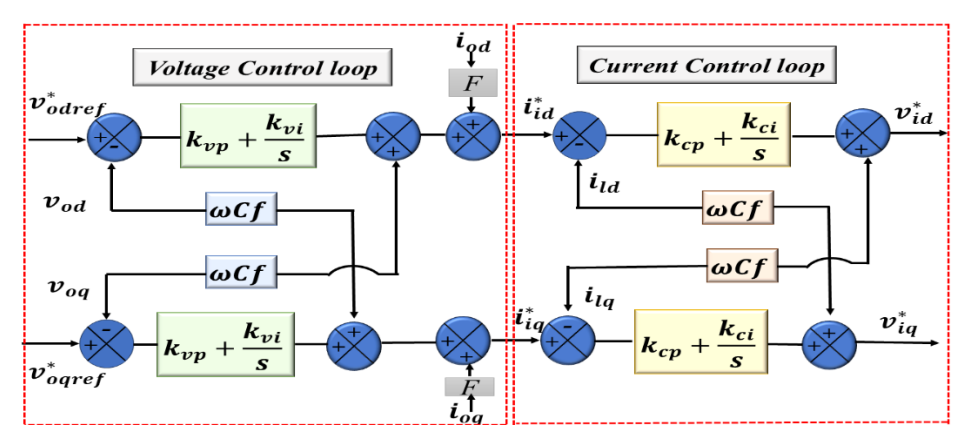


Fig.3.16 Voltage and current control loop

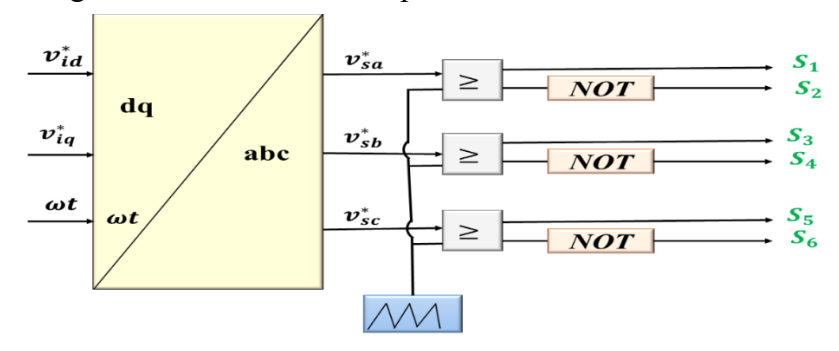


Fig.3.17 PWM sinusoidal switching reference generation for inverter

3.4.2 Model Predictive Control

Model Predictive Control (MPC), also known as receding horizon control, is a powerful technique commonly used in industrial control systems. It takes into account major inverter limits, such as the static power converters' limited switching states. Using the system model, MPC predicts the behaviour of variables for each switching state and chooses the best state by minimizing a quality function that represents intended system performance. This technique is ideal for systems with restrictions and nonlinearities, since it provides flexibility and simplicity by expressing control objectives as a cost function [132].

Fig.3.27 illustrates how a Voltage Source Inverter (VSI) with an LC filter is used in this study. A detailed model of the VSI, including its control technique and interface with the LC filter, is provided to demonstrate its performance under various load conditions. The gating signals G_a , G_b and G_c define the inverter's switching states, as indicated below:

$$G_a = \begin{cases} 1, & \text{if } G_1 \text{ ON and } G_4 \text{ Off} \\ 0, & \text{if } G_1 \text{ Off and } G_4 \text{ ON} \end{cases}$$
(3.55)

$$G_b = \begin{cases} 1, & \text{if } G_2 \text{ ON and } G_5 \text{ Off} \\ 0, & \text{if } G_2 \text{ Off and } G_5 \text{ ON} \end{cases}$$
(3.56)

$$G_{c} = \begin{cases} 1, & \text{if } G_{3} \text{ ON and } G_{6} \text{ Off} \\ 0, & \text{if } G_{3} \text{ Off and } G_{6} \text{ ON} \end{cases}$$
(3.57)

To express these switching states in the $\alpha\beta$ reference frame, convert them as follows:

$$G = \frac{2}{3}(G_a + aG_b + a^2G_c) = G_\alpha + jG_\beta \text{ , where } a = e^{j(2\pi/3)}.$$
 (3.58)

$$\begin{bmatrix} G_{\alpha} \\ G_{\beta} \end{bmatrix} = \frac{2}{3} \begin{bmatrix} 1 & -\frac{1}{2} & -\frac{1}{2} \\ 0 & \frac{\sqrt{3}}{2} & -\frac{\sqrt{3}}{2} \end{bmatrix} \begin{bmatrix} G_{a} \\ G_{b} \\ G_{c} \end{bmatrix}$$
(3.59)

The inverter's output voltage space vectors are defined as:

$$v_i = \frac{2}{3}(v_{aN} + av_{bN} + a^2v_{cN}) \tag{3.60}$$

The inverter's phase-to-neutral voltages are denoted by v_{aN} , v_{bN} , v_{cN} .. The voltage of the vector v_i can be linked to the switching mode vector G using equation (3.58).

$$v_i = V_{DC}G \tag{3.61}$$

Fig.3.18 depicts the switching modes and voltage vectors generated by the VSI using (3.58) and (3.61), accounting for all conceivable combinations of switching signals G_a , G_b , and G_c Eight voltage vectors (v_0 through v_7) are considered output options.

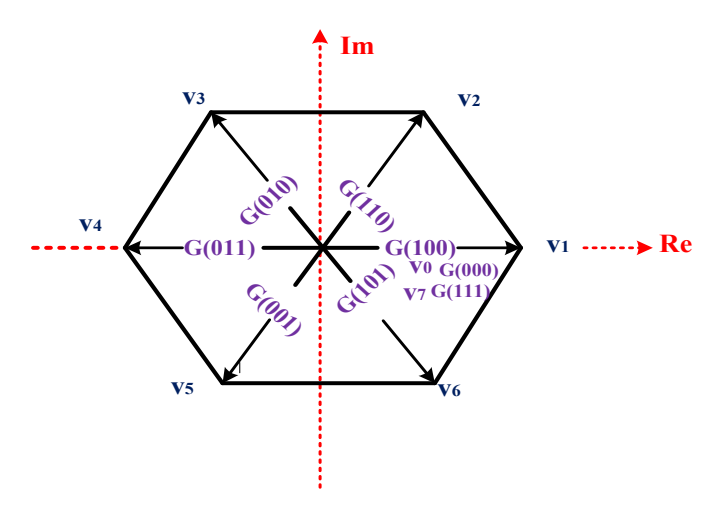


Fig.3.18 Eight possible voltage vector created by the inverter

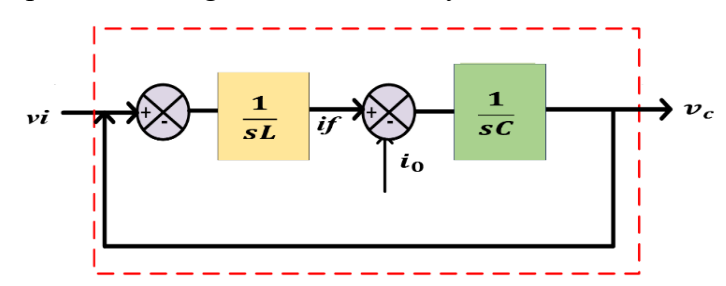


Fig.3.19 Filter model

Vectorial notation is used to represent the filter current (i_f) , output voltage (v_c) , and current (i_0) as space vectors, as shown in equations (3.62), (3.63) and (3.64).

$$i_f = \frac{2}{3} (i_{fa} + ai_{fb} + a^2 i_{fc})$$
(3.62)

$$V_c = \frac{2}{3}(v_{ca} + av_{cb} + a^2v_{cc}) \tag{3.63}$$

$$i_0 = \frac{2}{3}(i_{0a} + ai_{0b} + a^2i_{0c}) \tag{3.64}$$

Fig.3.19 shows a block diagram of an LC filter. The vectorial equation for filter inductance and capacitance can be stated as equation (3.65) and (3.66):

$$L\frac{di_f}{dt} = v_i - v_c \tag{3.65}$$

$$C\frac{dv_c}{dt} = i_f - i_o (3.66)$$

Where, L and C represent the inductance and capacitance of the LC filter, i_f and v_c are the measured values, and v_i is determined using equation (3.60).

A state-space system can be used to represent the following mathematical expression:

$$\frac{dx}{dt} = Ax + Bv_i + B_d i_0 \tag{3.67}$$

where,
$$x = \begin{bmatrix} i_f \\ v_c \end{bmatrix}$$
, $A = \begin{bmatrix} 0 & -\frac{1}{L} \\ \frac{1}{C} & 0 \end{bmatrix}$, $B = \begin{bmatrix} \frac{1}{L} \\ 0 \end{bmatrix}$, and $B_d = \begin{bmatrix} 0 \\ -\frac{1}{C} \end{bmatrix}$

The system's output voltage (v_c) is expressed as equation (3.68).

$$v_c = \begin{bmatrix} 0 & 1 \end{bmatrix} x \tag{3.68}$$

The filter's discrete-time model is derived from equation.3.52 for a sample time Ts and expressed as:

$$x(k+1) = A_q x(k) + B_q v_i(k) + B_{dq} i_0(k)$$
(3.69)

$$\underbrace{\begin{bmatrix} i_f(k+1) \\ v_c(k+1) \end{bmatrix}}_{x(k+1)} = \underbrace{e^{AT_s}}_{Aq} \underbrace{\begin{bmatrix} i_f(k) \\ v_c(k) \end{bmatrix}}_{x(k)} + \underbrace{\int_{0}^{T_s} e^{A\tau} B d\tau}_{Bq} v_i(k) + \underbrace{\int_{0}^{T_s} e^{A\tau} B_d d\tau}_{B_{dq}} i_0(k)$$

This model predicts the output voltage (v_c) for a given input voltage vector (v_i) . Predictive control is used to select the optimal voltage vector. To predict the output voltage (v_c) using expression (3.68), the output current (i_o) is required. This may be calculated by utilizing the equation (3.70).

$$i_0(k-1) = i_f(k-1) - \frac{c}{T_c} \left(v_c(k) - v_c(k-1) \right)$$
(3.70)

Assume $i_0(k-1) = i_0(k)$ for short sample intervals Ts, where load does not change considerably during each sampling interval

As shown in Fig.3.19, the output voltage $v_c(k)$, and the filter current $i_f(k)$, are used to estimate the output voltage at the next sampling period, $v_c(k+1)$, for all possible voltage vectors that the VSI may create.

To pick the ideal voltage vector v_i for the VSI, seven forecasts for $v_c(k+1)$ are compared using a cost function (g). The voltage vector (v_i) that reduces the cost function is chosen and the associated switching mode that reduces the cost function is used during the next sampling period. The stages below provide a summary of the control strategy. Outline a cost function. Create a model that contains all possible VSI switching states. Create a prediction model for the loads.

3.5 RESULTS AND DISCUSSION

A 12kW standalone hybrid PV-Wind system has been modelled in MATLAB/Simulink. Hybrid standalone system with proposed control algorithm is tested under transient conditions such as PV array irradiation variation, wind speed variations and different loading conditions. The behavior of the system is analyzed based on battery charging/discharging, DC bus voltage (V_{DC}), PCC voltage (V_{pcc}), battery power (P_{bat}), PV power (P_{PV}), load active power demand (Q₁).

The result evaluation of the hybrid system is carried out in two parts:

- 3.5.1 Performance evaluation of PV-BESS hybrid microgrid using proposed modified MPPT and inverter droop control.
- 3.5.2 Performance evaluation of PV-Wind-BESS hybrid microgrid using proposed modified MPPT and inverter droop Control

3.5.1 Performance evaluation of PV-BESS hybrid microgrid using proposed modified MPPT and inverter droop control.

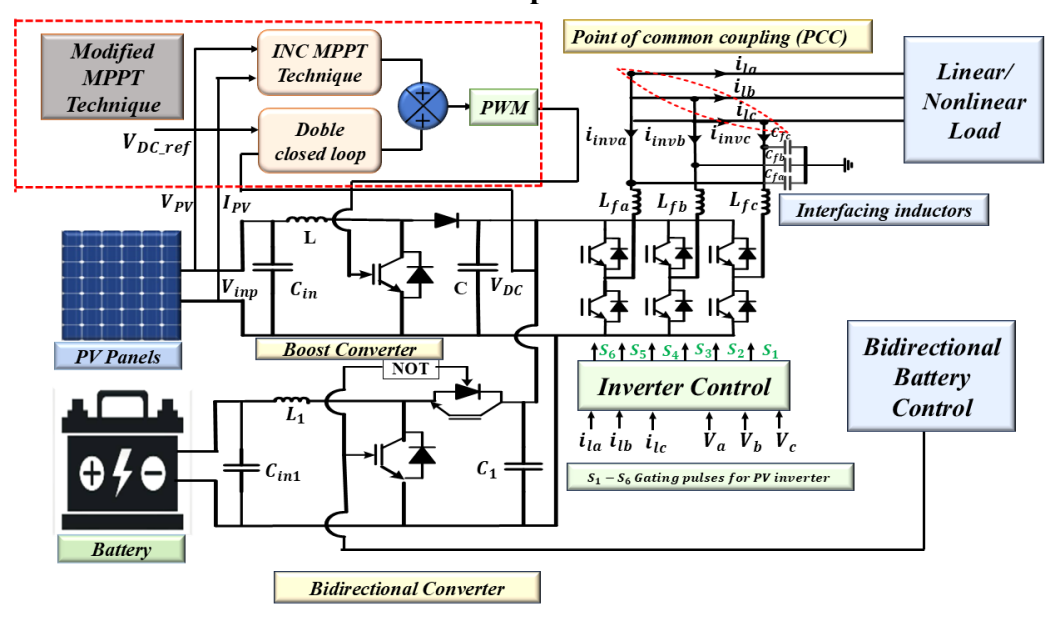


Fig.3.20 PV-BESS hybrid standalone microgrid

Schematic representation of the presented Hybrid Standalone PV-Battery system is illustrated in Fig.3.20 presented system mainly consists of three major components. The first is a solar energy conversion unit that consists of two stages: a boost converter and a voltage source inverter (VSI). The second is a battery storage system that includes a bidirectional converter. The third main component is different types of load coupling at PCC and LC filter which improve the overall efficiency of a photovoltaic system by reducing losses and harmonic induced by voltage fluctuations. Modified MPPT technique is used for maximum power tracking from SPV array. The uses of battery storage reduce the fluctuation in output power of the PV array, maintain DC

bus voltage and assists the network during peak load demand hours. This section presents a modified MPPT technique for maximizing the solar output power in a standalone PV battery system by regulating the DC-bus voltage.

- a. To improve the dynamic performances of hybrid standalone PV systems, a modified control technique that combines the incremental conductance (INC) technique with a double closed loop controller is proposed for tracking the maximum power from the PV source and maintaining the DC bus voltage.
- b. The different parameters of the presented system are investigated under various irradiation condition, linear/nonlinear load and balance/unbalanced load condition.
- c. The EN50530 MPPT efficiency test was carried out considering both fast and slow-varying irradiance levels to examine the effectiveness of the proposed control strategy. d. The standalone PV system is integrated with BESS through a bidirectional converter to maintain the nominal DC voltage conditions by charging/discharging
- converter to maintain the nominal DC voltage conditions by charging/discharging the battery due to intermittent solar photovoltaic (SPV) generation and also considering the BESS SOC constraints.
- e. Sinusoidal and balanced load current and voltage at point of common coupling (Vpcc) are maintained under nonlinear and unbalanced loading conditions. In addition, power balance among the battery, PV, and load is obtained.

The proposed modified control technique's superiority was demonstrated by comparing its performance to Incremental conductance (INC) MPPT, Perturb & Observe (P&O) MPPT, Particle Swarm Optimization (PSO), and Cuckoo Search Optimization (CSO)-based MPPT techniques under various load and irradiation conditions.

3.5.1.1 System response under different irradiation condition

In this case, the performance of the presented hybrid system under variable irradiation conditions is analyzed, as shown in the Fig 3.21. A linear load of 10kVA with 0.89 lag power factor (pf) is considered, simulated result and corresponding various parameters viz. V_{pcc}, I_{load}, P_{PV}, P_I, Q_I, P_{bat}, SOC and V_{DC} of the system are shown in Fig.3.21. It is observed from the figure voltage at point of common coupling (V_{pcc}) and I_{load} are found to be balanced and sinusoidal. Initially power generated from solar is 12kW and active load demand is 8.8kW which is fulfilled by solar PV and the excess power (3.2kW) produced from solar PV is utilized to charge the battery. Inverter is supplying reactive power demand of load and DC bus voltage is maintained at 750V as shown in Fig.3.21. Solar irradiance is reduced at t = 0.1s from 1000W/m^2 to 850 W/m^2 it reduces power generation of solar PV to 10kW, load demand is still 8.8kW which is supplied by PV and excess power (1.2kW) produced from solar module is utilized to charge the battery . Further solar irradiance is reduced to 650W/m^2 at t = 0.2 s, thus PV output power is also reduced to 8kW. In this condition deficit load power(1kW) demand is taken from the battery hence battery is discharging in this condition also DC bus voltage is maintained at 750V. Corresponding SOC graph of the battery is presented in Fig. 3.21.

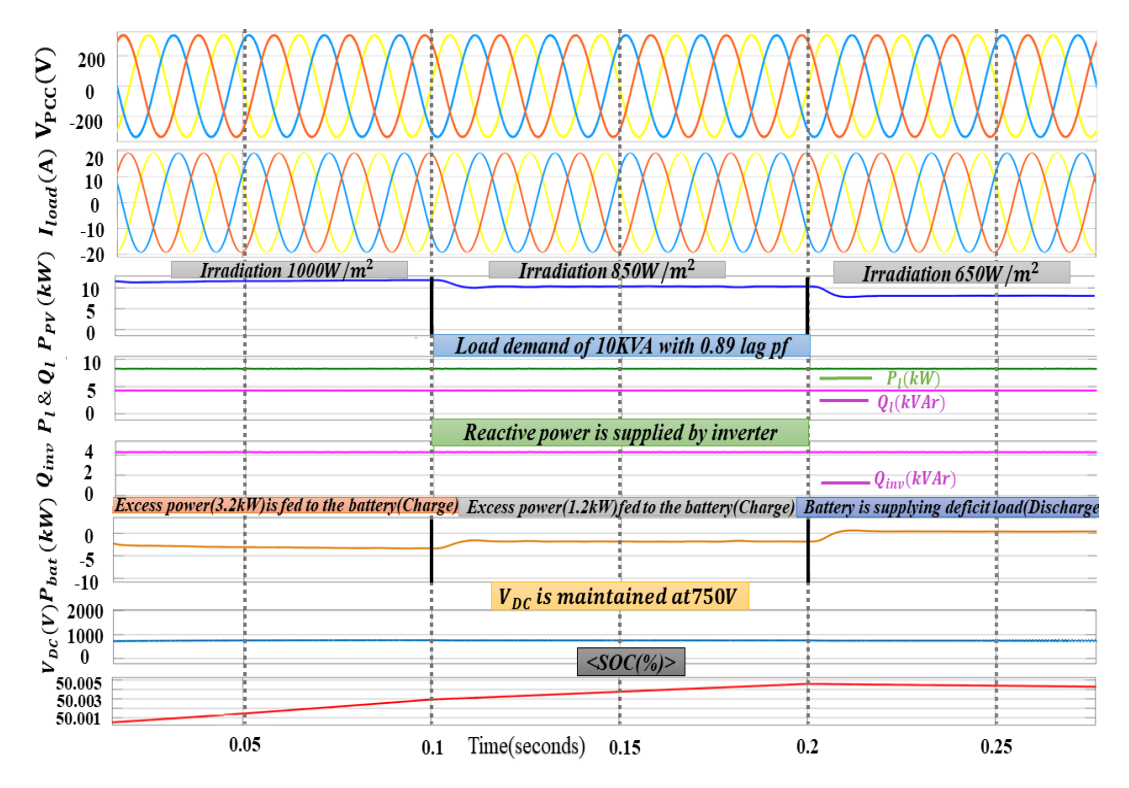


Fig.3.21 Waveform under linear load and irradiation variation

3.5.1.2 System response under load varying condition

In this case, performance of the proposed hybrid system for variable linear load is analyzed as shown in Fig.3.22. Solar PV generate 12 kW active power at 1000W/m^2 irradiation. Initially load demand is 10 kVA with 0.89 lag pf which means active power load demand is 8.8 kW and power generated from PV is 12 kW. Surplus power load (3.2kW) produced from solar photovoltaic module is used to charge the battery and inverter is supplying reactive power. Voltage at PCC (V_{pcc}) and load current (I_{load}) are balanced and sinusoidal. DC bus voltage has been maintained at 750V.

At t=0.15s solar irradiation is 1000W/m^2 so the power generated from the PV is 12 kW while load demand is increased to 14.38 kW. Now the remaining power (2.38 kW) is taken from the battery as depicted in fig.3.22. to provide constant power to the load. From the Fig.3.22. It can be observed that system is stable and balance during load variable and also during battery charging and discharging condition. Voltage at PCC (V_{pcc}) and load current (I_{load}) are sinusoidal and balanced. The DC bus voltage remains constant at 750V.

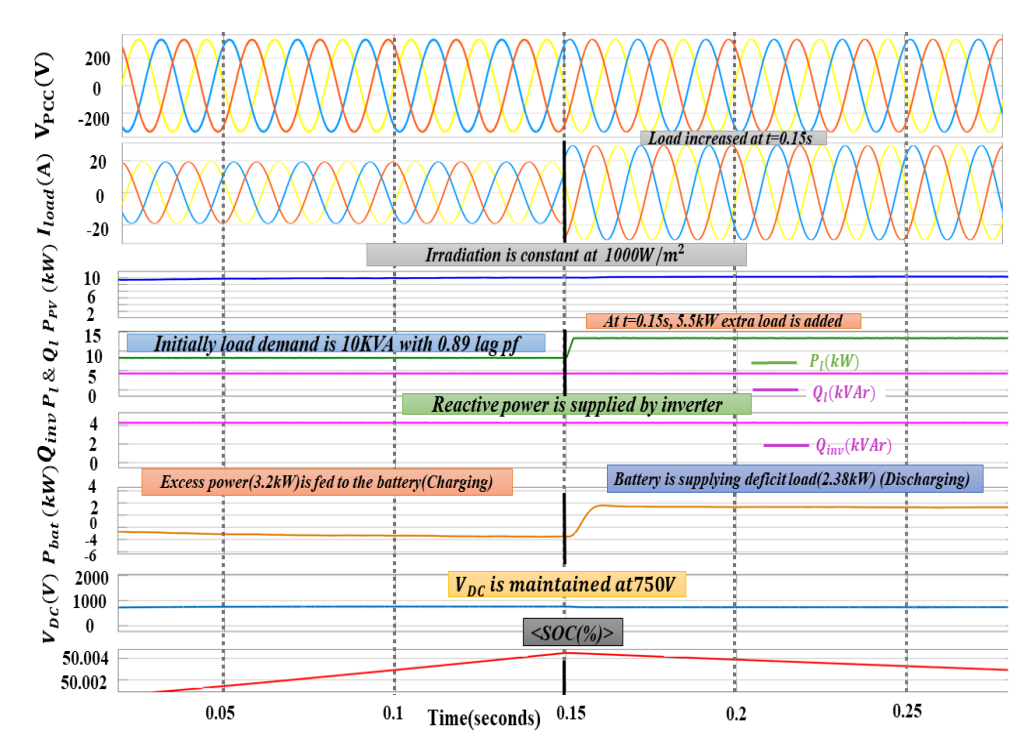


Fig.3.22 Waveform under load variation

3.5.1.3 System response under variable nonlinear load condition

Fig.3.23. depict the system's performance under nonlinear load (3-phase bridge rectifier with $R=200\Omega$, L=0.1H). PV generates 12kW active power at $1000W/m^2$ irradiation and the power load demand from is 1.6kW which is supplied by PV. The excess power generated from SPV is utilized to charge the battery as presented in fig. Voltage at point of common coupling is balanced and sinusoidal.

At t=0.15s an extra load of 5kVA with 0.89 lag pf is added. Solar irradiation is 1000W/m² so the power generated from the PV is 12kW while load demand is increased to 6.03 kW. So, excess power (5.57kW) produced from solar PV is utilized to charge the battery and inverter is supplying reactive power.

From Fig.3.23, shows the voltage at PCC (V_{pcc}) and load current (I_{load}) are balanced and sinusoidal even under non-linear load variation condition. DC bus voltage remains constant at 750V.

3.5.1.4 System response under unbalanced load condition

In this case performance analysis of a proposed system under nonlinear unbalanced load conditions has been done. Fig.3.24. shows response the presented system under unbalanced load condition (one line of the nonlinear load is disconnected for time interval t=0.15s-0.25s). In this condition also it can be observed that voltage at point of common coupling (V_{pcc}) is balanced and sinusoidal. Power load demand is met by solar photovoltaic module and excess power produced from solar photovoltaic is utilized to charge the battery as depicted in Fig.3.24. DC bus voltage (V_{DC}) is maintained at 750V.

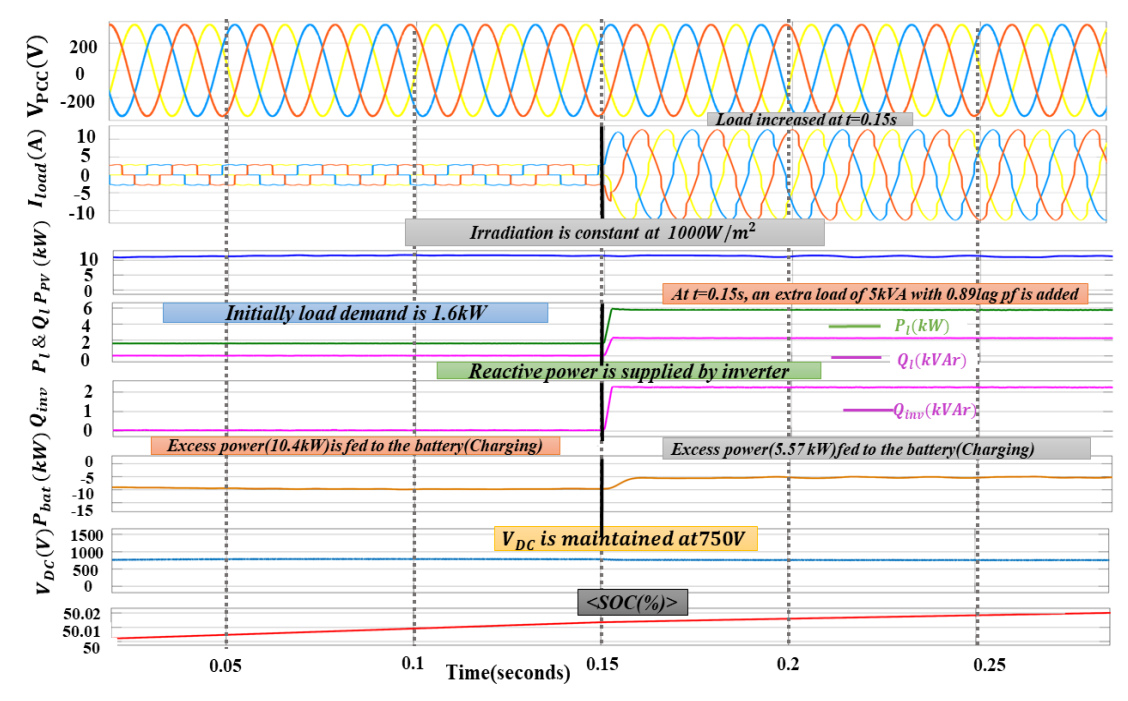


Fig.3.23 Waveform under nonlinear load condition

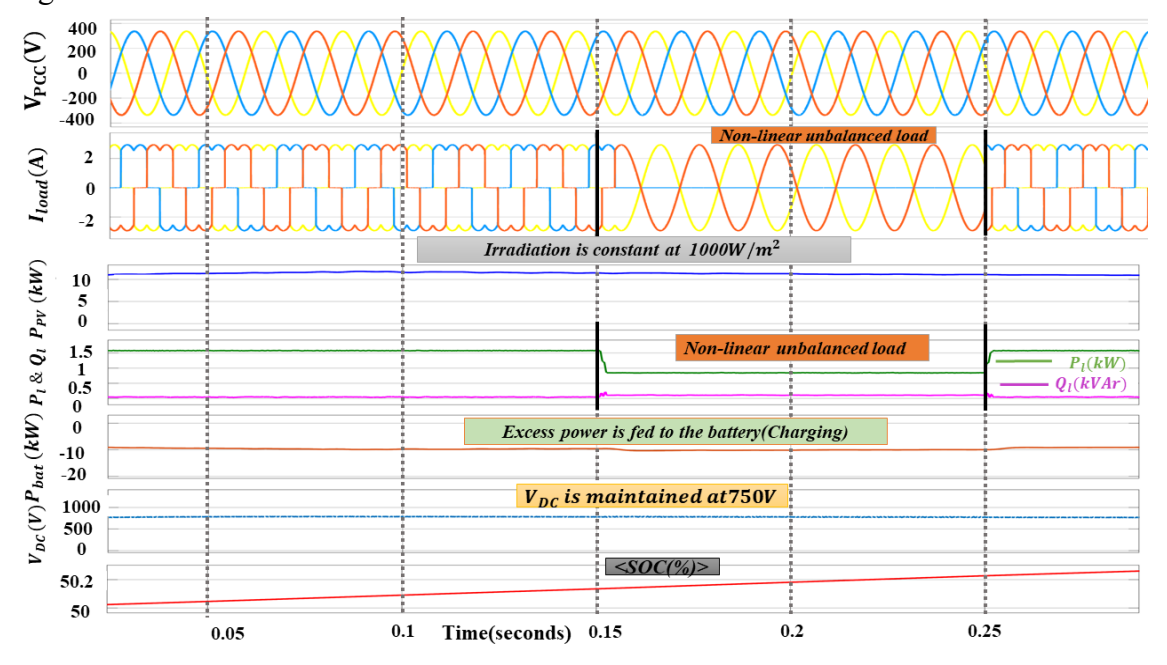


Fig.3.24 Waveform under nonlinear unbalance load condition

3.5.1.5 Comparison of PV power output at different irradiance using proposed modified MPPT technique and existing control techniques

Fig.3.25 illustrates a solar PV module's transient response and maximum power tracking under different irradiation conditions The variation in the irradiation intensity of the solar PV module for the selected time period. is shown in Table 3.1. Table 3.1 and Fig.3.25. make this evident compared to P&O, INC, PSO, and CSO MPPT controllers, the proposed enhanced MPPT controllers track more power and exhibit no oscillation.

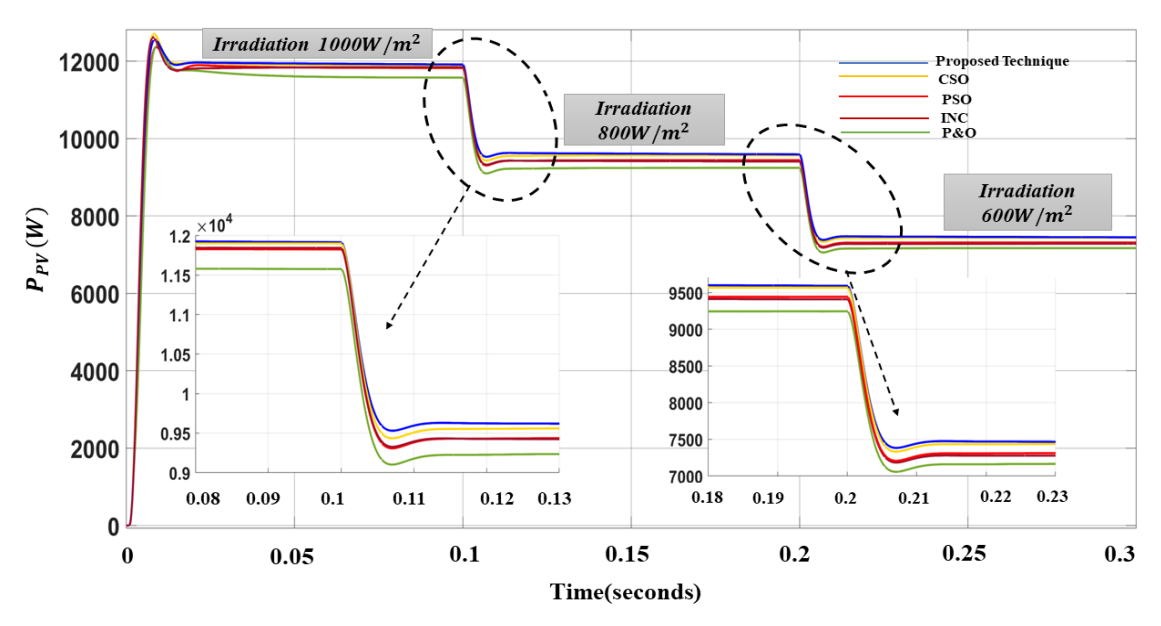


Fig.3.25 Transient response of PV power output for nonlinear load under various irradiation conditions

Table 3.1. Comparison of proposed modified MPPT technique at different irradiation using P&O, INC, PSO, and CSO based MPPT techniques

S.	Control Techniques	Time(second	Irradiation	Power
No		s)		Tracked(kW)
1.		0.0s - 0.1s	1000W/m^2	11.48
	P&O	0.1s -0.2s	800W/m^2	09.47
		0.2s -0.3s	600W/m^2	07.13
2.		0.0 s - 0.1s	1000W/m^2	11.52
	INC	0.1s -0.2s	800W/m^2	09.37
		0.2s -0.3s	600W/m^2	07.22
3.		0.0s - 0.1s	1000W/m ²	11.82
	PSO	0.1s -0.2s	800W/m^2	09.46
		0.2s -0.3s	600W/m^2	07.32
4.		0.0 s - 0.1s	1000W/m^2	11.87
	CSO	0.1s -0.2s	800W/m^2	09.52
		0.2s - 0.3s	600W/m^2	07.49
5.	Proposed modified	0.0 s - 0.1s	1000W/m^2	11.97
	Technique	0.1s -0.2s	800W/m^2	09.69
	(INC technique with	0.2s-0.3s	600W/m ²	07.64
	double closed loop controller)			

3.5.1.6 Comparison of transient response of DC bus voltage on different irradiation using proposed modified MPPT technique and existing control techniques

The transient response of DC bus voltage for P&O, INC, PSO, CSO and proposed modified MPPT controller is as shown in Fig.3.26 Table 3.2 describes the graph. Fig. 3.26 exhibits the superior performance of the proposed MPPT technique over the other compared MPPT techniques. The behavior of the system under irradiation variation has been studied. DC bus voltage settling time and undershoot is smaller in the case of the proposed control technique than other compared techniques.

Table. 3.2 Transient assessment of DC voltage for nonlinear loads with P&O, INC, PSO, CSO and proposed modified controller on different irradiation

S.No	Control Techniques	Time (seconds)	Irradiatio n	Settling Time	DC bus voltage	Remarks
1.	P&O	0.0s - 0.1s	1000W/m ²	0.08s	750V	Overshoot of 100V and oscillation present
		0.1s -0.2s	800W/m ²	0.07s	750V	Undershoot of 25V present
		0.2s -0.3s	600W/m ²	0.07s	750V	Undershoot of 15V present
2.	INC	0.0 s - 0.1s	1000W/m ²	0.07s	750V	Overshoot of 8V, Undershoot of 20Vand oscillation present
		0.1s -0.2s	800W/m ²	0.07s	750V	Undershoot of 24 V present
		0.2s -0.3s	600W/m ²	0.06s	750V	Undershoot of 15V present
3.	PSO	0.0s - 0.1s	1000W/m ²	0.06s	750V	Overshoot of 110V present
		0.1s -0.2s	800W/m ²	0.07s	750V	Undershoot of 22 V present
		0.2s -0.3s	600W/m ²	0.06s	750V	Undershoot of 15V present

4.	CSO	0.0 s - 0.1s	1000W/m ²	0.02s	750V	Overshoot of 38V present
		0.1s -0.2s	800W/m ²	0.06s	750V	Undershoot of 15 V present
		0.2s - 0.3s	600W/m ²	0.05s	750V	Undershoot of 8V present
5.	Proposed Modifies	0.0 s - 0.1s	1000W/m ²	0.01s	750V	Overshoot of 40V present
	MPPT Technique (INC	0.1s -0.2s	800W/m ²	0.01s	750V	Undershoot of 3V present (negligible)
	technique with double closed loop controller)	0.2s-0.3s	600W/m ²	0.01s	750V	Undershoot of 3V present(negligible)

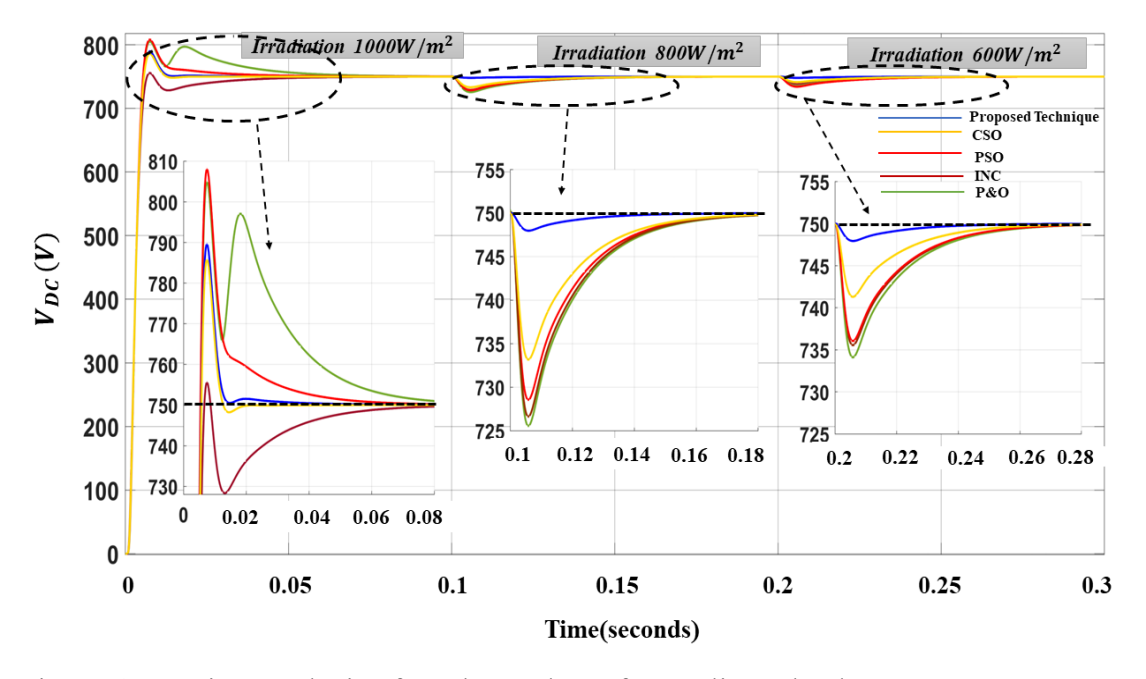


Fig.3.26 Transient analysis of DC bus voltage for nonlinear load

3.5.1.7 Comparison of MPPT Efficiency test EN50530 using developed and existing control techniques

One of the standard testing conditions applied to a standalone PV system is the EN50530 MPPT efficiency test, which evaluates the MPPT algorithm's performance under dynamically varying circumstances

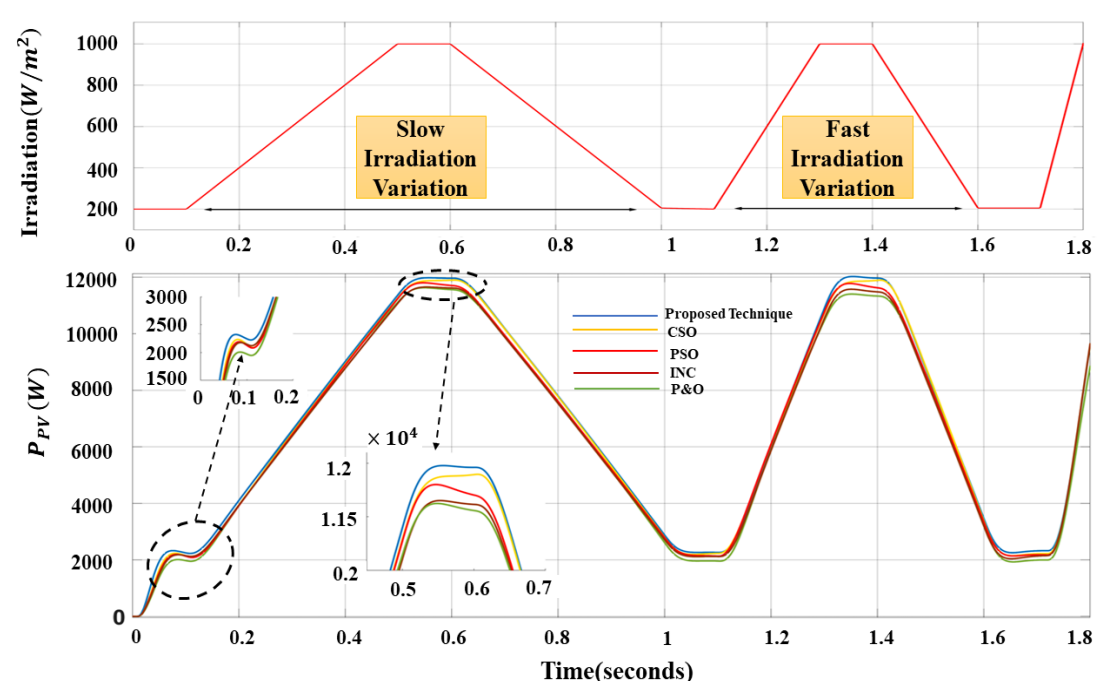


Fig.3.27 PV power output waveform of different MPPT algorithms for MPPT EN50530 efficiency test

In this specific case, we conducted an analysis of the MPPT techniques under dynamic changes in irradiance level, accounting for both fast and slow variations.

We employed the trapezoidal signal to design the slow and fast irradiance levels, as shown in Fig.3.27. The MATLAB 2023a simulation environment was used to analyse the power achieved by all MPPT methods based on irradiance level variations. Fig.3.27 illustrates the maximum power generated by various MPPT algorithms during the EN50530 efficiency test. Fig.3.27 and Table.3.3 shows that among all MPPT techniques, the proposed modified MPPT achieves the highest power. The proposed MPPT technique performs extremely well at lower levels of irradiance, as demonstrated by the blue colour curve. This is also evident for the proposed MPPT, which functions most effectively at higher levels of irradiance.

Table 3.3. Maximum power obtained using MPPTs at various time intervals

S.No.	Control Techniques	$P_{max}(kW)$ at $(0.0-0.1 \text{sec})$	P _{max} (kW) at (0.4-0.5sec)	P _{max} (kW) at (1.3-1.4sec)
1.	P&O	2.01	11.54	11.53
2.	INC	2.10	11.55	11.55
3.	PSO	2.11	11.62	11.60
4.	CSO	2.13	11.81	11.81
5.	Proposed Modified Technique	2.20	11.95	11.95

3.5.2 Performance evaluation of PV-Wind-BESS hybrid microgrid using proposed modified MPPT and inverter droop Control

Fig.3.28 depicts a hybrid microgrid system with wind, photovoltaic (PV), and battery energy storage components that operate in parallel with an inverter. This configuration integrates renewable energy sources (RES) and energy storage to provide linear and nonlinear loads via point of common coupling (PCC). To ensure optimal power extraction from wind and PV systems, the proposed modified MPPT technique is utilized. The system employs droop control to ensure synchronized and steady power sharing between the parallel inverters linked with the wind and PV modules. Furthermore, a bidirectional DC-DC converter is integrated between the battery and the DC link to govern the bidirectional flow of energy, allowing for both charging and discharging operations according to system requirements.

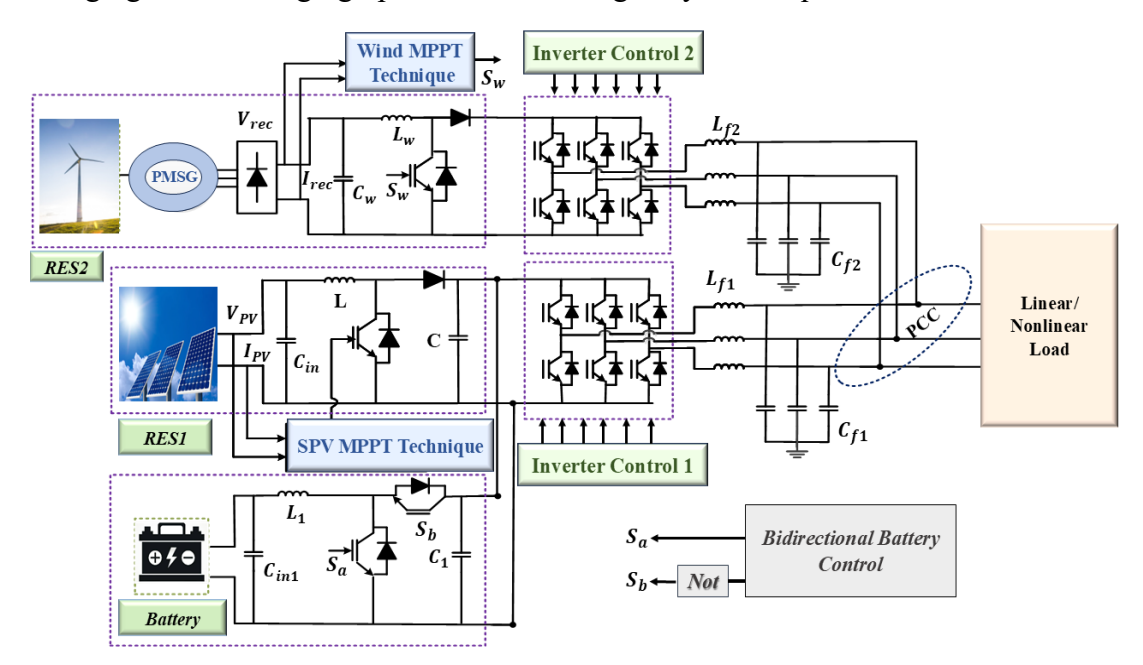


Fig.3.28 PV-Wind-BESS hybrid standalone microgrid

3.5.2.1 System response under battery charging condition

Fig.3.29 depicts system performance during battery charging conditions. A linear load of 20 kVA with 0.9 lag pf (18kW and 8.717Kvar) was examined. The SPV and wind subsystems produce 11.97 and 9.38 kW, respectively, for a total of 21.35 kW. Surplus power of 3.35 kW is used to charge batteries efficiently. In this scenario, the voltage at the point of common coupling (Vpcc) is balanced and sinusoidal. Solar photovoltaic module and wind power generation meet power load need, and excess power from photovoltaic and wind is utilized to charge the battery, as shown in fig.3.29. The DC bus voltage (VDC) is kept at 750 V.

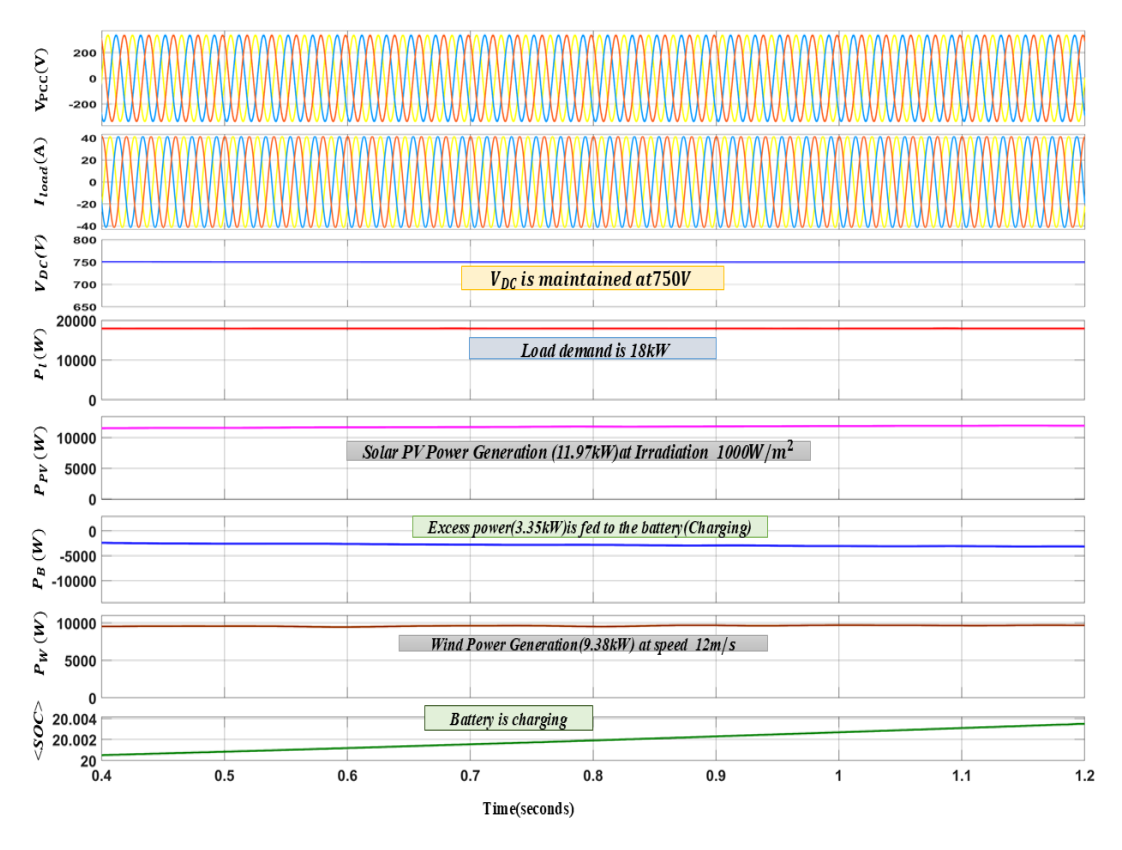


Fig.3.29 Waveform under battery charging conditions

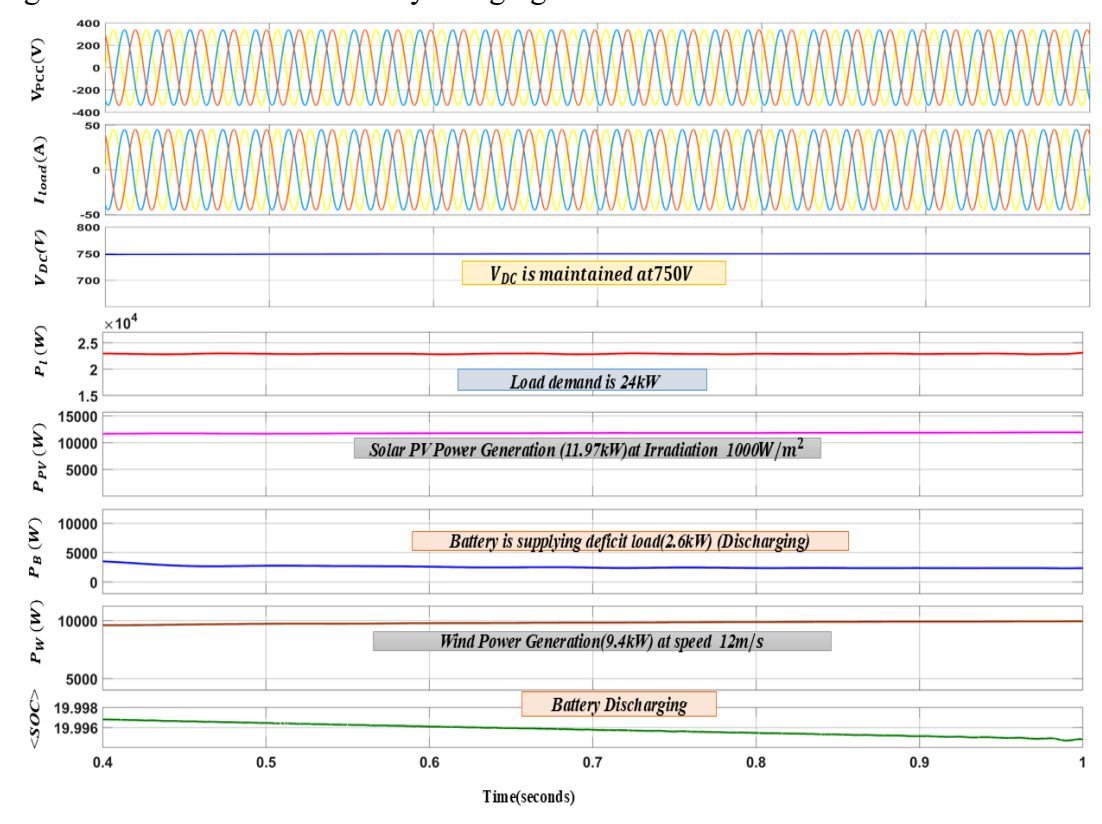


Fig.3.30 Waveform under battery discharging condition

3.5.2.2 System response under battery discharging condition

Fig. 3.30 demonstrates system performance under battery discharge situations. A linear load of 24 kW is tested. The SPV and wind subsystems generate 11.97 and 9.38 kW, for a total of 21.35 kW. To meet the power shortfall, the battery discharge 2.57 kW while maintaining a constant DC bus voltage of 750V. In this case, the voltage at the point of common connection (Vpcc) is balanced and sinusoidal. The battery compensates for the deficiency by discharging 2.57 kW to meet the overall load. The DC bus voltage (VDC) is kept at 750 volts.

3.5.2.3 System response under non-linear variable load condition $I_{load}(A)$ $V_{DC}(V)$ 700 V_{DC} is maintained at750V $P_l(W)$ 1.8 oad demand is 15.5kW Load demand is 18.5kW $P_{PV}(W)$ Solar PV Power Generation (11.97kW) at Irradiation 1000W/m² 5000 $P_B(W)$ -5000 Excess power(5.8kW) is fed to the battery(Charging) Excess power(2.85kW)is fed to the battery(Charging) -10000 Wind Power Generation(9.38kW) at speed 12m/s 8000 20.004 20.002 Time(seconds)

Fig.3.31 Waveform under non-linear variable load condition

Fig.3.31. depict the system's performance under nonlinear load (3-phase bridge rectifier with $R=20\Omega$, L=100mH). The solar PV (SPV) and wind energy subsystems contribute 11.91 kW and 9.38 kW, respectively, resulting in a total generation of 21.35 kW. Initially, the load demand is 15.5 kW, leading to a surplus of 5.8 kW, which is utilized to charge the battery energy storage system. At t=0.6s an additional 3 kW load is introduced, increasing the total demand to 18.5 kW. Despite the increased demand, the total generation still exceeds the load, allowing a reduced surplus of 2.85 kW to continue charging the battery. As shown in Figure 3.22, the voltage at the point of common coupling (V_{pcc}) and the load current (I_{load}) remain balanced and sinusoidal, even under nonlinear loading conditions. Furthermore, the DC bus voltage is effectively regulated at a constant level of 750 V, confirming the robustness of the control strategy under dynamic and nonlinear load variations.

3.5.2.4 System response under variable irradiation condition

Fig.3.32 depicts the system response under variable irradiation condition. A 18 kW load is used to evaluate the hybrid SPV-wind microgrid under dynamic solar irradiance. At 1000 W/m², the SPV provides 11.97 kW, while the wind turbine supplies 9.38 kW, for a total of 21.35 kW. The additional 3.35 kW is utilized for battery charging. After 0.5 seconds, the solar irradiance drops to 600 W/m², resulting in a reduced SPV output of 7.5 kW. With wind power at 9.38 kW, total generation drops to 16.88 kW. As the load remains at 18 kW and generation decreases, a 1.2 kW shortfall occurs. The battery quickly switches from charging to discharging mode, effectively bridging the gap and providing continuous power supply. Despite a significant decline in solar irradiation, the system maintains a steady DC bus voltage

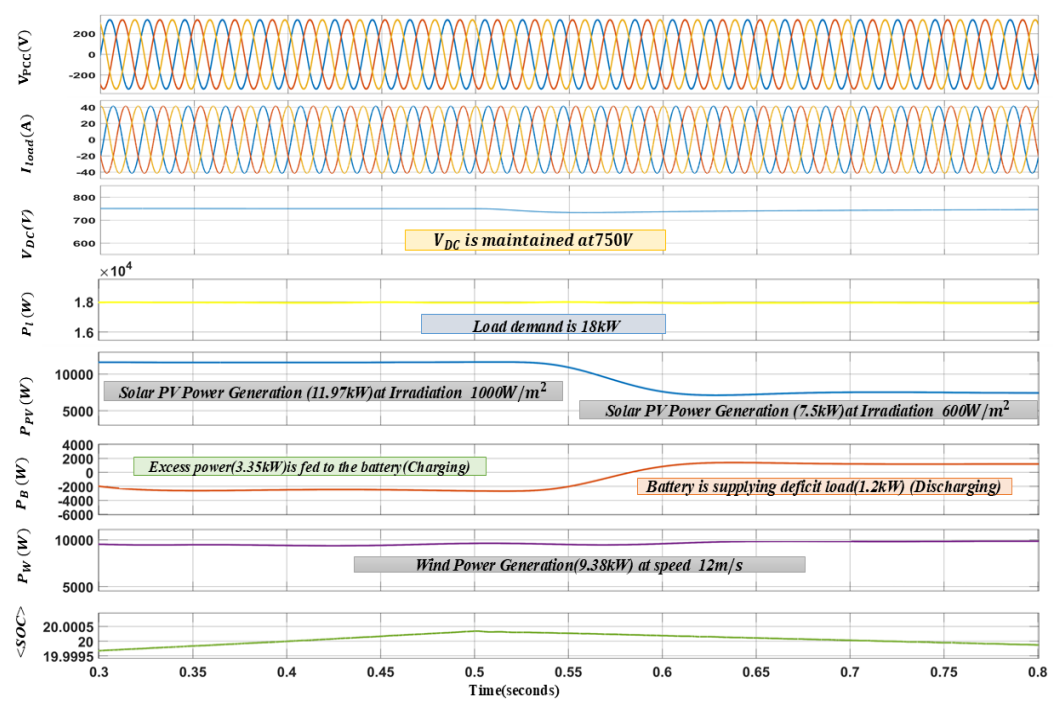


Fig.3.32 Waveform under variable irradiation condition

3.5.2.5 System response under variable wind speed condition

Fig.3.33 depicts the system performance under variable wind condition. The system's performance is evaluated under a constant load of 16 kW, with a fixed solar irradiance of 1000 W/m² and variable wind speed. Initially, the solar and wind subsystems generate 11.97 kW and 9.38 kW, respectively, resulting in a total power output of approximately 21.35 kW. Since the load demand is only 16 kW, the surplus power of 5.3 kW is utilized to charge the battery, placing the system in battery charging mode. However, at 0.5 seconds, a sudden drop in wind speed to 8.4 m/s reduces the wind power output to 4.5 kW. With solar generation remaining stable, the combined available power becomes 16.43 kW. As this value still slightly exceeds the load demand, the battery continues to charge, albeit at a reduced rate.

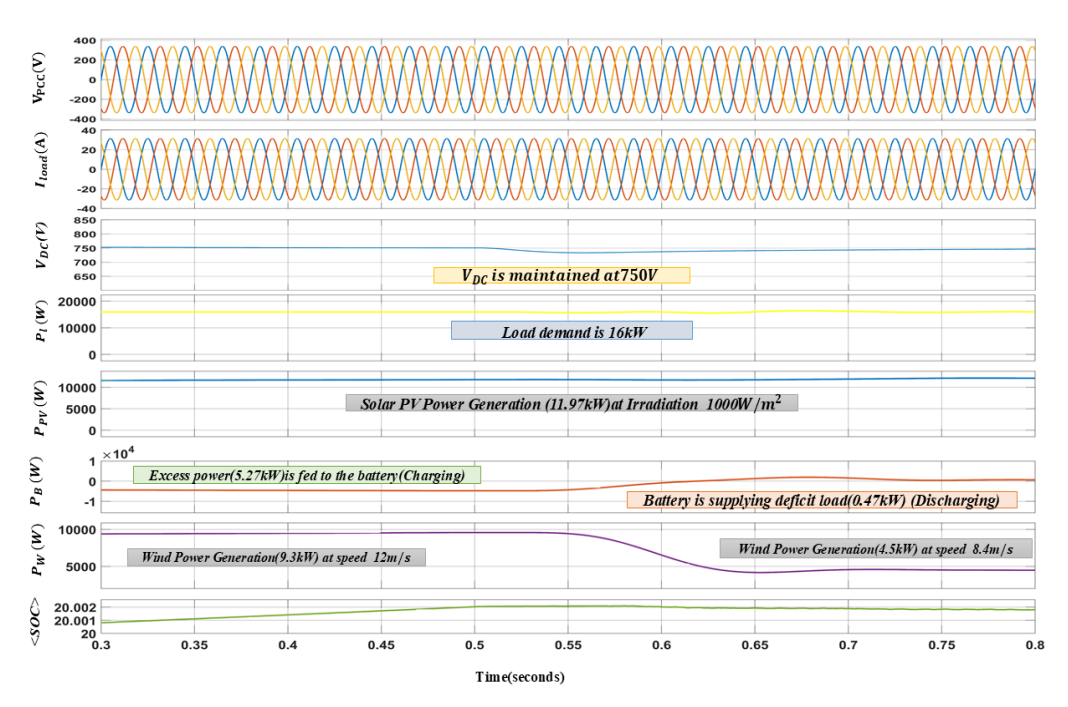


Fig.3.33 Waveform under variable wind speed condition

3.5.2.6 Comparative analysis of transient response of DC bus voltage under variable wind speed using proposed and existing control techniques

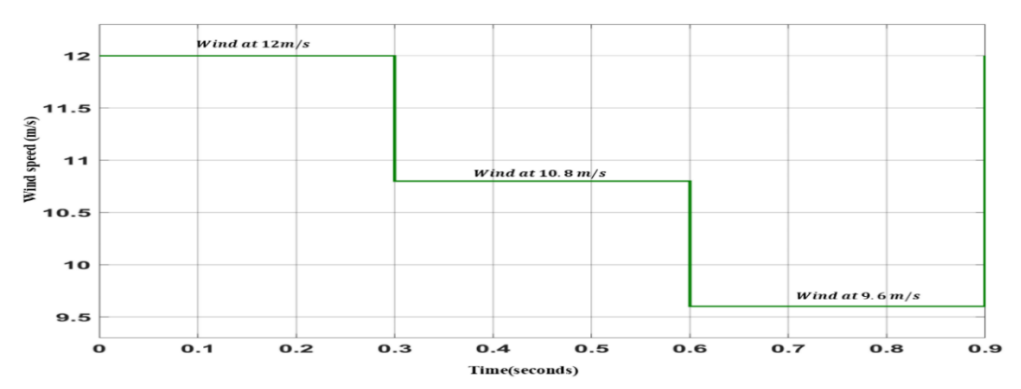


Fig.3.34 Variable wind speed

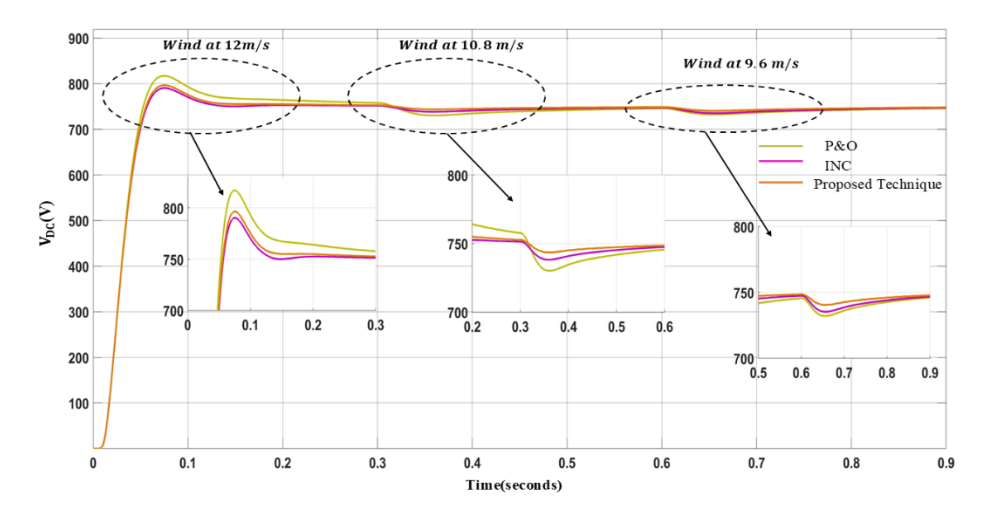


Fig.3.35 Transient response of DC bus voltage under variable wind speed

The dynamic performance of the DC link voltage is analyzed under different wind speed conditions—12 m/s, 10.8 m/s, and 9.6 m/s—using three MPPT techniques: P&O, INC, and the proposed method as shown in fig.3.35. At a wind speed of 12 m/s, all techniques initially show a sharp rise in V_{DC} , with the proposed technique achieving a faster settling time and minimal overshoot compared to P&O and INC. As the wind speed drops to 10.8 m/s, noticeable fluctuations occur in the voltage profiles of P&O and INC, indicating poorer dynamic response and slower convergence. In contrast, the proposed technique maintains a more stable voltage with reduced undershoot and quicker voltage recovery. At the lowest wind speed of 9.6 m/s, the performance gap becomes more apparent; the proposed method consistently regulates the DC link voltage closer to the desired level with minimal ripple, while both P&O and INC show more deviation and slower recovery. Overall, the proposed MPPT technique outperforms conventional methods by offering improved voltage stability, faster transient response, and better adaptability under varying wind conditions.

3.5.3 Performance evaluation and result discussion using proposed modified MPPT technique and Model Predictive Control technique for inverter

Fig.3.36 Schematic diagram of hybrid standalone PV microgrid with MPC controller MATLAB simulation results for a hybrid standalone PV microgrid are presented to validate the inverter's Model Predictive Control (MPC) technique and compare its performance with a droop controller. A 12-kW solar PV system is used, with a three-phase bridge rectifier (R = 180 Ω , L = 200 mH) representing a nonlinear load. The simulations include three-phase waveforms for load current (I_0), load voltage(V_0), PV power (P_{pv}), battery power (P_{bat}), load active power (P), reactive power (Q), DC bus voltage (V_{DC}), and state of charge (SOC), demonstrating performance under linear and nonlinear load conditions.

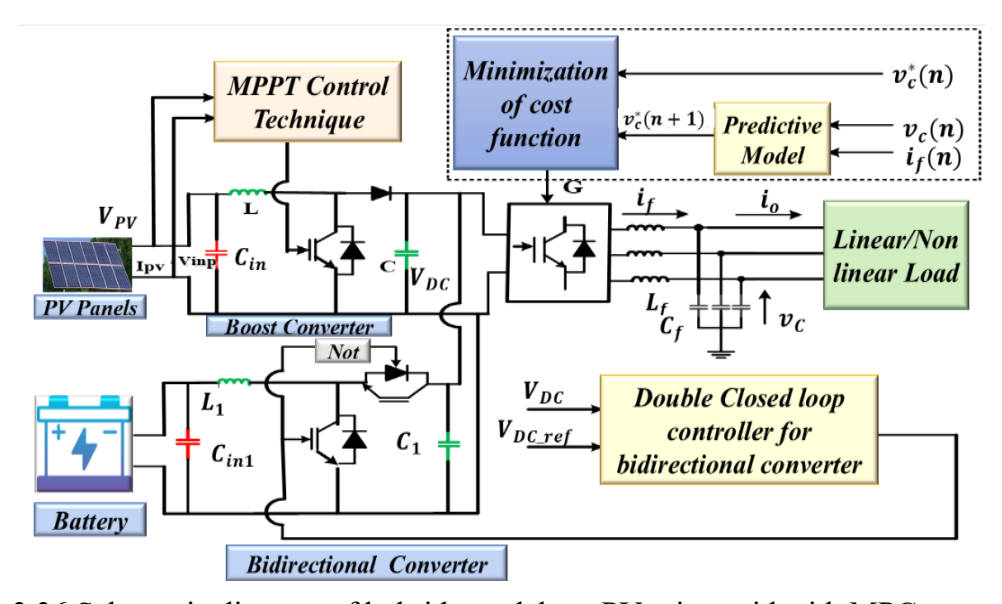


Fig. 3.36 Schematic diagram of hybrid standalone PV microgrid with MPC controller

3.5.3.1 System response under variable linear load demand

The system's performance under varying linear load conditions is assessed using the MPC control technique. Initially, the load demand is 10 kVA (8 kW, 4.8 kVAr) with a 0.8 lagging power factor, which rises to 14 kW after 0.4 second. Initially, the solar PV fulfils the load demand (8 kW), and the excess power (4 kW) charges the battery. The battery discharges after 0.4 seconds due to increased load demand, supplying the 2-kW deficit power. Throughout, the voltage and current are sinusoidal and balanced, the DC bus voltage is constant at 750 V, and the power balance between the solar PV, load, and battery is maintained, as illustrated in Fig.3.37.

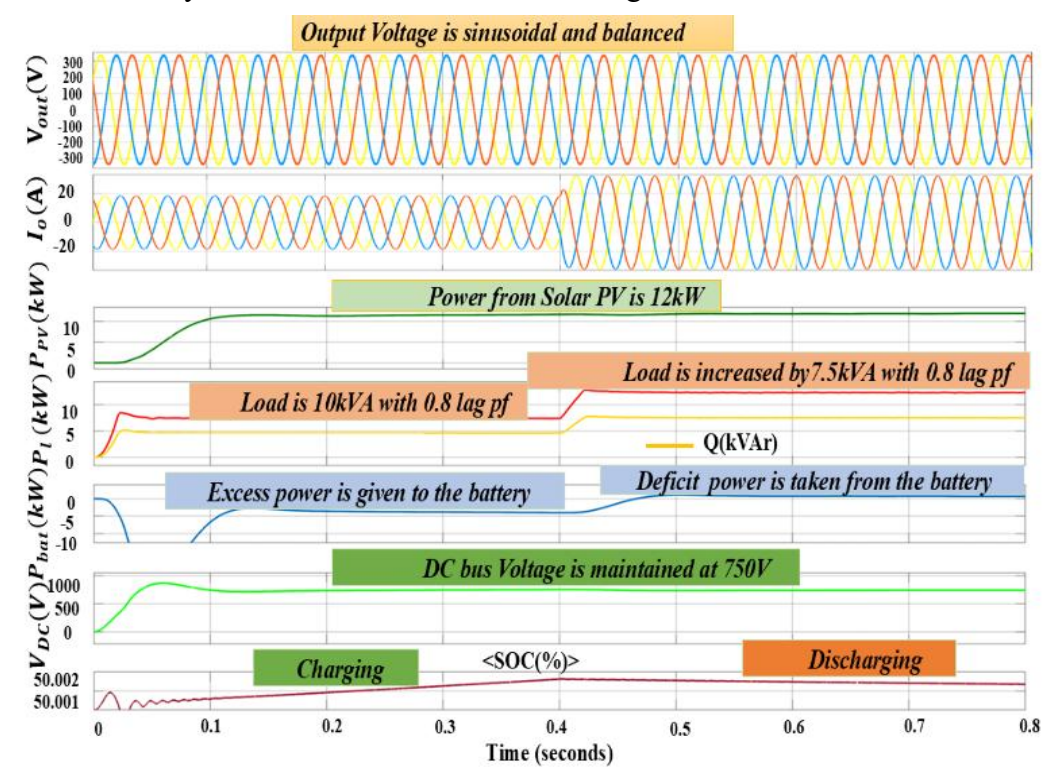


Fig.3.37 System response under variable linear load demand

3.5.3.2 System response under variable non-linear load demand

The system's performance with MPC is investigated under varying non-linear load conditions as shown in fig.3.38. To begin, a non-linear load (bridge rectifier with RL load R = 180 Ω , L=200mH) is applied. After 0.4 seconds, an additional load of 7.5 kVA (6 kW, 3.6 kVAr) with a 0.8 lagging power factor is added. Initially, solar PV satisfies load demand while excess electricity charges the battery. After 0.4 seconds of increased load demand, the PV continues to supply the load while any excess power generated is used to charge the battery.

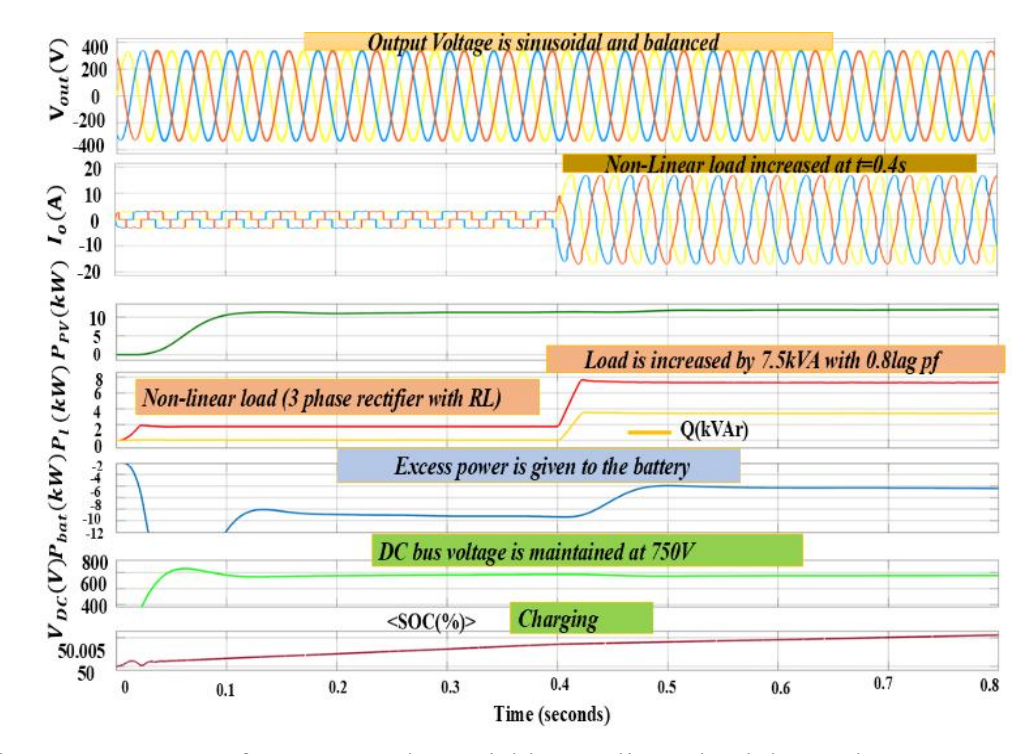


Fig.3.38 System performance under variable non-linear load demand

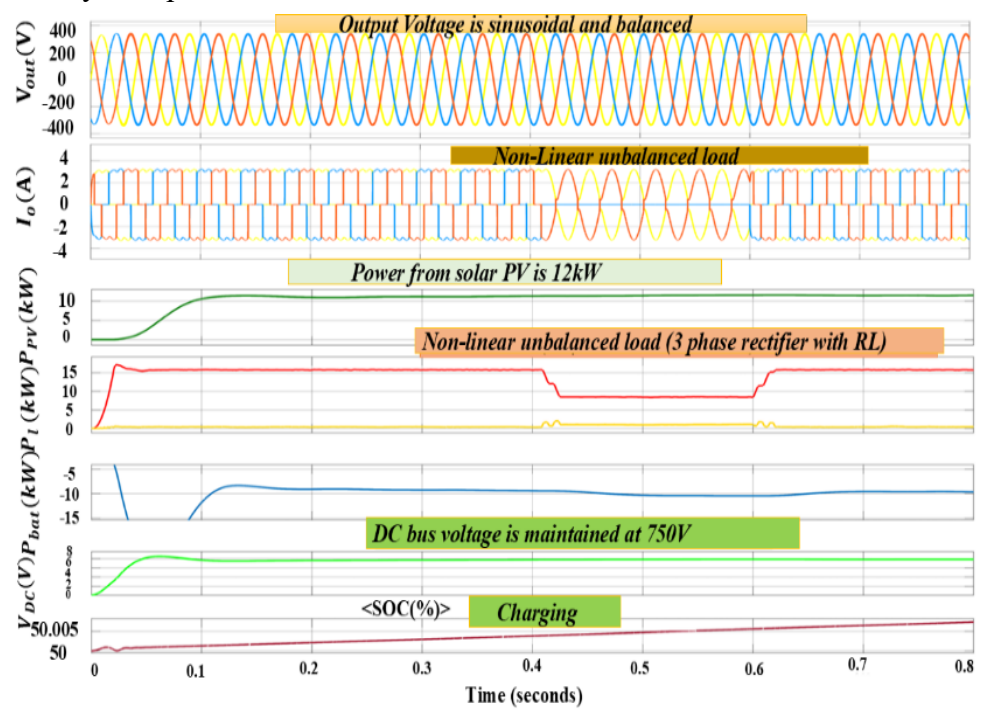


Fig.3.39 System performance under unbalance non-linear load demand

3.5.3.3 System response under unbalanced non-linear load demand

This section evaluates the network's performance with MPC under imbalanced load conditions. Disconnecting a single phase of the load current results in load unbalancing for 0.4 to 0.6 seconds as shown in Fig.3.39. It has been found that even under these conditions, the voltage and current are balanced and sinusoidal.

3.5.3.4 Comparative analysis of Droop controller and Model Predictive Control techniques with the proposed modified MPPT technique

Fig.3.40(a) and 3.40(b) show a performance comparison of total harmonic distortion (THD) and DC bus voltage using Model Predictive Control (MPC) and a droop controller. Table.3.4 and Fig.3.40show that MPC has less harmonic distortion than droop controller. Additionally, Fig.3.40 shows that DC bus voltage is maintained at 750 V with MPC, whereas 739V is used with droop controller.

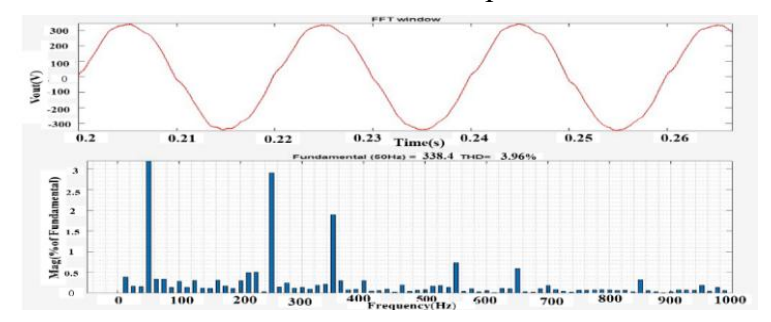


Fig.3.40(a) Harmonic Spectrum of output voltage using droop controller for non-linear load

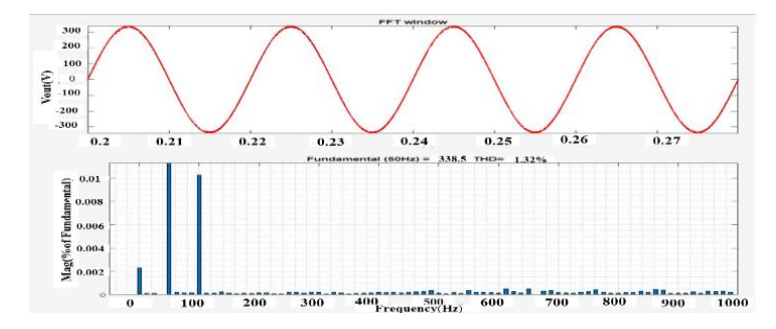


Fig.3.40(b) Harmonic Spectrum of output voltage using MPC for non-linear load

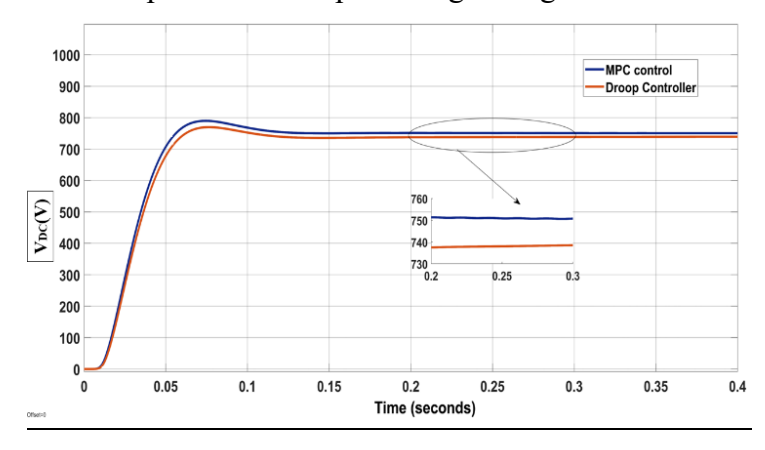


Fig.3.41 DC bus voltage response of non-linear load using droop controller and MPC

Table. 3.4 Comparison of THD of output voltage using droop controller and MPC with the proposed MPPT technique

	THD % of Load Output voltage			
System Parameter	Droop Contro ller	Model Predictive Control (MPC)		
Linear load	2.93	1.12		
Non-Linear Load	3.96	1.32		
Unbalanced Load	3.83	1.24		

3.6 SCALABILITY AND COST IMPLICATION OF DOUBLE CLOSED LOOP MPPT WITH INCREMENTAL CONDUCTANCE

The Double Closed Loop MPPT with Incremental Conductance (INC) is a control strategy that combines the robustness of closed-loop PI regulation with the adaptability of the INC algorithm for solar PV systems. The outer voltage loop ensures stable DC-link regulation, while the inner current loop tracks the PV operating point. This hybrid structure enhances dynamic response and stability, especially under irradiance fluctuations.

Hardware: Requires only basic voltage and current sensors plus a microcontroller or DSP with low computational overhead. Unlike ANN, no large training datasets are needed.

Algorithmic Load: Computationally lightweight — complexity is O (1) per step. This makes it easily scalable even for multiple PV strings without heavy hardware.

System Size: Double Closed Loop + INC is practical for small-scale rural PV microgrids (5–20 kW) because of its simplicity. It is also suitable for industrial-scale PV but may be less effective under partial shading compared to ANN.

The proposed PI-based control with INC+ Double Closed Loop offers very low CAPEX, as it relies on inexpensive microcontrollers and standard voltage-current measurements, making the cost negligible in both rural and industrial applications. OPEX is also minimal since tuning can be handled locally without retraining or software updates. In rural microgrids, this method provides cost-effective scalability and modest energy gains, making it attractive for low-income, low-infrastructure settings. In industrial systems, it enhances bus voltage regulation and system stability at scale, though its limited capability under complex shading reduces efficiency compared to ANN-based approaches.

3.7 CONCLUDING REMARKS

In this chapter a modified MPPT control technique, which includes Incremental conductance (INC) algorithm with double closed loop controller technique for hybrid standalone microgrid to regulate the DC bus voltage and to track the maximum power from solar PV under different atmospheric conditions has been developed. The effectiveness of the proposed modified MPPT technique in both steady state and transient conditions is demonstrated by the simulation results. EN50530 MPPT test is also carried out to test the efficacy of proposed MPPT control strategy. The point of common coupling voltage (Vpcc) has been found to be sinusoidal and balanced. The result shown that the proposed modified MPPT control strategy works well under linear/nonlinear and balanced unbalanced load. The voltage across DC bus has been maintained constant under different irradiation and variable load condition. Also, the continuous power to the load has been supplied by solar PV system and by battery energy storage system as per load requirement. To illustrate the superiority of the proposed MPPT technique, the proposed technique's results are compared with P&O, INC, PSO and CSO based MPPT control techniques. The proposed control techniques give better control of DC bus voltage in terms of undershoot, overshoot oscillation and settling time.

Furthermore, this chapter also examines inverter control techniques, with a particular emphasis on Droop Control and Model Predictive Control (MPC). A comparative assessment reveals that the MPC approach demonstrates superior dynamic performance, outperforming conventional control methods under various operating conditions.

CHAPTER-4

MPPT CONTROL TECHNIQUES FOR GRID INTEGRATED SOLAR PV BASED MICROGRID

4. 1 INTRODUCTION

In the previous chapter, the focus was on Maximum Power Point Tracking (MPPT) and inverter control strategies for standalone solar PV systems. These systems work independently of the grid, making them ideal for remote regions without access to traditional power networks. The control algorithms mentioned intended to maximize power output from the PV array while efficiently managing load changes via inverter regulation.

However, with the increasing energy demand, the growing penetration of renewable energy sources (RES), and the drive for sustainable energy solutions, grid-integrated solar PV systems are becoming more prevalent.

MPPT algorithms are essential for extracting maximum PV power under variable weather conditions, while advanced inverter control ensures efficient grid synchronization, voltage regulation, and power quality.

PV modules behave nonlinearly in unpredictable weather conditions, and the effectiveness of many control strategies under such conditions especially conventional ones—decreases significantly. It is essential to maximize the use of PV power in the system.

This chapter proposed a novel HLO-ANN (Horned Lizard optimized artificial neural network) MPPT technique for grid-integrated solar photovoltaic systems. Proposed algorithm ensure that grid integrated PV systems work best at the maximum power point regardless of weather conditions. The effectiveness of the proposed HLO-ANN has been validated through simulation and compared against other ANN-optimized MPPT techniques. Furthermore, Synchronous Reference Frame Theory (SRFT) has been employed for inverter control to ensure accurate current extraction and maintain voltage stability under dynamic conditions.

4. 2 MPPT TECHNIQUES FOR GRID INTEGRATED SOLAR PV SYSTEM

This chapter provides a thorough examination of Maximum Power Point Tracking (MPPT) strategies, with an emphasis on three major approaches: optimization-based MPPT, artificial neural network (ANN)-based MPPT, and a novel developed MPPT technique. The novel technology, known as the Horned Lizard ANN-based MPPT, combines the benefits of both ANN and optimization methodologies. Traditional MPPT algorithms frequently encounter difficulties such as sluggish convergence, exposure to local optima, and poor tracking efficiency in rapidly changing environmental conditions. The suggested method improves tracking accuracy, dynamic response, and overall performance by combining ANN learning capabilities

and optimization techniques' search efficiency. This hybrid technique maximizes electricity extraction from the solar PV system while maintaining grid stability and reliability. With greater versatility and resilience than traditional approaches, the Horned Lizard ANN-based MPPT methodology has been developed specifically for grid-integrated solar PV systems. Several MPPT techniques are taken into consideration for the investigations:

- a) Artificial Neural Network (ANN) MPPT
- b) Particle Swarm Optimization (PSO)-ANN MPPT
- c) Artificial Bee Colony (ABC)-ANN MPPT
- d) Harmony Search (HS) -ANN MPPT
- e) Teacher Learning Based Optimization (TLBO) -ANN MPPT
- f) Dwarf Mongoose Optimizer (DMO) -ANN MPPT
- g) Proposed novel Horned Lizard Optimization (HLO) -ANN MPPT

4.2.1 Artificial Neural Network (ANN) based MPPT control technique

The artificial neural network (ANN) is a replication of the biological neural network, which links various parameters to certain data points. ANN models can incorporate multiple parameters without the requirement of complex mathematical equations. ANN requires less theoretical work than conventional methods for relating several parameters with large amounts of uncertain data points. ANNs are trained using imported data through supervised learning or training. ANNs, like the human brain, are made up of several neurons. These neurons are linked by a fractional number called weight [133-134].

ANN topologies are categorized into two types: feedforward and feedback networks. The feedforward is extensively used since it requires less memory during implementation. It is particularly effective for non-linear systems like solar PV arrays. Fig.3 illustrates the internal structure of the feed forward artificial neural network (ANN), which consists of an input layer, hidden layer, output layer, weights, and bias. Furthermore, each layer's neurons are linked together via bias terms in the antecedent layers and the weights of the other neurons. Equation (4.1) defines the ANN model using weights and biases.

$$y = \sum_{i=1}^{n} \omega_{ij} x_i + b_i \tag{4.1}$$

where n represents the overall number of inputs, x_j represents the input training node, ω_{ij} is the equivalent input layer weights, and b_j is the bias related to the hidden layer. To further understand the feed-forward neural network methodology, the complex gradient method is utilized to update the weights and biases to get the desired outcomes. To obtain the desired outcome, there should be minimal variation between actual and output values. The mean square error (MSE) is selected as a cost function, expressed as equation (4.2):

$$MSE = \frac{1}{n} \sum_{i=1}^{n} \sum_{j=1}^{m} (Y_j(i) - T_j(i))^2$$
(4.2)

Where, n represents the input data, m represents the output signals, $Y_j(i)$ represents the true output, and $T_i(i)$ represents the desired output.

The block diagram of internal structure of ANN MPPT implementation is shown in Fig 4.1. Any Artificial Intelligence (AI) technique, in general, uses a dataset to train the model, identify patterns in the data, and generate desired results.

Three months' worth of temperature and sun irradiance data, were added to the ANN MATLAB code, and this ANN feedforward model was trained to produce the voltage (V_{ref}) . In order to create the duty cycle for the DC-DC boost converter, the PI controller assisted in settling the error difference between the generated voltage (V_{ref}) and PV voltage prior to applying the signal to the PWM converter.

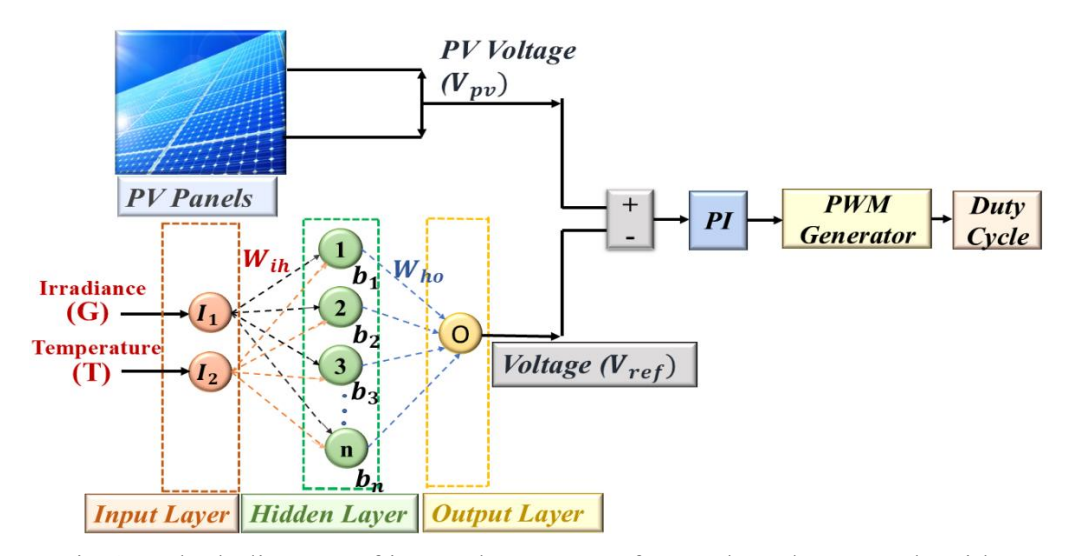


Fig.4.1 Block diagram of internal structure of ANN based MPPT algorithm

4.2.2 Optimized ANN based MPPT control techniques

The Optimized ANN MPPT Controller is an intelligent and adaptive control system that maximizes the power output of solar photovoltaic (PV) systems by precisely tracking the Maximum Power Point (MPP). This controller combines the predictive power of an Artificial Neural Network with the efficiency of an optimization algorithm, resulting in higher tracking accuracy and faster convergence in dynamic environments. The best reference voltage corresponding to the MPP is predicted by an ANN model trained on historical or real-time solar statistics, including irradiance and temperature parameters. The optimization algorithm is implemented into the system to fine-tune the ANN model's weights and biases. This weight optimization reduces the discrepancy between projected and actual MPP voltages, improving the controller's accuracy and dependability [135].

During operation, the controller continually monitors real-time PV parameters and dynamically adjusts the operating point to keep the system at or close to the MPP, even

when irradiance, temperature vary rapidly. The optimized ANN MPPT controller outperforms conventional MPPT techniques (e.g., P&O or Incremental Conductance) in terms of response time, oscillation reduction, and efficiency.

This controller greatly improves the performance of solar PV systems by combining the characteristics of both ANN and optimization methods, making it perfect for applications that require high precision, adaptability, and real-time responsiveness.

Steps involved in optimized ANN Algorithm:

The Optimized ANN Algorithm is a hybrid optimization approach that uses an Artificial Neural Network (ANN) and an optimization technique to improve network performance. This procedure has two major steps: Choosing the optimal ANN topology (number of neurons in the hidden layer) and optimizing the initial weights of the ANN model.

Step 1: Choose the best ANN topology.

The topology of an artificial neural network relates to the network's structure, including the number of neurons in the hidden layers. Instead of manually determining the number of neurons (which may result in unsatisfactory performance), an iterative optimization approach is utilized to find the best configuration.

Step 2: Optimizing the Initial Weights of the ANN Model.

Optimizing the initial weight values of an artificial neural network (ANN) is crucial for improving the learning process by enabling faster convergence and higher accuracy. The process begins with the random initialization of weights to prevent symmetry issues. The ANN is then trained using these initial weights, and the first Mean Squared Error (MSE) is measured to evaluate performance. To enhance training efficiency, optimization techniques such as PSO, ABC, HS, TLBO, DMO and HLO methods are employed to search for weight combinations that minimize the training error. The optimized initial weights, which result in a lower MSE, are then used to configure the ANN model in MATLAB, replacing the default weight initialization in the "nntool" interface. By using these optimized weights, the ANN achieves faster convergence, lower MSE, and requires fewer training epochs compared to traditional training methods, ultimately improving the network's overall performance.

4.2.2.1 Particle Swarm Optimization (PSO)- ANN MPPT control techniques

Kennedy and Eberhart's 1995 [136] presentation introduced the PSO method, a multivariable function optimization technique with many local optimal points. The PSO algorithm was based on observations of natural social behaviour, such as bird flocking and fish schooling. The PSO stands out from other global optimization approaches due to its ease of implementation and rapid convergence. Researchers are increasingly exploring the usage of PSO in PV systems alongside MPPT.

PSO used the flocking analogy to depict cooperative "birds," or particles, acting together in a "flock," also known as a swarm. Each particle in the swarm has a fitness value mapped by an objective function and an individual velocity. This value determines the direction and distance of travel. Particles communicate information received from their separate search processes. A particle's position is determined by two variables: the best solution found by the particle (P_{best}), which is saved for individual use, and the best particle in the neighbourhood (g_{best}), which is stored for the swarm. The particle swarm adjusts its direction and velocity to achieve optimal positioning. Each particle eventually moves to an ideal position or near a global optimum. Equations (4.3) and (4.4) represent the PSO velocity and position update rules respectively [137]

$$v_i(k+1) = wv_i(k) + c_1r_1 \cdot (P_{best} - x_i(k)) + c_2r_2 \cdot (g_{best} - x_i(k))$$
(4.3)

$$x_i(k+1) = x_i(k) + v_i(k+1)$$

$$i = 1, 2, \dots, N$$
(4.4)

In the equation, x_i and v_i represent particle i's velocity and position, k is the iteration number, w is the inertia weight, r_1 and r_2 are uniformly distributed random variables, and c_1 and c_2 are the cognitive and social coefficients, respectively. The individual best location of particle i is denoted by $P_{best,i}$ while the best position of the entire swarm is represented by $g_{best,i}$.

4.2.2.2 Artificial Bee Colony (ABC)- ANN MPPT control techniques

The artificial bee colony algorithm is a swarm-based meta-heuristic approach for solving multidimensional and multimodal optimization issues. The ABC method classifies artificial bees into three groups: employed, onlooker, and scouts' bees. An employed bee is one that is actively seeking or exploiting food sources. The term "onlooker" refers to a bee waiting in the hive to find a food source. Employed bees who cannot enhance their food sources after a set number of attempts become scouts and abandon their food sources. The quantity of food sources equals the number of employed and onlooker bees. In optimization, a food source's position represents a potential solution, while its nectar amount indicates the quality (fitness) of the solution [138].

During initialization, the ABC generates a randomly dispersed population of SN solutions. The equation below produces each solution within its limits:

$$x_i^j = x_{min}^j + rand[0,1](x_{man}^j - x_{min}^j) i = 1,2,...,j = 1,2,...,D$$
 (4.5)

In this equation, x j min and x j max indicate the minimum and maximum of the parameter j, and D is the number of optimization parameters. After initialization, the population of solutions undergoes C = 1, 2, (maximum cycle number) MCN cycles of employed, onlooker, and scout bees' search operations.

In each cycle, each employed bee generates a new solution (v_{ij}) and evaluates its fitness (fit_i) using equation (4.6).

$$v_{ij} = x_{ij} + \varphi_{ij} \left(x_{ij} - x_{kj} \right) \tag{4.6}$$

where $k \in \{1, 2..., SN\}$ and $j \in \{1, 2..., D\}$ are randomly selected indexes. Although k cannot be the same as i, φ_{ij} is a random number between -1 and 1. Following the information sharing by the employed bees, The onlooker uses equation (4.7) to discover a new solution v_{ij} near x_i , depending on the probability P_i

$$P_i = \frac{fit_i}{\sum_{n=1}^{SN} fit_n} \tag{4.7}$$

where fit_i represents the fitness value of solution x_i

If a candidate solution v_{ij} falls beyond the allotted search space, it is adjusted to fit. The suitability of each new candidate solution v_{ij} is compared to that of itspredecessor. If the new answer has equal or higher fitness than the previous one, it takes its position in the memory. Otherwise, the previous one remains in memory. A greedy selection technique is used to choose between the old and candidate models. After each search cycle, if a solution's fitness cannot be improved and the "limit" number of trials is reached, the scout bee abandons the solution and searches for a new one randomly. Equation (4.6) will give the new answer, x_i .

4.2.2.3 Harmony Search (HS) ANN MPPT control techniques

The Harmony Search (HS) algorithm is an evolutionary algorithm inspired by the music harmony improvisation process. It involves five main steps. First, the algorithm initializes its parameters, including HMCR (Harmony Memory Considering Rate), BW (Bandwidth), PAR (Pitch Adjustment Rate), the number of iterations (NI), and the harmony memory size (HMS). The optimization goal is defined to either maximize or minimize the objective function $f(x_i)$ where x_i represents potential solutions [139]. Next, the harmony memory (HM) is populated with candidate solutions within the upper and lower boundaries using the equation (4.8):

$$x_i = lower \ bound + R_1 * (Upperbound - lower bound)$$
 (4.8)

Where R_1 is a random number between 0 and 1.

In the improvisation step, new harmony vectors are generated by combining HMCR, PAR, and BW. Two random values a and b (between 0 and 1) are used. If a > HMCR a new value is generated using the initialization formula. If, a < HMCR, a value from the HM is selected. If b < PAR, the value is adjusted using equation (4.9):

$$x_{j}' = x_{new,j} \pm BW \times rand \tag{4.9}$$

The memory is updated by comparing the newly generated vector with the worst vector in HM. If the new vector is better, it replaces the worst one.

Finally, the algorithm checks the stopping criteria, such as the maximum number of iterations. Once the criteria are met, the search process ends, and the best solution in

the harmony memory is selected.

4.2.2.4 Teacher Learning Based Optimization (TLBO) ANN MPPT control techniques

This algorithm comprises two phases: teacher and student. The TLBO algorithm offers advantages such as no need for control variable adjustments, rapid speed, and greater convergence to the global optimum. The TLBO algorithm excels in identifying the GMPP in all conditions, making it a top choice for the aforementioned aims. The following sections describe the two phases [140].

1) Teacher-phase

A teacher is a subject-matter expert who trains students. According to the TLBO algorithm, the instructor is the optimal answer among the population. During the teacher-phase, students choose a situation similar to the teachers. If the as i_{th} student's new position is shown as $x_i^{(k+1)}$ and their existing position is shown as $x_i^{(k)}$, equation (4.10) may be used to connect the two situations:

$$x_i^{(k+1)} = x_i^{(k)} + \Delta x_i \tag{4.10}$$

 Δx_i represents the student's progression or regression. In the teacher phase, students want to align with the teacher's perspective, hence the sentence Δx_i should be changed accordingly. So, we have:

$$\Delta x_i = r_i (T_A - F * MA) \tag{4.11}$$

The term T_A refers to the teacher's optimal solution to a given situation. The term MA refers to the student's average position. (2) indicates that students approach their teacher's stance more closely. Furthermore, r_i is a random parameter ranging from 0 to 1. The expression F, often called the teaching coefficient, is defined as equation (4.12):

$$F = round(1 + rand) \leftrightarrow F = 1 \text{ or } 2 \tag{4.12}$$

Position (k + 1) is acceptable if its objective function outperforms that of position (k). The output of this phase is used as input for the student phase.

2) Student-phase

The student-phase is a reaction amongst students. In other words, the first student evaluates their situation in comparison to other students. If one student's state is better than another, the update will be based on the first student's state. Otherwise, the update is based on another student's status. That means

$$x_{i}^{(k+1)} = x_{i}^{(k)} + r_{i} \left(x_{i}^{(k)} - x_{j}^{(k)} \right)$$

$$\forall Fit \left(x_{i}^{(k)} \right) > Fit \left(x_{j}^{(k)} \right)$$
(4.13)

$$x_{i}^{(k+1)} = x_{i}^{(k)} + r_{i} \left(x_{j}^{(k)} - x_{i}^{(k)} \right)$$

$$\forall Fit \left(x_{j}^{(k)} \right) > Fit \left(x_{i}^{(k)} \right)$$
(4.14)

Fit is the fitness function that determines the best and worst scenarios. To be acceptable, the new position (k + 1) must have a better fit function (objective function) than the previous position (k).

4.2.2.5 Dwarf Mongoose Optimizer (DMO)-ANN MPPT control techniques

The dwarf mongoose optimizer (DMO) was developed by examining the foraging behaviour of dwarf mongooses. The presented meta-heuristic technique (DMO) generates the population of DM animal as equation (4.15) [141]:

$$X_m(0) = X_{min}(1-R) + R.X_{max}, \quad m = 1:N_{DM}$$
(4.15)

where m is an integer as a counter, which is equivalent to 1, 2, 3, 4, 5,, N_{DM} ; N_{DM} is the whole population of dwarf mongooses. In equation (4.15), the sign "." denotes the dot product, which is a fundamental method of combining two vectors, denoting the product of each element in the vector and its corresponding one in the other vector of the same dimension. X_m provides the position of each DM (m), whereas X_{min} and X_{max} represent the lowest and highest boundaries. R is a randomized vector with dimension (D) proportional to the total number of control variables, and N_{DM} is the total size of the DM group.

Next, during the initialization of the DM locations, the fitness rating (FS_m) of each solution (X_m) is calculated. The alpha female is chosen based on the likely fitness value (α_m) of each group, as shown below:

$$\alpha_m = \frac{FS_m}{\sum_{m=1}^{N_{DM}} FS_m} \tag{4.16}$$

 α_m represents the probability value for each animal in the group

In the alpha structure, the number of DMOs is proportional to the population size less the number of babysitters (Bs). The sign (peep) monitors the alpha's vocalizations, keeping the DMOs on track. Each DMO naps in the first sleeping space that has been assigned to them. To create the next position toward the expected food position, the DMO uses the calculation indicated in equation (4.17).

$$X_m(T+1) = R \times peep + X_m(T), \quad m = 1: N_{DM} - Bs$$
 (4.17)

where Bs represents the total number of babysitters in the group and T denotes the current iteration.

Instead of building a home for the juvenile dwarf mongooses, they are transported from one sitting mound to another. In addition to seeking for food, the alpha group looks for a different mound to visit after the childcare exchange need is met. To reproduce this, the average value of the seated mound is estimated for each iteration, and it may be represented as equation (4.18):

$$SM_m = \frac{FS_m(T+1) - FS_m(T)}{\max(|FS_m(T) - FS_m(T+1)|)} \tag{4.18}$$

Where $FS_m(T)$ represents the fitness score of the current solution (X_m) at the current iteration (T), and $FS_m(T+1)$ represents the fitness score of the updated solution (X_m) at the subsequent iteration (T+1).

The observed sitting mound's mean value (ψ) is provided below

$$\varphi_m = \frac{\sum_{m=1}^{N_{DMA}} SM_m}{N_{DMA}} \tag{4.19}$$

Based on the overall success of the DMOs, the next step represents a success or failure assessment while generating a new mound. To simulate the scout mongoose, use the equation (4.20):

$$X_{m}(T+1) = \begin{cases} X_{m}(T) + CF \times R. \left(M - X_{m}(T)\right) & \text{if } \varphi_{m+1} > \varphi_{m} \\ X_{m}(T) - CF \times R. \left(M - X_{m}(T)\right) & \text{if } \varphi_{m+1} < \varphi_{m} \end{cases} m = 1: N_{DM}$$

$$(4.20)$$

where CF decreases steadily as iterations progress, as seen in equation (4.21), and M appears to be a vector that influences the DMOs' eventual sleeping area relocation, as determined in equation (4.22). The CF factor represents the value of the parameter that governs the DMO organization's collective volitive motion.

$$CF = \left(1 - \frac{T}{T_{max}}\right)^{\left(\frac{2\times T}{T_{max}}\right)} \tag{4.21}$$

$$M = \sum_{m=1}^{N_{DMA}} \frac{X_m \times SM_n}{X_m} \tag{4.22}$$

 T_{max} denotes the maximum number of iterations.

To improve searching skills, the alpha-directed knowledge-acquisition technique is used with the formula outlined in equation (4.17) to provide a likely food location: $X_m(T+1) =$

$$\begin{cases} X_{Alpha}(T) + R. \left(X_m(T) - X_m(T) - X_{Rd}(T) \right) & \text{if } r_1 < PSF \\ X_m(T) + R \times peep & \text{else } m = 1: N_{DM} - Bs \end{cases}$$

$$\tag{4.23}$$

where $X_m(T+1)$ represents the modified answer X_m at the following iteration (T+1). $X_{Alpha}(T)$ represents the alpha location with the smallest goal worth; R is a randomized vector of dimension (D); $X_m(T)$ provides the current solution X_m at the current iteration (T); X_{Rd} refers to the position of a randomly chosen DMA; r_1 is a randomly produced value within the range [0, 1]; and PSF indicates the probability of the selection factor.

4.2.2.6 Novel Horned Lizard Optimization (HLO) ANN MPPT control techniques

HLOA is a novel metaheuristic optimization algorithm influenced by the protective behaviour of the horned lizard. The four tactics for defence are crypsis skin lightening/darkening, bloodstream spitting, and movement-to-escape. They offer an appropriate balance of exploration and exploitation throughout the solution search region. Considering the advantages of the HLO algorithm, it has been combined with the ANN MPPT approach [142].

After the establishment of the ANN network topology, an HLO-based ANN approach is developed to determine the optimal initial weights of the ANN model. These are determined to enhance the model's output prediction as the presumed initial weight values are corrected. This proposed approach produces optimal beginning weights. The ideal initial weights are utilized to train the ANN model with MATLAB's "nntool" program. The optimized initial weights are then substituted with the conventional training weights in area containing the beginning weights of the "nntool" box.

As a result, the performance of the ANN model based on the improved training approach utilizing real data outperforms conventional ANN. A significant benefit of utilizing HLO-trained neural network technology in MPPT-based solar photovoltaic (PV) systems is that it has the capability to detect the maximum power point of the PV system in a more fast and accurate manner, while requiring less computing effort than conventional methods. This makes it a feasible option for improving the performance of PV systems. The Irradiation (G) and Temperature (T) of the weather are the inputs of the ANN approach, which yields the maximum power measurement of the solar array erected at the MPP. Fig.4.2 is a flow diagram illustrating the steps involved in combining the Horned Lizard optimization algorithm with the ANN feedforward model in order to obtain HLO-ANN MPPT.

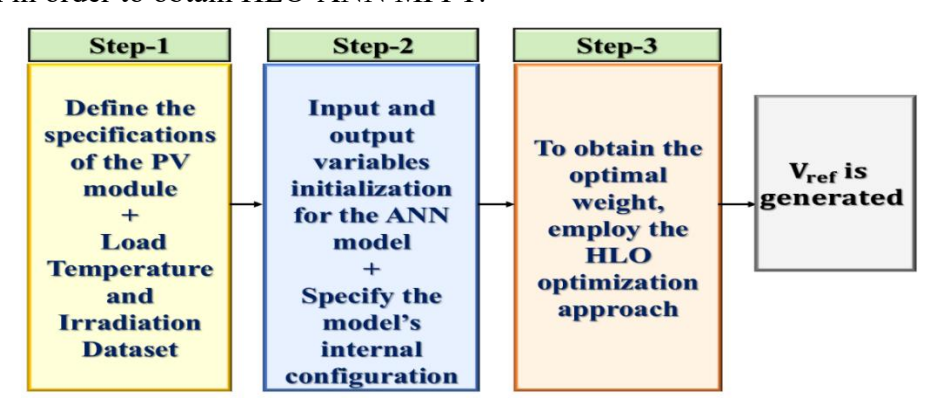


Fig.4.2 Block diagram of HLO-ANN MPPT Technique

Horned Lizard Optimization Technique

The scientific name for the horned lizard is Phrynosoma. This reptile is native to northern Mexico and the south-central regions of the United States. They are suited to harsh climates that are semi-arid or desert. All reptiles, including horned lizards, rely on thermoregulation to stay warm because they cannot create body heat in response to changing temperatures. The horned lizard can brighten or darken its skin to control solar thermal gain. Thus, at high temperatures, the skin lightens, while at low temperatures, it darkens. Dark skin absorbs and transforms all wavelengths of light to heat. Temperature impacts the alpha-melanophore stimulating hormone, causing

horned lizards' skin to change colour quickly. Grasshoppers, beetles, spiders, ticks, butterflies are few of the species that horned lizards consume. Their principal passive mode of defence is crypsis. This strategy involves the ability to assimilate into its surroundings via colour, pattern, and shape. Horned Lizards change colour to fit the ground and have spines that cover their body outlines, making them difficult to identify. Moving to escape is another passive defensive strategy. As a defensive mechanism, this lizard ejects a burst of blood that extends over a meter when threatened. In this work, each of the stated lizard defence actions is mathematically modelled as part of the optimization process.

Approach 1: Crypsis Behaviour

Crypsis allows organisms to blend in with their surroundings by copying colour, texture, or even becoming translucent, which makes it more challenging for prey or predators to identify them. (refer Fig 4.4). It is an adaptive behaviour which assists organisms, hence enhancing their chances of survival in the wild. The crypsis approach is expressed mathematically using colour theory. The International Commission on Illumination (CIE) categorized sources of light based on their emitted energy across the visible spectrum (400-700 nm) for various wavelength. The organization developed a colour assessment system, such as $L \alpha^* \beta^*$ for Cartesian and $L c^* h$ for polar coordinates, to determine colours in a colour space. In the $L \alpha^* \beta^*$ system, L represents brightness, whereas α^* and β^* represent chromatic coordinates, as seen below.

$$\alpha^* = \begin{cases} +\alpha, & Indicates \ red \\ -\alpha, & Indicates \ areen \end{cases}$$
(4.24)

$$\alpha^* = \begin{cases} +\alpha, & Indicates \ red \\ -\alpha, & Indicates \ green \end{cases}$$

$$\beta^* = \begin{cases} +\beta, & Indicates \ yellow \\ -\beta, & Indicates \ blue \end{cases}$$
(4.24)

The $L c^* h$ system specifies brightness, intensity of colour, and hue angle. Hue describes the color family (red, yellow, green, and blue) and all colors in between by moving in a circle around the "equator". The hue circle numbers run from 0 to 360°, beginning with red at 0° and progressing counter clockwise via yellow, green, blue, and back to red. The L-axis indicates the colour's luminous intensity. Colours can be classified as light or dark by comparing their value. Fig.4.3 illustrate examples of both colour systems.

Rectangular coordinates are converted to polar coordinates using equation.4.26

$$c^* = \sqrt{(\alpha^{*2} + \beta^{*2})} \tag{4.26}$$

$$h = arcTg\left(\frac{\beta^*}{\alpha^*}\right) \tag{4.27}$$

The values of c* and h stand for hue and chroma, respectively. Hue angle, or h, has a value between 0 and 360 degrees and is given in degrees. The following are the inverse formulas:

$$\alpha^* = c^* \cos(h) \tag{4.28}$$

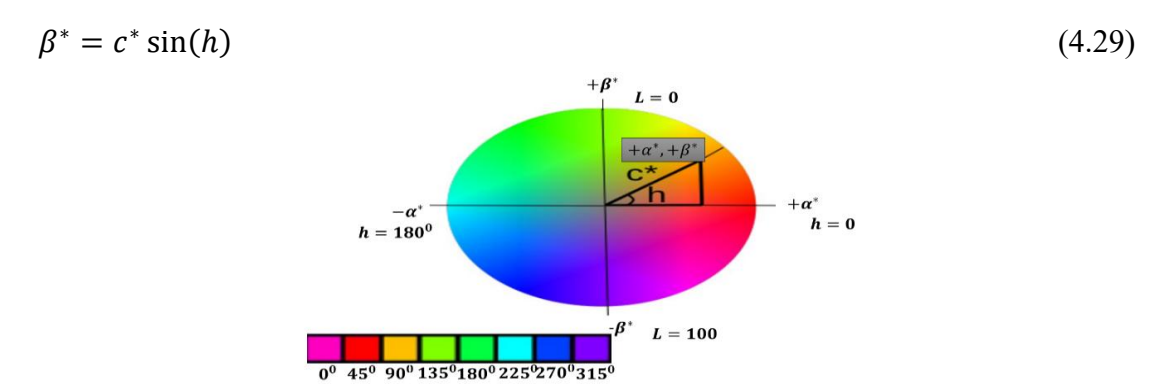


Fig.4.3 Representation of colour space for CIE, $L \alpha^* \beta^*$ and $L c^* h$



Fig.4.4 Crypsis behavior of Horned Lizard.

Let (α_q^*, β_p^*) and (α_r^*, β_s^*) be any two colours in an ordered pair, with $p \neq q \neq r \neq s$, without losing generality. So, using the arithmetic procedures listed in equations (4.30) and (4.31), any two new colours, such as colourvar1 and colourvar2, can be created.

$$colourvar1 = \beta_p^* - \alpha_q^* - \alpha_r^* + \beta_s^*$$
(4.30)

$$colourvar2 = \beta_p^* - \alpha_q^* + \alpha_r^* - \beta_s^*$$
(4.31)

These colours can be expressed with a single equation, as illustrated in equation (4.32).

$$colourvar = \beta_p^* - \alpha_q^* \pm [\alpha_r^* - \beta_s^*]$$
(4.32)

The inverse form of equation (4.32) is as follows:

$$colourvar = c_1 \sin(h_p) - c_1 \cos(h_q) \pm [c_2 \cos(h_r) - c_2 \sin(h_s)]$$

$$(4.33)$$

Where angles intersect at $h_p \neq h_q \neq h_r \neq h_s$, and chroma $c_1 \neq c_2$. The equation below represents the arithmetic operation of chromatic coordinates.

$$\overrightarrow{x_{l}}(t+1) = \overrightarrow{x_{best}}(t) + \left(\delta - \frac{\delta \cdot t}{Max_iter}\right) \left[c_{1}\left(\sin\left(\overrightarrow{x_{r_{1}}}(t)\right) - \cos\left(\overrightarrow{x_{r_{2}}}(t)\right)\right) - \left(-1\right)^{\delta}c_{2}\left(\cos\left(\overrightarrow{x_{r_{2}}}(t)\right) - \sin\left(\overrightarrow{x_{r_{4}}}(t)\right)\right]$$

$$(4.34)$$

Where, $\overrightarrow{x_l}$ (t+1) indicate the new search agent location in the solution search region for iteration t+1, $\overrightarrow{x_{best}}$ (t) is the finest search agent for iteration t, r_1 , r_2 , r_3 and r_4 , are integer random numbers created between 1 and the maximum number of search agents, with r_1 , $\neq r_2$, $\neq r_3$, $\neq r_4$, $\overrightarrow{x_{r_1}}$, $\overrightarrow{x_{r_2}}$, $\overrightarrow{x_{r_3}}$ and $\overrightarrow{x_{r_4}}$ represent the r_1 , r_2 , r_3 and r_4 search agents selected, and Max_iter represents the maximum number of iteration. δ is a binary value, which is set to 2 [27]. Random integers c_1 and c_2 are chosen with $c_1 \neq c_2$.

Algorithm. 1 δ procedure

1: Start procedure

2: if rand () $\leq \frac{1}{2}$ then

3: return 0

4: else

5: return 1

6: end if

7: End procedure

Approach 2: Skin lightening or darkening

The skin of the horned lizard can be tinted lighter or darker, depending on whether it wants to reduce or boost the amount of solar thermal gain it receives. Thermal energy adheres to the same conservation principles as light energy. Equation (4.35) illustrates the lightening-skin approach. Equation (4.36) represents the darkening skin approach.

$$\overrightarrow{x_{worst}}(t) = \overrightarrow{x_{best}}(t) + \frac{1}{2} Light_1 sin\left(\overrightarrow{x_{r_1}}(t) - \overrightarrow{x_{r_2}}(t)\right) - (-1)^{\delta} \frac{1}{2} Light_2 sin\left(\overrightarrow{x_{r_3}}(t) - \overrightarrow{x_{r_4}}(t)\right)$$

$$(4.35)$$

$$\overrightarrow{x_{worst}}(t) = \overrightarrow{x_{best}}(t) + \frac{1}{2} Dark_1 sin\left(\overrightarrow{x_{r_1}}(t) - \overrightarrow{x_{r_2}}(t)\right) - (-1)^{\delta} \frac{1}{2} Dark_2 sin\left(\overrightarrow{x_{r_3}}(t) - \overrightarrow{x_{r_4}}(t)\right)$$

$$(4.36)$$

 $\overline{x_{worst}}$ (t) and $\overline{x_{best}}$ (t) represent the worst and best search agents discovered, respectively. $Light_1$ and $Light_2$ are random numbers generated between Lightening1 (0 value) and Lightening2 (0.4046661 value). Similarly, $Dark_1$ and $Dark_2$ are random numbers generated between Darkening1 (0.5440510) and Darkening2 (1) using normalized Table 1 data.

The skin-darkening or skin-lightening technique results in the replacement of the worst search agent from the previous iteration.

Table.4.1 Colour palette designed for skin lightening or darkening.

Name	Color	Hexadecimal	Decimal	Normalized
$Lightening_1$		E8E8E8	15263976	0.0
Lightening ₂		9398BF	9672895	0.4046661
$Lightening_3$		763660	7747080	0.5440510
$Lightening_4$		161617	1447447	1

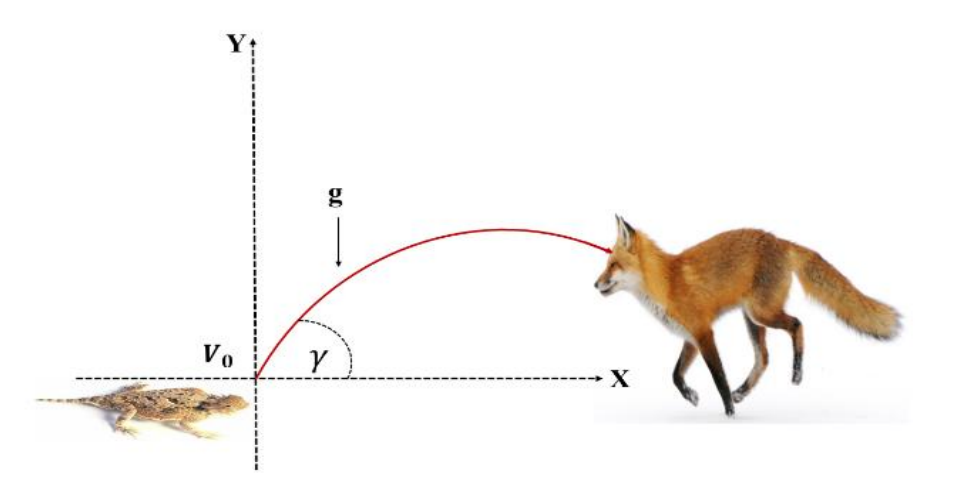


Fig.4.5 Horned lizard shooting blood

Algorithm.2 Skin lightening or darkening procedure

1: Generate Light₁ and Light₂ randomly from Table 4.1

2: Generate Dark₁ and Dark₂ randomly from Table 4.1

3: Generate r_1, r_2, r_3 and r_4 integer value randomly between [1, size maximum search agents], where $r_1, \neq r_2, \neq r_3, \neq r_4$

4: if δ then

5: Apply lightening skin. Evaluate equation (4.35)

6: else

7: Apply darkening skin. Evaluate equation (4.36)

8: **end if**

9: End procedure

Approach 3: Blood Squirting

The Horned Lizard attracts enemies by shooting blood from its eyes. Fig.4.5 depicts the shooting blood defence mechanism as a projectile motion. In order to determine projectile motion equations, we divide it into two components: horizontal (X-axis) and vertical (Y-axis). [27]:

The shot of blood travels uniformly in the horizontal direction, so it's equation of motion is expressed by:

$$\vec{v} = \overrightarrow{v_0} + \int_0^t \vec{g} dt = \overrightarrow{v_0} + \vec{g} t \tag{4.37}$$

In a vertical direction shot of blood defines a uniformly accelerated rectilinear motion, as shown below.

$$\vec{r} = \overrightarrow{r_0} + \int_0^t (\overrightarrow{v_0} + \vec{g}t)dt = \overrightarrow{r_0} + \overrightarrow{v_0}t + \frac{1}{2}\vec{g}t^2 \qquad where, \quad \overrightarrow{r_0} = \vec{0} \quad (4.38)$$

Equations 4.39 and 4.40 represent the vector equations, position and velocity

respectively.

$$\overrightarrow{v_0} = v_0 \cos(\gamma) t \overrightarrow{j} + \left((v_0 \sin(\gamma)) t - \frac{1}{2} g t^2 \right) \overrightarrow{k}$$

$$\tag{4.39}$$

$$\vec{v} = \vec{r} = (v_0 \cos(\gamma) \vec{j} + (v_0 \sin(\gamma)) - g) \vec{k}$$
(4.40)

we can express the trajectory as follows:

$$\overrightarrow{x_{l}}(t+1) = \left[v_{0}\cos\left(\gamma \frac{t}{\text{Max_iter}}\right) + \varepsilon\right] \overrightarrow{x_{best}}(t) + \left[v_{0}\sin\left(\gamma - \frac{\gamma t}{\text{Max_iter}}\right) - g + \varepsilon\right] \overrightarrow{x_{l}}(t)$$

$$(4.41)$$

Where,
$$v_0 = 1$$
, $\gamma = \frac{\pi}{2}$, $\varepsilon = 1e^{-6}$ and $g = 9.8 \text{ m/s}^2[27]$.

Approach 4: Move to escape

The horned lizard uses a random quick movement tactic to avoid predators. A function that comprises a local and global movement has been presented for the mathematical modelling of this prevention technique; it is defined in expression (4.42) and represented in Fig.4.6. In this expression, walk $\left(\frac{1}{2} - \varepsilon\right) \overrightarrow{x_i}(t)$ is a local movement around $\overrightarrow{x_i}(t)$, whereas adding $\overrightarrow{x_{best}}(t)$ results in a displacement throughout the solution search space.

$$\overrightarrow{x_i}(t+1) = \overrightarrow{x_{best}}(t) + walk\left(\frac{1}{2} - \varepsilon\right)\overrightarrow{x_i}(t)$$
(4.42)

Where, walk generates a random number between -1 and 1.

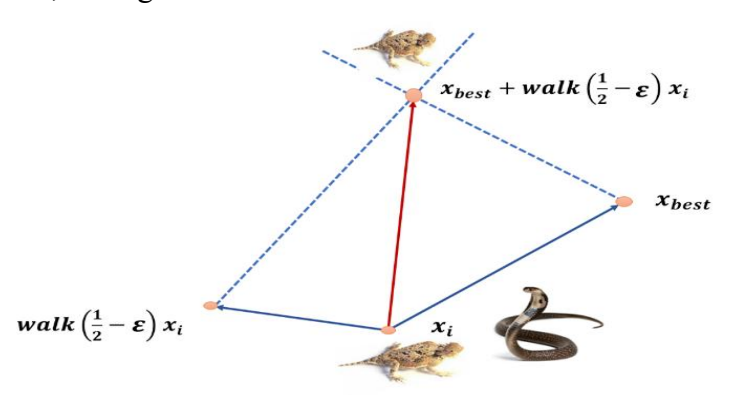


Fig.4.6 Horned lizard escaping from predators

Approach 5: Alpha-melanophore stimulating hormone rate

Temperature affects alpha-melanophore stimulating hormone (alpha-MSH), causing rapid colour change on horned lizard skin. The alpha-melanophore rate value of horned lizards is defined in the equation (4.43).

$$melanophore(i) = \frac{Fitness_{max} - Fitness(i)}{Fitness_{max} - Fitness_{min}}$$
(4.43)

 $Fitness_{min}$ and $Fitness_{max}$ are the finest and worst fitness values in the current iteration, and Fitness(i) is the current fitness value of the i-th search agent. In equation (4.44)., a low alpha-MSH rate (< 0.3) takes the place of search agents.

$$\overrightarrow{x_{l}}(t) = \overrightarrow{x_{best}}(t) + \frac{1}{2} \left[\overrightarrow{x_{r_{1}}}(t) - (-1)^{\delta} \overrightarrow{x_{r_{2}}}(t) \right]$$

$$(4.44)$$

Where, r_1 and r_2 are random integers created from 1 to the maximum number of search agents.

with, $r_1 \neq r_2$, $\overrightarrow{x_{r_1}}$ and $\overrightarrow{x_{r_2}}$ are the r_1 and r_2 th search agent selected.

Algorithm.3 Alpha-melanophore procedure

- 1: Start procedure
- 2: for i=1 to size population do
- 3: if $melanophore(i) \le 0.3$ then
- 4: Approach 5: $\overrightarrow{x_1}$ search agent replaced in equation (4.44)
- 5: end if
- 6: end for
- 7: End procedure

Algorithm.4 Pseudo-code of the Horned lizard Optimization procedure

- **1**. Initialization of parameters. Specify the number of search agents, population size, and maximum number of iterations
- **2.** Generate the initial population randomly.
- 3. while < maximum number of iterations do
- 4. if crypsis? then
- **5.** *Approach 1: Crypsis. Compute equation (4.34)*
- 6. else
- 7. if flee? then
- **8**. Approach 4: Move to escape. Compute equation (4.42)
- 9. else
- **10.** Approach 3: Blood Squirting. Compute equation (4.41)
- 11. end if
- 12. *end if*
- 13. Replace the worst search agents by skin darkening (compute equation (4.36)) or lightening (compute equation (4.35)). They are selected randomly
- 14. If Low alpha-melanophore rate? Then
- **15.** Approach-5 Replace search agents with low alphamelanophore rate by applying equation-4.44 Algorithm 3.
- 16. *end if*

- 17. Calculate x_{new} , the fitness value of the new search agents
- **18.** *If* $x_{new} < x_*$ *then*
- **19**. $x_* = x_{new}$
- 20. end if
- **21.** Iteration=iteration+1
- 22. end while
- **23.** Display x_* the best optimal solution
- 24. end

4.3 RESULT EVALUATION AND DISCUSSION USING PROPOSED NOVEL HLO-ANN MPPT CONTROL TECHNIQUE

The schematic diagram of the proposed grid integrated solar PV system is depicted in Fig. 4.7. The Solar PV has a capacity of 12.79 kW which generates DC output and is linked to a boost converter in order to generate regulated DC output. The boost converter serves as an interface between the inverter's DC-link capacitor and the solar PV array. Inverters convert regulated DC output into AC voltage while offering the advantages of harmonics reduction, reactive power compensation, etc. The inverter is coupled to PCC through interfacing inductors (L_f) to compensate the current ripples. The linear/non-linear/balanced/unbalanced/ variable loads evaluated in the present research work are connected in series to the power grid of 415 V (line-to-line voltage), 50 Hz via the line impedances. The present research work employs two control strategies: the proposed HLO-ANN MPPT control technique is implemented to extract the maximum power from the PV array, and the Synchronous reference frame (SRF) theory is employed for controlling the inverter. Parameters of the system are provided in Appendix.

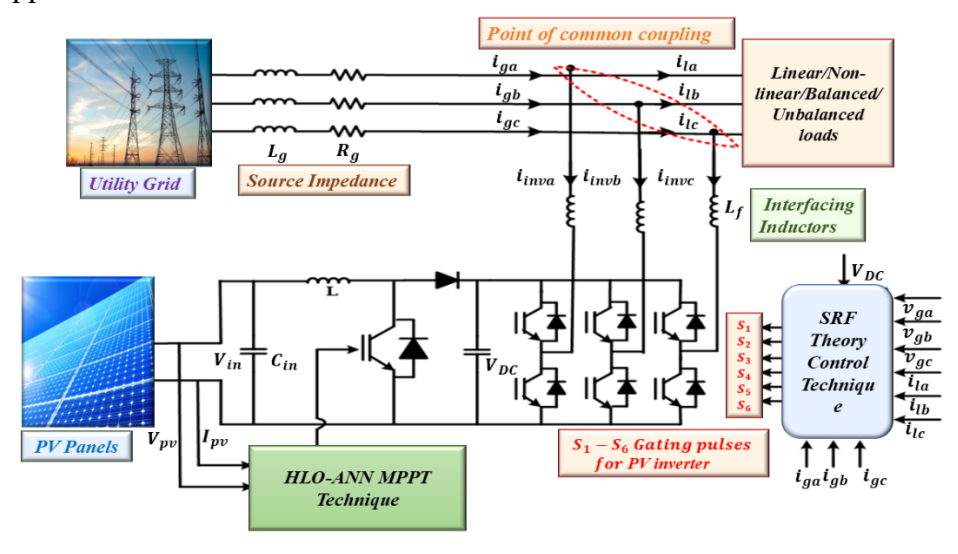


Fig.4.7 Schematic diagram of proposed grid integrated solar PV system.

In the present research work real time dataset for both temperature and irradiance has been downloaded from NASA's open-source website and NREL which provides historical atmospheric data for a certain area. A three-month dataset of northern part of India (Shahabad Daulatpur village Rohini Delhi), and southern part of India (Chikkaballapur, Karnataka) including sun temperature and irradiance have been utilized for this study. The hourly change in irradiance levels demonstrates that solar irradiance fluctuates from 0 W/m²to over 900 W/m². Using an irradiance dataset for constructing the MPPT has the benefit of assisting in training the neural network (ANN) model in accordance with the real-time practical condition of changing irradiance levels across a 24-hour cycle.Fig.4.8 shows the scenarios considered for comparative analysis.

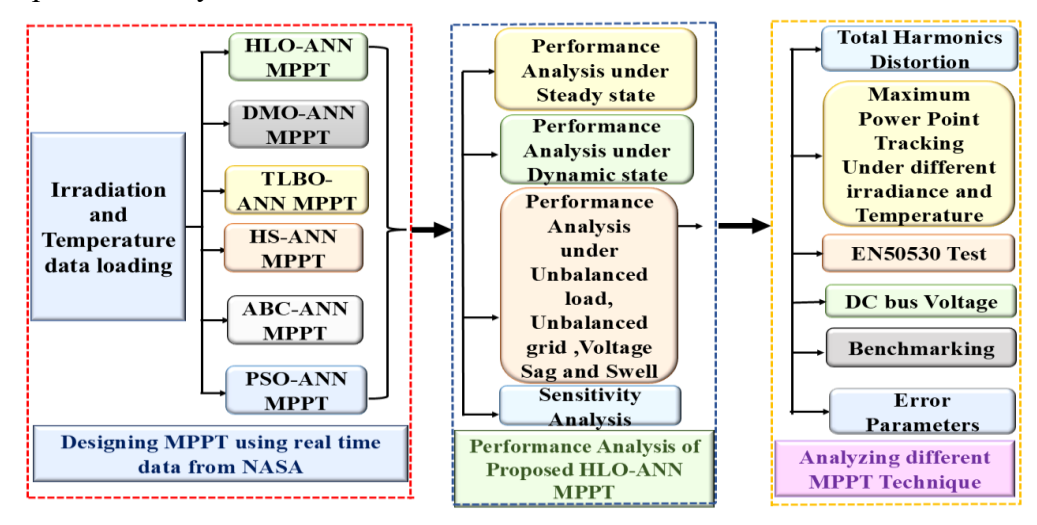


Fig.4.8 Block diagram of scenarios considered during comparative analysis

This section displays the MATLAB/Simulink results for the grid integrated solar PV system's performance assessment. Various input and output situations have been tested to determine the effectiveness of the control method. The performance is also tested in abnormal grid conditions. The photovoltaic (PV) system produces 12.79 kW power. A 3ϕ bridge rectifier with parameters R=180 ohm and L=120 mH is taken as a nonlinear load. The subsequent sections illustrate three phase waveforms representing the following: voltage at the point of common coupling (V_{pcc}) , grid voltage (V_g) , grid current (I_g) , load current (I_l) , inverter current (I_{inv}) , DC bus voltage (V_{DC}) , and the active and reactive power of the load and inverter grid, denoted as P_l , Q_l , P_{inv} , Q_{inv} , P_g , Q_g .

4.3.1 Performance evaluation of the system under variable load and Standard Test Conditions (STC)

In a steady state, the inverter contributes to maintaining the balanced and sinusoidal three phase grid current. Also, the inverter maintains grid current harmonic distortion within IEEE-519 standards and balances the flow of power. Figure 4.9 illustrates the current and power waveforms of the grid, load, and inverter under variable load

conditions and Standard Test Conditions (STC), i.e., solar irradiance of 1000 W/m² and cell temperature of 25°C.".

In the steady-state condition initially a bridge rectifier with RL load (R = 180Ω , 120 mH) has been considered as a nonlinear load, Initially the nonlinear load (1.9kW) demand is fulfilled by the solar PV and excess power (10.64 kW) is sent to the grid. Since, the grid receives the excess power from the source, voltage and current are in phase opposition which can be seen from the waveform.

At t= 0.15 s system's load has been increased to 16.32 kVA with 0.85 lagging power factor (14kW and 8.4 kVAR). At this instance, solar PV provides 12.54kW and deficit power(3.36kW) is taken from the grid. In this condition since grid supply the deficit load hence voltage and current are in phase which can be noticed from Fig.4.9 Also reactive power is supplied by inverter ang grid is maintaining zero reactive power which means system is working under unity power factor mode (UPF) and the DC bus voltage remains constant at 750 V.

Table.4.2 Power sharing among inverter, grid, and load for variable loads condition.

	t=0.0s -0.1	.5s	t=0.15s -0.20s (load is increased)				
$P_l = 1.9 \text{kW}$	<i>P_{inv}</i> =12.5 4kW	P_g =10.64 kW	P _l =1.9kW+14k W=15.9kW	<i>P_{inv}</i> =12. 54kW	P_g =- 3.36kW		
Q_l =0k VAR	$Q_{inv} = 0$ kVAR	Q_g =0	Q_l =8.4kVAR	Q _{inv} =8. 4kVAR	Q_g =0		
$^{D_C(V)}I_I(A) \ I_{Inv}(A) I_g(A) V_{pcc}(V)$		Sinu	soidal and balance grid cu	rent			
V(A) 20 50 70 70 70 70 70 70 70 70 70 70 70 70 70			8				
$\binom{50}{6}$							
20 -20 -20 -20 -20 -20 -20 -20 -20 -20 -	20 20 20 20 20 20 20 20 20 20 20 20 20 2		is maintained at 750V	d current at t = 0.1	***		
1000 500 0 15000		V D(Load increased	at t=0.15s			
8 5000 8 5000					$\begin{array}{c c} P_l(W) \\ Q_l(VAR) \end{array}$		
0 = 0 0 15000 = 0 8 10000							
P _{tnv} 0				eficit norman is to be	$ \begin{array}{c} P_{inv}(W) \\ Q_{inv}(VAR) \end{array} $		
Ø 5000 Ø -5000 Ø -10000	eficit power is taken j	$\begin{array}{c c} Fom the grid \\ \hline P_g(W) \\ \hline Q_g(VAR) \end{array}$					
0.0	5 0	.1 0.15	5 0.2	0.25	$Q_g(VHK)$		

Fig.4.9 Performance of the system under variable load condition

Time (seconds)

4.3.2 Performance evaluation of the System under variable load and irradiation condition

Fig.4.10 shows the performance of the proposed control strategy under variable load and irradiation conditions. Initially the nonlinear load (1.9kW) demand is fulfilled by the solar PV and excess power (10.64 kW) is sent to the grid.

At t=0.15 s, the irradiation level drops from 1000 W/m2 to 650 W/m^2 , resulting in a drop in PV power from 12.54 kW to 7.56 kW. This reduces inverter current (I_{inv}) and grid current (I_g). Load demand (1.9kW) is fulfilled by solar PV power and excess power (5.66kW) is sent to the grid.

At t=0.2s. load is increased to 3.48kW, under this condition as well solar supply the load and excess power (4.08kW) is sent to the grid. Since, the grid receives the excess power from the source, voltage and current are in phase opposition which can be seen from the waveform. The power balance is still being maintained by the system. It is noticeable that the grid current is sinusoidal and balanced in spite of the variable nonlinear load and variable irradiation condition. Also, DC bus voltage remains constant at 750 V.

Table 4.3 Power sharing among inverter, grid, and load for variable load and irradiation conditions.

t=0.0s-0.15s			t=0.15s-decrease	`	adiation		t=0.20s-0.30s (loa increased)		
P _l =1.9 kW	<i>P_{inv}</i> =12. 54kW	P_g =10.6 4kW	$P_l = 1.9 \text{kW}$	P _{inv} =7.5 6kW	P_g =5.6 6kW	P _l =3.4 8kW	<i>P_{inv}</i> =7.5 6kW	P_g =4.0 8kW	
Q_l =0k VAR	$Q_{inv} = 0$ kVAR	$Q_g=0$	Q_l =0k VAR	$Q_{inv} = 0$ kVAR	Q_g =0	Q_l =0k VAR	Q_{inv} =0k VAR	Q_g =0	

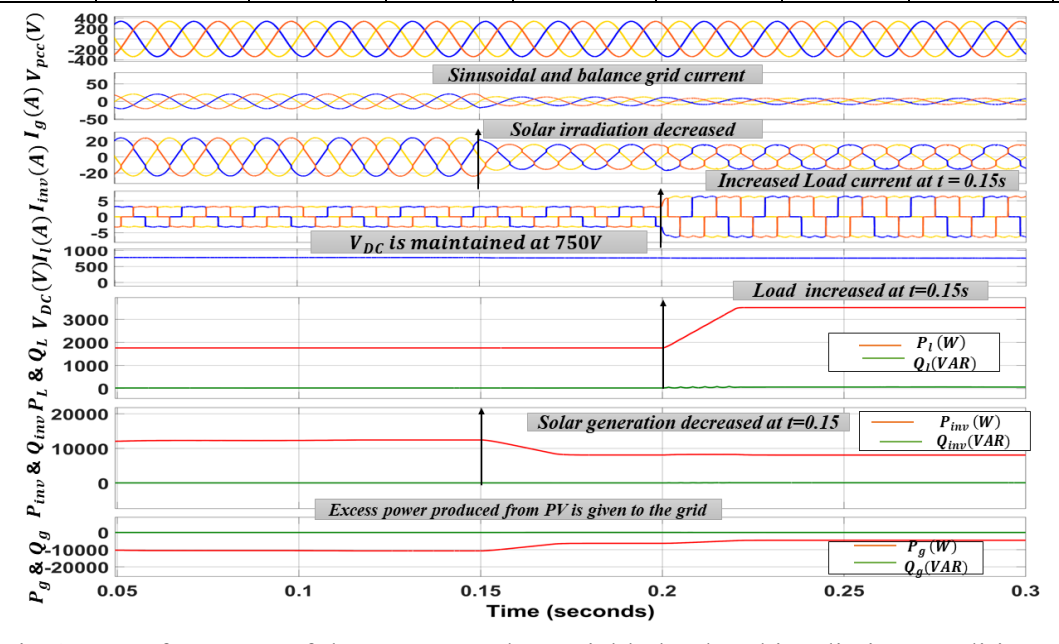


Fig.4.10 Performance of the system under variable load and irradiation condition

4.3.3 Performance evaluation of the System under abnormal grid conditions (Sag, Swell and unbalanced grid voltage) and load unbalance

This section analyses the system's performance at abnormal load and grid voltage conditions. Removing one phase of the load current causes load unbalancing from t=0.06s to 0.12 s, 45V(p-p) voltage decrease from t=0.12 to 0.18 s is causes voltage sag which decreases load current. Similarly, voltage increase of 45V(p-p) from t=0.18-0.24s, causes voltage swell which increases load current, and voltage unbalance occurs from t=0.24-0.30s in the grid voltage, as illustrated in Fig.4.11. Grid currents remain balanced and sinusoidal regardless of abnormal grid and load conditions. DC bus voltage maintained at 750 V.

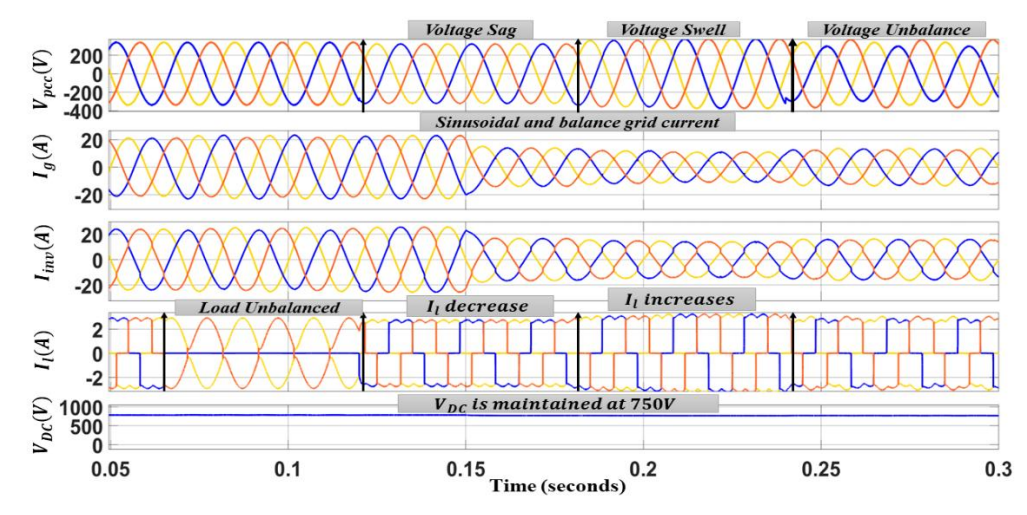


Fig.4.11 Performance of the system under abnormal grid and load unbalance conditions

4.3.4 Sensitivity analysis of HLO-ANN MPPT technique

In this article, a sensitivity analysis of the HLO-ANN assesses how variations in the parameters of the HLO algorithm impact the performance of the ANN, specifically concentrating on search agents and convergence has been presented in Fig.4.12 and Table.4.

The analysis demonstrates that employing 30 search agents for HLO-ANN is ideal since it provides a suitable trade-off between convergence speed and error minimization. While 40 search agents provide a somewhat lower error, their convergence rate is slower, making 30 search agents a more practical choice for efficient optimization. This balance is critical in real-world applications where model correctness and computational economy are equally important. Faster convergence with a decent number of search agents requires fewer computational resources and time to complete. Having a low error while keeping rapid convergence increases the ANN's overall performance in making accurate predictions.

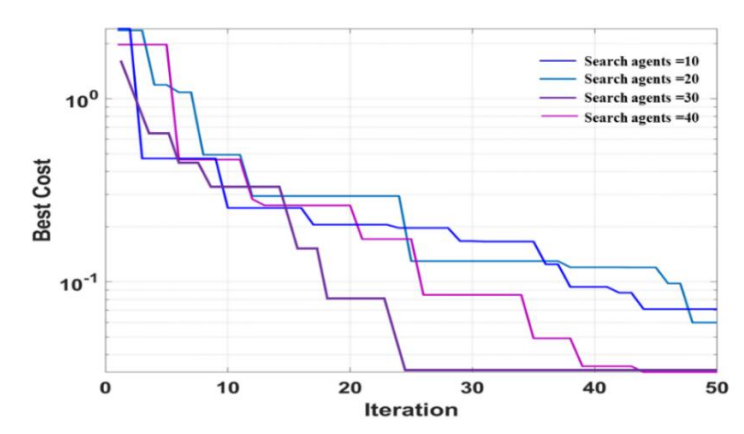


Fig.4.12 Sensitivity analysis for different search agents of proposed HLO-ANN MPPT technique

Table 4.4 Sensitivity analysis for different search agents of proposed HLO-ANN MPPT technique

Search agents	s Error (MSE) Iteration count (Convergence)		Run time (seconds)
10	0.06991	44	153.055
20	0.05952	47	151.321
30	0.03314	24	128.462
40	0.03210	44	134.083

4.4 Comparative analysis of proposed HLO-ANN algorithm

To demonstrate the superiority of the proposed HLO-ANN MPPT technique, various parameters, including grid current harmonics, maximum power tracking under dynamic irradiation, EN50530 MPPT efficiency test, DC bus voltage regulation, cost function and error parameters, are compared to DMO-ANN, TLBO-ANN, HS-ANN, ABC-ANN, and PSO-ANN MPPT algorithms.

4.4.1 Comparative analysis of proposed HLO-ANN algorithm for grid current harmonics

Fig.4.13 shows the grid current (I_{grid}) FFT spectrum for a non-linear load under various load condition and grid voltage conditions. THD for the proposed control algorithm and other compared control algorithms that have been considered in this work are presented in Table 4.5. Table 4.5 shows that the proposed HLO-ANN MPPT contains 1.08% THD in the case of a non-linear load, 1.74% and 1.76% THD under grid voltage sag and swell conditions, and 2.04% and 2.71% THD under grid voltage imbalance and load unbalanced conditions. Table 4.5. shows that, in comparison to previous algorithms, the suggested technique has lower grid current THD. Also, harmonics distortion is with in IEEE standard.

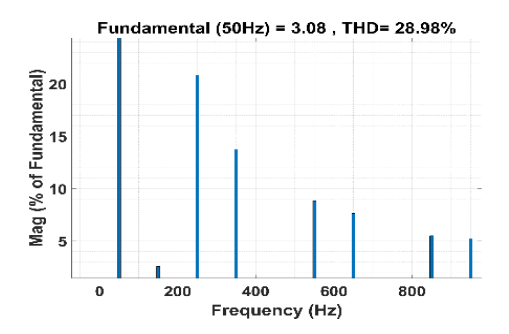


Fig.4.13 (a) FFT spectra of I_{load} for non-linear load,

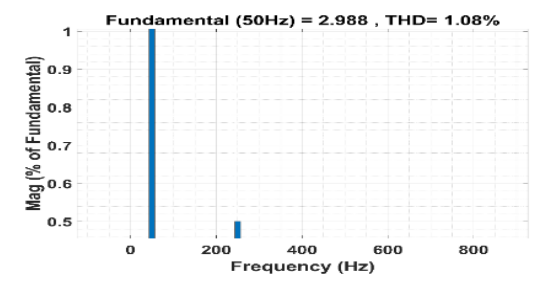


Fig.4.13(b) FFT spectra of I_{grid} for non-linear load,

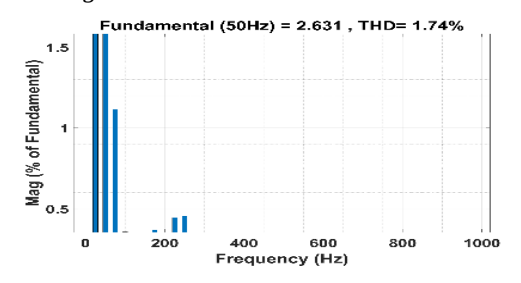


Fig4.13(c) FFT spectra of I_{grid} for grid voltage sag,

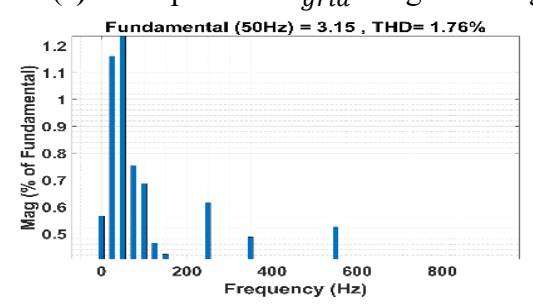


Fig.4.13(d) FFT spectra of I_{grid} for grid voltage swell,

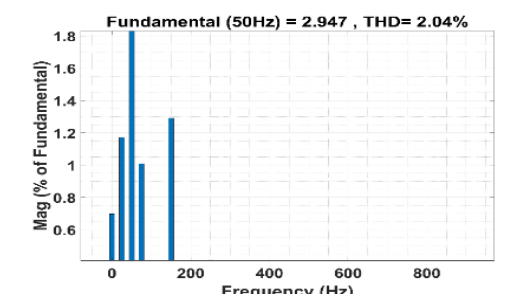


Fig.4.13. (e) FFT spectra of I_{grid} for grid voltage unbalance,

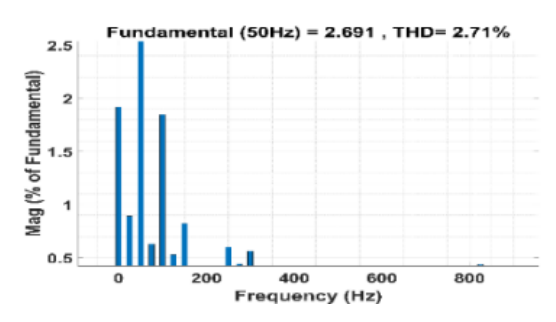


Fig.4.13. (f) FFT spectra of I_{grid} for unbalance load

Fig.4.13. FFT spectra of I_{load} and I_{grid} for proposed HLO-ANN algorithm

Table 4.5 Comparison of FFT spectrum of Proposed HLO-ANN MPPT technique with PSO-ANN, ABC-ANN, HS-ANN, TLBO-ANN, DMO-ANN MPPT techniques for THD in grid current

	Non-	Grid	Grid	Grid voltage	Non- linear
Algorithms	Linear	voltage sag	voltage	unbalance	load
	load		swell		unbalance
P&O	2.52%	3.55%	2.84%	3.61%	3.81%
INC	2.48%	3.29%	2.45%	3.43%	3.62%
PSO	2.41%	3.22%	2.31%	3.25%	3.53%
PSO-ANN	2.39%	3.21%	2.95%	3.22%	3.44%
ABC-ANN	2.25%	2.62%	2.84%	3.19%	3.27%
HS-ANN	2.18%	2.33%	2.51%	2.86%	3.16%
TLBO- ANN	1.75%	2.01%	2.11%	2.71%	2.98%
DMO- ANN	1.11%	1.85%	1.93%	2.42%	2.83%
HLO-ANN	1.08%	1.74%	1.76%	2.04%	2.71%

4.4.2 Comparative analysis of proposed HLO-ANN algorithm for dynamic irradiation variation.

In the present study, the irradiance dataset of northern part (Shahabad Daulatpur village, Delhi) and southern part (Chikkaballapur Karnataka) of India has been taken from the NASA and NREL to test the robustness of the proposed technique in different

geographical location. Fig.4.15 and Table.4.6 presents the comparative analysis of different algorithm employing Shahabad Daulatpur village, Delhi data whereas fig.4.16 and Table 4.6 presents the comparative analysis of different algorithm employing Chikkaballapur Karnataka data. To evaluate various MPPT algorithms, the dynamically reducing solar irradiance pattern of 1000, 800, 600, and 400 W/m² has been used in this particular case. In Fig.4.14, the power versus voltage curve illustrates the maximum power at various irradiance. The maximum power tracked by the grid integrated solar photovoltaic system (SPS). through various MPPT algorithm is shown in Fig.4.15, Fig 4.16 and Table 4.6, Table 4.7. After examining the enlarged regions more closely and referring to Tables 4.6 and 4.7, it is apparent that the HLO-ANN algorithm has better tracking performance than the other techniques in various geographical locations. The maximum power tracked by the proposed technique is higher, indicating the algorithm's robustness even in diverse geographical locations.

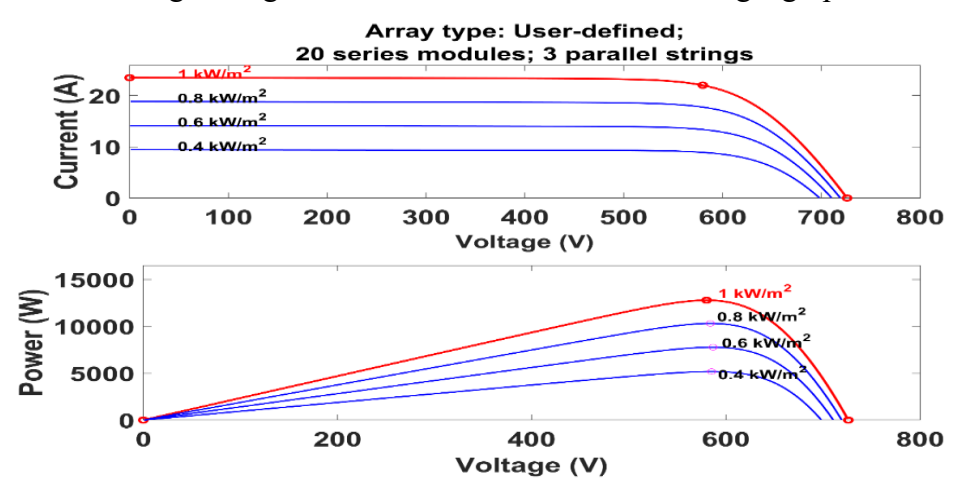


Fig.4.14 P-V and I-V characteristics for different irradiation of solar array

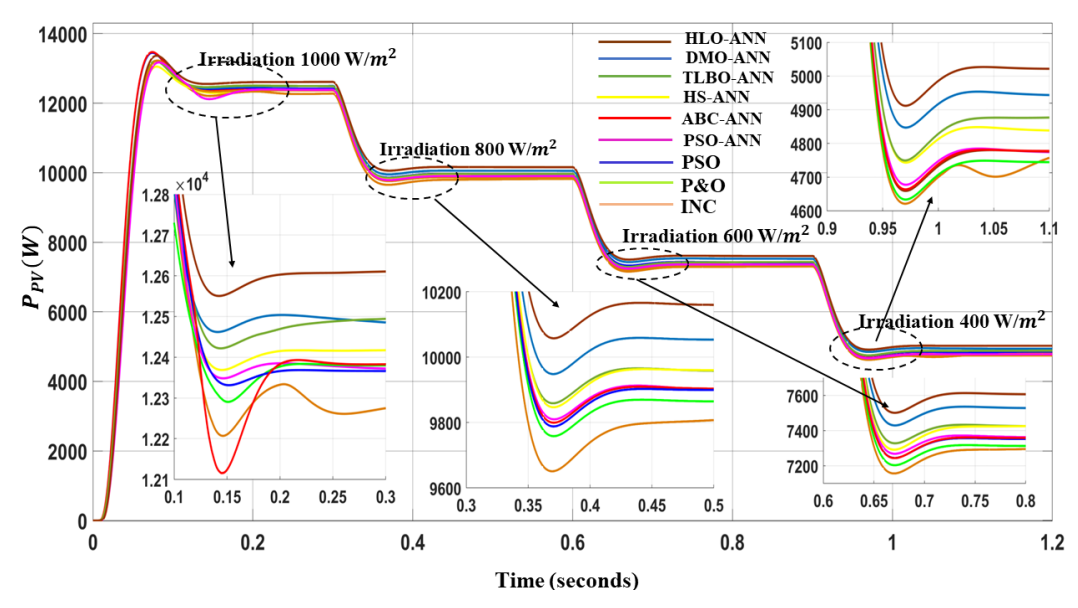


Fig.4.15 Maximum power tracked under dynamic irradiation variations (Shahabad Daulatpur village data)

Table.4.6 Comparison of Proposed HLO-ANN MPPT technique with PSO-ANN, ABC-ANN, HS-ANN, TLBO-ANN, DMO-ANN, PSO, INC and P&O MPPT techniques for maximum power tracking under different irradiation condition (Shahabad Daulatpur village data)

Algorithm	n Irradiance	P&O	INC	PSO	PSO - ANN	ABC - ANN	HS- ANN	TLB O- ANN	DM O- ANN	HLO - ANN
1000	P _{max} (kW)	12.29	12.3	12.3 7	12.3	12.3	12.4	12.5	12.5	12.6
(W/m ²)	Settling Time (s)	0.30	0.20	0.23	0.24	0.22	0.21	0.28	0.31	0.20
800	P _{max} (kW)	9.8	9.86	9.88	9.94	9.95	9.98	9.98	10.1	10.1 9
(W/m ²)	Settling Time(s)	0.17	0.11	0.16	0.14	0.14	0.13	0.14	0.13	0.11
600	P _{max} (kW)	7.32	7.37	7.40	7.40	7.41	7.43	7.42	7.51	7.62
(W/m ²)	Settling Time(s)	0.15	0.14	0.14	0.13	0.15	0.17	0.15	0.12	0.11
400	P _{max} (kW)	4.73	4.74	4.74	4.76	4.75	4.83	4.87	4.95	5.02
(W/m ²)	Settling Time(s)	0.20	0.15	0.16	0.16	0.15	0.16	0.14	0.15	0.14

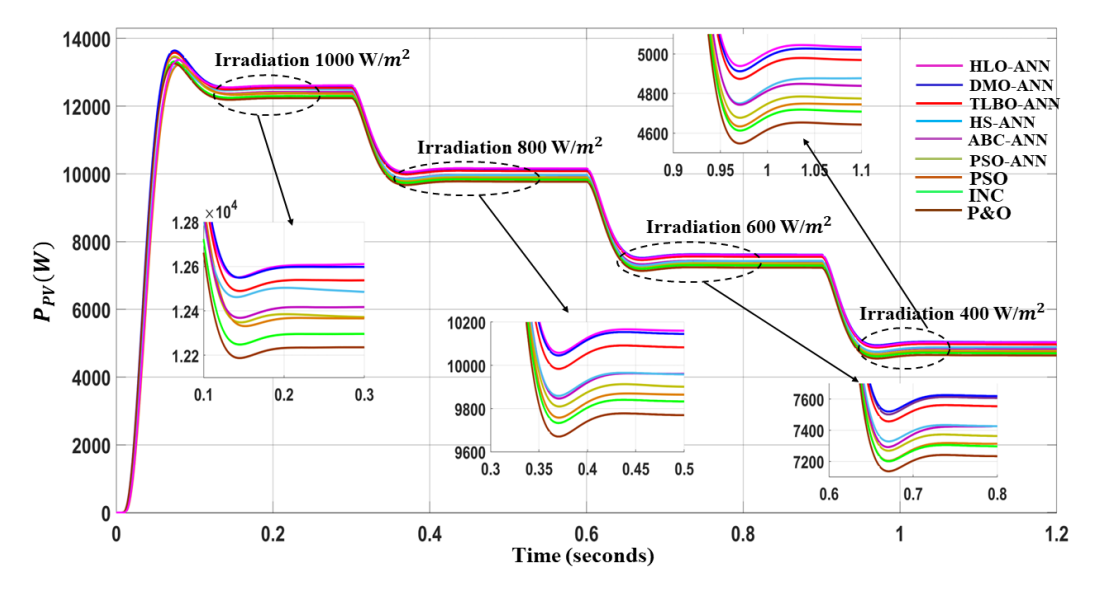


Fig.4.16 Maximum power tracked under dynamic irradiation variations (Chikkaballapur Karnataka data)

Table 4.7 Comparison of Proposed HLO-ANN MPPT technique with INC, P&O, PSO, PSO-ANN, ABC-ANN, HS-ANN, TLBO-ANN and DMO-ANN MPPT techniques for maximum power tracking under different irradiation condition (Chikkaballapur Karnataka data)

Algorithm	n	P&O	INC	PSO	PSO	ABC	HS-	TLB O-	DM O-	HLO
					ANN	ANN	ANN	ANN	ANN	ANN
/ Iı	rradiation									
	P_{max}	12.3	12.3	12.3	12.4	12.4	12.4	12.5	12.5	12.6
1000	(kW)	0	9	9	1	0	7	5	8	9
(W/m^2)	Settling	0.29	0.20	0.23	0.23	0.22	0.21	0.27	0.30	0.20
	Time (s)									
	P_{max}	9.81	9.87	9.88	9.95	9.95	9.98	9.99	10.1	10.2
800	(kW)								9	3
(W/m^2)	Settling	0.17	0.12	0.16	0.14	0.15	0.13	0.14	0.12	0.11
	Time(s)									
	P_{max}	7.33	7.39	7.40	7.41	7.41	7.43	7.45	7.53	7.66
600	(kW)									
(W/m^2)	Settling	0.15	0.14	0.14	0.13	0.15	0.17	0.15	0.12	0.11
	Time(s)									
	P_{max}	4.73	4.75	4.75	4.76	4.76	4.83	4.88	4.98	5.07
400	(kW)									
(W/m^2)	Settling	0.20	0.15	0.16	0.16	0.15	0.16	0.14	0.15	0.15
	Time(s)									

4.4.3 Comparative analysis of proposed HLO-ANN algorithm for dynamic temperature variation.

The HLO-ANN algorithm produces the highest maximum power production at 25°C (12.68 kW) as can be seen from Fig.4.17 and Table 4.8. As the temperature rises to 35°C and 45°C, all algorithms see a decline in maximum power production. At 45°C, HLO-ANN still has the highest Pmax among the algorithms, but it is significantly reduced to 11.59 kW. Most algorithms' settling times decrease as the temperature rises. The table clearly shows that HLO-ANN has the highest maximum power tracked at 25°C compared to other methods. The power output, however, declines when the temperature rises to 35°C and 45°C. This pattern is consistent with the typical behaviour of solar cells, which reduce efficiency as temperatures rise.

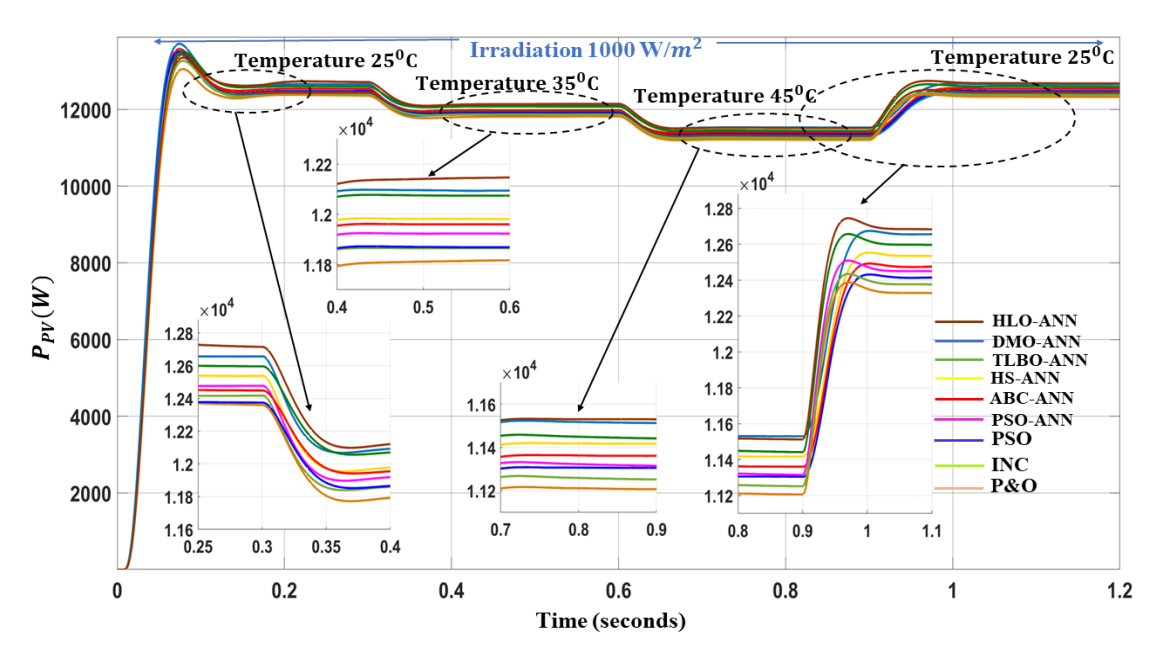


Fig4.17 Maximum power tracked using HLO-ANN MPPT technique and with other existing MPPT technique under different temperature condition

Table 4.8 Comparison of Proposed HLO-ANN MPPT technique with INC, P&O, PSO, PSO-ANN, ABC-ANN, HS-ANN, TLBO-ANN, DMO-ANN MPPT techniques for maximum power tracking under different temperature (Temp.)

Algo-	Temp. (25°C)	Settling Time	Temp. (35°C)	Settling Time	Temp. (45°C)	Settling Time	Temp. (25°C)	Settling Time
rithm	P _{max} (kW)	sec	P _{max} (kW)	sec	P _{max} (k W)	sec	P _{max} (kW)	sec
P&O	12.41	0.22	11.82	0.14	11.21	0.12	12.41	0.12
INC	12.42	0.20	11.94	0.13	11.31	0.14	12.42	0.12
PSO	12.44	0.21	11.94	0.12	11.32	0.19	12.43	0.13
PSO- ANN	12.52	0.22	11.96	0.12	11.35	0.20	12.52	0.12
ABC- ANN	12.55	0.23	11.96	0.11	11.38	0.20	12.55	0.12
HS- ANN	12.58	0.24	11.97	0.12	11.50	0.14	12.58	0.12
TLBO -ANN	12.60	0.24	12.15	0.09	11.52	0.17	12.60	0.11
DMO- ANN	12.63	0.22	12.17	0.11	11.58	0.19	12.63	0.10
HLO- ANN	12.68	0.20	12.18	0.11	11.59	0.10	12.68	0.09

4.4.4 MPPT Efficiency test EN50530

One of the standard testing conditions applied to a grid integrated SPS system is the EN50530 MPPT efficiency test, which evaluates the MPPT algorithm's performance under dynamically varying circumstances. An analysis of the MPPT techniques under dynamic changes in irradiance level has been conducted in this specific case, taking into account both fast and slow variation in irradiance level.

The design of the slow and fast irradiance levels was accomplished by employing the trapezoidal signal, as illustrated in Fig.4.18. MATLAB 2023a simulation environment was used to analyse the power achieved by all MPPTs based on irradiance level variations. Fig.4.19 depicts the maximum power achieved by several MPPT algorithms in the EN50530 efficiency test. According to Fig.4.19 and Table.4.9 the HLO-ANN MPPT method that has been proposed achieves the highest power (Pmax). The HLO-ANN MPP performs extremely well at lower levels of irradiance, as demonstrated by the maroon colour curve. This is also evident for the ANN-HHO MPPT, which functions most effectively at higher levels of irradiance.

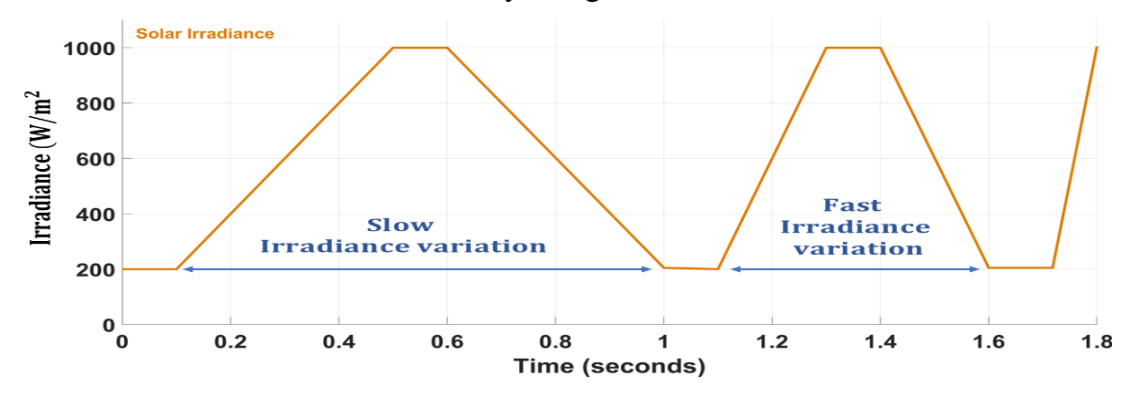


Fig.4.18 Dynamic variation in irradiation level for the standard MPPT efficiency test of EN 50530

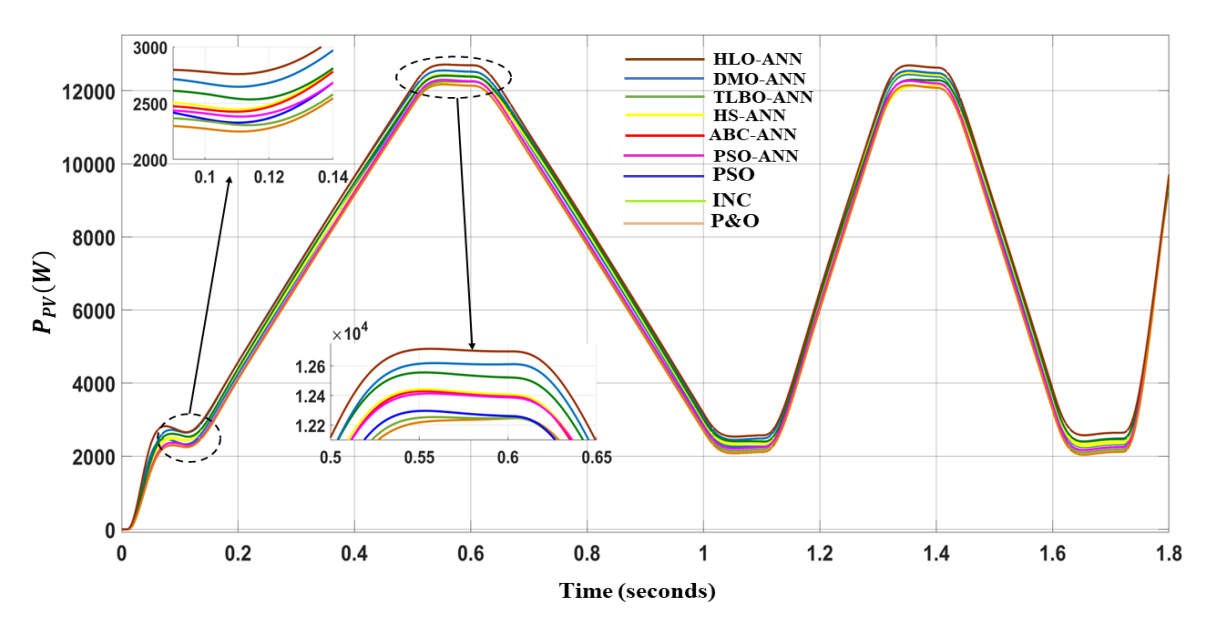


Fig4.19 Power versus time graphs for different MPPT algorithms

Table 4.9 Comparison of Proposed HLO-ANN MPPT technique with INC, P&O, PSO, PSO-ANN, ABC-ANN, HS-ANN, TLBO-ANN, DMO-ANN, PSO, INC and P&O MPPT techniques for ENE530 Test.

Algorithms	Irradiance 200W/m ²	Irradiance 1000W/m ²	Irradiance 200W/m ²	Irradiance 1000W/m ²
	(0.0s-0.2s)	(0.4s-0.7s)	(1.0s-1.2s)	(1.3s-1.4s)
	$P_{max}(kW)$	P_{max}	P_{max}	P_{max}
P&O	2.44	12.22	2.44	12.22
INC	2.45	12.22	2.45	12.22
PSO	2.47	12.23	2.47	12.23
PSO-ANN	2.48	12.44	2.48	12.44
ABC-ANN	2.48	12.47	2.48	12.47
HS-ANN	2.49	12.47	2.49	12.47
TLBO-ANN	2.56	12.54	2.56	12.54
DMO-ANN	2.61	12.60	2.61	12.60
HLO-ANN	2.68	12.68	2.68	12.68

4.4.5 Transient analysis of DC bus voltage at different irradiation

Fig.4.20 depicts the transient response of DC bus voltage for the proposed HLO-ANN and other MPPT algorithms, namely DMO-ANN, TLBO-ANN, HS-ANN, ABC-ANN, PSO-ANN, PSO, INC and P&O. The response of all algorithms to non-linear load has been examined under various irradiation situations. The suggested HLO -ANN algorithm has a better response in terms of settling time, undershoot, overshoot and maintaining the DC bus voltage at 750 regardless of irradiation level fluctuation. Table.4.10 shows that the proposed HLO-ANN MPPT has a shorter settling time than other MPPT algorithms at each case of irradiance level.

Table.4.10 Transient analysis of DC bus voltage using proposed HLO-ANN and DMO-ANN, TLBO-ANN, HS-ANN, ABC-ANN, and PSO-ANN for non-linear load

S.No	Control	Time	Irradiation	Settling	DC bus	Remarks
	techniques	(seconds)	(W/m^2)	time	Voltage	
				(seconds)	(V)	
1.	P&O	0.0 s - 0.1s	1000	0.062	750	Initial overshoot
		0.1s -0.2s	800	0.060	750	of 15V is present
		0.2s-0.3s	600	0.061	750	Undershoot of
		0.3s-0.4s	400	0.061	750	12V present
2.	INC	0.0 s - 0.1s	1000	0.610	750	Initial overshoot
		0.1s -0.2s	800	0.060	750	of 20V is present

		0.2s-0.3s	600	0.060	750	Undershoot of
		0.3s-0.4s	400	0.061	750	11V present
3.	PSO	0.0 s - 0.1s	1000	0.053	750	Initial overshoot
		0.1s -0.2s	800	0.069	750	of 40V is present
		0.2s-0.3s	600	0.069	750	Undershoot of
		0.3s-0.4s	400	0.069	750	10V present
4.	PSO-ANN	0.0 s - 0.1s	1000	0.063	750	Initial overshoot
		0.1s -0.2s	800	0.065	750	of 51V is present
		0.2s-0.3s	600	0.065	750	Undershoot of
		0.3s-0.4s	400	0.065	750	9V present
5.	ABC-	0.0 s - 0.1s	1000	0.063	750	Initial overshoot
	ANN	0.1s -0.2s	800	0.061	750	of 40V is present
		0.2s-0.3s	600	0.068	750	Undershoot of
		0.3s-0.4s	400	0.068	750	8V present
6.	HS-ANN	0.0 s - 0.1s	1000	0.019	750	Initial overshoot
		0.1s -0.2s	800	0.062	750	of 15V is present
		0.2s - 0.3s	600	0.062	750	Undershoot of
		0.3s-0.4s	400	0.061	750	8V present
7.	TLBO-	0.0s - 0.1s	1000	0.050	750	Initial overshoot
	ANN	0.1s -0.2s	800	0.051	750	of 20V is present
		0.2s -0.3s	600	0.069	750	Undershoot of
		0.3s-0.4s	400	0.069	750	7V present
8.	DMO-	0.0 s - 0.1s	1000	0.051	750	Initial overshoot
	ANN	0.1s -0.2s	800	0.050	750	of 15V is present
		0.2s -0.3s	600	0.040	750	Undershoot of 5V present
		0.3s-0.4s	400	0.040	750	
9.	HLO-	0.0s - 0.1s	1000	0.050	750	Initial overshoot of 15V is present
	ANN	0.1s -0.2s	800	0.020	750	
		0.2s -0.3s	600	0.020	750	Undershoot is
		0.3s-0.4s	400	0.020	750	negligible

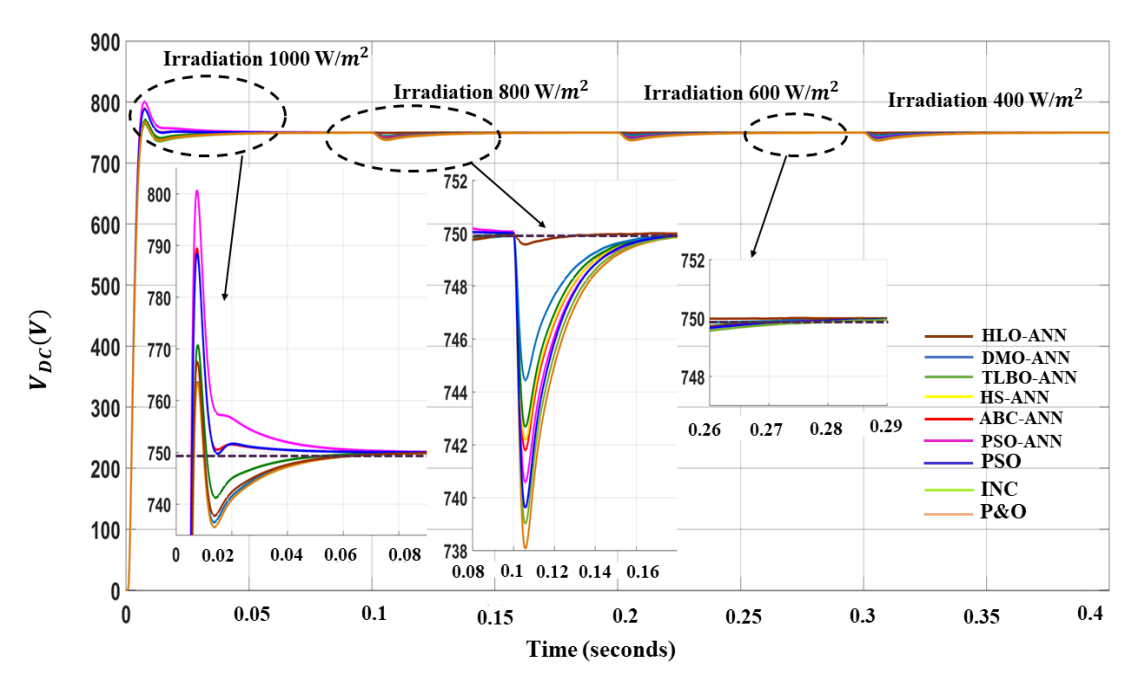


Fig.4.20 Transient analysis of DC bus voltage proposed HLO-ANN and DMO-ANN, TLBO-ANN, HS-ANN, ABC-ANN, and PSO-ANN for non-linear load.

4.4.6 Comparison of convergence rate and error parameters of different algorithms

One important parameter for evaluating the performance of any optimization approach is its convergence rate. As a result, all algorithms were subjected to a minimum cost function with the same number of iterations, boundary conditions, and search agents. Fig.4.21 depicts the convergence curves for all six algorithms. The chart shows that HLO-ANN outperforms the other five methods in terms of convergence speed and optimal solution capture. To minimize the mean square error, the curve with the lowest MSE optimization value was chosen. Fig.4.21 and Table 4.11 show that the HLO-ANN produced a higher-quality solution with a faster convergence time, whereas the other methods produced lower-quality solutions with premature convergence. Two additional error parameters, root mean square error (RMSE) and mean absolute error (MAE), have been investigated to strengthen algorithm analysis. The proposed HLO-ANN algorithm requires fewer iterations to converge with lower error parameters, whereas other algorithms require more iterations and have higher error values when compared to the HLO-ANN MPP technique, as shown in Fig.4.21 and Table 4.11.

4.4.7 Validation of the proposed algorithm considering test data set

Fig 4.22. presents the graph of absolute error between the ground truth and the estimates of the trained neural network along with the plot of ground truth verses the estimates of the neural network of the test data set for the unseen data. It is observed that absolute error is considerably low which confirms that the trained network performs significantly well on the unseen data and therefore can manage to track MPP during real time operations.

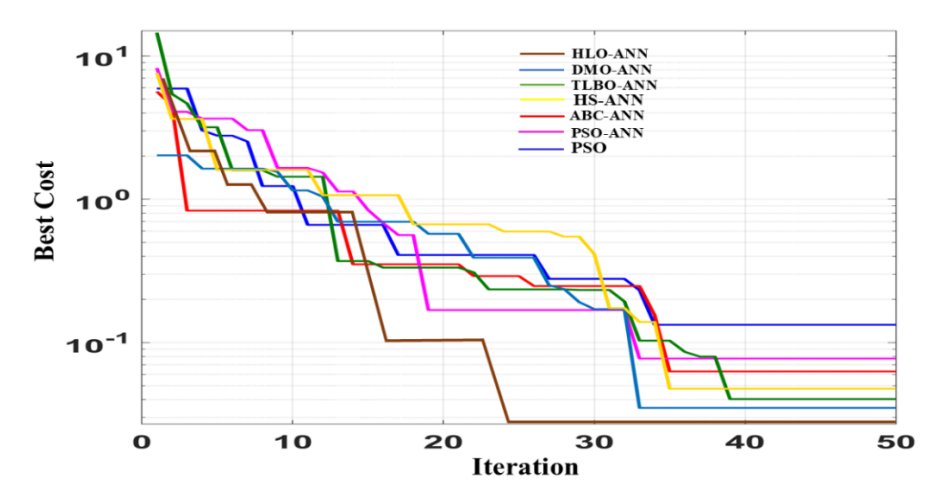


Fig.4.21 Convergence curve of all the algorithms

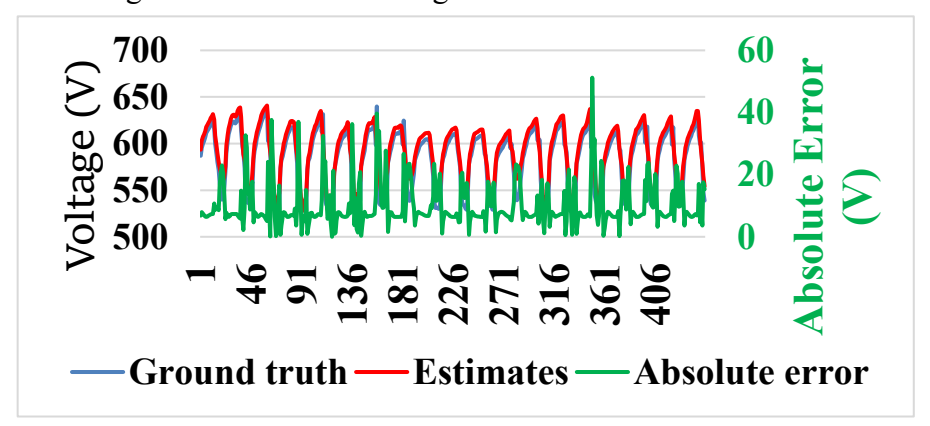


Fig.4.22 Validation of trained neural network

Table 4.11 Error parameters analysis for different MPPT algorithms

Algorithms	Mean Square Error (MSE) MSE $= \frac{1}{n} \sum_{i=1}^{n} \sum_{j=1}^{m} (Y_j(i) - T_j(i))^2$	Root Mean Square Error (RMSE) RMSE $= \sqrt{\frac{1}{n} \sum_{i=1}^{n} \sum_{j=1}^{m} (Y_j(i) - T_j(i))^2}$	Mean Absolute Error (MAE) MAE $= \frac{1}{n} \sum_{i=1}^{n} \sum_{j=1}^{m} (Y_j(i) - T_j(i))$
PSO	0.12997	0.36051	0.28778
PSO-ANN	0.07597	0.27562	0.21997
ABC-ANN	0.05997	0.24488	0.19546
HS-ANN	0.04697	0.21672	0.17300.
TLBO-ANN	0.03987	0.19967	0.15938.
DMO-ANN	0.03418	0.18487	0.14756
HLO-ANN	0.03306	0.18182	0.14512

4.4.8 Benchmark analysis

An essential step in assessing the efficacy and performance of the Horned Lizard Optimization-ANN (HLO-ANN) technique is benchmarking. It gives users a comprehensive and nuanced understanding of the benefits that HLO-ANN offers, empowering them to decide on its possible acceptance and future development. The HLO-ANN technique offers substantial improvements when compared to widely accepted traditional MPPT methods.

Table.12 Benchmarking performance of proposed HLO-ANN MPPT techniques with other MPPT techniques

Metric	P&O	INC	PSO	PSO-	ABC-	HS-	TLB	DMO	HLO-
Metric	1 & O	INC	130						
				ANN	ANN	ANN	О-	-ANN	ANN
							ANN		
Tracking	Slow	Mid	High	High	High	High	High	Very	Very
Efficiency								High	High
Tracking	Low	Mid	Mid	High	High	High	High	Very	Very
Accuracy								High	High
Convergen	Slow	Mid	Mid	Mid	Mid	Fast	Fast	Very	Very
ce Speed								Fast	Fast
Dynamic	Slow	Slow	Mid	Mid	Mid	Fast	Fast	Fast	Very
response									Fast
Prior	No	No	Yes						
tuning									
Tuning	High	High	Mid	Low	Low	Low	Low	Low	Low
Complexity									
Varying	Slow	Slow	Mid	Mid	Mid	Fast	Fast	Very	Very
atmospheri								Fast	Fast
c condition									
Simulation	Low	Low	Mid	Mid	High	High	High	High	Very
time									High

4.4.9 COMPUTATIONAL COMPLEXITY ANALYSIS

Computational complexity

Computational complexity evaluates the resources—time and memory—required by an algorithm as the input size increases. In optimization algorithms, particularly those involving a population of agents or candidate solutions, this complexity can be broken down as follows:

Time Complexity is a measure of how the running time of an algorithm grows with respect to key input parameters (such as number of agents, problem dimensions, and number of iterations). It expresses this growth asymptotically (e.g. using Big-O

notation), ignoring constant factors and lower-order terms. In optimization, common parameters involved include:

n = number of agents / candidate solutions / population size

d = number of decision variables / dimension of the search space

T = number of iterations.

Space complexity quantifies the amount of memory an algorithm uses relative to the input size. In optimization algorithms, space complexity is influenced by factors such as:

Memory required for storing agent positions and velocities: Typically, O(nd)

Memory for storing fitness values: O(d)

Memory for auxiliary data structures: Varies depending on the algorithm

The total space complexity is the sum of these components. For instance, if an algorithm requires O(nd) memory for storing agent positions and velocities and O(n) for storing fitness values, the overall space complexity would be O(nd)

Computational Complexity Analysis

Let n denote the number of agents, d the dimensionality of each agent's solution vector, and T the total number of iterations. We assume that basic operations (arithmetic, comparisons, random sampling, trigonometric functions, boundary checks, etc.) take constant time O(1), and that vector updates and fitness evaluation require time proportional to d.

In each iteration, the algorithm performs several procedures: Crypsis Behavior, Skin Lightening/Darkening, Blood Squirting, Move to Escape, Alpha-Melanophore, and Fitness Evaluation.

In the worst case, many of these update all n agents, each across d dimensions, resulting in O(nd) cost per procedure. Since all such procedures contribute on the same order, the aggregate cost per iteration remains: O(nd)

Thus, over T iterations, the total time complexity is:O(T.n.d)

The space complexity is O(nd), for storing the population and their associated data (fitness, best/worst etc.), plus lower-order overheads.

In practice, the algorithm's runtime is often less than the worst-case bound, because some procedures act only on subsets of agents (e.g. only the worst-performing agents, or those with low melanophore rate), and because convergence may occur well before T reaches its maximum. Empirical measurements in the MATLAB implementation confirm linear scaling with n and with d, validating the theoretical bound.

Table.13 Computational Complexity Analysis of HLO Algorithmic Procedures

Procedure	Agents Involved	Work per agents	Total per iteration
Initialization	All n agents once	Set up positions in	O(nd) (but this is
	(at start)	d dims, maybe	a one-time cost,
		initial fitness	not per iteration)
		evaluations →	,
		O(d) per agent	
Crypsis Behaviour	All n agents	Vector updates	0(nd)
(Approach 1)	_	over d dims +	, ,
		constant number	
		of trigonometric +	
		random ops →	
		O(d) each	
Skin Lightening /	Worst k agents,	For each affected	
Darkening	where $k \leq$	agent: vector	
(Approach 2)	nWorst case $k =$	update plus	Worst case $O(nd)$
	$\mid n \mid$	constant overhead	
		\rightarrow	
		O(d) each	
Blood Squirting /	All n agents	Vector updates	0(nd)
Projectile Motion		over d dims +	
(Approach 3)		constant	
		operations (sin,	
		$\cos, \text{ etc.}) \rightarrow$	
		O(d) each	
Move to Escape	All n agents	Random	0(nd)
(Approach 4)		walk/perturb +	
		vector update	
		over d dims →	
		O(d) each	
Alpha-Melanophore	All n agents for	Fitness	Worst case $O(nd)$
Rate (Approach 5)	fitness	normalization	worst case o (na)
Rate (Approach 3)	normalization; a	across n agents →	
	subset (say k') for	O(n); those	
	vector updates	changed \rightarrow vector	
	depending on	updates → vector	
	rate; worst case	O(d) per agent	
	$(k \approx n)$	o (a) per agent	
Fitness Evaluation	All n agents each	Evaluating fitness	<i>O(nd)</i>
1 mess 13 mauron	iteration	over d dims →	()
		O(d) per agent	
		o (u) per agent	

δ -Procedure /		Constant time per	Total overhead of
Random Sampling / Utility Functions	Used in many procedures; either per agent or per update; but each usage is $O(1)$	use	these is $O(n)$ or lower, dominated by the $O(nd)$ terms

Per-Iteration Cost

Putting all together, almost all major procedures have worst-case cost O(nd). Adding them up still gives per iteration cost:

Per – iteration
$$cost = O(nd) + O(nd) + O(nd) + \cdots + O(nd) = O(nd)$$
 (4.45)
(The extra $O(n)$ or $O(1)$ terms are lower order, hence subsumed by $O(nd)$)

Total Time Complexity

Since the algorithm runs for T iterations, the overall time complexity is: O(T.n.d)

"Since the dominant cost in nearly all procedures is O(nd) per iteration, the combined per-iteration complexity is O(nd), and over T iterations the total worst-case time complexity is O(T.n.d)".

4.4.10 SCALABILITY AND COST IMPLICATION OF HLO-ANN MPPT CONTROLLERS

The Horned Lizard Optimization—Artificial Neural Network (HLO–ANN) MPPT technique improves MPP tracking accuracy by using optimized ANN weights and bias values. Its deployment in real-world PV microgrids has unique scalability and cost considerations.

Scalability

- Hardware: ANN-based MPPT algorithms demand higher computational resources than conventional methods. Real-time implementation is feasible on Digital Signal Processors (DSPs), Field-Programmable Gate Arrays (FPGAs), or high-end microcontrollers, which have become increasingly affordable. Retraining the model is necessary only when the system encounters scenarios not previously represented in the training data. For small-scale photovoltaic (PV) arrays (e.g., 10–50 kW), standalone DSPs are sufficient. However, for megawatt-scale plants, distributed or cloud-assisted controllers may be required to handle the increased complexity and data processing demands.
- Data Dependence: ANN requires historical data (irradiance and temperature) for effective training. In rural setups, such datasets may be scarce or unreliable, limiting scalability. In industrial systems, SCADA ensures abundant, high-quality data.
- Algorithmic Load: HLO has a computational complexity of approximately

O(n×m) (population × iterations). This is acceptable for offline optimization of ANN weights, but frequent online retraining in resource-constrained rural systems could hinder scalability.

Cost and Practical Implications

- The deployment of intelligent controllers entails additional CAPEX (Capital Expenditure) for hardware and sensors, which can be significant in rural microgrids but marginal in industrial systems. OPEX (Operating Expenditure) primarily relates to maintenance and algorithm retraining, posing challenges in areas with limited technical expertise, while being easily manageable in industrial setups.
- In terms of energy yield, small rural systems experience modest gains with longer payback periods, whereas even minor efficiency improvements in large industrial microgrids translate into substantial additional generation and faster cost recovery. Thus, scalability remains constrained in rural contexts unless supported by subsidies or pre-trained models, while industrial environments with advanced infrastructure offer clear cost-benefit advantages.

4.5 CONCLUDING REMARKS

This chapter presents a novel control technique for Maximum Power Point Tracking (MPPT) in grid-integrated solar PV systems, utilizing a Horned Lizard Optimizationbased Artificial Neural Network (HLO-ANN). The proposed control algorithm has undergone rigorous testing and validation under a variety of operating conditions. These conditions include variable load scenarios, changes in solar irradiance, temperature fluctuations, grid voltage sag and swell events, unbalanced load situations, and other abnormal grid conditions. To thoroughly evaluate the performance of the proposed HLO-ANN control algorithm, a comparative analysis was conducted against other existing control techniques. The criteria for comparison included grid current harmonic distortion, the efficiency of maximum power point tracking at different levels of irradiance and temperature, performance on the EN50530 MPPT test, DC bus voltage regulation, convergence rate, sensitivity analysis and benchmarking functions. The results from these tests showed that the HLO-ANN algorithm exhibited significant improvements across all evaluated metrics. Specifically, it demonstrated superior capabilities in tracking the maximum power point, regulating voltage, mitigating grid current harmonics, improving convergence rates, and minimizing errors when compared to the other algorithms considered in the study. Furthermore, the HLO-ANN algorithm ensured the maintenance of a unity power factor mode of operation, and the total harmonic distortion of grid current was well below the acceptable threshold of 5%. This indicates that the proposed control technique not only enhances the efficiency of solar PV systems but also adheres to industry standards for power quality.

CHAPTER-5

INVERTER CONTROL TECHNIQUES FOR GRID-INTEGRATED PV BASED MICROGRID

5.1 INTRODUCTION

The previous chapters examined MPPT strategies for standalone and grid-connected PV systems. While MPPT ensures optimal power extraction and grid synchronization, effective grid integration also requires precise inverter control for maintaining power quality and stability. Integration of SPV with grid is achieved by voltage source inverter (VSI), which is responsible for DC–AC conversion and plays a very important role in grid synchronization. Proportional integral (PI) controller plays a crucial role in integration of SPV with grid including voltage regulation and frequency control.

Conventional proportional-integral (PI) controllers are commonly used to regulate VSI operation. However, these controllers typically rely on fixed gain parameters that are optimized for specific operating scenarios. As a result, their performance can significantly deteriorate when faced with unpredictable changes in solar irradiance, ambient temperature, loading patterns, and nonlinear grid conditions. One of the most critical tasks in this context is the regulation of the DC link voltage, which is sensitive to both renewable generation variability and load disturbances. Fixed-gain PI controllers often struggle to maintain stability and exhibit delayed responses, leading to issues such as voltage overshoots, undershoots, and persistent oscillations.

To address these limitations, this chapter proposes adaptive control schemes that dynamically adjust the proportional–integral (PI) controller gains in real-time. Two nature-inspired optimization techniques—Honey Badger Algorithm (HBA) and Cuckoo Search Optimization (CSO)—have been proposed and implemented in MATLAB to enhance the performance of microgrid. These algorithms continuously optimize the controller parameters based on system feedback, aiming to minimize deviations in the DC link voltage and enhance the overall dynamic response of the system. In addition to these, an Artificial Neural Network (ANN)-based PI control approach is also studied, leveraging data-driven learning to further improve adaptability under rapidly changing conditions.

Throughout this chapter, the Incremental Conductance (INC) algorithm is consistently used for Maximum Power Point Tracking (MPPT) in conjunction with the proposed and explored inverter control strategies. However, in Section 5.6, a dedicated comparative analysis is presented, wherein the HLO-ANN-based MPPT technique—developed in Chapter 4—is compared with the proposed inverter control approaches from this chapter. This comparison is aimed at evaluating the overall effectiveness and synergy of both independently developed techniques under diverse operating scenarios.

5.2 INVERTER CONTROL TECHNIQUES FOR GRID INTEGRATED SOLAR PV SYSTEM

Section 2.4 of Chapter 2 discusses several inverter control algorithms for grid-integrated solar PV systems, including linear, predictive, adaptive, intelligent, and robust controllers. These control approaches are critical in guaranteeing effective power injection into the system while preserving stability and power quality. This chapter will expand on that idea by focusing on specific inverter control strategies, such as the Synchronous Reference Frame Theory (SRFT) control technique, which is frequently utilized for grid synchronization and power quality improvement. Furthermore, the chapter will look at the traditional Proportional-Integral (PI) controller, which is widely used in PV inverters because to its simplicity and efficacy in regulating voltage and current.

Advanced PI controllers, including the ANN-based PI controller, which use machine learning for adaptive control, will be discussed in order to enhance system performance. The Cuckoo Search Optimization (CSO)-PI controller, which uses metaheuristic optimization to optimize control parameters for improved dynamic response, will also be demonstrated. Finally, to increase the robustness and efficacy of the inverter control, the Honey Badger Algorithm (HBA)-PI controller will be studied using bio-inspired optimization techniques. This chapter aims to provide a comprehensive understanding of these techniques and how they enhance the efficiency and dependability of grid-integrated solar PV systems.

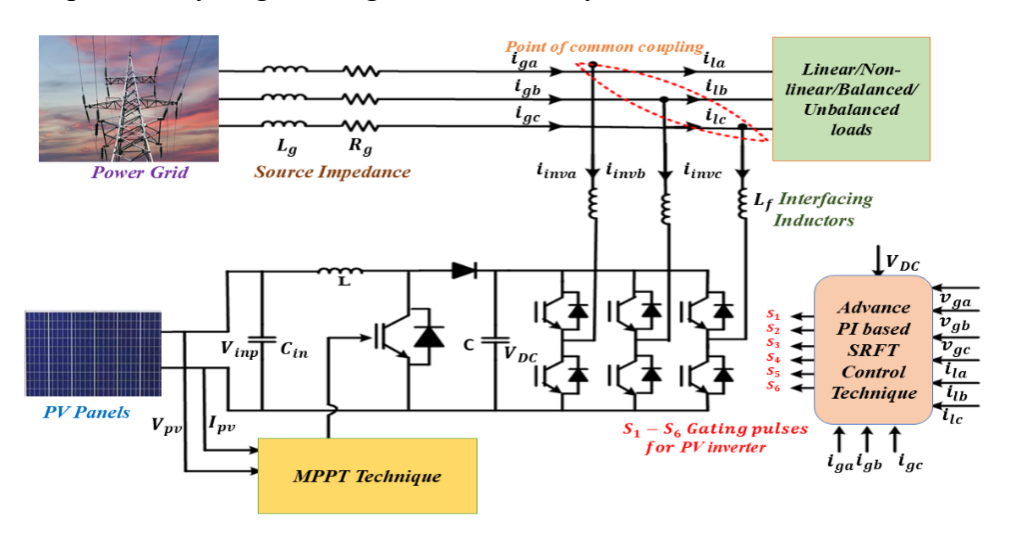


Fig.5.1 Schematic diagram of grid integrated PV system

5.2.1 Synchronous Reference Frame Theory

A PV system is connected to the utility grid via a DC/DC converter and a voltage source inverter. An inverter is responsible for DC-AC inversion and play a significant role in grid synchronization.

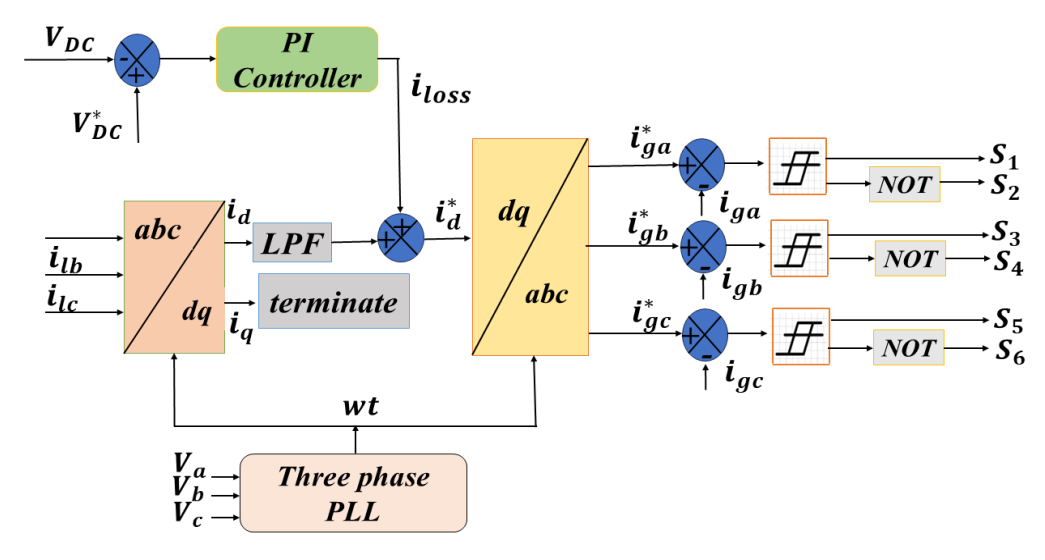


Fig.5.2 Schematic diagram of synchronous reference frame theory

The inverter controls the grid injected current in a grid connected PV system to adjust the real and reactive power supplied and to set the DC link voltage to its reference value. Voltage source inverter (VSI) consists of six IGBT switches as shown in Fig 5.1. Fig.5.2 depicts a block diagram of reference current estimation utilizing the SRF control algorithm in the UPF mode of operation. The SRF controller structure is made up of d-q-0 and $(d-q-0)^{-1}$ park transformations. The SRFT is an indirect control method for evaluating reference AC currents, which are utilized to generate gate pulses for controlling SPV inverters. Load current, PCC voltage, and DC bus voltage are sensed and considered as feedback signals in this method. Clark transformation method is used to convert three phase 'a-b-c' to' $\alpha - \beta$ ' co-ordinate, as expressed in equation (5.1). Phase-locked loop (PLL) is utilized to synchronize the VSI with the utility grid [143]-[144].

$$\begin{bmatrix} i_{\alpha} \\ i_{\beta} \end{bmatrix} = \sqrt{\frac{2}{3}} \begin{bmatrix} 1 & -\frac{1}{2} & -\frac{1}{2} \\ 0 & \frac{\sqrt{3}}{2} & -\frac{\sqrt{3}}{2} \end{bmatrix} \begin{bmatrix} i_{La} \\ i_{Lb} \\ i_{Lc} \end{bmatrix}$$
 (5.1)

These currents can be converted from the $\alpha - \beta$ to the d-q' frame using Park's transformation expressed by equation (5.2).

$$\begin{bmatrix} i_d \\ i_q \end{bmatrix} = \sqrt{\frac{2}{3}} \begin{bmatrix} \cos(wt) & \sin(wt) \\ -\sin(wt) & \cos(wt) \end{bmatrix} \begin{bmatrix} i_\alpha \\ i_\beta \end{bmatrix}$$
 (5.2)

where, ω is angular frequency of the synchronous rotating frame

A low pass filter is used to extract the fundamental active and reactive components of load currents. To operate the SRF algorithm in unity power factor mode, VSI must supply the reactive power demand of the load. Reactive reference component must be zero ($iq^*=0$), in order to compensate the reactive power demand of the load. While fundamental load current (id) is added with output of PI controller (i_{loss}) in order to

regulate the dc link voltage.

Active ac reference grid current is the sum of i_{loss} , and fundamental load current (id) which is expressed equation (5.3).

$$id^* = id + i_{loss} (5.3)$$

PV inverter's loss component is denoted by i_{loss} , which is the output of the PI controller in the voltage control loop, expressed by equation (5.4).

$$i_{loss} = K_P e(t) + K_i \int e(t)dt \tag{5.4}$$

Where, K_P & K_i are the proportional gain & integral gain and e(t) is voltage error signal.

The reverse Clark's and Park's transformations are then utilized to get three-phase reference source current as given in equations (5.5) and (5.6).

$$\begin{bmatrix} i_{\alpha}^* \\ i_{\beta}^* \end{bmatrix} = \sqrt{\frac{2}{3}} \begin{bmatrix} \cos(wt) & \sin(wt) \\ -\sin(wt) & \cos(wt) \end{bmatrix} \begin{bmatrix} i_d \\ 0 \end{bmatrix}$$
 (5.5)

$$\begin{bmatrix} i_{ga}^* \\ i_{gb}^* \\ i_{gc}^* \end{bmatrix} = \sqrt{\frac{2}{3}} \begin{bmatrix} 1 & 0 \\ -\frac{1}{2} & \frac{\sqrt{3}}{2} \\ -\frac{1}{2} & -\frac{\sqrt{3}}{2} \end{bmatrix} \begin{bmatrix} i_{\alpha}^* \\ i_{\beta}^* \end{bmatrix}$$
 (5.6)

Hysteresis current controllers (HCC) produce switching pulses by comparing reference currents to real currents within a hysteresis range. This technique is the simplest in terms of implementation, requiring only the error traced value, which is the difference between the grid current (i_{ga}, i_{gb}, i_{gc}) and the current references $(i_{ga}^*, i_{gb}^*, i_{gc}^*)$. This method involves switching actual source currents in an asynchronous procedure of ramping the actual current up and down so that it follows the reference current. Hysteresis controllers are relatively simple to develop when compared to other control systems. They do not require complex mathematical calculations. The quick response of hysteresis controllers to changes in the controlled variable is widely recognized. The controller takes immediate corrective action when the error exceeds the hysteresis band. Hysteresis controllers are more robust and resilient to parameter variations.

5.3 SYNCHRONOUS REFERENCE FRAME THEORY WITH ADVANCED PI -CONTROLLERS

For grid-integrated PV systems, synchronous reference frame theory (SRFT) is a widely used control approach that provides reactive power compensation, harmonic mitigation, and efficient power quality enhancement. Accurate control of active and reactive power components is made possible by SRFT, which converts grid currents from the α - β reference frame to the revolving d-q reference frame. However, when employed with SRFT, traditional PI controllers frequently have drawbacks such steady-state errors, difficulty tuning parameters, and poor adaptation under dynamic grid settings. Advanced optimization-based and intelligent PI controllers, such as Cuckoo Search Optimization (CSO)-PI, Honey Badger Algorithm (HBA)-PI, and

Artificial Neural Network (ANN)-PI controllers, have been coupled with SRFT in order to address these shortcomings

5.3.1 SRFT with ANN-PI Controller for Inverter

Artificial neural networks (ANNs) use parallel and distributed computing to describe nonlinear (static and dynamic) relationships between inputs and outputs. Artificial neural networks (ANNs) can learn general relations using weights and biases distributed over numerous layers and nodes. Fig.5.3 depicts the ANN structure employed in this study, consisting of two input layers, a hidden layer of ten neurons, and a single output layer. ANN's input layer connects to system inputs and projects weighted signals to subsequent hidden layers. The output layer receives weighted signals from the preceding layer and generates ANN output. The ANN was trained using the Levenberg-Marquardt (LM) back propagation learning methodology, which employs a chain rule mechanism. The output of the i^{th} node in the n^{th} layer is determined as equation (5.7) [147]-[148]:

$$x_i^{(n)} = f_i^{(n)} \left(net_i^{(n)} \right) = f_i^{(n)} \left(\sum_{n=1}^N w_i x_i^{(n-1)} \right)$$
 (5.7)

The output and activation functions of neurons at the i^{th} and n^{th} nodes are represented by $x_i^{(n)}$ and $f_i^{(n)}$, respectively. $x_i^{(n-1)}$ and w_i represent the input and connection weight of neurons at the nth node. The goal of training is to reduce the cost function E, which is the sum of the squared errors in the output layer expressed as equation (5.8).

$$E = \frac{1}{2} (\sum_{n=1}^{m} e_i^2) \quad \text{where } e_i = d_i - x_i$$
 (5.8)

Where d_i is the desired output of the i^{th} neuron and m is the number of output neurons. Weights are updated utilizing the Levenberg-Marquardt (LM) backpropagation learning technique, as equation (5.9):

$$w_i^* = f_i^{(n)} \left(net_i^{(n)} \right) \frac{x_i^{(n-1)}}{x_i^{(n)}} \sum_{i=1}^P w_{kj} w_{kj}^* - \gamma f_i^{(n)} \left(net_i^{(n)} \right) x_i^{(n-1)} e_i$$
 (5.9)

Where, $\gamma > 0$ represents adoption coefficient and P represents the next layer neuron. Levenberg-Marquardt activation function (LMAF) of the neuron is expressed as equation (5.10):

$$x_i^{(n)} = f_i^{(n)} \left(net_i^{(n)} \right) = \frac{2}{1 + e^{-net^{(n)}}} - 1 = \frac{1 - e^{-net^{(n)}}}{1 + e^{-net^{(n)}}}$$
 (5.10)

Fig.5.9(a) shows that LM algorithm trained the ANN controller with 70% information for training, 15% for testing, and 15% for validation. Fig.5.9(b) depicts the best validation performance, followed by testing of the verification set in the result section. The DC bus voltage error $e_n = V_{DC_{ref}} - V_{DC}$ and the change in error $\Delta e_n = e_n - e_n(k-1)$ defines the input of the following ANN.

$$x_{i}^{(\iota)}(k) = f_{i}^{(\iota)}(net_{i}^{(\iota)}) = net_{i}^{(\iota)}$$

$$x_{j}^{(\iota\iota)}(k) = f_{j}^{(\iota\iota)}(net_{j}^{(\iota\iota)}) = f_{i}^{(\iota\iota)}(\sum_{i} w_{i} x_{i}^{(\iota\iota)}(k))$$

$$x_{o}^{(\iota\iota\iota)}(k) = f_{o}^{(\iota\iota\iota)}(net_{j}^{(\iota\iota\iota)}) = f_{i}^{(\iota\iota\iota)}(\sum_{j} w_{o} x_{j}^{(\iota\iota)}(k))$$
(5.11)

To get the actual $V_{DC_{ref}}$, multiply the measured V_{DC} and output control signal of ANN. The weight of the ANN is given as equation (5.12):

$$w_{i}^{*}(k) = \frac{1}{2} \frac{\left[1 - (x_{j}^{(u)^{2}})\right]}{x_{j}^{(u)}} x_{i}^{(u)w_{o}}$$

$$w_{o}^{*}(k) = -\frac{\gamma}{2} \left[1 - (x_{o}^{(uu)^{2}})x_{j}^{(u)}\right]$$
(5.12)

 $w_i^* \rightarrow \text{Updated weight between neurons in the hidden layer and } w_o^* \rightarrow \text{Updated weight between hidden layer and output layer.}$

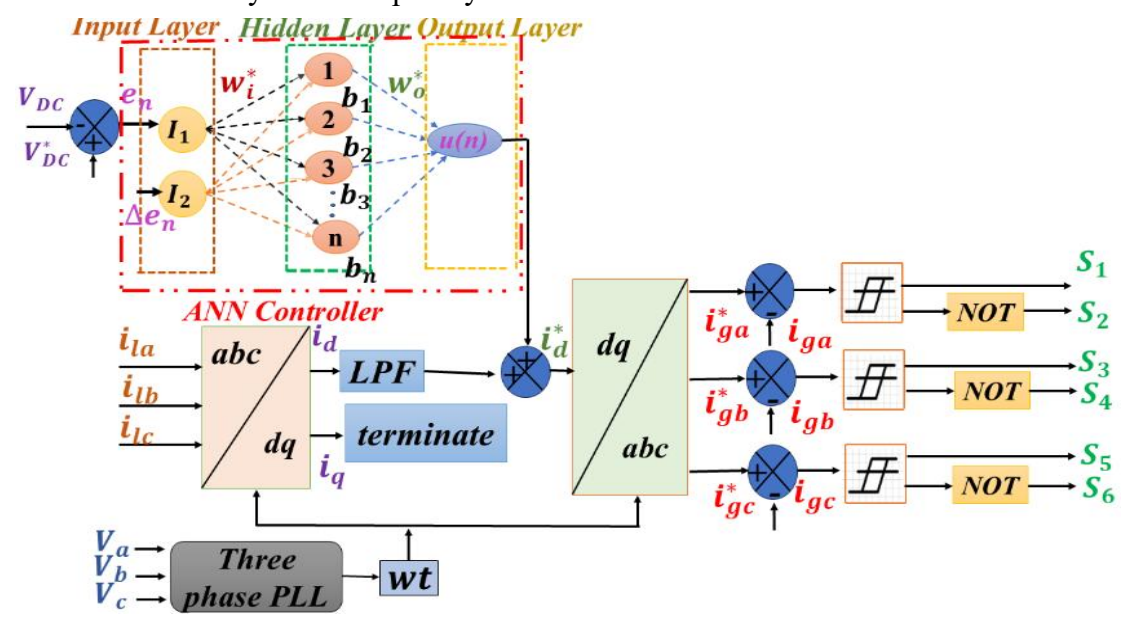


Fig.5.3 Block diagram of ANN based PI controller

5.3.2 SRFT with Optimization based -PI Controller for Inverter

To regulate the DC bus voltage, gain value of PI controller is tune and optimized by cuckoo search optimization technique and honey badger algorithm, PI controller mainly consists of two main components proportional and integral can be seen from equation (5.13) which are varied to get best possible results. Absolute error e(t) is taken into account which is the difference between the reference voltage and measured voltage.

$$e(t) = V_{DC}^{*}(t) - V_{DC}(t)$$
(5.13)

Objective function (MSE):

Mean square error is chosen as objective function to be reduced for DC bus voltage in order to get optimal PI controller gain K_P and K_i in the DC bus voltage regulator. Objective function of the SPV system can be represented as:

$$\min(O.F) = \min_{K_P, K_i} \left(\frac{1}{N} \sum_{t=1}^{N} (e(t))^2 \right)$$
 (5.14)

Where, N is the sample number, e(t) is the error. The main goal of this work is to create a optimization PI controller that is suitable for the suggested topology. Mean square error is employed as an objective function for the process of design and performance evaluation (MSE). This work employs and tests cuckoo search optimization methods to reduce error value.

For better analysis of the technique MAE and RMSE are also calculated as per equation (5.15) and (5.16).

Mean absolute error (MAE):

$$MAE = \frac{1}{N} \sum_{t=1}^{N} |e(t)|$$
 (5.15)

Root means square error (RMSE)

$$RMSE = \sqrt{\left(\frac{1}{N}\sum_{t=1}^{N} \left(e(t)\right)^{2}\right)}$$
 (5.16)

5.3.2.1 Cuckoo Search optimization

The Cuckoo Search optimization technique is a meta-heuristic optimization technique used for optimization problem-solving. It is nature-inspired meta-heuristic technique which is based on several cuckoo species' brood parasitism and Levy flights random walks. Brood parasitism can be classified into three categories: intra-specific, cooperative, and nest takeover. Some cuckoo species have the intelligence to mimic the host bird's color and shape in order to maximize its chances of reproduction. Cuckoos lay their eggs at a particular period of time in order to allow their eggs to hatch before the host birds. Cuckoos destroy a few of the host bird's eggs after they hatch in order to increase the possibility that their young would eat more food. Another frequent occurrence is the host birds finding and destroying the cuckoo's eggs. Sometimes they entirely depart their nest and migrate elsewhere and create a new one [145].

Lévy flight:

One crucial aspect of the cuckoo's reproduction strategy is looking for a nest that will serve as a convenient host bird. The hunt for the nest usually resembles the hunt for food, which is conducted in a quasi-random manner. Animals typically adopt paths or directions while in pursuit of food that can be represented mathematically by specific functions. The Lévy flight is one of the most popular models. According to a study, fruit flies, or Drosophila melanogaster, fly in a Lévy pattern as they explore their surroundings by taking a sequence of straight flight paths punctuated by sharp 90° turns. The meta-heuristic search algorithm for optimization problems adopts this behavior. Lévy flying is another characteristic of cuckoo nest-searching behaviors in CS. A Lévy flight is a arbitrarily walk that uses a power law to obtain the step sizes

from the Lévy distribution which is expressed by equation (5.17).

$$\gamma = \ell^{-\lambda} \tag{5.17}$$

where λ is the variance and ℓ is known as Lévy flight length. γ has an infinite variance because $\ell < \lambda < 3$.

Fig 5.4 shows a two-dimensional plane with Lévy flight. Because of the Lévy distribution, the steps are made up of number of small steps and, on occasion, big-step and long-distance jumps. In some cases, particularly for multimodal, nonlinear problems, these large hops may significantly increase the search efficiency of cuckoo search as compared to other meta-heuristic techniques.

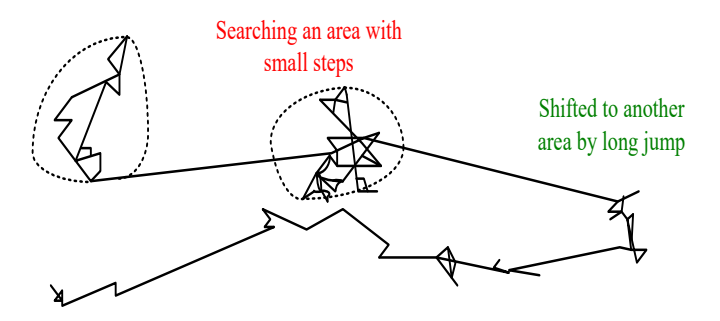


Fig.5.4 Lévy flight distribution

Cuckoo algorithms mostly adhere to three idealized CS criteria based on cuckoo brood parasite behavior:

- a) Each cuckoo lays one egg at a time, and it is deposited in a nest that is chosen at random.
- b) Next generation will inherit the best nest with the best eggs.
- c) The number of nests that are available is fixed, and the host bird has recognized a number of cuckoo eggs with a probability Pa, where $0 \le Pa \le 1$.

If the cuckoos' eggs are found, host bird has the option of leaving its nest or destroying them. In either case, given a fixed number of nests, a fresh nest will be created with a probability of Pa.

When producing a new cuckoo solution x^{t+1} a Lévy flight is carried out as required by the equation (5.18):

$$x^{t+1} = x_i^t + \alpha \oplus \text{L\'{e}}\text{vy}(\lambda)$$
 (5.18)

Where *i* is the number of samples, x_i^t is samples per egg, $\alpha > 0$ is known as step size, \oplus represents entry wise multiplication and number of iterations is denoted by *t*. α is given by equation (5.19).

$$\alpha = \alpha_0 \left(x_j^{(t)} - x_i^{(t)} \right) \tag{5.19}$$

The Lévy distribution expressed in equation (5.20) gives the value of Lévy (λ)

$$Lévy(\lambda) \approx u = \ell^{-\lambda}, \ (\ell < \lambda < 3)$$
 (5.20)

The following equation can be used to update the equation:

$$x_i^{k+1} \approx x_i^k + z \left(\frac{u}{\frac{1}{\sqrt{3}}}\right) (x_{best} - x_i)$$

$$(5.21)$$

where z is a levy coefficient. The values u & v are derived from normal distribution functions as represented below.

$$u, v \approx N(0, \varphi^2) \tag{5.22}$$

using the following equation, φ is determined.

$$\varphi^2 = \frac{\Gamma(1+\beta)\sin\frac{\pi\beta}{2}}{\Gamma(\frac{1+\beta}{2})\beta 2^{0.5(\beta-1)}}$$
(5.23)

Where $\beta = 1.5$ and Γ is the integral gamma function.

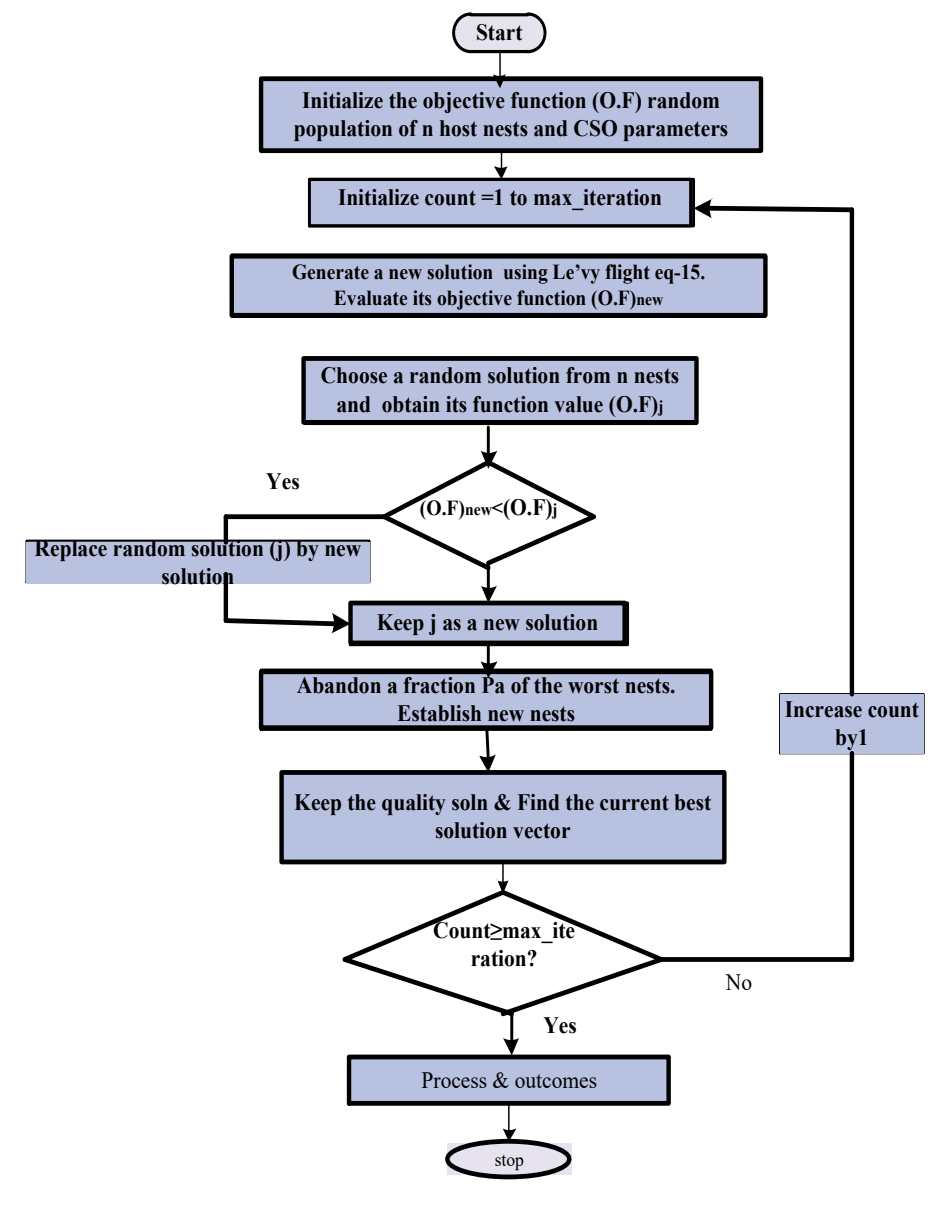


Fig.5.5 Flow chart of CSO-PI controller for presented grid tied SPV system

5.3.2.2 An overview of HBA optimization algorithm

Honey badgers are white and black fluffy-furred mammals found in semi-deserts, African rainforests, Southwest Asia and the Indian subcontinent. Honey Badger bodyweight are approximately 7-13 kilogram and body lengths are approximately 60-77 centimeter. They are a fearless forager that preys on 60 different species, including dangerous snakes. They are intelligent mammals that can use tools and enjoy honey. They prefer to live alone in self-dug tunnels and meet other badgers to mate only. They don't have a particular breeding season as cubs are born throughout the year. The following section discusses the HBA's mathematical model which is similar to honey badger behavior.

Because of the exploration and exploitation phases, HBA is theoretically considered a global optimization method. In general, meta-heuristic algorithms have sets of plausible solutions to the optimization problem. Each solution is iteratively updated automatically based on the nature of the technique. Exploration and exploitation are the two main components of every search technique. Exploration is ensured by expanding the search to far-reaching sections of the search space. Conversely, by exploitation, search agents converge on a previously selected attractive region, employing a local search approach [146].

Inspiration:

The honey badger technique copies the foraging manners of honey badgers. The honey badgers either sniff and dig for food or follow the honey guide bird. The 1st case is known as digging phase and 2nd is known as honey phase. Initially, it uses its sniffing abilities to determine the location of the prey; once it reached there, it moves near the prey to choose the finest spot for digging and catching the prey. In honey phase, it follows the honey guide birds to find a beehive directly.

Mathematical model:

HBA mainly consist of two phases "digging phase (Exploration)" and "honey phase (Exploitation)"

HBA algorithm Steps:

These subsections explain the HBA algorithm's mathematical formulation. Honey badger algorithm is a global optimization technique as it includes exploration & exploitation phase. Mathematically, populations of candidate's solution (Z) are expressed as equation (5.24):

$$Z = \begin{bmatrix} Z_{11} & Z_{12} & Z_{13} \dots Z_{1D} \\ Z_{21} & Z_{22} & Z_{23} \dots Z_{2D} \\ \dots \dots \dots \dots \dots Z_{2D} \\ Z_{n1} & Z_{n2} & Z_{n3} & \dots Z_{nD} \end{bmatrix}$$
(5.24)

 i^{th} Badger position $Zi = \begin{bmatrix} Z_i^1, Z_i^2, ..., Z_i^D \end{bmatrix}$

Step 1: Initialization Phase The following expression can be used to initialize the positions of honey badgers with n populations:

$$Zi = Lb_i + r1(Ub_i - Lb_i) \quad r1 \in [0,1]$$
 (5.25)

Where, Zi is ith Honey Badger location refers to a candidate solution in a population of size n and Lb_i & Ub_i is search space lower & upper bounds.

Step 2: Intensity definition Intensity is proportional to the prey's source strength and the distance between prey and the ith honey badger. Si is the scent intensity of the prey, movement will be quick if the scent is strong, and conversely. It is represented by inverse square law (ISL) as depicted in Fig.5.6 and determined by equation (5.26)

$$Si = r2\left(\frac{c}{4\pi(D_i)^{\wedge 2}}\right) \qquad r2 \in [0,1]$$
 Where
$$C = (Z_i - Z_{i+1})^2$$

$$D_i = Z_{prey} - Z_i$$

$$C \rightarrow \text{source strength}$$
 (5.26)

 $D_i \rightarrow$ distance between ith honey badger & prey

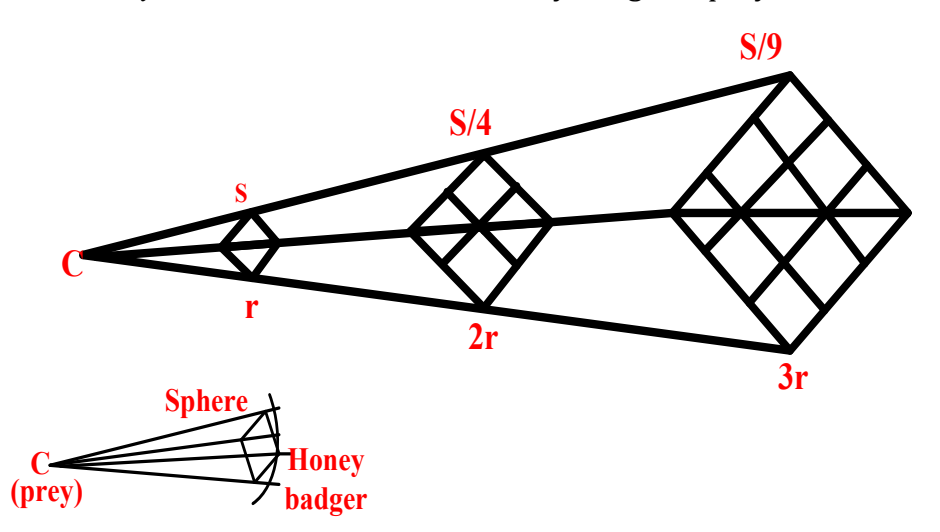


Fig. 5.6 ISL. Si is the scent intensity; C is position of prey and $r \in [0,1]$

Step 3: Update density factor (\gamma) The density factor (γ) governs time-varying randomness to allow a seamless conversion from exploration to exploitation. Update density factor (γ), which lowers over time to reduce randomness

$$\gamma = K \times exp\left(\frac{-t}{t_{max}}\right) \qquad K \ge 1 \tag{5.27}$$

Where, K is constant (default value is 2) and t_{max} is maximum iterations count.

Step 4: Escaping from the local solution

The present steps, as well as the following two ones, are used in the honey badger algorithm to escape the local solution area. In this condition, algorithm uses a flag F to change the search direction and allowing agents to rigorously examine the search space.

Step 5: Updating the positions of the searching agents

As explained, the honey badger algorithm position update process (x new) is categorized into 2 phases: "digging phase" and "honey phase". A more detailed

explanation is provided below:

Step 5.1: Digging phase.

A honey badger digs similar to the Cardioids shape manner as depicted in Fig.5.7. Cardioids motion can be represented using equation (5.28).

$$Z_{new} = Z_{Prey} + F\beta I_{zprey} + F\beta \gamma D_i r 3 \times |\cos(2\pi r 4) \times [1 - \cos(2\pi r 5)]|$$
 (5.28)

$$r 3, r 4 \& r 5 \in [0,1]$$

Where, Z_{Prey} is global best position and β is honey badger's ability to find food, by default value is 6.

F work as a flag that changes the search location; which can be obtained using equation 5.28.

A honey badger's digging phase is heavily affected by three factors: Scent intensity (Si) of the prey Z_{Prey} , honey badger-prey distance (Di), and the decreasing operator (γ). Furthermore, while digging, a badger may encounter any disturbance F, allowing it to locate even better prey as displayed in Fig.5.7.

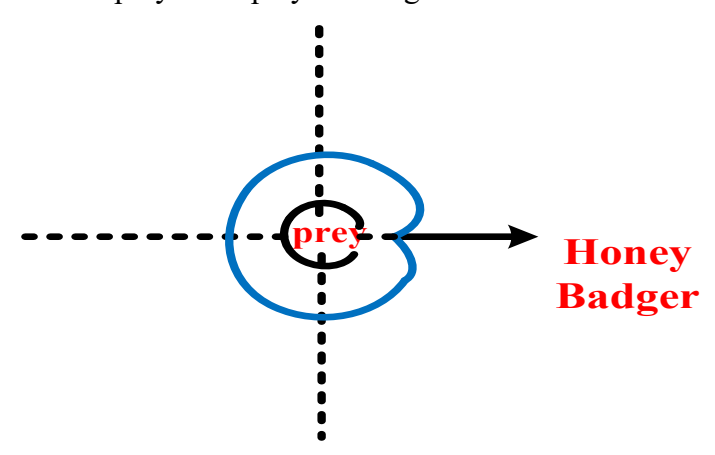


Fig.5.7 Digging phase: Black circular line displays the prey position & blue line is smell intensity

Step 5.2: Honey phase.

A honey badger following a honey guide bird to a beehive can be represented as equation (5.29)

$$Z_{new} = Z_{Prey} + Fr_7 \gamma D_i$$
 $r_7 \in [0,1]$ (5.29)

This study attempts to design an HBA-based PI controller that is appropriate for the proposed topology. Thus, mean square error (MSE) as explained in section (2.7) is considered as the objective function for the design process and performance evaluation. Honey badger optimization techniques are used and tested in this work to minimize error value. Fig. 5.8 depicts the flowchart of the proposed algorithm.

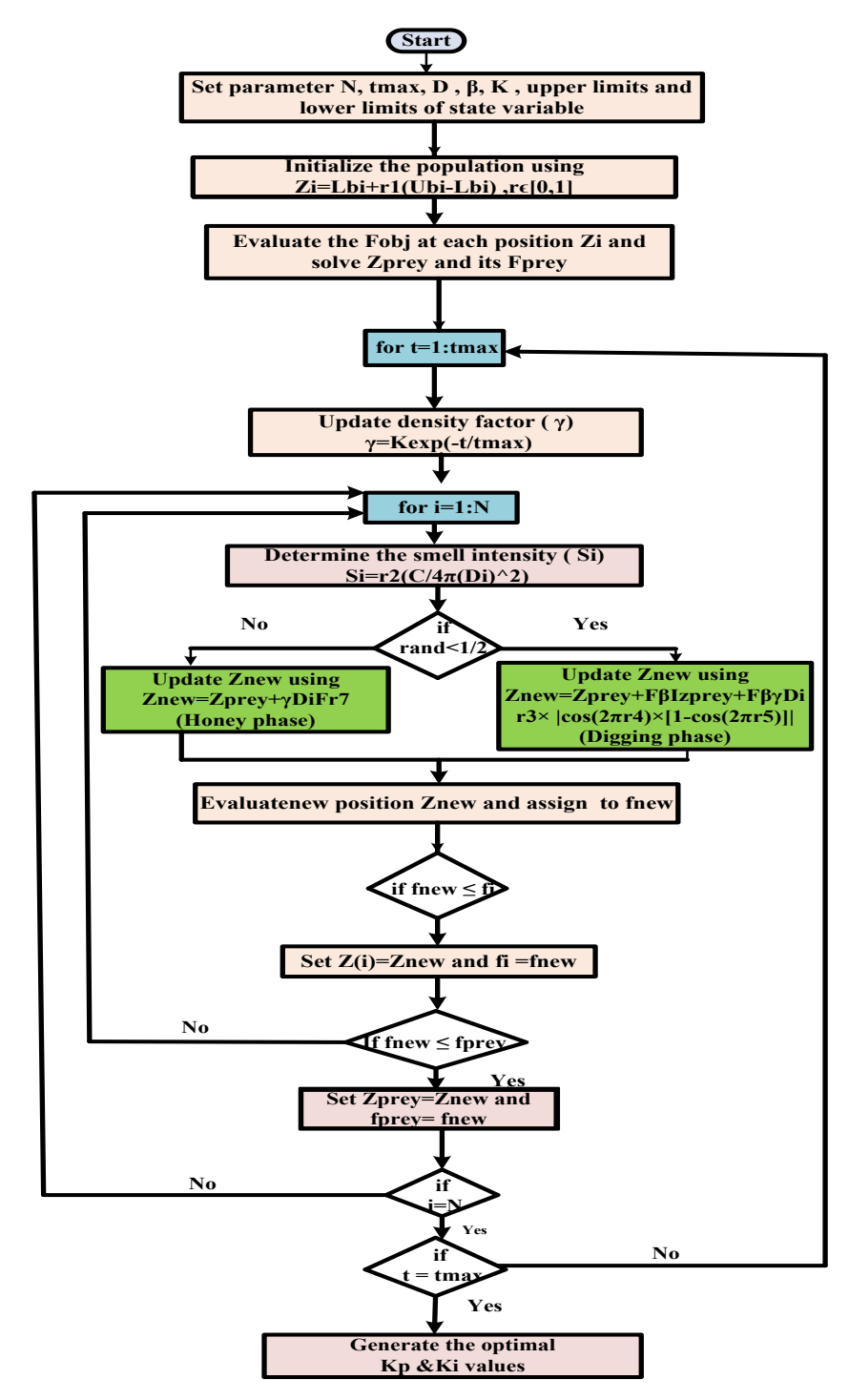


Fig. 5.8 Flow chart of HBA optimization for obtaining the PI values

5.4 Performance evaluation and result discussion

This section presents a detailed performance analysis of the proposed inverter control techniques—ANN-PI, Cuckoo Search optimized PI (Cuckoo-PI), and Honey Badger Algorithm optimized PI (HBA-PI)—under various grid and load conditions. The effectiveness of each technique is evaluated based on system performance during variable linear load, variable insolation, unbalanced non-linear load, and grid voltage disturbance scenarios, including sag and swell conditions.

5.4.1 Performance evaluation and result discussion using ANN-PI Controller

The proposed ANN controller is tested for robustness and efficacy under dynamic grid settings, including variable load and irradiation. The proposed algorithm has been developed in MATLAB and validated for power factor correction.

The accomplishment ANN controllers are evaluated using MSE, training performance, fit function, error histogram, and regression analysis. MSE is the square of the average variance between actual and target outputs. Lower MSE values suggest a close connection between target and actual data, whereas zero MSE implies no errors. Regression (R) values indicate how closely goal and actual outputs align. An R-value of 1 indicates perfect proximity, whereas 0 indicates a random connection between the target and actual data as shown in Fig.5.9(a),5.9(b) and 5.9(c).

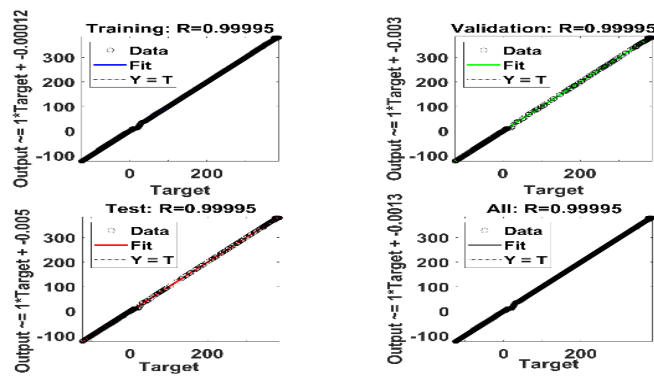


Fig. 5.9(a) Training, validation, set and all performance of the ANN controller.

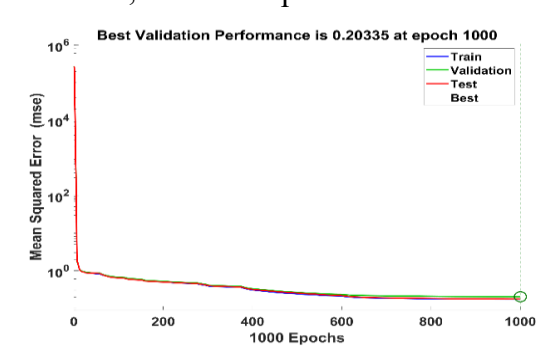


Fig. 5.9(b) Best validation performance of ANN controller

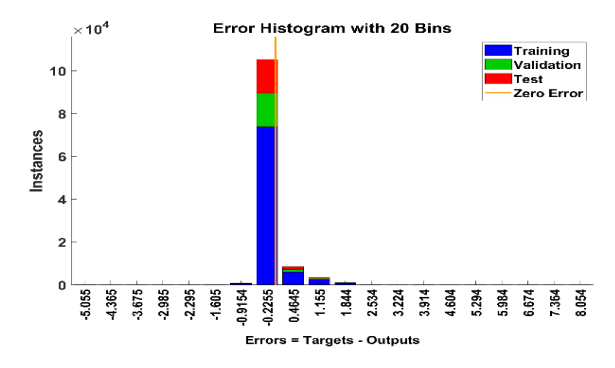


Fig5.9(c) Neural network error histogram

5.4.1.1 System performance under variable linear load and variable insolation condition

Fig.5.10. depicts the system's performance under varying linear load and insolation conditions. A linear load of 11.66kVA with 0.85 lag pf (active power of 10kW and reactive power of 6 kVAr) is evaluated. As the solar inverter generates 12.78kW of power until 0.15 seconds, the solar inverter meets the active load requirement of 10kW and feeds the remaining 2.78kW to the power grid. At 0.15 seconds, the load demand is increased by 8.16kVA with a power factor of 0.85 lag pf. In this situation, the total active load demand is 17kW, and the reactive load need is 10.2kVAr. The solar inverter supplies 12.78kW power to the load, while the remaining 4.22 power is drawn from the grid, and the inverter meets the reactive power demand. At t=0.25sec, insolation reduces from 1000 W/m^2 to 700 W/m^2, resulting in a reduction in solar power generation to 8.5kW. The remaining 8.5kW is obtained from the grid and supplied via an inverter, as shown in Fig.5.10. The grid supplies zero reactive power, implying that the system operates in a unity power factor mode and DC bus voltage is constant.

5.4.1.2 System performance under variable and unbalanced non-linear load condition

Fig.5.11 shows system's performance under variable nonlinear and unbalanced load conditions. A non-linear load (a three-phase rectifier with R=100ohm and L=120mH) is studied for analysis. At t=0.15s to t=0.2 sec, unbalancing of non-linear load is created by removing one phase, as shown in Fig.5.11. Under this circumstance, the suggested controller performs well by maintaining sinusoidal and balanced grid current and voltage at pcc (point of common coupling). At t=0.25 sec, load demand increases by 3.5kVA with a power factor of 0.85, resulting in a total load demand of 6.2kW active power and 3.3kVar reactive power. Under this circumstance, the solar inverter supplies the load requirement while feeding surplus power to the grid. The inverter also supplies reactive power by maintaining the UPF mode of operation.

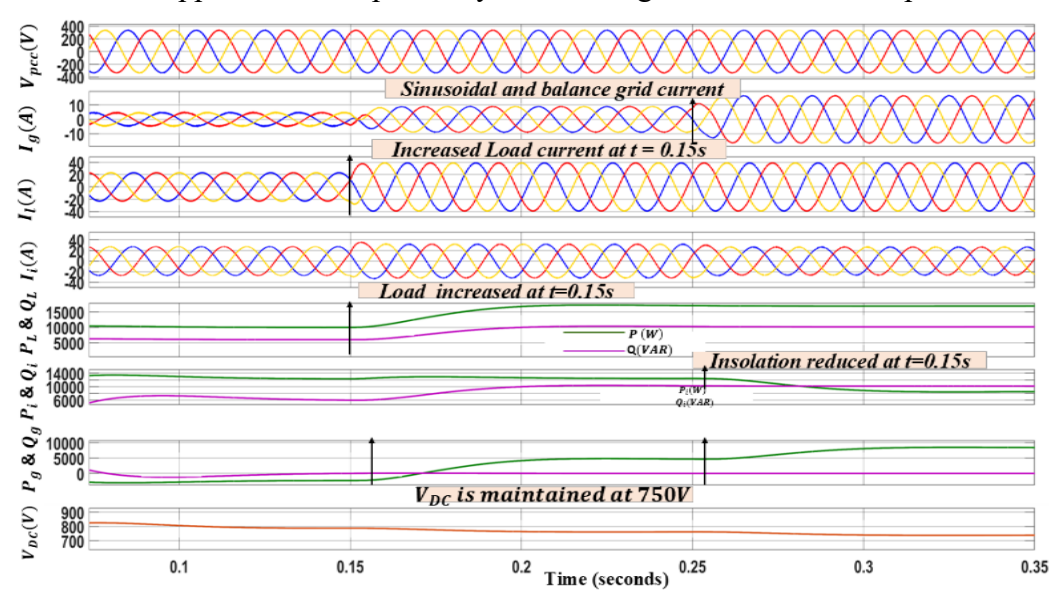


Fig.5.10 System performance under variable linear load and insolation condition

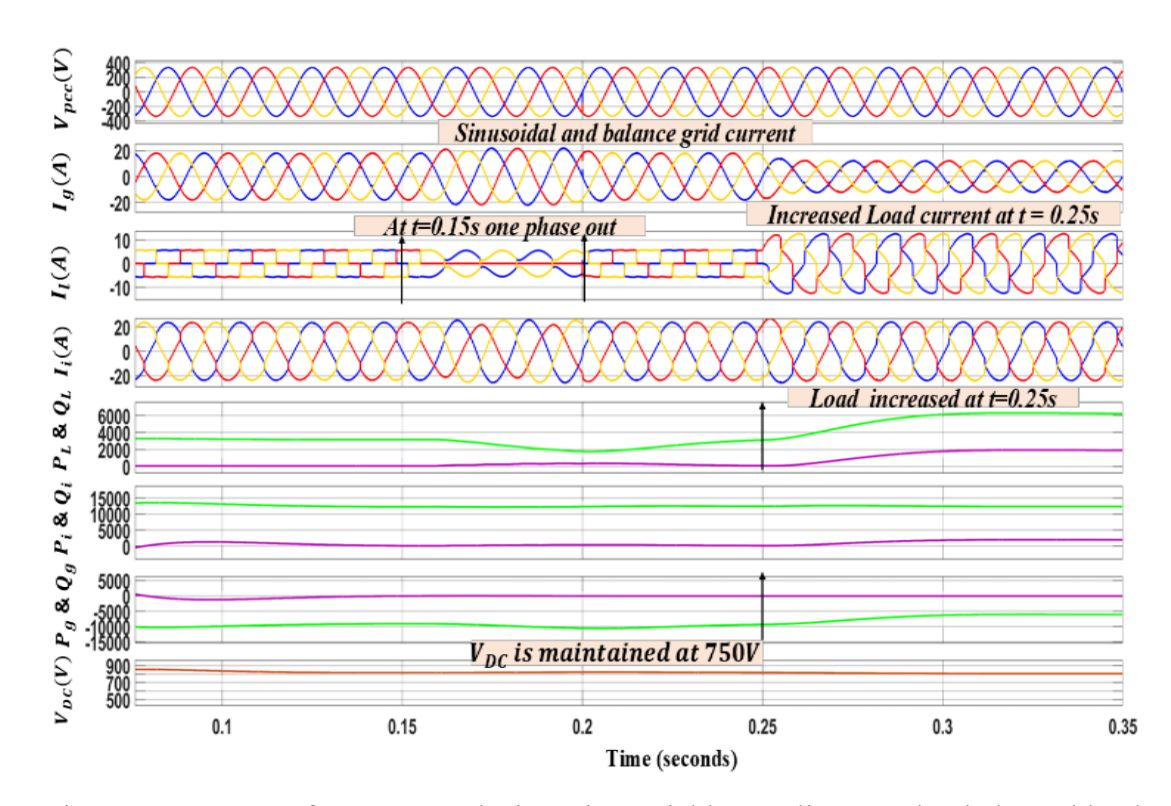


Fig.5.11 System performance analysis under variable non-linear and unbalanced load condition

5.4.1.3 System performance under grid voltage disturbance, sag and swell condition

Fig.5.12 depicts the system's performance under grid voltage sag, swell, and voltage disturbance conditions. Fig.5.12 shows that voltage sag occurs from t=0.1sec to t=0.2sec, voltage swells at t=0.2sec to t=0.3sec, and voltage is unbalanced at t=0.3sec to 0.35sec.It is evident that our system performs effectively under all three conditions by keeping voltage and current balanced and sinusoidal, as well as keeping the dc bus voltage constant.

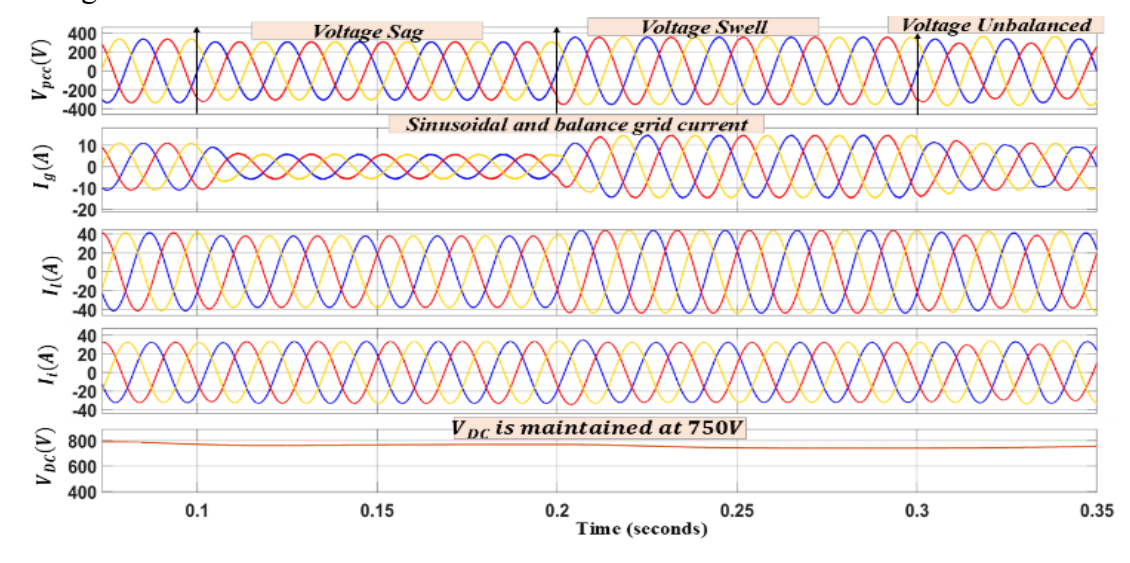


Fig. 5.12 System performance under grid voltage disturbance, voltage sag and swell

5.4.1.4 Comparative Analysis of ANN -PI controller with PI controller

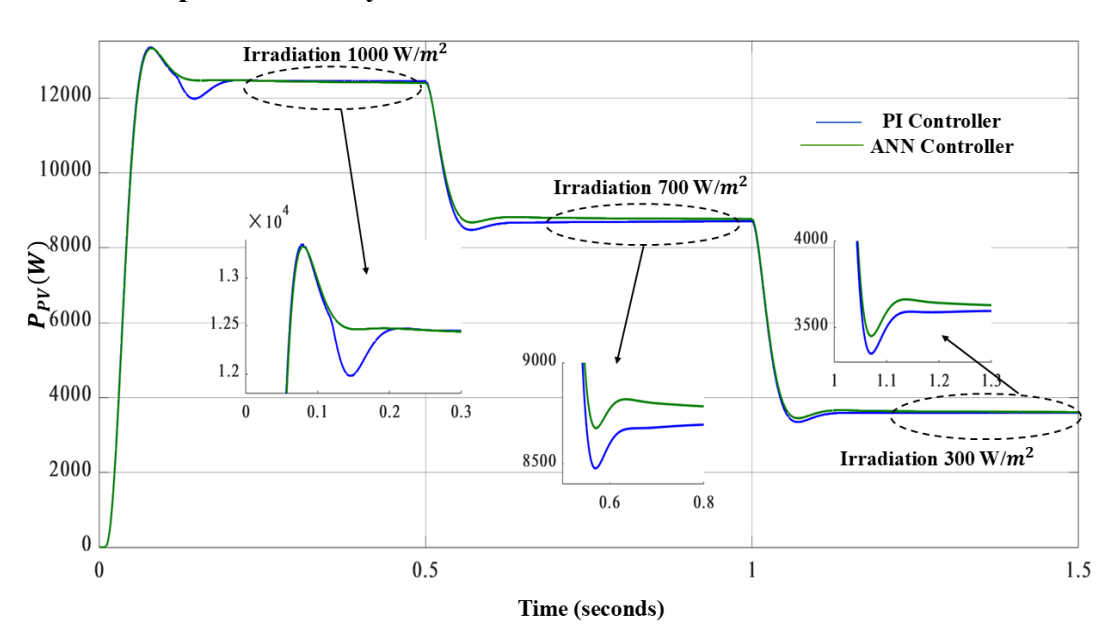


Fig.5.13 Comparison of PV power output with ANN-PI controller and PI controller Table.5.1 Comparison of PV power Output of ANN-PI with PI controller

Irradiation	Time interval	PI Controller P(kW)	ANN-PI Controller P(kW)
1000 W/m ²	(0.0s-0.6s)	12.39	12.58
700 W/m ²	(0.6s-1.2s)	8.65	8.89
300 W/m ²	(1.2s-1.8s)	3.50	3.73

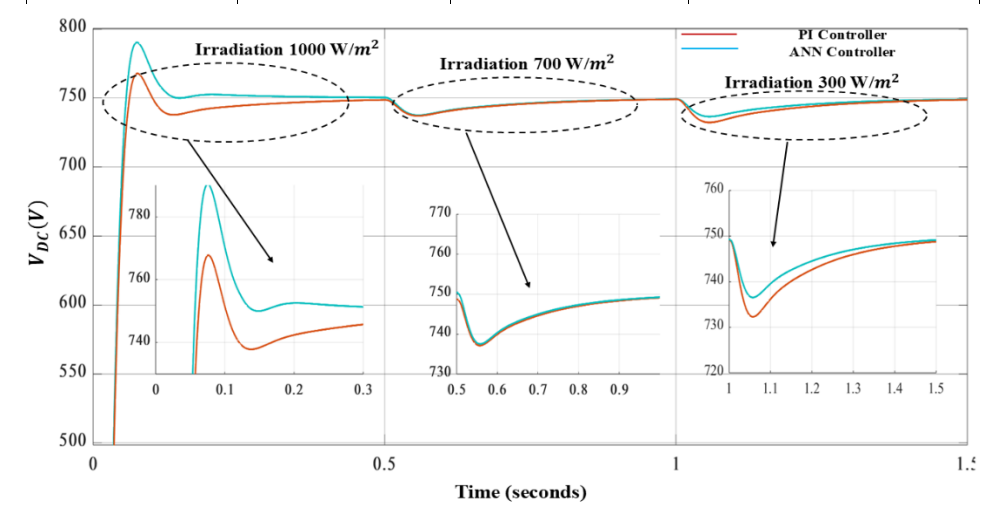


Fig.5.14 Comparison of DC bus voltage with ANN-PI controller PSO-PI and PI controller

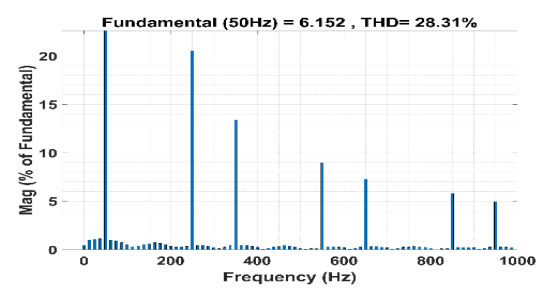


Fig. 5.15(a) Total harmonic distortion of non-linear load current

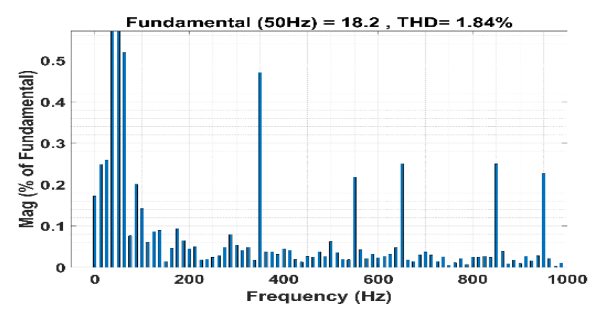


Fig.5.15(b)Total harmonic distortion of grid current for non-linear load Table.5.2 Comparison of grid current harmonics with ANN-PI and PI controller

Parameters	PI Controller (THD%)	ANN-PI controller (THD %)
Non linear load	2.56	1.84
Non-linear unbalanced load	2.59	2.57
Grid voltage unbalance	2.44	2.39
Voltage Sag	2.85	2.66
Voltage swell	2.58	2.13

Table.5.3 Comparison of ANN-PI with PI controller in term of performance dynamic

Parameter	PI Controller	ANN -PI controller
Control Adaptability	Fixed gains require	Self-learning dynamically adjusts
Control Adaptability	manual tunning	control parameters
Dynamic variation response	Slow reponse	Fast response
Total harmonic distortion	High	Low
Computational	Simple	
Requirement	implementation	Complex initial computation
Requirement	butrequires tunning	

The comparative analysis between the ANN-based PI controller and the conventional PI controller reveals notable performance improvements, particularly in terms of dynamic response and harmonic distortion reduction. As illustrated in Fig. 5.13, Fig.

5.14, and Table 5.1, the ANN-based controller demonstrates superior performance in both maximum power extraction from the solar PV system and DC bus voltage regulation, compared to the conventional PI controller.

Furthermore, Fig. 5.15(a) and Fig. 5.15(b) highlight the ANN controller's effectiveness in significantly reducing the Total Harmonic Distortion (THD) in both the nonlinear load current and the grid current. The quantitative results presented in Table 5.1 and Table 5.2 further confirm that the ANN-PI controller consistently outperforms the conventional PI controller under varying solar irradiance conditions.

At an irradiance level of 1000 W/m², the ANN-PI controller achieved a maximum power output of 12.58 kW, surpassing the PI controller's 12.39 kW. As irradiance decreased to 700 W/m², the ANN-PI still maintained a higher output of 8.89 kW compared to 8.65 kW from the PI controller. Under low irradiance conditions (300 W/m²), the ANN-PI controller continued to exhibit better tracking performance, delivering 3.73 kW in contrast to 3.50 kW from the conventional PI controller. These findings demonstrate that ANN-PI enables faster and more accurate tracking of the maximum power point, particularly under dynamic situations, while moderate improvement over the standard PI controller.

Table 5.2 presents the Total Harmonic Distortion (THD) values for two control strategies—conventional PI and ANN-PI controllers—under a range of operating conditions. The results clearly indicate that the ANN-PI controller consistently achieves lower THD levels, highlighting its enhanced capability in managing harmonic distortion. Under nonlinear load conditions, the ANN-PI controller achieves a THD of 1.84%, compared to 2.56% for the conventional PI controller.

Furthermore, even under more challenging conditions such as nonlinear unbalanced loads and grid voltage unbalance, the ANN-PI controller maintains competitive THD performance, underscoring its robustness and adaptability. In scenarios involving voltage sag and swell, the ANN-PI controller again outperforms the conventional PI controller, achieving THD values of 2.66% and 2.13%, respectively, as opposed to 2.85% and 2.58% observed with the PI controller.

These results collectively demonstrate that the ANN-PI control strategy offers improved harmonic suppression and dynamic performance, making it a more effective and reliable alternative for grid-connected solar PV systems operating under a wide range of normal and abnormal grid conditions.

Table 5.2 further illustrates the advantages of the ANN controller over the conventional PI controller. While the PI controller relies on fixed gains that require manual tuning, ANN controller exhibits self-learning capabilities, dynamically adjusting its control parameters for enhanced adaptability. Additionally, the ANN controller responds faster to dynamic variations, whereas the PI controller exhibits a slower response due to its fixed control structure. The ANN controller also ensures lower total harmonic distortion compared to the PI controller, enhancing overall power quality. However, despite these benefits, the ANN controller involves higher computational complexity during initial implementation, whereas the PI controller is

simpler to implement but demands periodic tuning for optimal performance.

Overall, the ANN-based controller demonstrates superior performance in terms of adaptability, harmonic reduction, and response time, making it a more effective solution for enhancing microgrid stability and power quality.

5.4.2 Performance evaluation and result discussion using CSO-PI Controller

To examine the proficiencies of the presented CSO technique, different loads and grid conditions are taken into consideration. The presented control technique is tested in power factor correction mode. System simulation parameters are listed in Appendix. Output response of all the quantities such as voltage at $PCC(V_{pcc})$, load current (I_1), DC bus voltage (V_{DC}) grid current (I_g), inverter current (I_{inv}) and real and reactive power sharing among power grid, Inverter and load are studied.

5.4.2.1 System performance under variable Linear load demand at different insolation condition

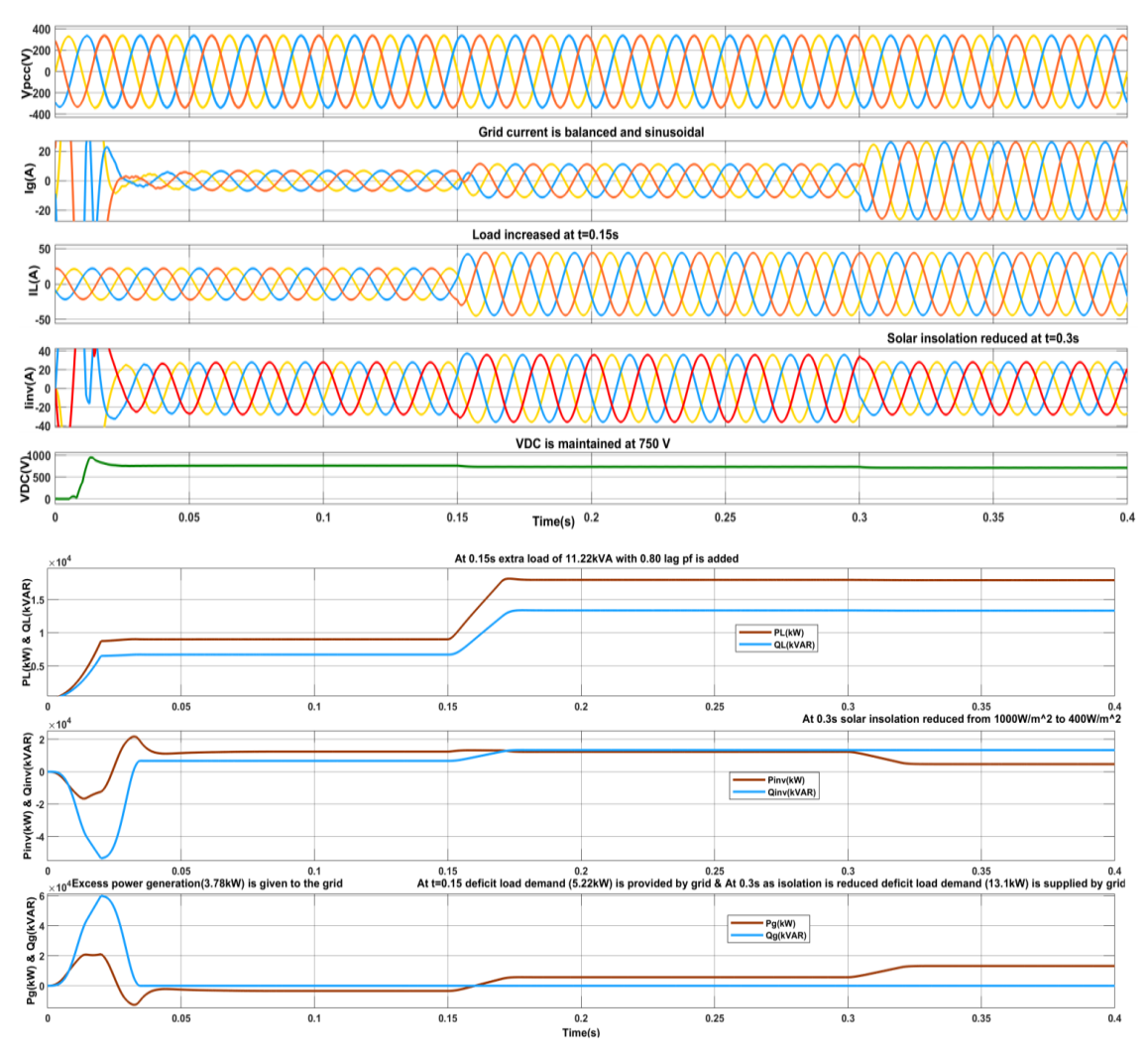


Fig.5.16. Waveforms of variable linear load with insolation variation

In this case, performance of the system for variable linear load and variable insolation are analyzed as shown in Fig 5.16. PV generate 12.78kW active power at 1000W/m^2 insolation. From t=0.0s -0.15s load demand is 11.22 kVA with 0.80 lagging pf

(P=9kW, Q=6.7kVAR). From Fig.5.16 it can be seen that grid current and voltage at PCC are sinusoidal and balanced. Active load demand is supplied by PV and excess power (3.78kW) is given to the grid. Reactive power requirement of the load is fulfilled by VSI and hence grid operates in UPF mode. It can also be noticed that grid current and voltage at PCC are out of phase which means power is supplied to the grid. DC voltage is maintained at 750V. At t=0.15s an extra load of 11.22kVA with 0.80 lagging pf is added, total load demand becomes P=18kW & Q=13.4kVAR Under this situation also grid current is balanced and sinusoidal. In this case PV supply 12.78kW active powers, grid supply 5.22kW deficit power of the load, inverter fulfill the reactive power demand of the load and grid operates in UPF mode.

At t=0.3s insolation is reduced from 1000W/m² to 400W/m² it reduces power generation of SPV from 12.78kW to 4. 9kW.Under this condition deficit load demand (13.1kW) is supplied by the grid. Also, it can be noticed from the figure.8 under varying load and insolation condition, grid current remain sinusoidal and balanced. DC bus voltage is regulated at 750V and system operates at UPF mode by CSO- PI controller under all the conditions.

5.4.2.2 System performance under variable nonlinear load demand at different insolation

In this case, CSO control technique is examined for variable nonlinear load (3phase rectifier with R=200Ω & L=100mH) and variable insolation condition whose waveform is as shown in Fig 5.17. PV generates 12.78kW active power at 1000W/m² insolation and the power load demand from t=0.0s-0.15s is 1.6kW which is supplied by PV. Grid current is balanced and sinusoidal in this situation. DC voltage is maintained at 750V. The excess power generated (11.181 kW) is given to the utility. Voltage at PCC and grid current are out of phase showing power is given to the utility. At t=0.15s an extra load of 11.22kVA, 0.80 lagging pf (9kW, 6.7kVAR) is added to the load. Grid current is balanced and sinusoidal under this condition as well. The active load demand is 10.6 kW which is accomplished by PV and extra power is given to the power grid (2.18kW) as shown in Fig.5.17 Reactive load demand is accomplished.

At t=0.3 s, insolation is reduced from 1000W/m² to 400W/m². As the insolation is reduced, the real power generated by the PV drop from 12.78 kW to 4.9kW. But grid current is maintained sinusoidal and balanced. Deficit load demand (5.7 kW) is taken from the power grid. Under dynamic condition, the reactive power load demand is fulfilled by inverter. Also, DC voltage is regulated at 750V by CSO based PI controller.

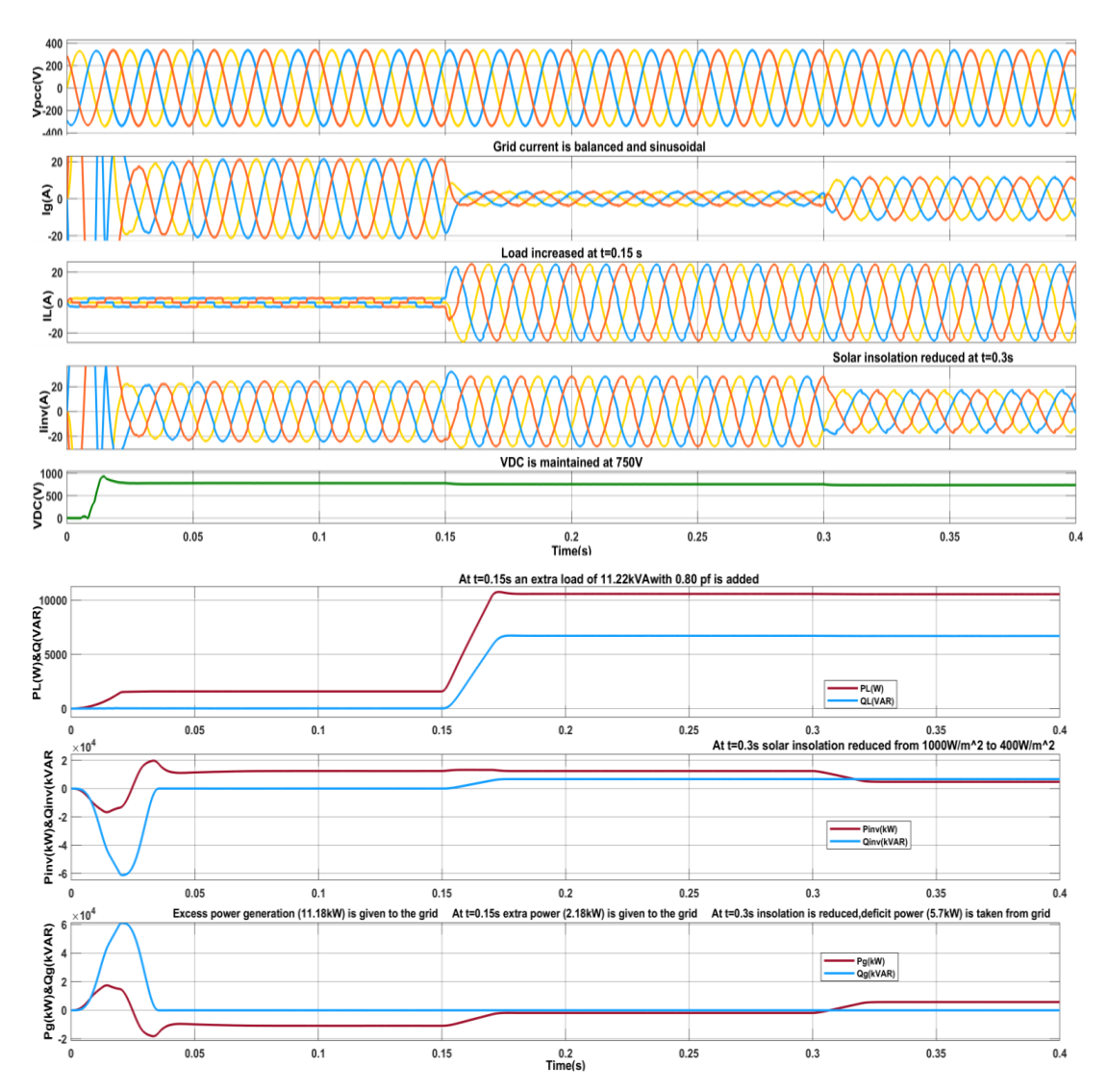


Fig 5.17 Waveforms of variable nonlinear load with insolation variation

5.4.2.3 System performance under non-linear unbalanced load condition

In this particular case performance analysis of a non-linear load at unbalanced load conditions are examined as shown in Fig 5.18 shows the system's response under unbalanced load condition when one line/phase of the non-linear load is disconnected for time interval t= 0.1s-0.3s. In this case it can be noted voltage at PCC and grid current are out of phase indicating that excess power produced by PV is given to the power grid. Under these cases, the presented CSO technique performs competently. Also, under unbalancing load condition grid currents is balanced and sinusoidal and DC voltage is regulated at 750V by CSO - PI controller. Further for unbalanced load condition FFT (fast Fourier transform) analysis is done for validating the harmonic reduction of the system using presented CSO technique. From the waveforms it can be seen that for nonlinear unbalanced load THD is 15.86% whereas grid current has 2.55% THD as shown in Fig 5.19(a) and 5.19(b), signify that the presented CSO technique works well for harmonic diminution under unbalanced non-linear load condition.

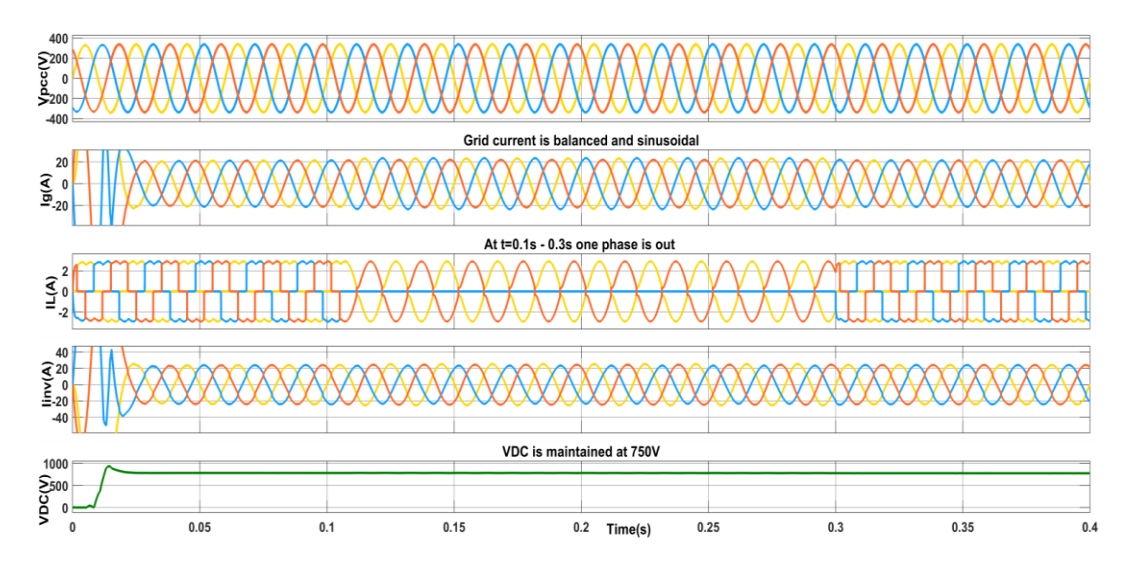


Fig. 5.18. Waveforms of non-linear load under unbalanced load condition

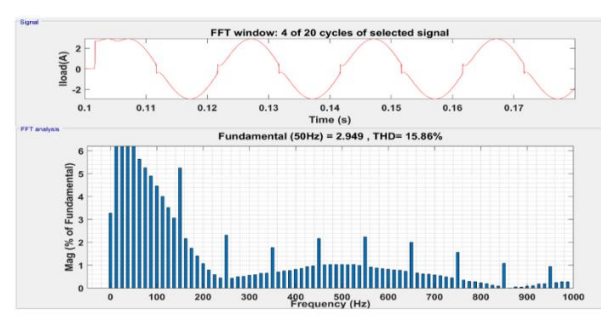


Fig. 5.19(a). THD of load current for non –linear unbalanced load

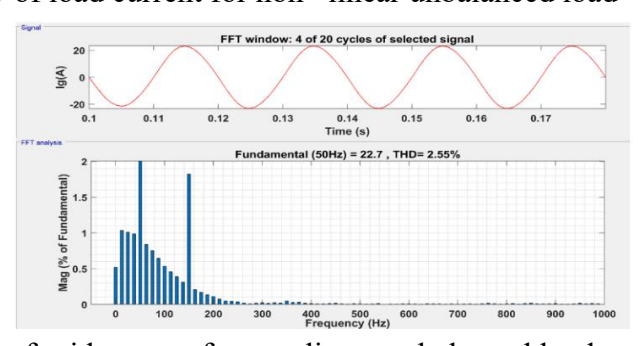


Fig 5.19(b). THD of grid current for non-linear unbalanced load

5.4.2.4 System performance uner non-linear load with unbalanced grid voltage condition

In case of unbalanced grid voltage condition for nonlinear load system performance has been examined as shown in fig 5.20 Grid voltage unbalancing is done at t= 0.2s by decreasing the phase 'b' voltage to 364V and increasing the phase 'c' to 450V.from the figure we can observed that even for grid unbalancing condition grid current and voltage at PCC are balanced and sinusoidal. Also, DC voltage is regulated at 750V by CSO based PI controller. Further for unbalanced grid condition FFT analysis has been done for validating the harmonic reduction of the system using presented CSO technique. From the graph it can be seen that for nonlinear unbalanced grid condition, load is THD is 31.47% whereas grid current has 2.27% THD as shown in Fig 5.21(a)

& 5.21(b), signify that the presented CSO technique works well for harmonic diminution for unbalanced non-linear load condition.

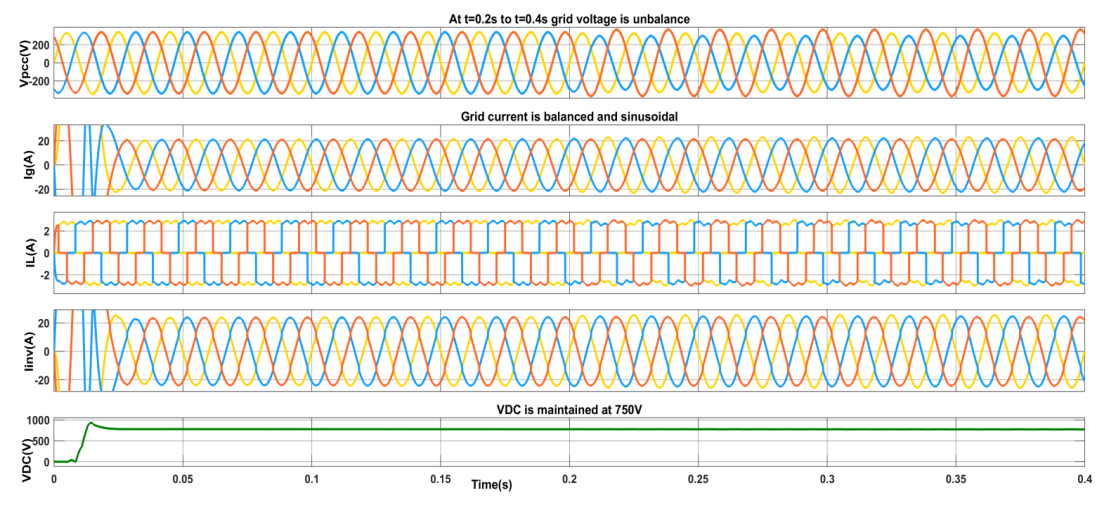


Fig 5.20. Waveforms of non-linear load under unbalanced grid voltage condition

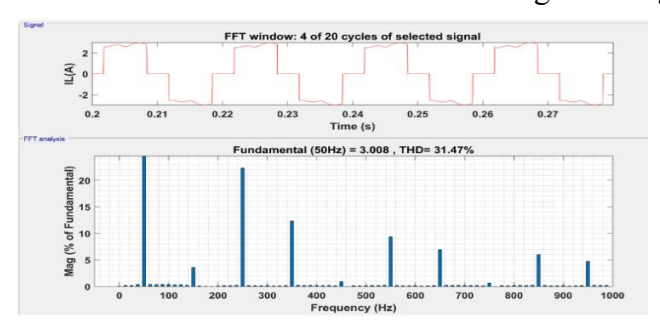


Fig. 5.21(a). THD of load current for non -linear load under unbalanced grid voltage

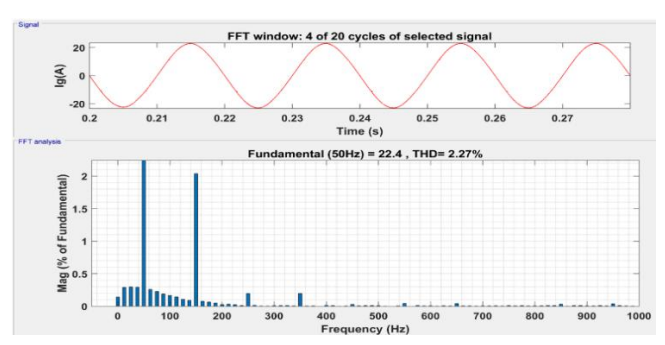


Fig. 5.21(b). THD of grid current for non –linear load under unbalanced grid voltage

5.4.2.5 System performance of nonlinear load for grid voltage sag and swell condition

System performance of nonlinear load for grid voltage sag and swell condition using CSO technique are examined as depicted in Fig.5.22. Voltage sag is initiated for time period t=0.1s-0.25s and voltage swell is initiated for time period t=0.25-0.4sec from the figure it can be noticed that voltage sag reduces load current and voltage swell increases load current even in this dynamic situation grid current is found to be sinusoidal and balanced. Also, DC bus voltage is regulated at 750Vusing presented CSO-PI controller.

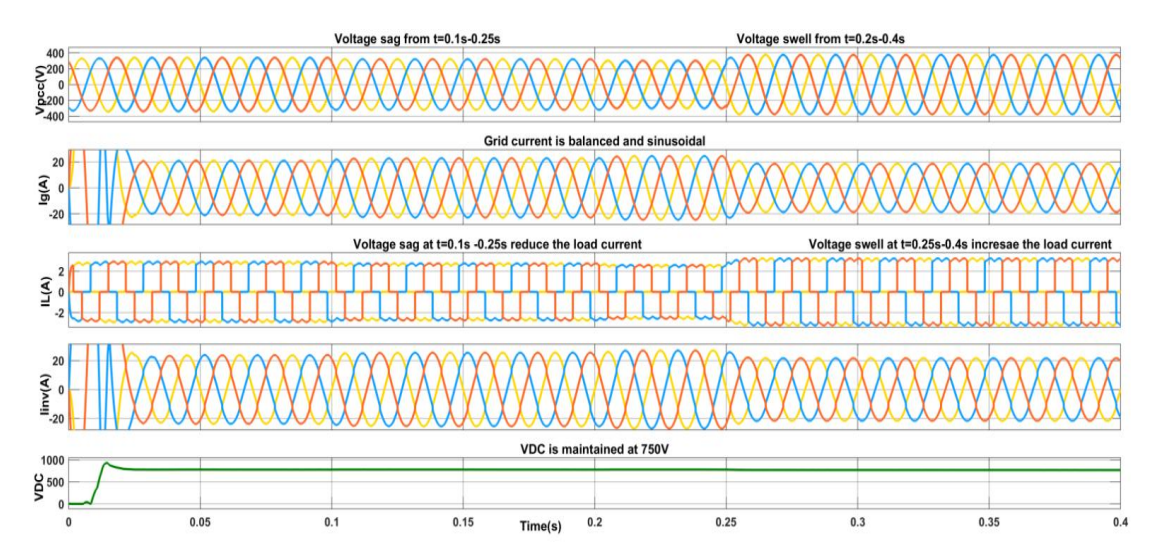


Fig.5.22. Waveforms of non-linear load under grid voltage sag and swell condition

5.4.2.6 Comparison analysis of proposed CSO-PI technique with PSO-PI and PI controller in term of total harmonics distortions

System performance of presented CSO control technique has been compared with PI controller and PSO- PI controller under aforementioned cases considered viz non-linear load, unbalanced load and different grid voltage condition and the result are as shown in Table 5.4. It has been observed that, CSO-PI controller is able to achieve less THD in grid current as compared to PSO -PI, and PI controller.

Table 5.4 Comparison of CSO- PI controller with PSO- PI controller and PI controller for grid current harmonics

Control Technique	Non-linear balanced load	Non-linear unbalance load	Grid voltage unbalance	Grid voltage sag	Grid voltage swell
PI controller	2.37%	3.38%	3.66%	2.93%	2.74%
PSO - PI Controller	2.18%	2.67%	2.58%	1.22%	2.41%
CSO - PI Controller	2.09%	2.55%	2.27%	1.02%	2.05%

5.4.2.7 Comparison analysis of proposed CSO-PI technique with PSO-PI and PI controller in term of performances indices

Further, performance indices of CSO-PI, PSO-PI and conventional PI under different load condition has been calculated and the results for the nonlinear load are mentioned in Table 5.5. From Table 5.5 it can be seen that value of performance indices for CSO-PI is less as compared to PSO-PI controller and PI controller respectively. So, from Table 5.5 it is clear that presented CSO technique gives better performance indices as compared to the other technique. Thus, justification for adopting CSO - PI controller is established.

Table 5.5 Comparison of different technique based on performance indices

Control Technique	MSE	MAE	RMSE
PI controller	5.11	3.86	2.26
PSO - PI Controller	4.44	2.11	2.107
CSO - PI Controller	2.88	1.69	1.697

5.4.2.8 Comparison analysis of proposed CSO-PI technique with PSO-PI and PI controller in term of maximum power point tracking and DC bus voltage regulation

Fig 5.23. shows the maximum power tracking of a SPV module under different irradiation circumstances. Table 5.6 displays the variation in the SPV module's irradiation level during the specified period. Table 5.6 and Fig.5.23 make this obvious. In addition to other control strategies that have been presented, CSO-PI controllers with CSO MPPT track maximum power. Furthermore, Fig .5.24 and Table 5.7 display the DC bus voltage response for the CSO-PI, PI-PSO, and PI Controller for nonlinear load. Fig.5.23 illustrates that there is an initial overshoot in every situation, whereas the CSO-PI controller has the least amount of undershoot. The CSO-PI controller outperforms the PI controller and PI-PSO in every irradiation scenario.

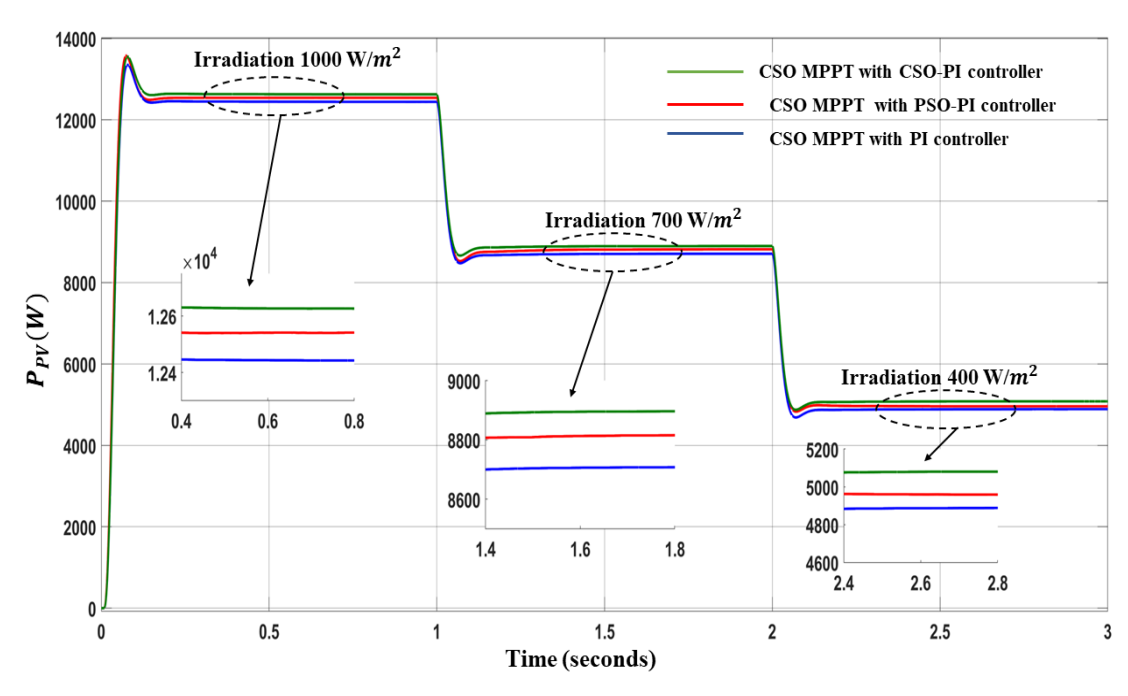


Fig 5.23. Comparison of maximum power obtained using different control algorithm

Table 5.6 Comparison analysis of maximum power obtained using different control algorithm

S.No	Irradiation	Time	PI Controller	PSO-PI controller	CSO-PI Controller
			P(kW)	P(kW)	P(kW)
1.	1000W/m ²	0.0s-1. s	12.53	12.55	12.68
2.	700W/m ²	1.0s-2.0s	8.72	8.86	8.90
3.	400W/m ²	2.0s-0.3s	4.93	4.94	5.18

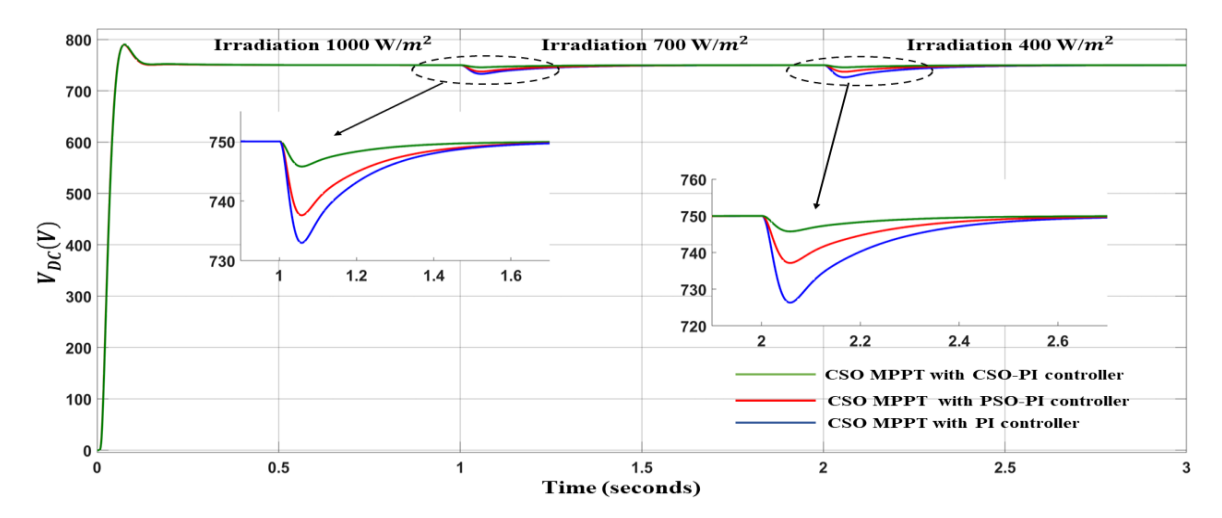


Fig 5.24. Comparison of DC bus voltage regulation using different control algorithm Table 5.7 Comparison analysis of DC bus voltage obtained using different control algorithm

	Overshoot	Undershoot	DC Voltage(V)
Control			
Algorithm			
PI controller	Initially	20V	750
	Present		
PSO-PI controller	Initially	10V	750
	Present		
CSO-PI	Initially	4V	750
controller	present		

5.4.3 Performance evaluation and result discussion using proposed HBA-PI Controller

In this section, HBA algorithm's performance is evaluated for controlling DC link voltage of a grid connected solar photovoltaic system under linear/nonlinear (balance/unbalanced) load and grid voltage sag & swell conditions in steady and dynamic states. To ensure the efficacy of proposed algorithm, IEEE global standard is taken into the consideration for total harmonics distortion of grid current at the point of common coupling

5.4.3.1 System response under linear load and irradiation variation

Steady state behavior of grid connected SPV system using HBA control algorithm has been shown in Fig.5.25 Waveform of all the parameter such as voltage at $PCC(V_{pcc})$, grid current (I_{grid}), inverter current (I_{inv}), load current (I_{load}), DC bus voltage (V_{DC}) and real and reactive power sharing among utility grid, VSI and load are examined under varying atmospheric & load condition.

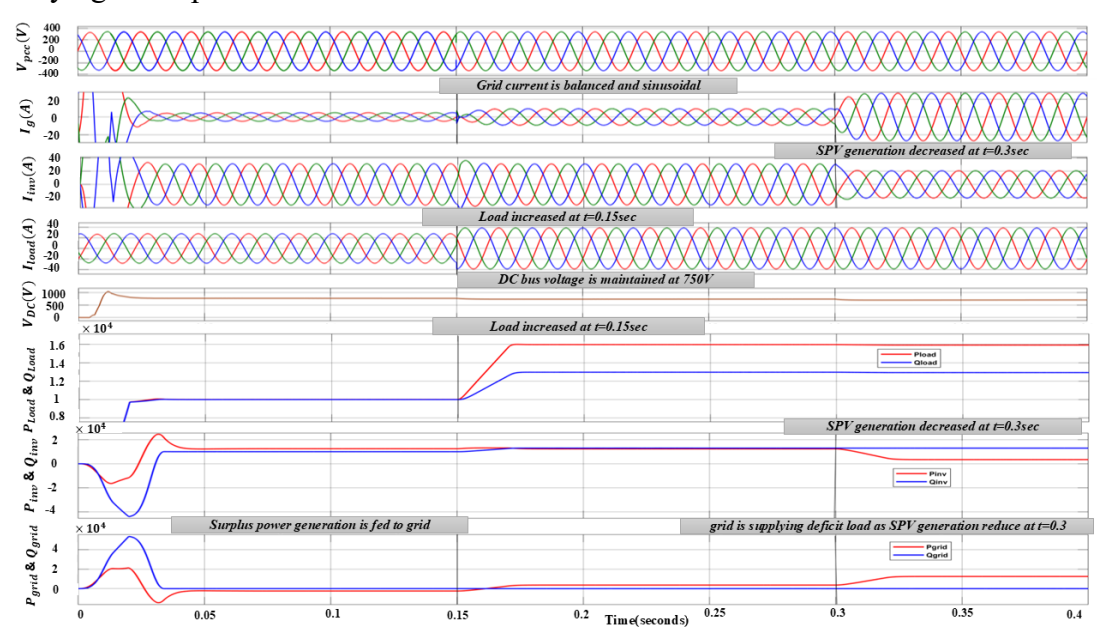


Fig.5.25 Waveform under linear load and irradiation variation

A linear load of 14.14 kVA, 0.71 lag pf is connected at point of common coupling (PCC). Solar photovoltaic system generates 12.78kW power and the active power demand of load is 10kW. The excess power (2.78 kW) is given to the utility grid. Reactive power demand of the load is 10kVA which is fulfilled by inverter which means grid operates in Unity power factor (UPF) mode. From Fig.5.25 it can be observed that grid current and voltage at PCC are sinusoidal and balanced. At t=0.15sec, an extra load of 6.7kVA 0.89pf (6kW, 3kVAR) is attached to the existing load. Now, the real power demand of load is 16kW which is provided by both inverter (12.78kW) and grid (3.22kW) and reactive power is fulfilled by inverter hence grid operate in UPF mode as depicted in fig.5.25. At t=0.3 sec, irradiation is dropped from 1000W/m² to 300W/m². As the irradiation level drop, the real power produced by the PV falls from 12.78 kW to 3.65 kW. Deficit power (12.35 kW) is therefore taken from

the grid. Even with changes in irradiation, the reactive power supplied by utility grid is zero demonstrating grid is working in UPF mode. Despite changes in load and irradiation, the grid current is balanced and sinusoidal. Also, DC link voltage is maintained at 750V.

5.4.3.2 System response under non-linear load and irradiation variation

In this section, HBA control algorithm is tested for nonlinear load (3-φ rectifier with R=200Ω and L=100mH) is attached at the PCC as shown in Fig.5.26. Solar photovoltaic system generates 12.78kW power and the real power demand of load is 1.6kW. The excess power (11.18 kW) is supplied to the grid. V_{pcc} and I_{grid} are out of phase shows that power is supplied to the utility grid. From fig.5.26 it can be notice that grid current and voltage at PCC are sinusoidal and balanced. DC voltage is maintained at 750V. At t=0.15sec, an extra load of 6.7kVA, 0.89 lagging pf (6kW, 3kVAR) is attached to the load. Now, the real power requirement of load is 7.6kW which is provided by VSI (7.6kW) and excess power is fed to the grid (5.18kW) as depicted in Fig.5.26. Reactive power demand of load is satisfied by voltage source inverter hence grid operates in UPF mode. At t=0.3 sec, irradiation is dropped from 1000W/m² to 300W/m². As the irradiation level drop, the real power produced by the PV falls from 12.78 kW to 3.65 kW. Deficit power (3.95 kW) is therefore taken from the grid. Even with changes in irradiation, the reactive power taken from the utility grid is zero demonstrating that system is working under UPF mode. Despite changes in load and irradiation, the grid currents remain balanced and sinusoidal. Fig 5.27(a) & 5.27(b) depicts the THD of I_{grid} and I_{load},. The load current has 30.44% THD, whereas the grid current has only 1.07% THD, demonstrating that the proposed honey badger control algorithm works well for mitigating the harmonics along with maintaining V_{DC} at 750V.

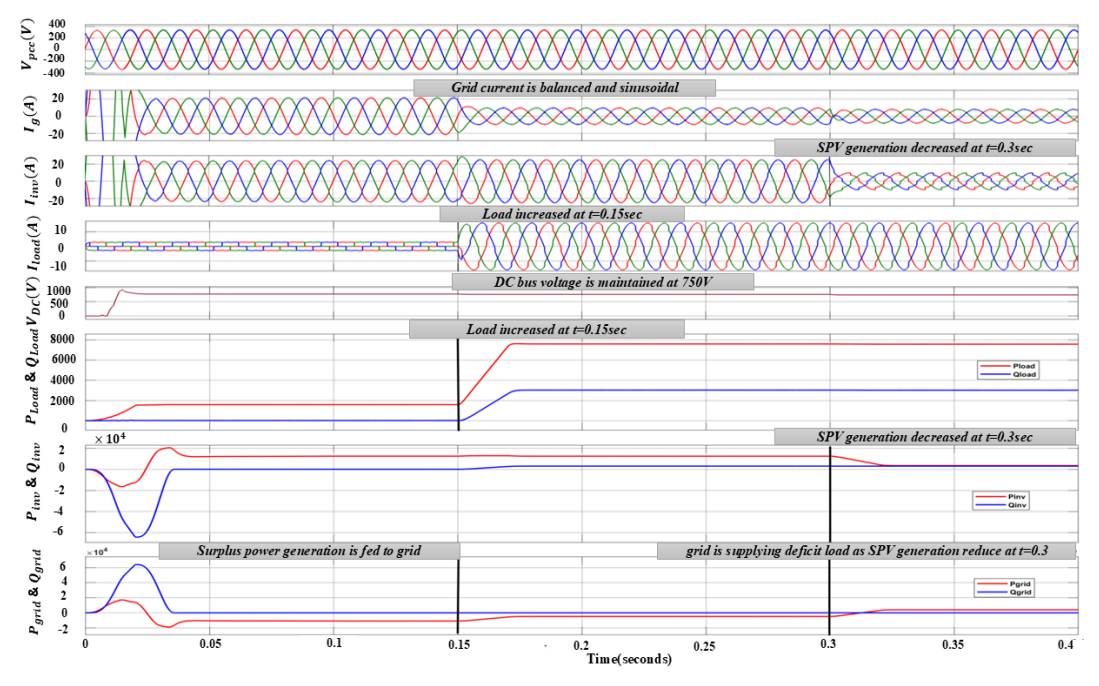


Fig. 5.26 Waveform under nonlinear load variation and irradiation variation

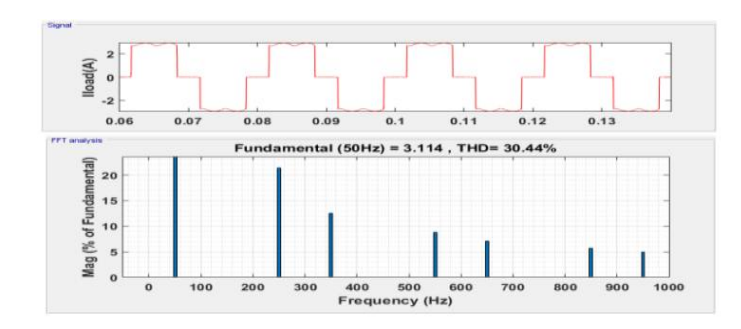


Fig.5.27 (a) THD of I_{load} for non -linear load

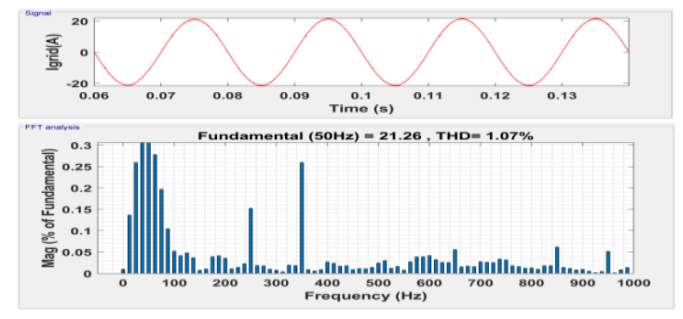


Fig.5.27 (b) THD of for I_{qrid} non-linear load

5.4.3.3 System response under non-linear unbalanced load condition

Fig.5.28 depict the system's behavior under unbalanced load when one line/phase of the nonlinear load (3- ϕ bridge rectifier with R=200 Ω , L=100mH is out for time period t= 0.1-0.3 sec. It can be seen that in nonlinear V_{pcc} and I_{grid} are out of phase showing that extra power generated by SPV is supplied to the grid. Under these conditions, the proposed honey badger algorithm performs satisfactorily. Also, It can be observed from Fig.5.28 grid current and voltage at PCC is sinusoidal and balanced. DC bus voltage is maintained at 750V. The load current of nonlinear load has 32.52% THD, whereas the grid current has only 2.41% THD as depicted in Fig. 5.29(a) and 5.29(b), demonstrating that the presented honey badger algorithm works well for harmonic mitigation if one line / phase is out of non-linear load.

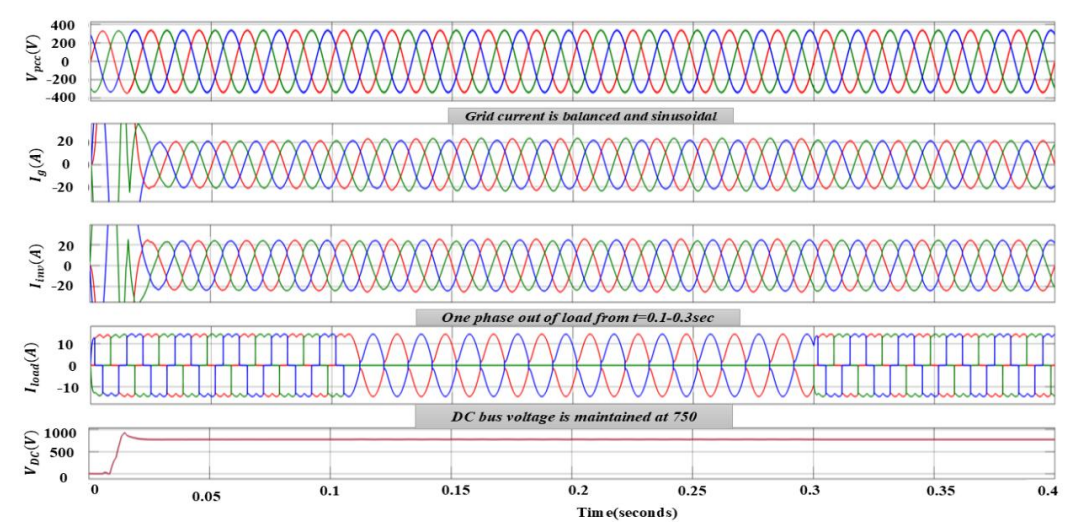


Fig.5.28 Waveform under nonlinear unbalance load variation

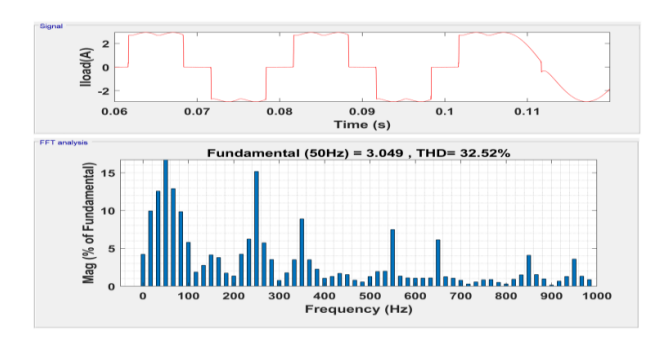


Fig.5.29 (a) THD of I_{load} under non - linear unbalanced load condition

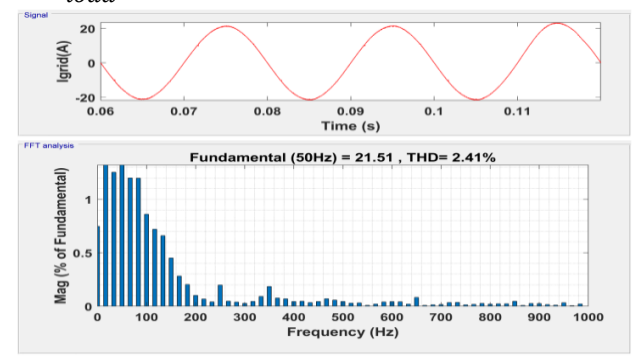


Fig. 5.29(b) THD of I_{arid} for nonlinear unbalance load condition

5.4.3.4 System response under unbalanced grid condition

Unbalance grid condition basically occurs when three phase voltages differ in amplitude which adversely affect the performance of the system. Simulation result of honey badger algorithm for grid unbalance condition with non-linear load (3- ϕ bridge rectifier with R=200 Ω , L=100mH) is as shown in Fig.5.30 Grid unbalancing is produced at t= 0.15sec by lowering the phase 'b' voltage to 364V and raising the phase 'c' value to 450V. From the figure it can be observed that even for grid unbalancing condition I_{grid} and V_{pcc} found to be sinusoidal. DC bus voltage is maintained at 750V.

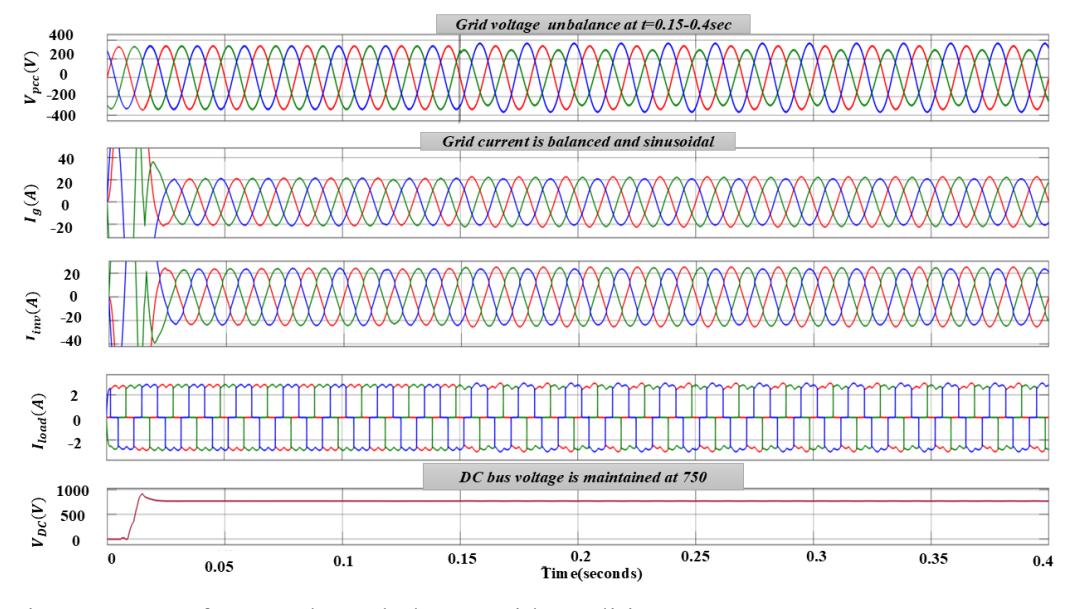


Fig.5.30 Waveform under unbalance grid condition

5.4.3.5 System response under grid voltage sag and voltage swell condition

Simulation results for voltage sag and swell condition of grid connected SPV system using honey badger algorithm is as shown in Fig.5.31. Voltage sag is created for time interval t=0.2-0.3sec and voltage swell is created for time interval t=0.3-0.4sec from the figure it can be noted that voltage sag reduces load current and voltage swell raises load current. Even in this dynamic situation I_{grid} is found to be sinusoidal and balanced. Also, DC bus voltage is maintained at 750V.

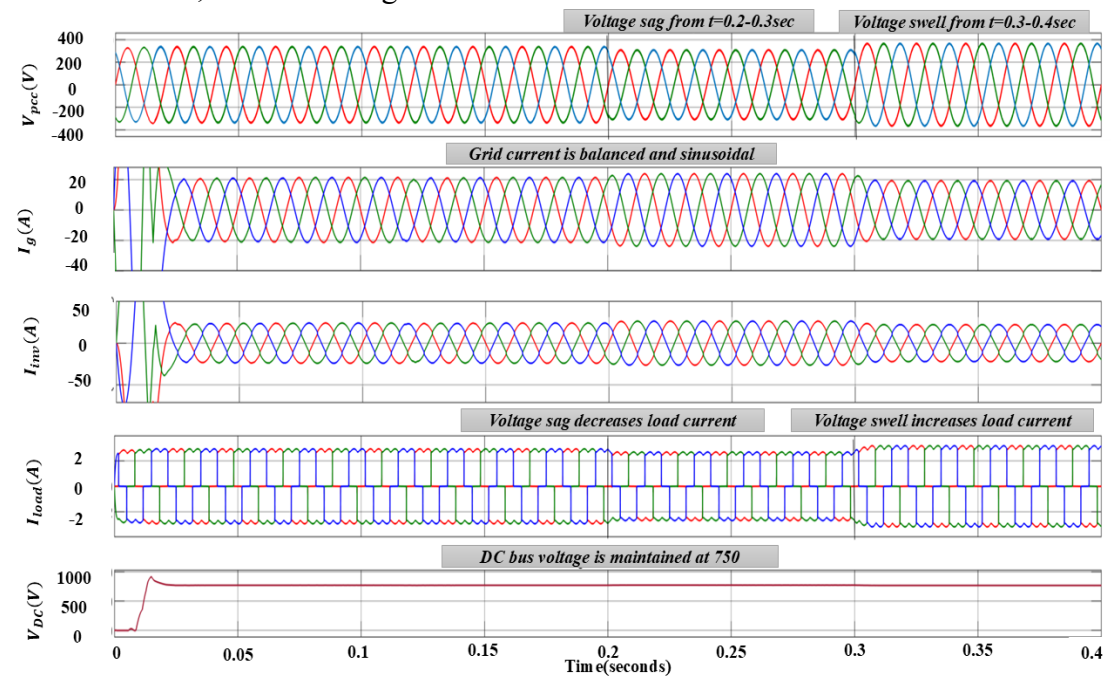


Fig.5.31 Waveform under grid voltage sag and swell condition

5.4.3.6 Comparison of proposed HBA-PI with PSO-PI and PI controller for grid current harmonics

Fig.5.32 (a), 5.32 (b), 5.32(c) and 5.32(d) depicts the THD spectra of load current (I_{load}) and grid current (I_{grid}) using different algorithm respectively for non linear load. These results represent 30.44% THD in load current, whereas grid current contains 1.66% THD using the PI controller 1.29% using PSO based PI controller and only 1.07% using HBA based PI controller for grid connected SPV systems. Similarly for other grid and load condition analysis has been done and the results are as shown in Table. 5.8. Hence, based on the above assessment it can be observed that the grid tied SPV system using HBA based PI controller is able to achieve less THD in grid current as compared to PSO based PI, and PI controller.

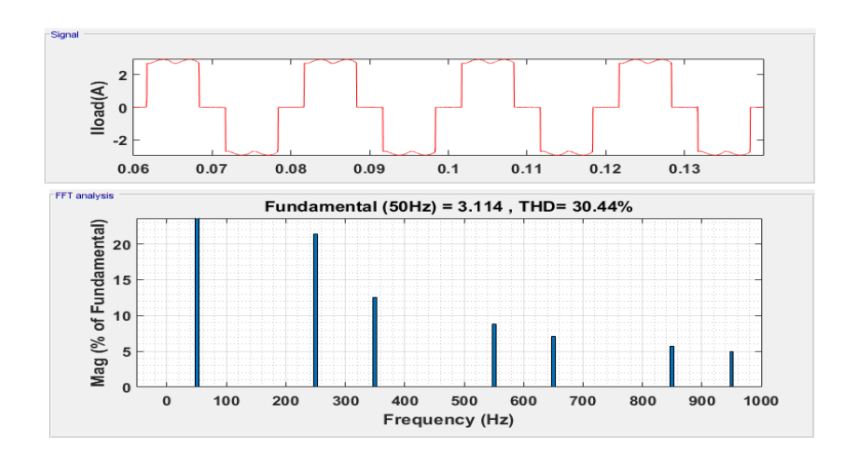


Fig. 5.32(a) THD of I_{load} for non linear load

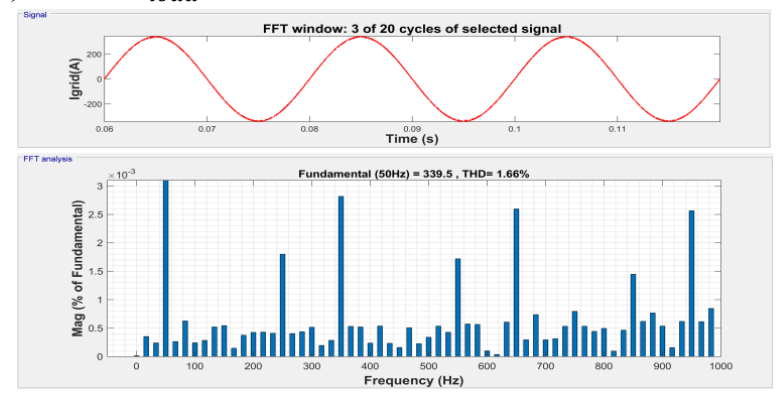


Fig. 5.32(b) THD of I_{grid} for non-linear load using PI controller

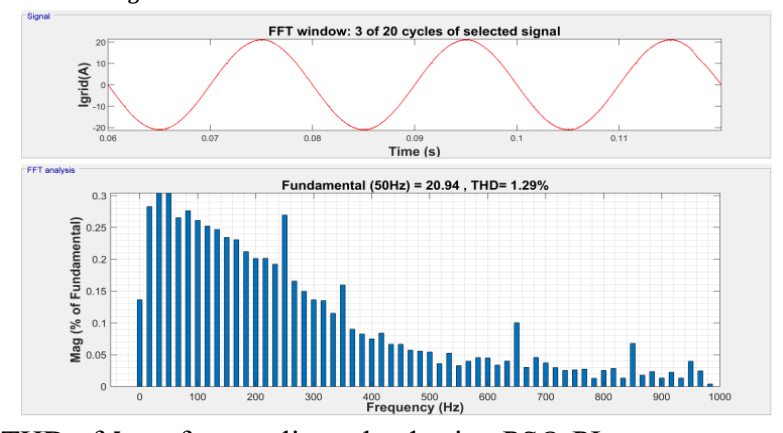


Fig.5.32(c) THD of I_{grid} for non-linear load using PSO-PI

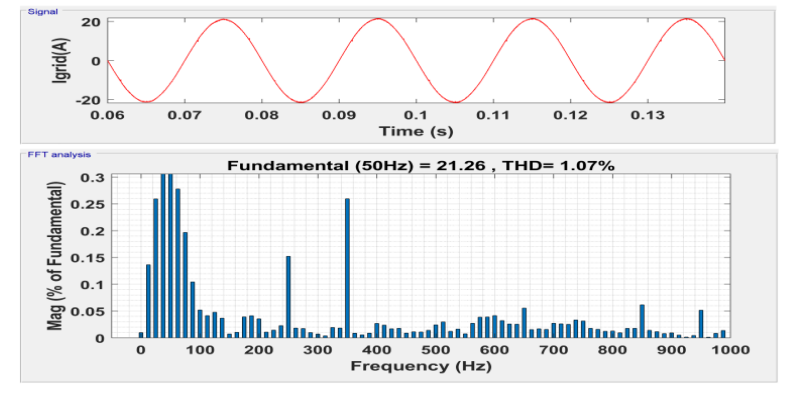


Fig.5.32(d) THD of I_{grid} for non linear load using HBA-PI

Table 5.8. Comparison of HBA - PI controller with PSO - PI controller & PI controller for THD in current

S.No	Control Algorithm	Non- linear load	Non-linear Unbalanced load	Grid voltage unbalance	Grid voltage sag	Grid voltage swell
1.	PI controller	1.66%	3.38%	3.67%	2.95%	2.73%
2.	PSO-PI controller	1.29%	2.50%	2.02%	1.21%	1.52%
3.	HBA-PI controller	1.07%	2.41%	1.14%	1.00%	1.11%

5.4.3.7 Transient analysis of PV output at different irradiation for nonlinear load with HBA- PI, PSO- PI and PI controller

The transient response and maximum power tracking of a solar PV module under various irradiation conditions are shown in Fig.5.33. Table.5.9 displays the variation in the solar PV module's irradiation level over the specified time period. It is evident from Fig.5.33 and Table .5.9. HBA-PI controllers track more power and have shorter settling times than PSO-PI controllers and PI controllers.

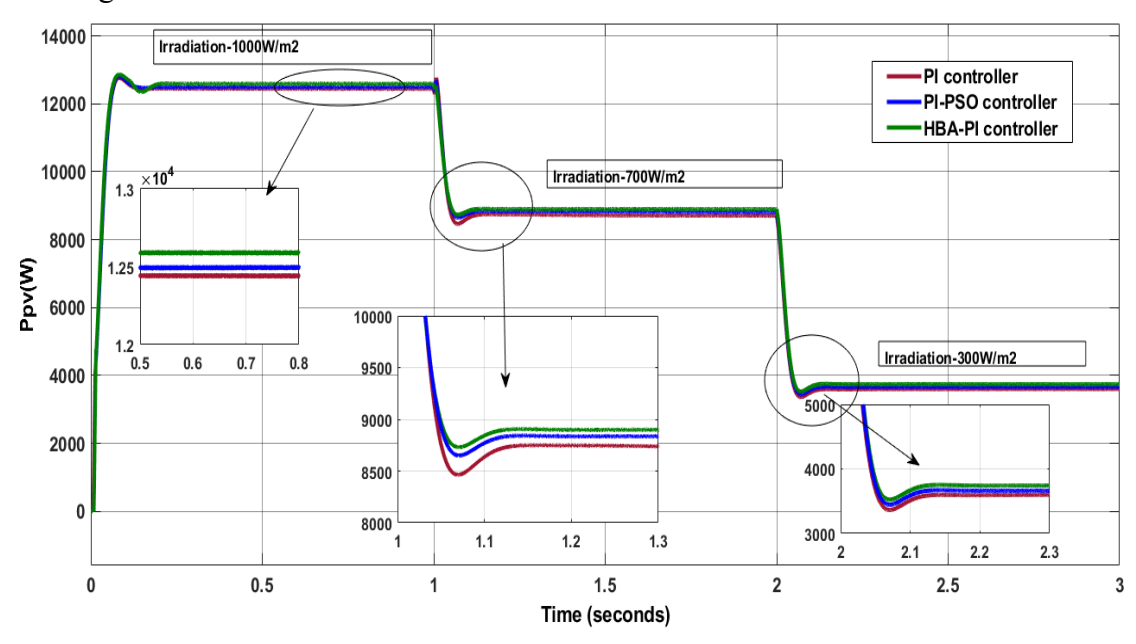


Fig.5.33 Transient response of INC MPPT technique at different irradiation using PI controller, PSO- PI controller and HBA- PI controller

Table 5.9. Comparison of INC MPPT technique at different irradiation using PI controller, PSO-PI controller and HBA-PI controller

S.No	S.No Irradiation Tim		PI Controller		PSO-PI controller		HBA-PI Controller	
3.110	o irradiation 11	Time	P(kW)	Settling time(s)	P(kW)	Settling time(s)	P(kW)	Settling time(s)
1.	1000W/m ²	0.0s- 1.0s	12.49	0.30	12.5	0.27	12.72	0.27
2.	700W/m ²	1.0s- 2.0s	8.67	0.26	8.71	0.13	8.94	0.13
3.	300W/m ²	2.0s- 3.0s	3.67	0.22	3.73	0.12	3.80	0.12

5.4.3.8 Transient analysis of DC link voltage for nonlinear load with HBA -PI, PSO - PI and PI controller

The DC link voltage response for the PI-HBA, PI-PSO, and PI Controller for nonlinear load is shown in Fig.5.34 and Table.5.10 Overshoots and settling time are maximum in the case of the PI controller, as shown in graph. Even though the PI-PSO algorithm reduces overshoots, the settling time is still larger in this case. In comparison to the PI controller and PI-PSO, the honey badger algorithm produces fewer overshoots and has a shorter settling time.

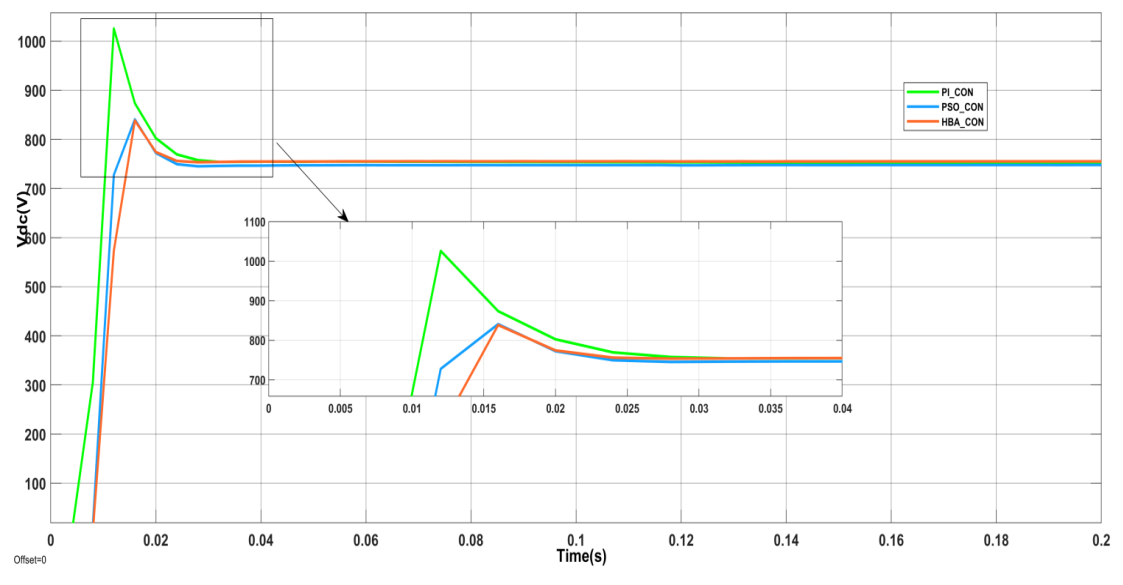


Fig.5.34 Response of DC bus voltage for non-linear load with HBA based PI, PSO based PI & PI controller

Table. 5.10 Transient analysis of DC link voltage for nonlinear load with PI, PSO -PI and HBA-PI controller on different irradiation

Control Algorithm	Settling time	Overshoot	Undershoot	DC Voltage(V)
PI controller	28ms	27.46%	Absent	748
PSO-PI controller	25ms	11.76%	Absent	747
HBA-PI controller	23ms	11.52%	Absent	750

5.4.3.9 Comparison of PI controller with PSO- PI and HBA-PI controller based on performance indices and time complexity

Table.5.11 shows the performance indices and Table.5.12 shows the gain value and time complexity of PI-controller, PSO-PI controller and HBA-PI controller. Convergence curve of presented HBA algorithm is as shown in Fig.5.35. From Table.5.11 it is clear that presented HBA technique provide less error than other two technique which means HBA gives better performance indices as compared to the PSO and PI technique. Thus, justification for adopting HBA for PI controller is established.

Table 5.11 Comparison of PI controller with PSO- PI and HBA-PI controller based on performance indices

Control Algorithm	MSE	MAE	RMSE
PI controller	4.53	2.13	2.13
PSO-PI controller	3.34	1.83	1.82
HBA-PI controller	2.11	1.45	1.45

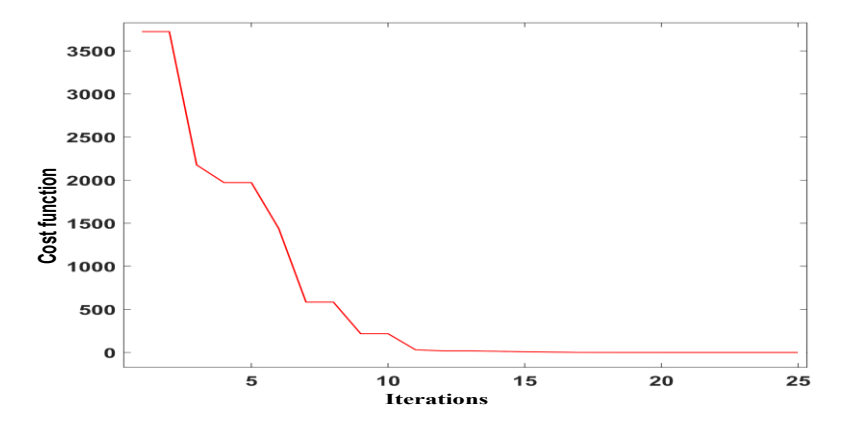


Fig5.35 Convergence curve of proposed HBA algorithm

.5.12 Gain value and Time complexity of 11,150 11 and 11b/1 11 con						
Controller	Gain value	of of PI	Time			
	controller		complexity			
	Кр	Ki	(sec)			
PI controller	0.5	3.0	-			
PSO-PI controller	0.7948	0.9484	2.583			
HBA-PI controller	0.005	0.03	1.850			

Table. 5.12 Gain value and Time complexity of PI, PSO-PI and HBA –PI controller

5.4.3.10 Stability Analysis

The voltage and current loop of the controller is initially linearized to develop the transfer function represented in the equations below in order to analyze the controller stability of the system. The voltage control loop comprises a PI controller with gain values Kp and Ki, while Cf represents the filter's capacitance. The current loop contains a hysteresis block, Ts is the inverter's half-switching time period, Lf represents filter inductance, and Rf is the filter's series resistance value. Fig.5.36 shows a full cascaded current and voltage loop, and Fig.5.37 shows a Bode plot with comments on the stability of the proposed controller. Table.5.13 illustrates the controller parameters and performance characteristics of proposed HBA controller Fig.5.37 shows that the closed loop system is stable because both the phase margin and the gain margin are positive and phase margin is greater than gain margin. The value of phase margin is equal to 60° at gain crossover frequency 302.84Hz and the gain margin is equal to 39.4dB at phase crossover frequency 5.1 kHz.

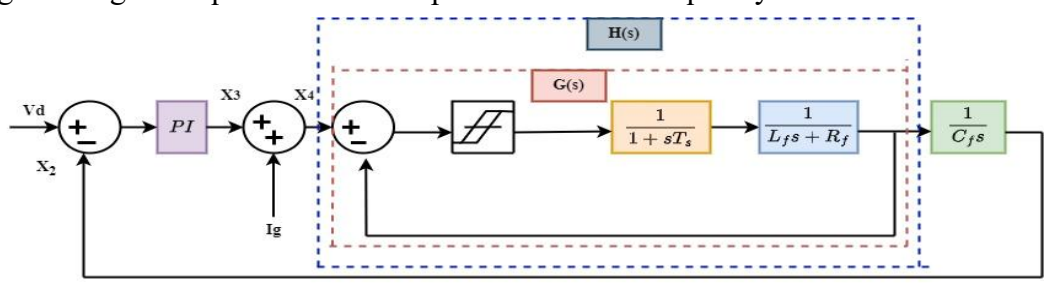


Fig. 5.36 Block diagram of Linearized proposed controller

Considering Ig=0, Transfer function of the system is expressed as follows, by equationn-(5.30)-(5.354)

$$G(s) = \frac{1}{L_f T_s(s)^2 + (L_f + T_s R_f) s + R_f}$$
(5.30)

$$H(s) = \left(\frac{G(s)}{1 + G(s)}\right) * \frac{1}{C_f(s)}$$
(5.31)

$$H(s) = \frac{1}{L_f C_f T_s s^3 + (L_f C_f + T_s R_f C_f) s^2 + (R_f C_f + C_f) s}$$
(5.32)

$$X4 = \left(Kp + \frac{K_i}{s}\right)\left(V_d - X_2\right) \tag{5.33}$$

$$T.F = \frac{X_2(s)}{V_d(s)} = \frac{K_p s + K_i}{L_f C_f T_s s^4 + (L_f C_f + T_s R_f C_f) s^3 + (R_f C_f + C_f) s^2 + K_p s + K_i}$$
(5.34)

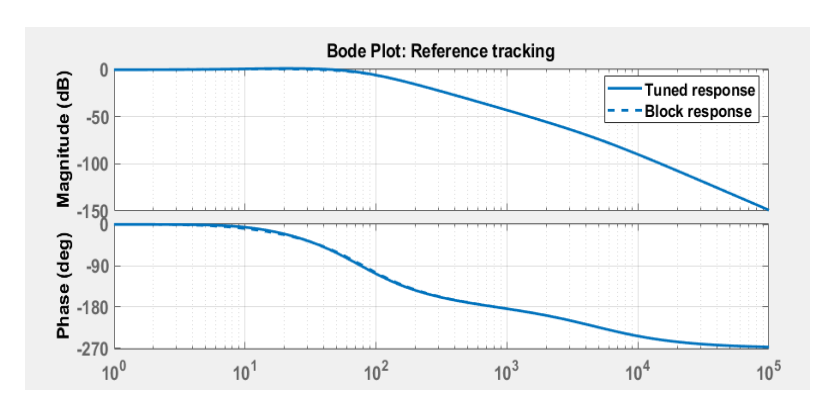


Fig.5.37 Stability analysis of controller through Bode plot

Table.5.13 Controller Parameters and performance characteristics of proposed HBA controller

S.No	Parameters	Tuned	Block
1.	Кр	0.004983	0.005
2.	Ki	0.048038	0.03
3.	Gain margin	39.4dB@817rad/s	39.6dB@828rad/s
4.	Phase margin	60deg@48.2rad/s	64.3deg@47.9rad/s
5.	Closed loop stability	Stable	Stable

5.5 COMPARISON OF ANN-PI, CSO-PI and HBA-PI CONTROLLER

Under different operating situations, the relative performance of ANN-PI, CSO-PI, and HBA-PI controllers has been examined in terms of photovoltaic (PV) power output and grid current harmonics. The HBA-PI controller continuously produces the maximum PV power output at all irradiance levels, as seen in Table 5.14. The HBA-PI controller reaches 12.72 kW at full irradiance (1000 W/m2), which is marginally more than the CSO-PI (12.68 kW) and ANN-PI (12.58 kW) controllers. Similarly, the HBA-PI controller performs better with 8.94 kW and 3.80 kW output under medium (700 W/m2) and low (300 W/m2) irradiation circumstances. This shows how well the HBA-PI controller maximizes the PV system's power extraction under various conditions.

In terms of power quality, Table 5.15 compares the grid current harmonics of each controller during various grid disturbances. The HBA-PI controller has the lowest total harmonic distortion in practically all circumstances, achieving 1.07% under non-linear load, 2.41% under non-linear unbalanced load, and much lower values under grid disturbances such as voltage unbalance (1.14%), sag (1.0%), and swell (1.11%). In

contrast, the ANN-PI and CSO-PI controllers produce greater harmonic levels, with the ANN-PI reaching up to 2.66% under voltage sag and the CSO-PI peaking at 2.55% under non-linear unbalanced load. These results demonstrate the HBA-PI controller's superior dynamic response and harmonic suppression capacity, making it a more robust and efficient solution for improving power extraction and quality in grid-integrated PV systems.

Table.5.14 Comparison of ANN-PI, CSO-PI and HBA-PI controller in term of PV power output

S.No	Irradiation	ANN-PI Controller	CSO-PI controller	HBA-PI Controller
		P(kW)	P(kW)	P(kW)
1.	1000W/m ²	12.58	12.68	12.72
2.	700W/m ²	8.89	8.90	8.94
3.	300W/m ²	3.73	3.76	3.80

Table.5.15 Comparison of ANN-PI, CSO-PI and HBA-PI controller in term of grid current harmonics

S.N o	Control Algorith m	Non- linear load	Non-linear Unbalanced load	Grid voltage unbalance	Grid voltage sag	Grid voltage swell
1.	ANN-PI controller	1.84%	2.57%	2.39%	2.66%	2.13%
2.	CSO-PI controller	2.09%	2.55%	2.27%	1.02%	2.05%
3.	HBA-PI controller	1.07%	2.41%	1.14%	1.00%	1.11%

5.6 COMPARISION OF HLO-ANN MPPT WITH HBA-PI, CSO-PI AND ANN-PI

In this section, the proposed HLO-ANN MPPT technique and the HBA-PI inverter controller are thoroughly compared to other PI-based control strategies, particularly the CSO-PI and ANN-PI controllers. Since both HLO-ANN MPPT and HBA-PI are novel approaches in this research, the goal of this comparison is to assess their overall efficacy and show how the proposed control approach performs better under different operating circumstances. To confirm the superiority of the developed approaches, key performance metrics such transient responsiveness, grid current harmonics and MPPT efficiency are analysed.

Table.5.16 Comparison of HLO-ANN MPPT with ANN-PI, CSO-PI and HBA-PI controller in term of grid current harmonics

S.No	Control Algorithm	Non- linear load	Non-linear Unbalanced load	Grid voltage unbalance	Grid voltage sag	Grid voltage swell
1.	ANN-PI controller	1.80%	2.53%	2.33%	2.64%	2.11%
2.	CSO-PI controller	2.01%	2.49%	2.22%	1.00%	2.01%
3.	HBA-PI controller	1.03%	2.37%	1.11%	1.00%	1.10%

Table.5.17 Comparison of HLO-ANN MPPT with ANN-PI, CSO-PI and HBA-PI controller in term of maximum power point tracking

S.No	Irradiation	ANN-PI Controller	CSO-PI controller	HBA-PI Controller
		P(kW)	P(kW)	P(kW)
1.	1000W/m ²	12.60	12.69	12.73
2.	700W/m ²	8.88	8.91	8.94
3.	300W/m^2	3.73	3.78	3.81

5.7 CONCLUDING REMARKS

This chapter thoroughly investigate the inverter control strategies for grid-integrated solar PV-based microgrids, emphasizing performance enhancement through advanced PI controller configurations. The results demonstrate that the proposed HBA-based PI controller significantly outperforms both the CSO-PI and ANN-PI controllers in improving the overall performance of grid-connected solar photovoltaic systems. Specifically, the HBA-PI controller achieves superior voltage regulation, effective reduction of total harmonic distortion (THD) well below the IEEE standard limit of 5%, and enhanced dynamic response across varying input, load, and grid conditions. Even though CSO-PI improves upon conventional and ANN-PI adds adaptability via self-learning and quicker response, HBA-based control ultimately delivers the highest efficiency and robustness. Moreover, the system consistently maintains unity power factor (UPF) operation, ensuring optimal power quality and grid stability. These findings establish the HBA-PI controller as the most effective solution for power quality enhancement, system stability, and maximum power point tracking in grid-integrated solar PV systems.

CHAPTER-6

ISLANDING DETECTION TECHNIQUE FOR GRID-INTEGRATED PV BASED MICROGRID

6.1 INTRODUCTION

As renewable energy sources, especially solar photovoltaic (PV) systems, become more prevalent in modern power networks, the idea of microgrids has become increasingly popular. While facilitating the shift to low-carbon energy systems, microgrids provide increased energy efficiency, better power quality, and greater flexibility. There are two main modes of operation for these systems: islanded and grid-connected. The issue of unintentional islanding, which occurs when a distributed generation (DG) unit keeps supplying electricity to a portion of the grid after disconnecting from the utility, is one of the most significant technical challenges in grid-connected operation. The safety of people, equipment protection, voltage and frequency stability, and the dependability of the entire power system are all seriously threatened by unintentional islanding. Thus, quick, precise, and trustworthy islanding detection technologies are necessary to ensure the safe and robust operation of grid-connected photovoltaic systems.

An extensive review of existing islanding detection techniques, encompassing both classical and modern approaches, is presented in Section 2.5 of Chapter 2.

This chapter presents a passive islanding detection technique (IDT) which is based on voltage ripple content at the point of common coupling (PCC) for grid integrated solar photovoltaic (SPV) system. While conventional passive detection techniques are commonly employed, they are not particularly effective at identifying islanding, especially when a minimal power mismatch exists. Furthermore, they may produce false detection in certain instances that are not islands. If islanding is not detected quickly, it may result in extremely hazardous and adverse situations. Passive detection techniques rely on power system parameters and might fail to detect islanding in certain scenarios. This chapter presents an efficient passive islanding detection approach for grid-integrated solar PV system. This technique employs time-domain spectral analysis to monitor the ripple component of the voltage source inverter (VSI) voltage at the PCC and identify discrepancies.

6.2 SYSTEM DISCRIPTION

In this study a grid connected solar PV based microgrid based on the UL1741 test system is used for the study as depicted in Fig 6.1.[149] As per UL 1741, the RLC load at PCC has a quality factor of 2 and is set to the resonance frequency of 50 ± 0.1 Hz. The load is expressed as a pure resistance(R), with a frequency of 50 Hz. This resistance has been adjusted so that it can absorb the rated power of the distributed generator module at the PCC voltage. Quality factor (Q_f) and impedance are represented in the following manner:

$$|Z| = \frac{1}{\sqrt{\left(\frac{1}{R^2}\right) + \left(\left(\frac{1}{wL}\right) - wC\right)^2}} \tag{6.1}$$

$$|Z| = \frac{1}{\sqrt{\left(\frac{1}{R^2}\right) + \left(\left(\frac{1}{wL}\right) - wC\right)^2}}$$

$$|Z| = \frac{R}{\sqrt{1 + Q_f^2 \left(\left(\frac{f_0}{f}\right) - \left(\frac{f}{f_0}\right)\right)^2}}$$
(6.1)

$$Q_f = R\sqrt{\frac{c}{L}} \tag{6.3}$$

In this study, distributed generation operates in unity power factor (UPF). Relationship between the PCC voltage (V_{pcc}) and power are represented by equation 6.4 & 6.5.

$$P_l = P_{inv} + \Delta P = \frac{V_{PCC}^2}{R} \tag{6.4}$$

$$Q_l = Q_{inv} + \Delta Q = V_{PCC}^2 \left(\frac{1}{wL} - wC\right)$$
(6.5)

When the switch is closed, load (P_l, Q_l) is fulfilled by the solar PV (P_{inv}, Q_{inv}) and the grid $(\Delta P, \Delta Q)$. Conversely, when the switch is open, the grid is isolated, creating a potential islanded zone that could result in hazardous operating conditions and serious power quality issues for the PV inverter and the RLC load.

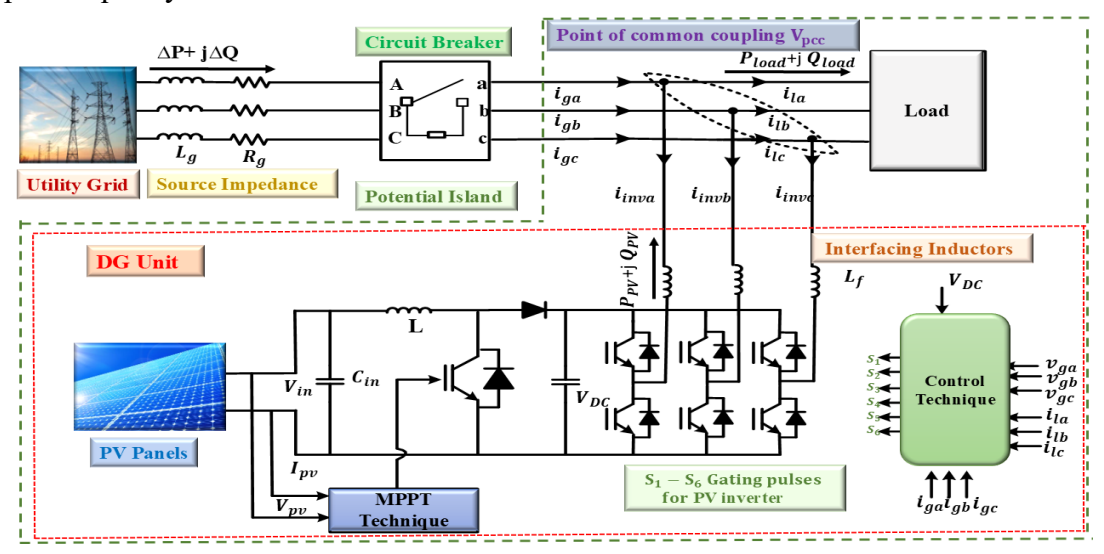


Fig.6.1 Schematic diagram of proposed model

6.3 VOLTAGE RIPPLE BASED ISLANDING DETECTION

Based on voltage ripples, the islanding detection technique is a computationally powerful passive technique that may be easily implemented in the inverter circuitry by observing the time domain spectrum content of voltage ripples [18]-[19]. Dead time effect, ripples in the DC link voltage, and high frequency switching in DG inverters leads to harmonic production. (V_{pcc}) . Since grid voltage (V_g) and load power (P_l) are regarded as constants, any power fluctuation in P_{inv} is instantly reflected in V_{pcc} . The DG unit have potential to meeting the load requirement in the case of zero power mismatch ($P_{inv}=P_l$). As a result, this is regarded as the worst scenario in this research since traditional passive techniques cannot identify islanding in this situation. In this study voltage ripple-based islanding is used which monitors the ripple content in the V_{pcc} waveform to successfully detect islanding. Fig 6.2 presents a block diagram of this methodology.

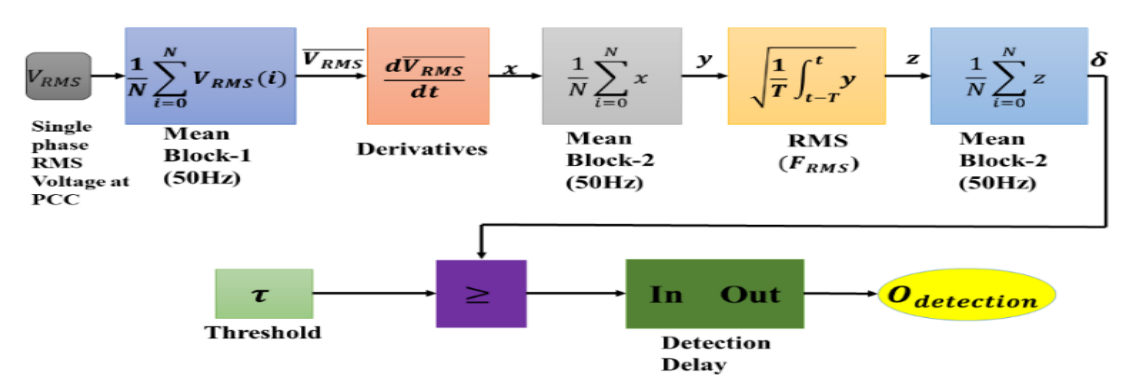


Fig. 6.2 Proposed Islanding technique

Fig.6.2 illustrates how the RMS voltage (V_{RMS})waveform's ripples are initially amplified by computing its derivative. After that, the RMS block processes the derivative signal to eliminate the DC component and determine how much ripple is there in the amplified waveform [150]-[151].

Each output stage is followed by three mean blocks: the first removes any noise at high frequencies in the source (V_{RMS}) over 50 Hz., the second removes any discontinuities in the derivative block's output, and the third mean block smooths out the RMS block's output.

Step1 displays the input waveform, representing the single-phase voltage (V) at the point of common coupling. Step 2 displays the V_{RMS} . The root mean square is determined over a one-cycle moving average window, using a nominal system frequency of 50 Hz.

$$V_{RMS} = \sqrt{\frac{1}{T} \int_{t-T}^{t} V^2}$$
 (6.6)

where T = 1/50 second. All frequency elements in the V_{RMS} above 50 Hz are considered noise and are removed employing mean block 1. This works similarly to a lowpass filter, which, as shown in fig.6.2(Step 3), suppresses any frequency elements over 50 Hz.

The filter output $\overline{V_{RMS}}$ is modelled as:

$$\overline{V_{RMS}} = \frac{1}{T} \int_{t-T}^{t} V_{RMS}. dt \tag{6.7}$$

This approach requires amplifying minor fluctuations in $\overline{V_{RMS}}$ to function properly. To obtain the x waveform, take the derivative of $\overline{V_{RMS}}$, as shown in Fig.6.2 (Step 4. The derivative is assessed after every 10 μ s sampling interval. To increase the technique's

efficacy, frequency components over 50 Hz in the x waveform are removed using a filter to produce y waveform illustrated in Fig. 6.2 (Step 5) waveforms x and y are represented as

$$\chi = \frac{d(\overline{V_{RMS}})}{dt} \tag{6.8}$$

$$y = \frac{1}{T} \int_{t-T}^{t} x \tag{6.9}$$

The z waveform was calculated by evaluating the root mean square value of y over a f_{RMS} frequency cycle. Fig. 6.2 (Step 6) illustrates how this is employed to calculate the amount of ripple content and remove any DC components in y. To get the islanding detection waveform δ , any frequency component over f_{MEAN} is removed from waveform z, as shown in fig.6.2 (Step 7). The waveforms z and δ are described as

$$z = \sqrt{\frac{1}{T_{RMS}} \int_{t-T_{RMS}}^{t} y} \tag{6.10}$$

$$\delta = \frac{1}{T_{MEAN}} \int_{t-T_{MEAN}}^{t} z \tag{6.11}$$

Where,
$$T_{MEAN} = \frac{1}{f_{MEAN}}$$
 and $T_{RMS} = \frac{1}{f_{RMS}}$

The detection waveform δ is checked against a preset threshold. Islanding is identified when δ surpasses a predetermined threshold over a set time period. Let τ is detection threshold, t_{δ} is the predetermined decision time delay, and Δt is the time period when δ surpasses τ . Islanding detection decision signal. $O_{\text{detection}}$ is modelled as

$$O_{\text{detection}} = \begin{cases} 1, & \text{if } \delta \ge \tau, ^{\circ} \Delta t \ge t_{\delta} \\ 0, & \text{if otherwise} \end{cases}$$

$$(6.12)$$

When $O_{\text{detection}}=1$, islanding is detected, while $O_{\text{detection}}=0$ implies no islanding. At this frequency, the ideal threshold and time delay were 12 V/s and 3ms, respectively

6.4 Performance analysis of islanding detection technique

A grid-connected solar PV-based microgrid, as depicted in Fig. 6.1, was simulated to evaluate the feasibility of the presented method. Table 1 shows the major parameters utilized during the simulation [15]-[16]. At 0.3 seconds, the switch opens, isolating the DG unit and load from the grid and initiating the islanding process. IEC Std. 62116 states that detecting islanding gets more difficult when the load's power consumption matches the distributed generation. The cases examined are as follows:

i.Islanding of grid integrated SPV system with 0 % of active power mismatch condition.

ii.Islanding of grid integrated SPV system with 30 % of active power mismatch condition.

iii.Sudden load variation at point of common coupling iv.Grid side distortion

6.4.1 Islanding of grid integrated SPV system with 0 % of active power mismatch condition.

Fig. 6.3, Fig. 6.4, Fig. 6.5 and Fig. 6.6 depict the simulation results for the various conditions considered in the study. Figures illustrate the waveforms of PCC voltage (V_{pcc}) , load current (I_l) , grid current (I_g) , VSI current (I_{inv}) , and DG de-energizing signal.

In first condition, zero active power mismatch condition has been considered which is one of the most difficult scenarios to detect islanding. Fig 6.3 shows that before islanding; the grid current is nearly zero due to the inverter's active power matching the load's consumption. Islanding leads to zero grid current and fluctuation in PCC voltage. It can be seen from the Fig 6.3 when islanding occurs at 0.3 seconds PCC RMS voltage ripple content increases. This is because when DG disconnects from the grid, it loses the grid's stabilizing effect, which causes the voltage fluctuation level to increase. The increased voltage fluctuation during islanding causes the amplitude of the produced waveform to exceed the threshold level. The technique detects islanding when the amplitude of the voltage waveform exceeds the threshold level. The DG denergizing signal, initially fix to '1' for normal condition, is changed to '0' after 3ms of islanding detection due to the method's latency.

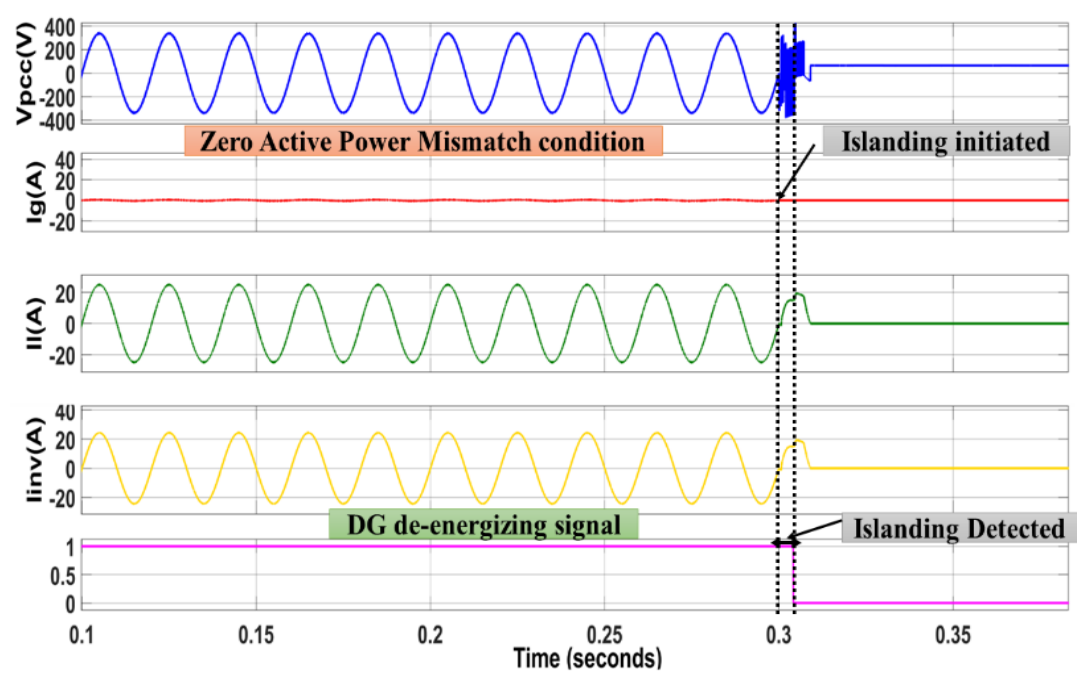


Fig.6.3 Islanding detection of grid integrated SPV system with zero active power mismatch

6.4.2 Islanding of grid integrated SPV system with 30 % of active power mismatch condition.

The second scenario examines the case where there is a 30% active power mismatch between the power generated by the DG and the load demand. This condition is relatively easier to detect compared to the zero-mismatch case, due to the existence of a noticeable power imbalance that results in observable changes in system parameters following islanding. Upon the occurrence of islanding at 0.3 seconds, the difference between the generated and consumed power manifests as a deviation in the PCC voltage and frequency. Unlike the zero-mismatch case, the power imbalance in this scenario leads to a more rapid and pronounced variation in voltage amplitude. This deviation pushes the waveform amplitude beyond the set threshold more quickly, thereby triggering the islanding detection mechanism. The proposed technique identifies the islanding condition within the designated detection time window. Similar to the previous case, the DG de-energizing signal is switched from '1' to '0' shortly after detection, ensuring a timely and safe disconnection of the inverter from the load. This action helps to prevent potential safety hazards and equipment damage that could arise from continued operation in an islanded mode.

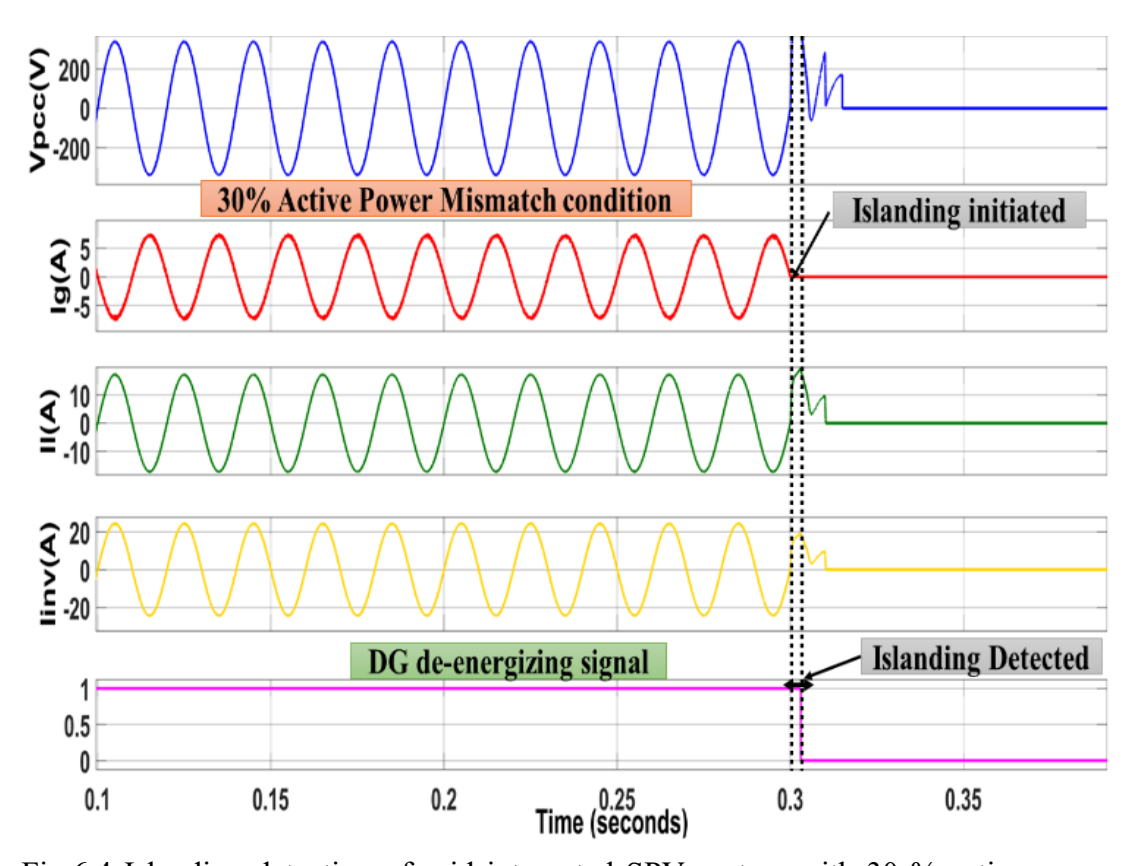


Fig.6.4 Islanding detection of grid integrated SPV system with 30 % active power mismatch

6.4.3 Sudden load variation at point of common coupling

In this scenario, the system experiences an abrupt change in the connected load while still being grid-connected. Such sudden variations in load demand can cause temporary fluctuations in PCC voltage and current that might resemble islanding-like behaviour's shown in Fig. 6.5 the detailed response when the load change occurs, there is a short-lived disturbance in the system parameters. However, the proposed detection technique correctly identifies this event as a non-islanding condition. The PCC voltage amplitude does not cross the islanding detection threshold, and the DG de-energizing signal remains fixed at '1', indicating normal operation. The system successfully continues to supply power to the load without any unnecessary inverter shutdown.

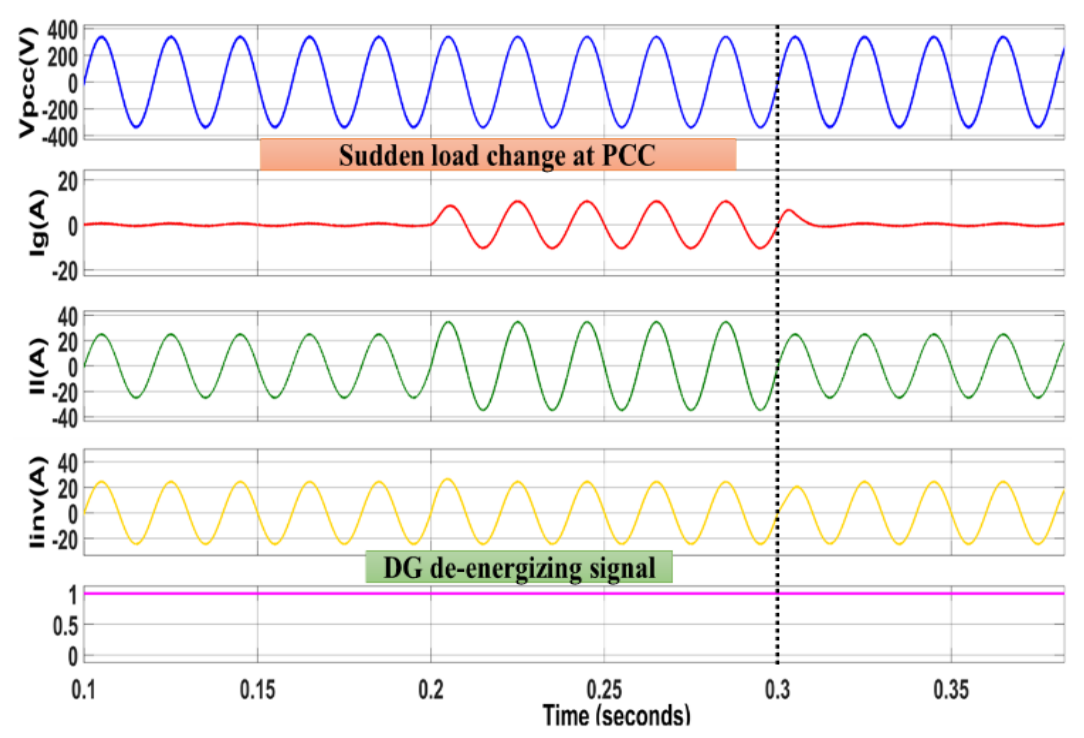


Fig. 6.5 Sudden load change at point of common coupling

6.4.4 Grid side distortion

Another critical scenario evaluated is the presence of voltage distortions on the grid side. Such distortions may arise due to faults, non-linear loads, or switching operations within the utility network. These distortions can affect the voltage waveform at the PCC, potentially causing false indications of islanding. The response illustrated in Fig. 6.6 confirms that the proposed method effectively filters out these disturbances. Although the PCC voltage shows visible waveform distortion, the amplitude remains within the acceptable threshold limits defined for islanding detection. As a result, the detection algorithm maintains the DG de-energizing signal at '1', avoiding a false islanding response. This case highlights the method's robustness to harmonic disturbances and waveform anomalies, reinforcing its suitability for operation in practical grid environments where such conditions frequently occur.

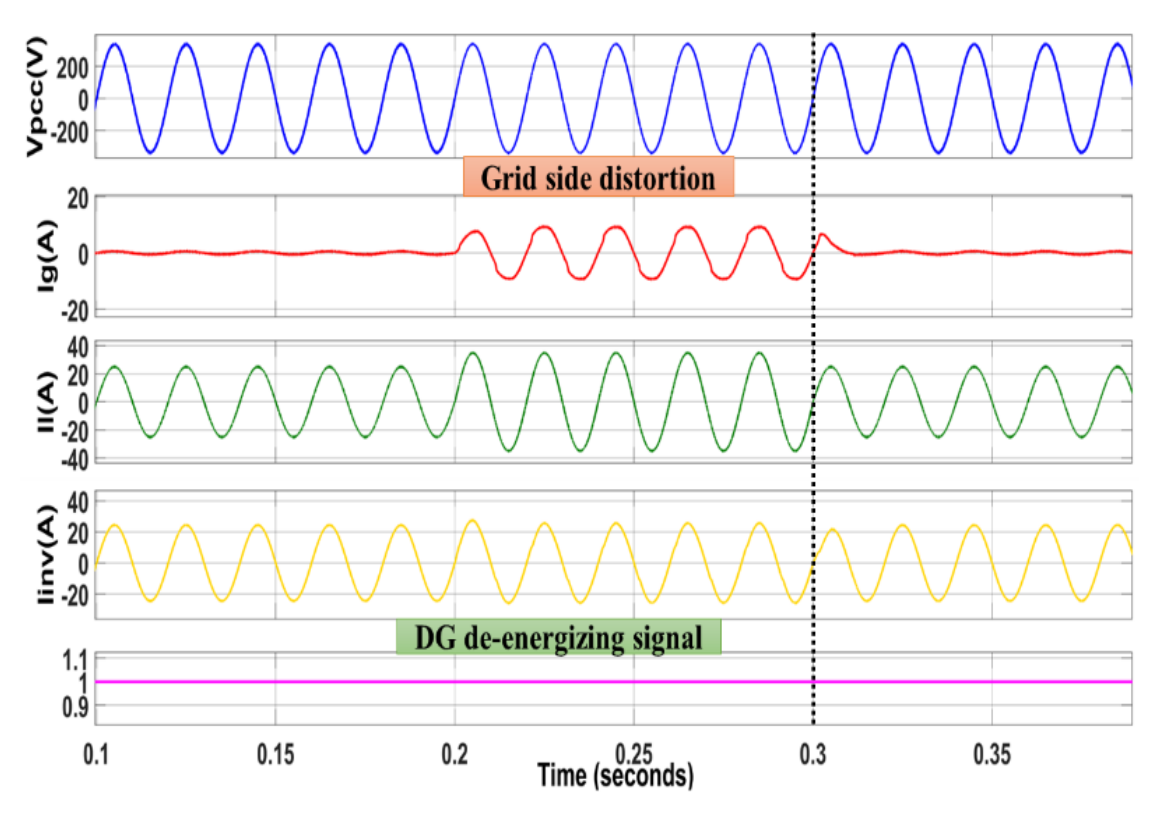


Fig.6.6 Waveform of grid side distortion

6.5 Comparative Analysis of Proposed Islanding detection

Table 6.1 displays the comparisons between the proposed strategy and conventional techniques based on various parameters. Compared to the conventional strategy, the technique examined in this work provides a number of advantages. It eliminates the NDZ, is relatively easy to compute, detects islanding quickly, and has no false detection and has no effect on power quality

Table.6.1 Comparison of proposed islanding detection technique with existing techniques

Parameter	Conventional Passive IDT (OU/UV and ROCOF)	Proposed Passive IDT	
Non Detection Zone(NDZ)	Large NDZ	Zero	
Detection time	Up to 2 s	3ms	
False Detection	High	None	
Detection Parameter	Absolute value	Ripple Content	

6.6 CONCLUDING REMARKS

In this chapter a passive islanding detection technique which is based on voltage ripple content at the point of common coupling for grid integrated solar photovoltaic system is presented. In order to detect islanding, the approach uses the voltage ripple content at PCC, along with a specified threshold value and delay duration. To detect the islanding and non-islanding conditions, the presented scheme is tested under different islanding and non-islanding conditions. From the simulation results it has been found that presented islanding detection technique detect islanding even under the most extreme condition, where the inverter output power is almost equivalent to the load consumption. As a result, the presented islanding detection technique offers the zero non detection zone. Verification of non-islanding conditions takes place in typical scenarios such as load switching and grid side distortion. Additionally, in the aforementioned non-islanding circumstances, no island signal is generated, confirming that there is no of false detection. Comparative investigation revealed that the suggested method outperforms standard passive techniques such as Over/Under Voltage and Rate of Change of Frequency, notably in terms of reducing detection time, eliminating the Non-Detection Zone, and preventing false trips.

CHAPTER-7

CONCLUSION, SOCIAL IMPACT OF RESEARCH AND FUTURE SCOPE OF WORK

7.1 INTRODUCTION

The global transition toward sustainable and resilient energy systems has underscored the importance of Renewable Energy Source (RES)-based microgrids, particularly those utilizing solar photovoltaic (SPV) technology. SPV systems offer effective solutions to pressing global challenges, including reducing carbon emissions, enhancing energy security, and enabling electrification in remote and underserved regions. Their modular design, environmental benefits, and rapidly declining costs have made them increasingly viable for both standalone and grid-connected applications. However, the intermittent nature of solar energy, along with challenges in grid integration and system stability, necessitates the development of advanced control strategies to ensure efficient and reliable operation. This thesis addresses these critical issues through comprehensive modeling, the design of novel control algorithms, and rigorous performance evaluation of SPV-based microgrids under various operating scenarios. By advancing the deployment and reliability of solarbased energy systems, this work directly contributes to the United Nations Sustainable Development Goals, particularly SDG 7 (Affordable and Clean Energy) and SDG 13 (Climate Action).

7.2 CONCLUSION OF THE STUDY

This thesis presents a comprehensive investigation into the performance enhancement and control strategies of solar photovoltaic (SPV)-based microgrids through the development and implementation of novel algorithms and advanced methodologies.

The initial chapters introduced the concept of solar photovoltaic (SPV)-based microgrids and emphasized the critical importance of efficient maximum power extraction, advanced inverter control, and reliable islanding detection in modern SPV systems. They also outlined the motivation for the study, identified key research gaps, and clearly defined the research objectives. Furthermore, an extensive review of existing literature was conducted, covering MPPT methodologies, inverter control strategies, and islanding detection techniques. The review highlighted notable limitations of conventional approaches, including slow convergence rates, sensitivity to environmental fluctuations, and inadequate performance under abnormal operating conditions. These limitations established the foundation for the novel contributions presented in this research. The key concluding remarks of the chapter are summarized below:

Chapter 3 presents a hybrid standalone solar PV microgrid integrated with battery energy storage and introduces a modified novel MPPT technique that combines the Incremental Conductance (INC) algorithm with a double closed-loop controller. This approach ensures maximum power extraction, stable DC link voltage, and enhanced

power quality through harmonic mitigation. The inner current loop provides fast dynamic response, while the outer voltage loop maintains voltage stability, contributing to overall system robustness, reliability, and adaptability under varying load conditions. The proposed method is validated through simulations demonstrating its effectiveness in dynamic operational scenarios.

Chapter 4 describes the design and implementation of a novel Horned Lizard Optimized Artificial Neural Network (HLO-ANN) MPPT technique for grid-connected solar PV systems. The proposed HLO-ANN technique combines the fast-learning capability of ANN with the global optimization strength of the Horned Lizard Optimization technique, allowing for precise and adaptive tracking of the maximum power point under dynamic environmental and load conditions. This methodology outperforms traditional and standard ANN-based MPPT methods, making it ideal for modern grid-connected PV systems.

Chapter 5 focuses on the design and implementation of a novel Honey Badger Algorithm-based PI (HBA-PI) controller for inverter control in grid-integrated solar PV systems. Inverter control plays a vital role in ensuring efficient DC-AC conversion, grid synchronization, and stable system performance under fluctuating environmental and load conditions. The proposed HBA-PI controller is specifically developed to achieve precise regulation of the DC link voltage, ensuring reliable power delivery from the PV array to the grid. In addition to the HBA-PI approach, this chapter also explores other optimization-based control techniques, including Cuckoo Search Optimized PI (CSO-PI) and Artificial Neural Network-based PI (ANN-PI) controllers. However, the primary focus remains on the HBA-PI controller due to its superior convergence speed, robustness, and dynamic response in maintaining voltage stability and enhancing overall system efficacy.

Chapter 6 This chapter presents a passive islanding detection technique for gridintegrated solar PV systems based on voltage ripple analysis at the point of common coupling (PCC). The presented method uses time-domain spectral analysis to detect abnormal ripple content in the VSI output voltage. Islanding is confirmed when the ripple exceeds a defined threshold for a specific duration. Unlike conventional passive techniques, this method effectively detects islanding even under minimal power mismatch without false detections. It demonstrates high accuracy and rapid detection within 3ms across various operating conditions, with no non-detection zones observed.

7.3 SOCIAL IMPACT OF RESEARCH

This research contributes significantly to the technical advancement of solar photovoltaic (SPV)-based microgrids, aligning with India's national mission to promote renewable energy through initiatives such as the PM-KUSUM Yojana, Solar Rooftop Scheme, and broader goals under the National Solar Mission. By developing robust MPPT algorithms, intelligent inverter control strategies, and efficient islanding detection methods, the thesis addresses critical challenges related to energy reliability, grid stability, and power quality

These improvements promote wider adoption of clean and affordable energy, especially in rural and under-electrified areas, fostering energy access, economic growth, and social development. The outcomes of this research directly align with multiple United Nations Sustainable Development Goals, notably SDG 3 (Good Health and well-being), SDG 7 (Affordable and Clean Energy), SDG 9 (Industry, Innovation, and Infrastructure), SDG 11 (Sustainable Cities and Communities), and SDG 13 (Climate Action). Additionally, by supporting sustainable infrastructure and cleaner energy solutions, this work indirectly contributes to several other SDGs, reflecting its comprehensive role in advancing sustainable development and energy equity.

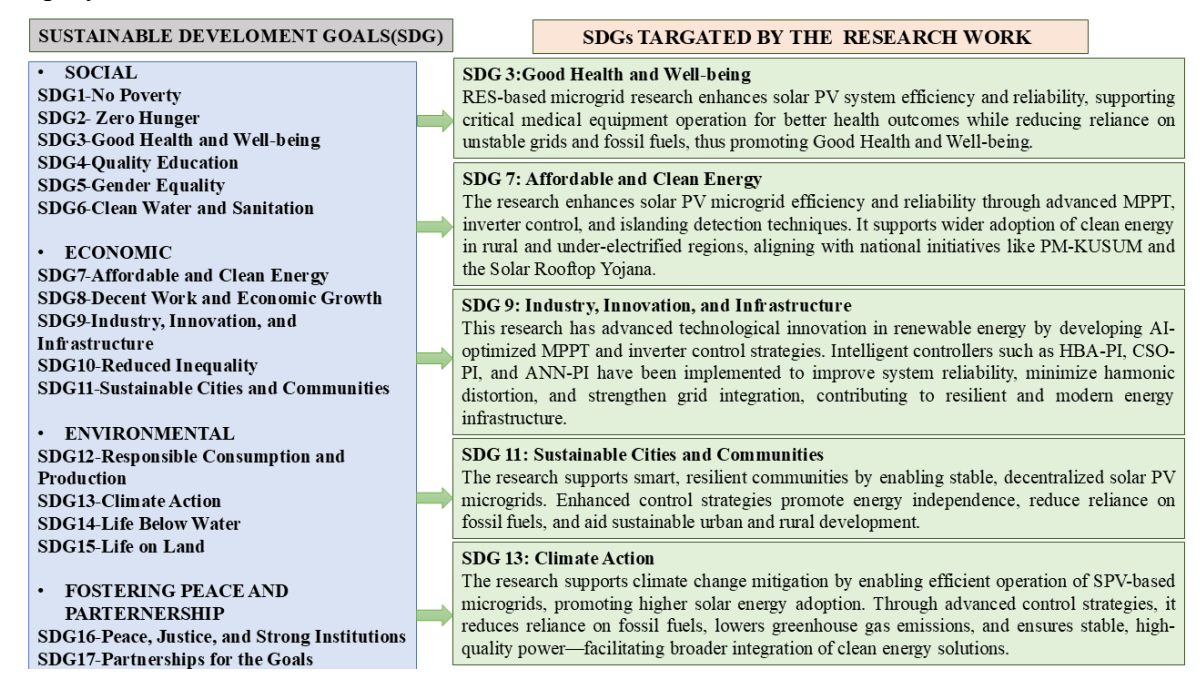


Fig.7.1 SDGs targeted by the research work

7.4 FUTURE SCOPE

- The proposed intelligent control algorithms can be validated through real-time hardware implementation on platforms such as DSPs, FPGAs, or microcontrollers. This validation will assess their practical feasibility, dynamic performance, and robustness in real-world operating conditions, bridging the gap between simulation and actual deployment.
- The developed control strategies can also be extended to hybrid energy systems integrating renewable sources like wind turbines and biomass, thereby enhancing system reliability and ensuring continuous power supply.
- With increasing digitalization, it becomes essential to consider techno-economic analysis and system reliability. Future research can explore secure communication protocols, intrusion detection systems, and fault-tolerant control mechanisms to

enhance the security and dependability of microgrids.

- As PV microgrids become increasingly digitized and vulnerable to cyber threats like data spoofing, DoS, and false signal injection, future work may integrate cybersecurity frameworks—such as blockchain-based data validation, secure authentication protocols, and intrusion detection algorithms—into MPPT control systems to detect and mitigate malicious intrusions and ensure secure, resilient energy management.
- Resilience measures, paired with advanced adaptive control strategies and realtime monitoring of PV output and DC bus conditions, could enable PV microgrids to maintain stable operation and self-recover under faults, islanding events, or extreme weather disturbances.
- Creating a digital twin of the PV microgrid enables real-time simulation of
 environmental changes, shading patterns, and load variations to adjust ANN
 weights or PI controller parameters before deployment, allowing predictive
 maintenance and proactive decision-making that reduces downtime and improves
 operational efficiency for both rural and industrial systems.

References

- [1] P. Mohammadi, R. Darshi, S. Shamaghdari and P. Siano, "Comparative Analysis of Control Strategies for Microgrid Energy Management with a Focus on Reinforcement Learning," in IEEE Access, vol. 12, pp. 171368-171395, 2024, doi: 10.1109/ACCESS.2024.3495032.
- [2] IEA (2024), Share of renewable electricity generation by technology, 2000-2030, IEA, Paris https://www.iea.org/data-and-statistics/charts/share-of-renewable-electricity-generation-by-technology-2000-2030, Licence: CC BY 4.0.
- [3] http://www.mnre.gov.in/
- [4] M. W. Altaf, M. T. Arif, S. N. Islam and M. E. Haque, "Microgrid Protection Challenges and Mitigation Approaches—A Comprehensive Review," in IEEE Access, vol. 10, pp. 38895-38922, 2022, doi: 10.1109/ACCESS.2022.3165011.
- [5] Mathew, Mobi, Md Shafayet Hossain, Sajeeb Saha, Som Mondal, and Md Enamul Haque. "Sizing approaches for solar photovoltaic-based microgrids: A comprehensive review." *IET Energy Systems Integration* 4, no. 1 (2022): 1-27.
- [6] X. Kong, X. Liu, L. Ma and K. Y. Lee, "Hierarchical Distributed Model Predictive Control of Standalone Wind/Solar/Battery Power System," in IEEE Transactions on Systems, Man, and Cybernetics: Systems, vol. 49, no. 8, pp. 1570-1581, Aug. 2019, doi: 10.1109/TSMC.2019.2897646.
- [7] P. P. Patankar, M. M. Munshi, R. R. Deshmukh and M. S. Ballal, "A Modified Control Method for Grid Connected Multiple Rooftop Solar Power Plants," in IEEE Transactions on Industry Applications, vol. 57, no. 4, pp. 3306-3316, July-Aug. 2021, doi: 10.1109/TIA.2021.3075195.
- [8] S. Sen and M. Kumar, "Distributed-MPC Type Optimal EMS for Renewables and EVs Based Grid-Connected Building Integrated Microgrid," in IEEE Transactions on Industry Applications, vol. 60, no. 2, pp. 2390-2408, March-April 2024, doi: 10.1109/TIA.2023.3332055.
- [9] J. Linares-Flores, A. Hernández-Mendez, J. A. Juárez-Abad, M. A. Contreras-Ordaz, C. García-Rodriguez and J. F. Guerrero-Castellanos, "MPPT Novel Controller Based on Passivity for the PV Solar Panel-Boost Power Converter Combination," in IEEE Transactions on Industry Applications, vol. 59, no. 5, pp. 6436-6444, Sept.-Oct. 2023, doi: 10.1109/TIA.2023.3274618.
- [10] B. Mandal and P. S. Bhowmik, "A Deep Neural Network-Based Highly Simplified Intelligent Approach for Maximum Power Point Tracking of Dye-Sensitized Solar Panel System," in IEEE Journal of Emerging and Selected Topics in Industrial Electronics, vol. 6, no. 1, pp. 196-203, Jan. 2025, doi: 10.1109/JESTIE.2024.3428350.
- [11] M. Merai, M. W. Naouar and I. Slama-Belkhodja, "An Improved DC-Link Voltage Control Strategy for Grid Connected Converters," in IEEE Transactions on Power Electronics, vol. 33, no. 4, pp. 3575-3582, April 2018, doi: 10.1109/TPEL.2017.2707398.
- [12] Z. Liang, X. Lin, Y. Kang, B. Gao and H. Lei, "Short Circuit Current Characteristics Analysis and Improved Current Limiting Strategy for Three-phase Three-leg Inverter under Asymmetric Short Circuit Fault," in IEEE Transactions on Power Electronics, vol. 33, no. 8, pp. 7214-7228, Aug. 2018, doi: 10.1109/TPEL.2017.2759161.

- [13] S. Chauhan and B. Singh, "Control of Solar PV Arrays Based Microgrid Intertied to a 3-Phase 4-Wire Distribution Network," in IEEE Transactions on Industry Applications, vol. 58, no. 4, pp. 5365-5382, July-Aug. 2022, doi: 10.1109/TIA.2022.3171529.
- [14] G. F. Silva, A. Donaire, M. M. Seron, A. McFadyen and J. Ford, "String Stability in Microgrids Using Frequency Controlled Inverter Chains," in IEEE Control Systems Letters, vol. 6, pp. 1484-1489, 2022, doi: 10.1109/LCSYS.2021.3114143.
- [15] D. Dong, B. Wen, P. Mattavelli, D. Boroyevich and Y. Xue, "Modeling and Design of Islanding Detection Using Phase-Locked Loops in Three-Phase Grid-Interface Power Converters," in IEEE Journal of Emerging and Selected Topics in Power Electronics, vol. 2, no. 4, pp. 1032-1040, Dec. 2014, doi: 10.1109/JESTPE.2014.2345783.
- [16] J. A. Pinto, K. P. Vittal and K. M. Sharma, "Passive Islanding Detection Scheme Based on Instantaneous Voltage and Current for a Multi-DG Microgrid," in IEEE Access, vol. 12, pp. 160715-160727, 2024, doi: 10.1109/ACCESS.2024.3484293.
- [17] A. Ali et al., "Investigation of MPPT Techniques Under Uniform and Non-Uniform Solar Irradiation Condition—A Retrospection," in IEEE Access, vol. 8, pp. 127368-127392, 2020, doi: 10.1109/ACCESS.2020.3007710.
- [18] R. B. Bollipo, S. Mikkili and P. K. Bonthagorla, "Hybrid, optimal, intelligent and classical PV MPPT techniques: A review," in CSEE Journal of Power and Energy Systems, vol. 7, no. 1, pp. 9-33, Jan. 2021, doi: 10.17775/CSEEJPES.2019.02720.
- [19] M. Kumar, K. P. Panda, J. C. Rosas-Caro, A. Valderrabano-Gonzalez and G. Panda, "Comprehensive Review of Conventional and Emerging Maximum Power Point Tracking Algorithms for Uniformly and Partially Shaded Solar Photovoltaic Systems," in IEEE Access, vol. 11, pp. 31778-31812, 2023, doi: 10.1109/ACCESS.2023.3262502.
- [20] Azad, M.L., Das, S., Sadhu, P.K., Satpati, B., Gupta, A. and Arvind, P., 2017, April. P&O algorithm based MPPT technique for solar PV system under different weather conditions. In 2017 International Conference on Circuit, Power and Computing Technologies (ICCPCT) (pp. 1-5). IEEE.
- [21] Kumari, J.S., Babu, D.C.S. and Babu, A.K., 2012. Design and analysis of P&O and IP&O MPPT techniques for photovoltaic system. *International Journal of Modern Engineering Research*, 2(4), pp.2174-2180.
- [22] Jately, V., Azzopardi, B., Joshi, J., Sharma, A. and Arora, S., 2021. Experimental Analysis of hill-climbing MPPT algorithms under low irradiance levels. *Renewable and Sustainable Energy Reviews*, 150, p.111467.
- [23] Selvan, D.S., 2013. Modeling and simulation of incremental conductance MPPT algorithm for photovoltaic applications. *International Journal of Scientific Engineering and Technology*, 2(7), pp.681-685.
- [24] Tey, K.S. and Mekhilef, S., 2014. Modified incremental conductance MPPT algorithm to mitigate inaccurate responses under fast-changing solar irradiation level. *Solar Energy*, *101*, pp.333-342.
- [25] Ferdous, S.M., Shafiullah, G.M., Oninda, M.A.M., Shoeb, M.A. and Jamal, T., 2017, November. Close loop compensation technique for high performance MPPT using ripple correlation control. In 2017 Australasian Universities Power Engineering Conference (AUPEC) (pp. 1-6). IEEE.

- [26] Lasheen, M., Abdel Rahman, A.K., Abdel-Salam, M. and Ookawara, S., 2017. Adaptive reference voltage-based MPPT technique for PV applications. *IET Renewable Power Generation*, 11(5), pp.715-722.
- [27] T. M. de Lima and J. A. C. B. Oliveira, "FPGA-Based Fuzzy Logic Controllers Applied to the MPPT of PV Panels—A Systematic Review," in IEEE Transactions on Fuzzy Systems, vol. 32, no. 8, pp. 4260-4269, Aug. 2024, doi: 10.1109/TFUZZ.2024.3392846.
- [28] H. Rezk, M. Aly, M. Al-Dhaifallah and M. Shoyama, "Design and Hardware Implementation of New Adaptive Fuzzy Logic-Based MPPT Control Method for Photovoltaic Applications," in IEEE Access, vol. 7, pp. 106427-106438, 2019, doi: 10.1109/ACCESS.2019.2932694.
- [29] M. Rezkallah, A. Hamadi, A. Chandra and B. Singh, "Real-Time HIL Implementation of Sliding Mode Control for Standalone System Based on PV Array Without Using Dumpload," in IEEE Transactions on Sustainable Energy, vol. 6, no. 4, pp. 1389-1398, Oct. 2015, doi: 10.1109/TSTE.2015.2436333.
- [30] U. K. Kalla, B. Singh, S. S. Murthy, C. Jain and K. Kant, "Adaptive Sliding Mode Control of Standalone Single-Phase Microgrid Using Hydro, Wind, and Solar PV Array-Based Generation," in IEEE Transactions on Smart Grid, vol. 9, no. 6, pp. 6806-6814, Nov. 2018, doi: 10.1109/TSG.2017.2723845.
- [31] O. Abdel-Rahim and H. Wang, "A new high gain DC-DC converter with model-predictive-control based MPPT technique for photovoltaic systems," in CPSS Transactions on Power Electronics and Applications, vol. 5, no. 2, pp. 191-200, June 2020, doi: 10.24295/CPSSTPEA.2020.00016.
- [32] M. Mao, Z. Xu, Q. Yuan and H. Li, "Current Interharmonic Prediction Control Based on MPC and Lyapunov for Grid-Connected PV System," in IEEE Journal of Emerging and Selected Topics in Power Electronics, vol. 12, no. 3, pp. 2686-2696, June 2024, doi: 10.1109/JESTPE.2024.3384317.
- [33] K. Y. Yap, C. R. Sarimuthu and J. M. -Y. Lim, "Artificial Intelligence Based MPPT Techniques for Solar Power System: A review," in Journal of Modern Power Systems and Clean Energy, vol. 8, no. 6, pp. 1043-1059, November 2020, doi: 10.35833/MPCE.2020.000159.
- [34] N. I. Nahin, S. P. Biswas, S. Mondal, M. R. Islam and S. M. Muyeen, "A Modified PWM Strategy With an Improved ANN Based MPPT Algorithm for Solar PV Fed NPC Inverter Driven Induction Motor Drives," in IEEE Access, vol. 11, pp. 70960-70976, 2023, doi: 10.1109/ACCESS.2023.3291339.
- [35] H. Renaudineau et al., "A PSO-Based Global MPPT Technique for Distributed PV Power Generation," in IEEE Transactions on Industrial Electronics, vol. 62, no. 2, pp. 1047-1058, Feb. 2015, doi: 10.1109/TIE.2014.2336600.
- [36] R. Sangrody, S. Taheri, A. -M. Cretu and E. Pouresmaeil, "An Improved PSO-Based MPPT Technique Using Stability and Steady State Analyses Under Partial Shading Conditions," in IEEE Transactions on Sustainable Energy, vol. 15, no. 1, pp. 136-145, Jan. 2024, doi: 10.1109/TSTE.2023.3274939.
- [37] J. Ahmed and Z. Salam, "A soft computing MPPT for PV system based on Cuckoo Search algorithm," 4th International Conference on Power Engineering, Energy and Electrical Drives,

- Istanbul, Turkey, 2013, pp. 558-562, doi: 10.1109/PowerEng.2013.6635669.
- [38] D. A. Nugraha, K. L. Lian and Suwarno, "A Novel MPPT Method Based on Cuckoo Search Algorithm and Golden Section Search Algorithm for Partially Shaded PV System," in Canadian Journal of Electrical and Computer Engineering, vol. 42, no. 3, pp. 173-182, Summer 2019, doi: 10.1109/CJECE.2019.2914723.
- [39] S. Mirjalili, S. M. Mirjalili, and A. Lewis, "Grey wolf optimizer," Advances in Engineering Software, vol. 69, pp. 46–61, Mar. 2014.
- [40] M. Adly and A. H. Besheer, "An optimized fuzzy maximum power point tracker for stand alone photovoltaic systems: Ant colony approach," 2012 7th IEEE Conference on Industrial Electronics and Applications (ICIEA), Singapore, 2012, pp. 113-119, doi: 10.1109/ICIEA.2012.6360707.
- [41] N. Kumar, I. Hussain, B. Singh and B. K. Panigrahi, "Normal Harmonic Search Algorithm-Based MPPT for Solar PV System and Integrated with Grid Using Reduced Sensor Approach and PNKLMS Algorithm," in IEEE Transactions on Industry Applications, vol. 54, no. 6, pp. 6343-6352, Nov.-Dec. 2018, doi: 10.1109/TIA.2018.2853744.
- [42] Nagadurga, T., Narasimham, P.V.R.L. and Vakula, V.S., 2022. Global maximum power point tracking of solar PV strings using the teaching learning-based optimization technique. *International Journal of Ambient Energy*, 43(1), pp.1883-1894. doi:10.1080/01430750.2020.1721327
- [43] Chandrasekharan, S., Subramaniam, S. and Veerakgoundar, V., 2023. Honey badger optimization algorithm based maximum power point tracking for solar photovoltaic systems. *Electric Power Systems Research*, 221, p.109393.
- [44] Moustafa, G., Smaili, I.H., Almalawi, D.R., Ginidi, A.R., Shaheen, A.M., Elshahed, M. and Mansour, H.S., 2023. Dwarf mongoose optimizer for optimal modeling of solar PV systems and parameter extraction. *Electronics*, 12(24), p.4990.
- [45] M. H. Ibrahim, S. P. Ang, M. N. Dani, M. I. Rahman, R. Petra and S. M. Sulthan, "Optimizing Step-Size of Perturb & Observe and Incremental Conductance MPPT Techniques Using PSO for Grid-Tied PV System," in IEEE Access, vol. 11, pp. 13079-13090, 2023, doi: 10.1109/ACCESS.2023.3242979.
- [46] A. Bharatee, P. K. Ray and P. S. Puhan, "Implementation of Improved Mixed Droop Technique with Sliding-Mode Control for Active Power Distribution in a Grid-Interactive Microgrid," in IEEE Transactions on Industrial Informatics, vol. 20, no. 9, pp. 10750-10760, Sept. 2024, doi: 10.1109/TII.2024.3396523.
- [47] Kumar, D.; Chauhan, Y.K.; Pandey, A.S.; Srivastava, A.K.; Kumar, V.; Alsaif, F.; Elavarasan, R.M.; Islam, M.R.; Kannadasan, R.; Alsharif, M.H. A Novel Hybrid MPPT Approach for Solar PV Systems Using Particle-Swarm-Optimization-Trained Machine Learning and Flying Squirrel Search Optimization. *Sustainability* **2023**, *15*, 5575. https://doi.org/10.3390/su15065575.
- [48] A. Chouksey, S. Awasthi, and S. K. Singh, "Fuzzy cognitive networkbased maximum power point tracking using a self-tuned adaptive gain scheduled fuzzy proportional integral derivative controller and improved artificial neural network-based particle swarm optimization," Fuzzy Sets Syst., vol. 381, pp. 26–50, Feb. 2020.
- [49] N. Priyadarshi, F. Azam, A. K. Sharma, and M. Vardia, "An adaptive neuro-fuzzy

- inference system-based intelligent grid-connected photovoltaic power generation," in Advances in Computational Intelligence, S. K. Sahana and V. Bhattacharjee, Eds. Singapore: Springer, 2020, pp. 3–14.
- [50] M. Lasheen and M. Abdel-Salam, "Maximum power point tracking using Hill Climbing and ANFIS techniques for PV applications: A review and a novel hybrid approach," Energy Conversion and Management, vol. 171, pp. 1002–1019, Sep. 2018.
- [51] S. Mohanty, B. Subudhi, and P. K. Ray, "A grey wolf-assisted perturb & observe MPPT algorithm for a PV system," IEEE Transactions on Energy Conversion, vol. 32, no. 1, pp. 340–347, Mar. 2017.
- [52] L. Xiong, L. Liu, X. Liu and Y. Liu, "Frequency Trajectory Planning Based Strategy for Improving Frequency Stability of Droop-Controlled Inverter Based Standalone Power Systems," in IEEE Journal on Emerging and Selected Topics in Circuits and Systems, vol. 11, no. 1, pp. 176-187, March 2021, doi: 10.1109/JETCAS.2021.3052006.
- [53] Kaundinya, D.P., Balachandra, P. and Ravindranath, N.H., 2009. Grid-connected versus stand-alone energy systems for decentralized power—A review of literature. *Renewable and sustainable energy reviews*, 13(8), pp.2041-2050.
- [54] Ali Khan, M.Y., Liu, H., Yang, Z. and Yuan, X., 2020. A comprehensive review on grid connected photovoltaic inverters, their modulation techniques, and control strategies. *Energies*, *13*(16), p.4185.
- [54] J. Dannehl, C. Wessels, and F. W. Fuchs, "Limitations of Voltage-oriented PI current control of grid-connected PWM rectifiers with LCL filters," IEEE Trans. Ind. Electron., vol. 56, no. 2, pp. 380–388, Feb. 2009.
- [55] G. Shen, X. Zhu, J. Zhang and D. Xu, "A New Feedback Method for PR Current Control of LCL-Filter-Based Grid-Connected Inverter," in IEEE Transactions on Industrial Electronics, vol. 57, no. 6, pp. 2033-2041, June 2010, doi: 10.1109/TIE.2010.2040552.
- [56] D. N. Zmood and D. G. Holmes, "Stationary frame current regulation of PWM inverters with zero steady-state error," IEEE Trans. Power Electron., vol. 18, no. 3, pp. 814–822, May 2003.
- [57]Lolamo, M., Kumar, R. and Sharma, V., 2024. Enhancing power quality of PV-DSTATCOM integrated grid with modified adaptive LMS control. *Electrical Engineering*, pp.1-14.
- [58] Pattnaik S, Kumar MR, Mishra SK, Gautam SP, Appasani B, Ustun TS. DC Bus Voltage Stabilization and SOC Management Using Optimal Tuning of Controllers for Supercapacitor Based PV Hybrid Energy Storage System. *Batteries*. 2022; 8(10):186. https://doi.org/10.3390/batteries8100186
- [59] P. Paikray, S. C. Swain, R. Dash and P. C. Panda, "A review on current control techniques for inverter for three phase grid connected renewable sources," 2017 Innovations in Power and Advanced Computing Technologies (i-PACT), Vellore, India, 2017, pp. 1-6, doi: 10.1109/IPACT.2017.8245203.
- [60] D. E. Kim and D. C. Lee, "Feedback linearization control of threephase UPS inverter systems," IEEE Trans. Ind. Electron., vol. 57, no. 3, pp. 963–968, Mar. 2010.
- [61] Athari, H., Niroomand, M. and Ataei, M., 2017. Review and classification of control systems in grid-tied inverters. *Renewable and Sustainable Energy Reviews*, 72, pp.1167-1176.

- [62]N. Altin, S. Ozdemir, H. Komurcugil and I. Sefa, "Sliding-Mode Control in Natural Frame With Reduced Number of Sensors for Three-Phase Grid-Tied LCL-Interfaced Inverters," in IEEE Transactions on Industrial Electronics, vol. 66, no. 4, pp. 2903-2913, April 2019, doi: 10.1109/TIE.2018.2847675.
- [63] Shih-Liang Jung and Ying-Yu Tzou, "Discrete sliding-mode control of a PWM inverter for sinusoidal output waveform synthesis with optimal sliding curve," in IEEE Transactions on Power Electronics, vol. 11, no. 4, pp. 567-577, July 1996, doi: 10.1109/63.506122.
- [64] Blaabjerg, F., Teodorescu, R., Liserre, M. and Timbus, A.V., 2006. Overview of control and grid synchronization for distributed power generation systems. *IEEE Transactions on industrial electronics*, 53(5), pp.1398-1409.
- [65] Tilli, A. and Tonielli, A., 1998. Sequential design of hysteresis current controller for three-phase inverter. *IEEE Transactions on Industrial Electronics*, 45(5), pp.771-781.
- [66] T. Kato, K. Inoue and M. Ueda, "Lyapunov-Based Digital Control of a Grid-Connected Inverter With an LCL Filter," in IEEE Journal of Emerging and Selected Topics in Power Electronics, vol. 2, no. 4, pp. 942-948, Dec. 2014, doi: 10.1109/JESTPE.2014.2322613.
- [67] Abedi, A., Rezaie, B., Khosravi, A. and Shahabi, M., 2020. DC-bus Voltage Control based on Direct Lyapunov Method for a Converter-based Stand-alone DC Micro-grid. *Electric Power Systems Research*, 187, p.106451.
- [68] Damen A, Weiland S. Robust Control. Measurement and Control Group Department of Electrical Engineering Eindhoven University of Technology P.O. Box 513, Draft version, July 2002.
- [69] Hornik T, Zhong Q Ch. A current-control strategy for voltage-source inverters in microgrids based on H∞ and repetitive control. IEEE Trans Power Electron 2011;26(3), [March].
- [70]Yang S, Lei Q, Peng FZ, Qian Z. A robust control scheme for grid-connected voltage source inverters. IEEE Trans Ind Electron. 2010.
- [71] Chhabra M, Barnes F, Robust current controller design using mu-synthesis for grid-connected three phase inverter. In: IEEE 40th Photovoltaic Specialist Conference. 2014. pp. 1413–1418.
- [72] Fu, X., Fu, Q. and Tang, W., 2019. Grid connection technique based on μ theory for a two-stage PV structure. *IET Power Electronics*, 12(6), pp.1545-1553.
- [73] Merai, M., Naouar, M.W., Slama-Belkhodja, I. and Monmasson, E., 2018. An adaptive PI controller design for DC-link voltage control of single-phase grid-connected converters. *IEEE Transactions on Industrial Electronics*, 66(8), pp.6241-6249.
- [74] Elnady, A. and AlShabi, M., 2019. Operation of parallel inverters in microgrid using new adaptive PI controllers based on least mean fourth technique. *Mathematical Problems in Engineering*, 2019(1), p.4854803.
- [75] Ghamari, S.M., Mollaee, H. and Khavari, F., 2020. Design of robust self-tuning regulator adaptive controller on single-phase full-bridge inverter. *IET Power Electronics*, 13(16), pp.3613-3626.
- [76] Shakeel, F.M. and Malik, O.P., 2020. On-line self-tuning adaptive control of an inverter in a grid-tied micro-grid. *Electric Power Systems Research*, 178, p.106045.

- [77] M. Nauman and A. Hasan, "Efficient implicit model-predictive control of a three-phase inverter with an output LC filter," IEEE Trans. Power Electron., vol. 31, no. 9, pp. 6075–6078, Sep. 2016.
- [78] L. Guo, N. Jin, C. Gan, and K. Luo, "Hybrid voltage vector preselectionbased model predictive control for two-level voltage source inverters to reduce the common-mode voltage," IEEE Trans. Ind. Electron., vol. 67, no. 6, pp. 4680–4691, Jun. 2020
- [79] D. F. Valencia, R. Tarvirdilu-Asl, C. Garcia, J. Rodriguez and A. Emadi, "A Review of Predictive Control Techniques for Switched Reluctance Machine Drives. Part I: Fundamentals and Current Control," in IEEE Transactions on Energy Conversion, vol. 36, no. 2, pp. 1313-1322, June 2021, doi: 10.1109/TEC.2020.3047983.
- [80]P. Cortés, A. Wilson, S. Kouro, J. Rodriguez and H. Abu-Rub, "Model Predictive Control of Multilevel Cascaded H-Bridge Inverters," in IEEE Transactions on Industrial Electronics, vol. 57, no. 8, pp. 2691-2699, Aug. 2010, doi: 10.1109/TIE.2010.2041733.
- [81] M. Tomlinson, H. d. T. Mouton, R. Kennel, and P. Stolze, "A fixed switching frequency scheme for finite-control-set model predictive control—Concept and algorithm," IEEE Trans. Ind. Electron., vol. 63, no. 12, pp. 7662–7670, Dec. 2016.
- [82]H. Chen, D. Wang, S. Tang, X. Yin, J. Wang, and Z. J. Shen, "Continuous control set model predictive control for three-level flying capacitor boost converter with constant switching frequency," IEEE J. Emerg. Sel. Topics Power Electron., vol. 9, no. 5, pp. 5996–6007, Oct. 2021
- [83] M. Trabelsi, L. Ben-Brahim, A. Gastli and H. Abu-Rub, "Enhanced Deadbeat Control Approach for Grid-Tied Multilevel Flying Capacitors Inverter," in IEEE Access, vol. 10, pp. 16720-16728, 2022, doi: 10.1109/ACCESS.2022.3149289
- [84] M. Pichan, H. Rastegar, and M. Monfared, "Deadbeat control of the standalone four-leg inverter considering the effect of the neutral line inductor," IEEE Trans. Ind. Electron., vol. 64, no. 4, pp. 2592–2601, Apr. 2017. [12] X. Xing, C. Zhang, A. Chen, H. Geng, and C. Qin, "Deadbeat control strategy for circulating current suppression in multiparalleled three-level inverters," IEEE Trans. Ind. Electron., vol. 65, no. 8, pp. 6239–6249, Aug. 2018.
- [85]J. Rodriguez et al., "State of the art of finite control set model predictive control in power electronics," IEEE Trans. Ind. Informat., vol. 9, no. 2, pp. 1003–1016, May 2013.
- [86] Wei, Z.X., Doctor, F., Liu, Y.X., Fan, S.Z. and Shieh, J.S., 2020. An optimized type-2 self-organizing fuzzy logic controller applied in anesthesia for propofol dosing to regulate BIS. *IEEE Transactions on Fuzzy Systems*, 28(6), pp.1062-1072.
- [87] Zhang, Q., Zhai, Z., Sun, S., Liu, X., Qian, J., Liu, S. and Fang, W., 2023. Fuzzy optimization for improving transient synchronization stability of VSCs in series-compensated system. *IEEE Transactions on Industry Applications*, 60(2), pp.3578-3587.
- [88] Zaky, Mohamed S., and Mohamed K. Metwaly. "A performance investigation of a four-switch three-phase inverter-fed IM drives at low speeds using fuzzy logic and PI controllers." *IEEE Transactions on Power Electronics* 32.5 (2016): 3741-3753.
- [89] Duţu, Liviu-Cristian, Gilles Mauris, and Philippe Bolon. "A fast and accurate rule-base generation method for Mamdani fuzzy systems." *IEEE Transactions on Fuzzy Systems* 26.2 (2017): 715-733
- [91] Marmouh, S., Boutoubat, M. and Mokrani, L., 2018. Performance and power quality

- improvement based on DC-bus voltage regulation of a stand-alone hybrid energy system. *Electric Power Systems Research*, 163, pp.73-84.
- [92] Abiodun, O.I., Jantan, A., Omolara, A.E., Dada, K.V., Umar, A.M., Linus, O.U., Arshad, H., Kazaure, A.A., Gana, U. and Kiru, M.U., 2019. Comprehensive review of artificial neural network applications to pattern recognition. *IEEE access*, 7, pp.158820-158846.
- [93] Mehrasa, M., Babaie, M., Sharifzadeh, M. and Al-Haddad, K., 2021. An input—output feedback linearization control method synthesized by artificial neural network for grid-tied packed E-cell inverter. *IEEE Transactions on Industry Applications*, 57(3), pp.3131-3142.
- [94] Singh, P., & Lather, J. S. (2020). Artificial neural network-based dynamic power management of a DC microgrid: a hardware-in-loop real-time verification. *International Journal of Ambient Energy*, 43(1),1730–1738.https://doi.org/10.1080/ 01430750.2020. 1720811
- [95] Lu, R., Hong, S.H. and Yu, M., 2019. Demand response for home energy management using reinforcement learning and artificial neural network. *IEEE Transactions on Smart Grid*, 10(6), pp.6629-6639.
- [96] Wen, Y.W., Peng, S.H. and Ting, C.K., 2021. Two-stage evolutionary neural architecture search for transfer learning. *IEEE Transactions on Evolutionary Computation*, 25(5), pp.928-940.
- [97] Vargas, O.S., Aldaco, S.E.D.L., Alquicira, J.A., Vela-Valdés, L.G. and Núñez, A.R.L., 2023. Adaptive network-based fuzzy inference system (ANFIS) applied to inverters: a survey. *IEEE Transactions on Power Electronics*, 39(1), pp.869-884.
- [98] Xue, G., Chang, Q., Wang, J., Zhang, K. and Pal, N.R., 2022. An adaptive neuro-fuzzy system with integrated feature selection and rule extraction for high-dimensional classification problems. *IEEE Transactions on Fuzzy Systems*, 31(7), pp.2167-2181.
- [99] S. E. De León-Aldaco, H. Calleja and J. Aguayo Alquicira, "Metaheuristic Optimization Methods Applied to Power Converters: A Review," in IEEE Transactions on Power Electronics, vol. 30, no. 12, pp. 6791-6803, Dec. 2015, doi: 10.1109/TPEL.2015.2397311.
- [100] S. E. De León-Aldaco, H. Calleja and J. Aguayo Alquicira, "Metaheuristic Optimization Methods Applied to Power Converters: A Review," in IEEE Transactions on Power Electronics, vol. 30, no. 12, pp. 6791-6803, Dec. 2015, doi: 10.1109/TPEL.2015.2397311.
- [101] A. Wazir and N. Arbab, "Analysis and optimization of IEEE 33 bus radial distributed system using optimization algorithm," J. Emerg. Trands Appl. Eng, vol. 1, no. 2, pp. 1–5, 2016.
- [102] V. Jambulingam, Particle Swarm Optimizer: Economic Dispatch with Valve Point Effect Using Various PSO Techniques. Diplom.de, 2014.
- [103] G. S. Chaurasia, A. K. Singh, S. Agrawal, and N. K. Sharma, "A metaheuristic firefly algorithm based smart control strategy and analysis of a grid connected hybrid photovoltaic/wind distributed generation system," Sol. Energy, vol. 150, pp. 265–274, Jul. 2017
- [104] W. Bai, M. R. Abedi, and K. Y. Lee, "Distributed generation system control strategies with PV and fuel cell in microgrid operation," Control Eng. Pract., vol. 53, pp. 184–193, Aug. 2016.
- [105] Li, C., Cao, C., Cao, Y., Kuang, Y., Zeng, L. and Fang, B., 2014. A review of islanding

- detection methods for microgrid. Renewable and Sustainable Energy Reviews, 35, pp.211-220.
- [106] Worku, M.Y., Hassan, M.A., Maraaba, L.S. and Abido, M.A., 2021. Islanding detection methods for microgrids: A comprehensive review. *Mathematics*, 9(24), p.3174.
- [107] Panigrahi, B.K., Bhuyan, A., Shukla, J., Ray, P.K. and Pati, S., 2021. A comprehensive review on intelligent islanding detection techniques for renewable energy integrated power system. *International Journal of Energy Research*, 45(10), pp.14085-14116.
- [108] Syamsuddin S, Rahim NA, Krismadinata Selvaraj J. Implementation of TMS320F2812 in islanding detection for Photovoltaic Grid Connected Inverter. In: International Conference for Technical Postgraduates (TECH POS); 2009. p. 1–5.
- [109] Mohamad H, Mokhlis H, Bakar AHA, Ping HW. A review on islanding operation and control for distribution network connected with small hydro power plant. Renewable and Sustainable Energy Reviews 2011;15:3952–62.
- [110] Smith GA, Onions PA, Infield DG. Predicting islanding operation of grid connected PV inverters. In: IEE Proceedings of Electric Power Applications, 2000;147:1–6.
- [111] Lopes LAC, Huili S. Performance assessment of active frequency drifting islanding detection methods. IEEE Transactions on Energy Conversion 2006;21:171–80.
- [112] Zeineldin HH, Kennedy S. Sandia frequency-shift parameter selection to eliminate nondetection zones. IEEE Transactions on Power Delivery 2009;24:486–7.
- [113] Menon, V., & Nehrir, M.H. (2007). Ahybrid islanding detection technique using voltage unbalance and frequency set point. IEEE Trans Power Syst, 22(1), 442–448.
- [114] Mahat, P., Chen, Z., & Bak-Jensen, B. (2008). Review of islanding detection methods for distributed generation, In electric utility deregulation and restructuring and power technologies, 2008. DRPT 2008. Third international conference on (pp. 2743–2748). Piscataway: IEEE.
- [115] Yin, J., Chang, L., & Diduch, C. (2006). A new hybrid anti-islanding algorithm in grid connected three-phase inverter system, In 2006 IEEE power electronics specialists conference (pp. 1–7).
- [116] Etxegarai, A., Eguía, P. and Zamora, I., 2011, April. Analysis of remote islanding detection methods for distributed resources. In *Int. conf. Renew. Energies power quality* (Vol. 1, No. 9).
- [117] Daubechies, I. (1990). The wavelet transform, time-frequency localization and signal analysis. IEEE Trans Inf Theory, 36(5), 961–1005.
- [118] Zhu, Y., Yang, Q., Wu, J., Zheng, D., & Tian, Y. (2008). A novel islanding detection method of distributed generator based on wavelet transform, In electrical machines and systems, 2008. ICEMS 2008. International conference on (pp. 2686–2688). Piscataway: IEEE.
- [119] Panigrahi, B.K., Bhuyan, A., Shukla, J., Ray, P.K. and Pati, S., 2021. A comprehensive review on intelligent islanding detection techniques for renewable energy integrated power system. *International Journal of Energy Research*, 45(10), pp.14085-14116.
- [120] S. Bera, S. Chakraborty, S. Kar and S. R. Samanta ray, "Hierarchical Control for Voltage Unbalance Mitigation Considering Load Management in Stand-Alone Microgrid," in IEEE Transactions on Smart Grid, vol. 14, no. 4, pp. 2521-2533, July 2023, doi:

- 10.1109/TSG.2022.3222490.
- [121] Verma, P., Garg, R. and Mahajan, P., 2020. Asymmetrical interval type-2 fuzzy logic control based MPPT tuning for PV system under partial shading condition. *ISA transactions*, 100, pp.251-263.
- [122] Kumar, A., Garg, R. and Mahajan, P., 2021. Modified synchronous reference frame control of solar photovoltaic-based microgrid for power quality improvement. *Arabian Journal for Science and Engineering*, 46, pp.1001-1018.
- [123] P. Azer and A. Emadi, "Generalized State Space Average Model for Multi-Phase Interleaved Buck, Boost and Buck-Boost DC-DC Converters: Transient, Steady-State and Switching Dynamics," in IEEE Access, vol. 8, pp. 77735-77745, 2020, doi: 10.1109/ACCESS.2020.2987277.
- [124] M. Nassary, E. Vidal-Idiarte and J. Calvente, "AC/DC Four-Switches Boost Buck Converter for EV Battery Charging," 2023 IEEE 17th International Conference on Compatibility, Power Electronics and Power Engineering (CPE-POWERENG), Tallinn, Estonia, 2023, pp. 1-7, doi: 10.1109/CPE-POWERENG58103.2023.10227436.
- [125] Dzhankhotov, V. and Pyrhönen, J., 2012. Passive \$ LC \$ filter design considerations for motor applications. *IEEE Transactions on Industrial Electronics*, 60(10), pp.4253-4259.
- [126] T. Selmi, M. Abdul-Niby, L. Devis and A. Davis, "P&O MPPT implementation using MATLAB/Simulink," 2014 Ninth International Conference on Ecological Vehicles and Renewable Energies (EVER), Monte-Carlo, Monaco, 2014, pp. 1-4, doi: 10.1109/EVER.2014.6844065.
- [127] K. Jain, M. Gupta and A. Kumar Bohre, "Implementation and Comparative Analysis of P&O and INC MPPT Method for PV System," 2018 8th IEEE India International Conference on Power Electronics (IICPE), Jaipur, India, 2018, pp. 1-6, doi: 10.1109/IICPE.2018.8709519.
- [128] H. Renaudineau et al., "A PSO-Based Global MPPT Technique for Distributed PV Power Generation," in IEEE Transactions on Industrial Electronics, vol. 62, no. 2, pp. 1047-1058, Feb. 2015, doi: 10.1109/TIE.2014.2336600.
- [129] Ahmed, J. and Salam, Z., 2014. A Maximum Power Point Tracking (MPPT) for PV system using Cuckoo Search with partial shading capability. *Applied energy*, 119, pp.118-130.
- [130] O. Lopez-Lapena, M. T. Penella and M. Gasulla, "A Closed-Loop Maximum Power Point Tracker for Subwatt Photovoltaic Panels," in IEEE Transactions on Industrial Electronics, vol. 59, no. 3, pp. 1588-1596, March 2012, doi: 10.1109/TIE.2011.2161254.
- [131] N. Pogaku, M. Prodanovic and T. C. Green, "Modeling, Analysis and Testing of Autonomous Operation of an Inverter-Based Microgrid," in IEEE Transactions on Power Electronics, vol. 22, no. 2, pp. 613-625, March 2007, doi: 10.1109/TPEL.2006.890003.
- [132] I. S. Mohamed, S. A. Zaid, M. F. Abu-Elyazeed and H. M. Elsayed, "Model predictive control-a simple and powerful method to control UPS inverter applications with output LC filter," 2013 Saudi International Electronics, Communications and Photonics Conference, Riyadh, Saudi Arabia, 2013, pp. 1-6, doi: 10.1109/SIECPC.2013.6551018.
- [133] Mishra, M., Mahajan, P. & Garg, R. Implementation and comparison of metaheuristically modified ANN MPPT controllers under varying solar irradiance conditions. Electr Eng (2023). https://doi.org/10.1007/s00202-023-02165-y.
- [134] Rizzo, S.A. and Scelba, G., 2015. ANN based MPPT method for rapidly variable shading

- conditions. Applied Energy, 145, pp.124-132.
- [135] Abdolrasol, M.G., Hussain, S.S., Ustun, T.S., Sarker, M.R., Hannan, M.A., Mohamed, R., Ali, J.A., Mekhilef, S. and Milad, A., 2021. Artificial neural networks-based optimization techniques: A review. *Electronics*, 10(21), p.2689.
- [136] Settles, M., 2005. An introduction to particle swarm optimization. *Department of Computer Science, University of Idaho*, 2, p.12.
- [137] Renaudineau, H., Donatantonio, F., Fontchastagner, J., Petrone, G., Spagnuolo, G., Martin, J.P. and Pierfederici, S., 2014. A PSO-based global MPPT technique for distributed PV power generation. *IEEE Transactions on Industrial Electronics*, 62(2), pp.1047-1058.
- [138] soufyane Benyoucef, A., Chouder, A., Kara, K. and Silvestre, S., 2015. Artificial bee colony based algorithm for maximum power point tracking (MPPT) for PV systems operating under partial shaded conditions. *Applied Soft Computing*, 32, pp.38-48.
- [139] Kumar, N., Hussain, I., Singh, B. and Panigrahi, B.K., 2016, November. Normal harmonic search algorithm based MPPT of solar PV system. In 2016 7th India International Conference on Power Electronics (IICPE) (pp. 1-6). IEEE.
- [140] Rezk, H. and Fathy, A., 2017. Simulation of global MPPT based on teaching—learning-based optimization technique for partially shaded PV system. *Electrical engineering*, 99, pp.847-859.
- [141] Moustafa, G., Smaili, I.H., Almalawi, D.R., Ginidi, A.R., Shaheen, A.M., Elshahed, M. and Mansour, H.S., 2023. Dwarf mongoose optimizer for optimal modeling of solar PV systems and parameter extraction. *Electronics*, 12(24), p.4990.
- [142] Peraza-Vázquez, H., Peña-Delgado, A., Merino-Treviño, M., Morales-Cepeda, A.B. and Sinha, N., 2024. A novel metaheuristic inspired by horned lizard defense tactics. *Artificial Intelligence Review*, 57(3), p.59.
- [143] B. Singh, S. Dwivedi, I. Hussain, and A. K. Verma, "Grid integration of solar PV power generating system using QPLL based control algorithm," Proc. 6th IEEE Power India Int. Conf. PIICON 2014, 10.1109/34084POWERI.2014.7117785.
- [144] N. Gupta, R. Garg and P. Kumar, "Characterization study of PV module connected to microgrid,"2015 Annual IEEE India Conference (INDICON), New Delhi, India, 2015, pp. 1-6, doi: 10.1109/INDICON.2015.7443360.
- [145] Joshi, A.S., Kulkarni, O., Kakandikar, G.M. and Nandedkar, V.M., 2017. Cuckoo search optimization-a review. *Materials Today: Proceedings*, 4(8), pp.7262-7269.
- [146] Chandrasekharan, S., Subramaniam, S. and Veerakgoundar, V., 2023. Honey badger optimization algorithm based maximum power point tracking for solar photovoltaic systems. *Electric Power Systems Research*, 221, p.109393.
- [147] Bhattacharya, A. and Chakraborty, C., 2010. A shunt active power filter with enhanced performance using ANN-based predictive and adaptive controllers. *IEEE transactions on industrial electronics*, 58(2), pp.421-428.
- [148] Singh, P. and Lather, J.S., 2022. Artificial neural network-based dynamic power management of a DC microgrid: A hardware-in-loop real-time verification. *International Journal of Ambient Energy*, 43(1), pp.1730-1738.
- [149] Gupta, N. and Garg, R., 2018. Algorithm for islanding detection in photovoltaic

generator network connected to low-voltage grid. *IET Generation, Transmission & Distribution*, 12(10), pp.2280-2287.

[150] Guha, B., Haddad, R.J. and Kalaani, Y., 2016. Voltage ripple-based passive islanding detection technique for grid-connected photovoltaic inverters. *IEEE Power and Energy Technology Systems Journal*, 3(4), pp.143-154.

[151] Somalwar, R.S., Shinde, D.A. and Kadwane, S.G., 2023. Performance evaluation of voltage ripple-based passive islanding detection method for a single-phase utility-connected micro-grid system. *IETE Journal of Research*, 69(2), pp.854-861.

APPENDIX

I. Photovoltaic specifications

Parameters	Value
Maximum Power(W)	213.15
Voltage at MPP $V_{mp}(V)$	28
Current at MPP I _{mp} (A)	7.35
Open circuit voltage V _{oc} (V)	36.3
Short circuit current I _{sc} (A)	7.84
V _{oc} temperature coefficient (% deg.C)	-0.361
I _{sc} temperature coefficient (% deg.C)	0.102
Photovoltaic temperature (deg.C)	25
Number of cell (N _{cell})	60
Series cells (N_S)	3
Parallel cells (N_p)	20

II. SPV System specifications

	Parameters	Attributes
PV Array	Power Ppv	12.79kW
	PV short circuit current (I _{sc})	23.52A
	PV open circuit voltage (Voc)	726V
	PV current at MPP (I _{mpp})	22.05A
	PV voltage at MPP (V _{mpp})	580V
DC-DC Converter	Duty ratio (α)	0.5-0.6
	Converter Inductor (L)	6mH
	Capacitor (C)	$3\mu F$
	Switching frequency	10 kHz
	DC link voltage (V _{DC})	750V
	Interfacing inductor (L _f)	7mH
Bidirectional converter	Inductor (L1)	0.00019Н
	Capacitor (C1)	350 μF
	DC link voltage (V _{DC})	750V
	Interfacing inductor (L _f)	6mH
	Filter Capacitance (Cf)	101.14uF
	Series Resistance (Rf)	0.001H

	V _{LL} (Line - line voltage)	415V
Grid	Grid frequency	50Hz
	Grid Resistance (R _s)	0.11ohm
	Grid Inductance (L _s)	0.35mH

III. Wind turbine and PMSG generator specifications

Parameters	Value
Rated Mechanical Power	12.3kW
Base wind speed	12m/s
Max mechanical power at 12 m/s	0.85 pu
Actual mechanical power at 12 m/s	$0.85 \times 12.3 \text{ kW} = 10.455 \text{ kW}$
Generator efficiency	90%
Electrical output power at 12 m/s	$0.9 \times 10.455 \text{kW} = 9.41 \text{kW}$
Stator phase resistance (Rs)	0.0485
Inductance q- and d-axis $(L_q \text{ and } L_d)$	0.395e-3,0.395e-3
Flux linkage (ψ)	0.1194
pitch angle in degree (β)	0
Power Coefficient (Cp)	0.4097
Air density $kg/m^3(\rho)$	1.225
Radius in m (R)	1.30
C1, C2, C3, C4, C5 and C6	0.5176, 116, 0.4, 5, 21, and 0.0068.
Area swept by the blades in $m^2(A_r)$	5.31
Tip speed ration (TSR)	8.1

Curriculum Vitae

Basic Information

Name: - SHRUTI PRAJAPATI

Date of Birth: - 21/09/1997 Place of Birth: - Deoria, UP Nationality: - Indian

Educational Qualification

Pursuing PhD from Department of Electrical Engineering, Delhi Technological University, Delhi.

PhD Title: Control Techniques for Improved Performance of Microgrid Integrated with RES

Research Interest

Designing control techniques for RES based microgrid using advanced techniques,

- Development of MPPT algorithm for Solar PV based microgrid.
- Development of MPPT technique for hybrid res based microgrid and DC bus voltage regulation.
- Development of Inverter control techniques for grid integrated SPV based microgrid.
- Development of Islanding detection technique for grid integrated SPV based microgrid.

Contact Details

Email: shrutiprajapati 2k21phdee03@dtu.ac.in, shruti7704@gmail.com

Mobile No.: - (+91)-9880857884